A Hybrid Numerical Method for 3D Multiphysics Modeling of Ultrasonic Transit-Time Flowmeters

Including Sound Propagation in Real Pipe Flows

Panagiotis Papathanasiou

Thesis for the degree of Philosophiae Doctor (PhD)
University of Bergen, Norway
2023

UNIVERSITY OF BERGEN

A Hybrid Numerical Method for 3D Multiphysics Modeling of Ultrasonic Transit-Time Flowmeters

Including Sound Propagation in Real Pipe Flows

Panagiotis Papathanasiou

Thesis for the degree of Philosophiae Doctor (PhD)
at the University of Bergen

Date of defense: 20.10.2023

Year: 2023

Title: A Hybrid Numerical Method for 3D Multiphysics Modeling of Ultrasonic Transit-Time Flowmeters

Name: Panagiotis Papathanasiou

Print: Skipnes Kommunikasjon / University of Bergen

Preface

This work has been the result of collaboration between the University of Bergen, Norway and Endress+Hauser Flow, Switzerland. I would like to thank everyone who was directly or indirectly involved in the challenging and long task of the realization of a doctoral thesis.

Firstly, I want to express my sincere gratidude, to Prof. Per Lunde, my main supervisor at the University of Bergen. I am grateful that he shared with me his broad and deep knowledge of physics, acoustics, and ultrasonic flowmeters. His advice on theoretical and technical matters as well as on the approach of solving problems has increased the quality of this work. His critical thinking, his advice, and our discussions motivated me to push the boundaries and go the extra mile in order to solve seemingly unsolvable problems.

I would like to offer my sincere thanks to my supervisors at Endress+Hauser Flow, Dr. Michal Bezděk and Dr. Vivek Kumar. I deeply appreciate that they offered their unparalleled expertise on ultrasonics and fluid dynamics, respectively. Many ideas became clearer through our deep, productive and exciting discussions, while the road to the final goal became less steep thanks to their supervision, commitment, and guidance.

I am deeply grateful to Dr. Wolfgang Drahm, my manager at Endress+Hauser Flow, who gave me the opportunity to work on this topic, always believed in me and encouraged me to complete the thesis. He made sure that I stay on track, manage the high load of work, and plan correctly and efficiently. He helped me prioritize and inspired me with his words during the course of the thesis.

I would like to offer my special thanks to Prof. Emer. Magne Vestrheim at the University of Bergen, for our long and invaluable meetings. His knowledge, and experience in the field of ultrasonic flowmeters as well as his wisdom and pertinent remarks were crucial for improving and successfully completing this work.

I would like to extend my sincere thanks to my colleagues at Endress+Hauser Flow, Dr. Simon Triebenbacher, Marc Hollmach, Pierre Überschlag, and Rolf Sonderkamp. Simon provided me with his expertise on software and numerical simulations, Marc offered his know-how on signal-processing and analysis of results, Pierre supported me with flow measurements and piezoelectricity topics, and Rolf, with his unprecedented experience in ultrasonic flow measurement, believed in this work from the beginning and assisted to initiate it.

Finally yet just as importantly, my final thanks is directed to the people in my private life, who were vital for the accomplishment of the thesis. I want to express my gratitude to my parents who have always been there for me, at every step of the way, with their love, trust, and support. A special thanks also goes to my friends, at different countries of the world, who made even the difficult times seem much easier and pleasant.

Dedication

To my mother Ελένη and to my father Γιώργος.

Abstract

Ultrasonic Transit-Time Flowmeters (UTTF) and their modeling are on the main focus in this dissertation. UTTF can be categorized into clamp-on and inline devices depending on the needs of applications for flow measurement. Simulations, studies, and experimental verification of inline gas devices with high demands of accuracy are performed in the present work. It is demonstrated that with the use of simulations, it is conceivable to accelerate innovation, as well as to continuously improve measurement accuracy and technology for the fast-growing market of UTTF.

In the present thesis, a multiphysics, hybrid numerical method is proposed i.e., a combination of a Finite Element Method (FEM) and a Finite Volume Method (FVM), for the purpose of 3D simulations and investigation of physical phenomena that affect the behavior of UTTF. The developed method, 'Simulations of Piezoelectricity, Acoustics, Coupled with CFD' (SimPAC^2), is used as a design tool of UTTF, as well as for the improvement of understanding the operation of UTTF. For the simulation, the UTTF is split into parts and the respective, more appropriate method is used for each part. More specifically, FEM is utilized for the simulation of piezoelectricity and structural acoustics in the solid parts i.e., the transducers and, if desired, partially the meter-body of the flowmeter. FEM is also used for the simulation of wave propagation in a part of the moving fluid medium. Acoustics and computational fluid dynamics (CFD) are considered in the moving fluid medium, as well as their interaction with each other with the use of FVM, which is traditionally more appropriate for CFD and large simulations that need to be highly parallelized. The hybrid SimPAC^2 method requires complex interfaces between the FEM and FVM method, which are created in the course of the present work.

A comparison of SimPAC^2 results with pure CFD, FEM and measurements is carried out. A chain verification takes place, starting from a simulation of a simple geometry of piezoelectric elements in air in zero and uniform flow. Complexity is added with the simulation of a diametrical single-path flowmeter equipped with either piezoelectric elements or real transducers. Finally, a real industrial flowmeter with two chordal paths is simulated and measured in a flow rig, with the agreement of the results satisfying the set criteria. The simulations allowed for the systematic study and quantification of complex, much-anticipated effects in UTTF, such as 3D cavity effects, the position of flush, recessed, and protruded transducers, as well as the flow effect around the transducers and in the meter-body.

The performed 3D multiphysics simulations capture interactions between ultrasonic waves and flow in the 3D geometry that are, by definition, not possible to be captured by 2D simulations. Before SimPAC^2, the performance of systematic 3D multiphysics simulations was computationally expensive or impossible to perform. Thus, the simulation of a full 3D geometry of an UTTF is achieved from input voltage on the transmitter to output voltage on the receiver. It is demonstrated that SimPAC^2 can be further used as a tool for the design and optimization of UTTF, the reduction of the development cycle and the improvement of accuracy and linearity.

Abstract in Norwegian

Ultralyd mengdemålere av typen Ultrasonic Transit-Time Flowmeters (UTTF) og deres modellering er hovedfokus i denne avhandlingen. UTTF kan kategoriseres i clamp-on og inline-målere avhengig av behovene til applikasjoner for mengdemåling. Simuleringer, studier og eksperimentell verifisering av inline-målere med høye krav til nøyaktighet utføres i dette arbeidet. Det er demonstrert at ved bruk av simuleringer er det mulig å akselerere innovasjon, samt å kontinuerlig forbedre målenøyaktighet og teknologi for det raskt voksende markedet for UTTF.

I denne avhandlingen foreslås en multifysikk, hybrid numerisk metode, dvs. en kombinasjon av en Finite Element Method (FEM) og en Finite Volume Method (FVM), for 3D-simuleringer og undersøkelse av fysiske fenomener som påvirker oppførselen til UTTF. Den utviklede metoden, 'Simulations of Piezoelectricity, Acoustics, Coupled with CFD' (SimPAC2), brukes som et designverktøy for UTTF, samt for å forbedre forståelsen av virkemåten av UTTF. For simuleringen er UTTF delt inn i to deler, og den respektive, mer passende metoden brukes for hver del. Konkret brukes FEM for simulering av piezoelektrisitet og strukturell akustikk i de faste delene, dvs. transduserne og om ønskelig, delvis i målerøret. FEM brukes også til simulering av bølgeutbredelse i deler av mediet. Akustikk og simulasjoner ved Computational Fluid Dynamics (CFD) vurderes i mediet, samt deres interaksjon med hverandre ved bruk av FVM, som tradisjonelt er mer passende for CFD og store simuleringer som trenger sterk parallellisering. Den hybride SimPAC2-metoden krever komplekse grensesnitt mellom FEM- og FVM-metoden, som er utviklet i løpet av denne oppgaven.

En sammenligning av SimPAC2-resultater med simuleringer basert på kun CFD og FEM, samt sjekket mot fysisk utførte målinger. En kjedeverifisering utføres, med utgangspunkt i en simulering av en enkel geometri av piezoelektriske elementer i luft uten strømning og i jevn strømning. Kompleksiteten økes med simuleringen av en diametral en-stråle mengdemåler utstyrt med enten piezo-elektriske elementer eller ekte transdusere. Til slutt ble en industriell mengdemåler med to kordale strålebaner simulert og verifisert i en kalibreringsrigg. Resultatene stemte overens innen fastsatte kriterier. Simuleringene gjorde det mulig å systematisk studere og kvantifisere komplekse, forventede effekter i UTTF, for eksempel 3D-hulromseffekter for flush monterte, tilbaketrekkende eller utstikkende transdusere.

De utførte 3D-multifysikksimuleringene fanger opp interaksjoner mellom ultralydbølger og strømning i 3D-geometrien som per definisjon ikke kan fanges opp av 2D-simuleringer. Før SimPAC2 var det dyrt eller umulig å utføre systematiske 3D-multifysikksimuleringer. Dermed oppnås simulering av en full 3D-geometri av en UTTF fra inngangsspenning på senderen til utgangsspenning på mottakeren. Det er demonstrert at SimPAC2 kan brukes videre som et verktøy for design og optimalisering av UTTF, reduksjon av utviklingssyklusen og forbedring av nøyaktighet og linearitet.

Table of Contents

List of Symbols

Abbreviations

1D One-dimensional

2D Two-dimensional

3D Three-dimensional

AC Alternating current

APE Acoustic perturbation equations

ASM Angular spectrum method

BC Boundary condition

BEM Boundary Element Method

CAWE Convected acoustic wave equation

CFD Computational Fluid Dynamics

CGNS CFD general notation system

CNA CFD - Non-acoustic

csv Comma separated values

DES Detached Eddy simulation

DG Discontinuous Galerkin

DNS Direct numerical simulation

DS Downstream

DUT Device under test

EBRSM Elliptic blending Reynolds-stress model

EDAT Elastodynamic Acoustic Toolbox

FDM Finite Difference Method

FEM Finite Element Method

FFT Fast-Fourier transformation

FlowDC Flow disturbance compensation

FPCF Flow profile correction factor

FVM Finite Volume Method

GB Giga-bytes

GPU Graphical processing unit

HIRM Helmholtz integral ray-tracing method

HPC High-performance computing

IDDES Improved delayed detached eddy simulation

Int1 Interface 1 in fluid towards the sender

Int1 Interface 2 in fluid towards the receiver

IoT Internet of Things

LAE Linearized acoustic equations

LDV Laser Doppler velocimetry

LEE Linearized Euler equations

LEFD Linearized equations of fluid dynamics

LES Large Eddy simulation

MB Mega-bytes

N-S Navier-Stokes

NDT Non-destructive testing

PDE Partial differential equation

PE Pierce equation

pMUT Piezoelectric micromachined ultrasonic transducer

PZT Lead zirconate titanate

R&D Research and development

RANS Reynolds-Averaged-Navier-Stokes

RKEPS Realizable k-ϵ

RSM Reynolds-stress model

S-FEM Smoothed Finite Element Method

SBFEM Scaled Boundary Finite Element Method

SCS Swiss calibration services

SimPAC^2 Simulations of Piezeoelectricity, Acoustics, Coupled with CFD

SIMPLE Semi-Implicit Method for Pressure Linked Equations

SPD Spectral power density

SRS Scaled-resolving simulation

SST Shear-stress transport

T1 Downstream transducer 2

T1 Upstream transducer 1

TE Thickness-extensional

ToF, ToF Time-of-flight

US Upstream

USM Ultrasonic Flowmeter

UTTF Ultrasonic Transit Time Flowmeter

WMLES Wall-modelled large eddy simulation

Greek Symbols

$[\boldsymbol{\epsilon}]$ Dielectric constant tensor for constant strain

α Parameter for the Gaussian function

α_M, β_k Rayleigh parameters

$\bar{\boldsymbol{\tau}}$, $\bar{\tau}_{ij}$ Averaged viscous stress tensor

$\boldsymbol{\tau^t}$, τ^t_{ij} Reynolds stresses tensor

$\boldsymbol{\tau_{inc}}, \tau_{inc,ij}$ Incompressible stress tensor

$\boldsymbol{\tau}, \tau_{ij}$ Viscous, deviatoric stress tensor

δ_{ij} Kronecker delta

γ Ratio of specific heat capacities

Λ Lame constant

λ Acoustic wavelength

μ Lame constant, dynamic viscosity

μ_T Eddy viscosity

ν Poisson ratio, kinematic viscosity

ν_T Kinematic eddy viscosity

Ω Domain or configuration of a body

ω Angular frequency

Φ, ϕ Acoustic velocity scalar potential

π Mathematical constant

Ψ Vector potential

ψ Electric potential

ρ, ρ_0, ρ' Total density, ambient density, acoustic density

τ_w Shear stress

θ Inclination angle between the transducer main axis and the axis of the pipe

θ_i Inclination angle for path i

ε Dissipation rate

Mathematical Symbols

$\bar{\square}$ Time-averaged quantity

$\ddot{\square}$ Second partial derivative with respect to time

$\dot{\square}$ Partial derivative with respect to time

$\frac{\partial}{\partial t}$ Partial derivative with respect to time

$\frac{\partial}{\partial x}$, $\frac{\partial}{\partial y}$, $\frac{\partial}{\partial z}$ Partial derivative with respect to x, y, and z

$\frac{d}{dt}$ Total derivative with respect to time

$\int$, $\iint$, $\iiint$ integral, double integral, triple integral

$\nabla\cdot$ divergenve

$\nabla\times$ curl

∇ nabla operator, gradient

∇^2 Laplacian

$\square'$ Fluctuation of quantity

$\square^T$ Transpose of vector or tensor

$\sum$ disretized summation

D_t material derivative

j Imaginary unit

tr([□]) trace of a tensor

Latin Symbols

$[\boldsymbol{c^E}]$ Tensor of elasticity moduli for constant electric field

$[\boldsymbol{c}]$ Tensor of elasticity moduli

$[\boldsymbol{e}]$ Piezoelectric constant tensor

$[\boldsymbol{I}]$ Identity matrix

$[\boldsymbol{S}]$ Strain tensor

$[\boldsymbol{T}]$ Stress tensor

$\%\text{deviation}_{CFD}$ Flow-velocity deviation calculated with CFD

$\%\text{deviation}$, $\%deviation$ Flow-velocity deviation

$\%\text{deviation}_{\text{corr}}$, $\%deviation_{corr}$ Flow-velocity deviation corrected

$\%\text{error}_c$ Error of speed of sound

$\%\text{Error}_{\text{zero-cross}}$ Maximum error due to zero-crossing selection

$\%dev_{\Delta t}$ Δt deviation

$\%dev_{ToF,0}$ ToF deviation for zero flow

$\%dev_{ToF}$ ToF deviation

ś Condensation

$\bar{\boldsymbol{D}}_{\boldsymbol{s}}$ Mean rate of strain tensor

$\boldsymbol{D_s}$ Rate of strain tensor

$\boldsymbol{D}$ Electric displacement vector

$\boldsymbol{d}, \boldsymbol{r}$ Position vector

$\boldsymbol{e_x}, \boldsymbol{e_y}, \boldsymbol{e_z}$ Unit vector in x,y,z direction

$\boldsymbol{E}$ Electric field vector

$\boldsymbol{n}$ Unit vector

$\boldsymbol{t(n)}$ Traction

$\boldsymbol{u}, u_i$ Mechanical displacement (vector and in direction i)

$\boldsymbol{v'}, v'$ Acoustic velocity (vector, scalar)

$\boldsymbol{v_0}, v_0$ Ambient flow velocity (vector, scalar)

$\boldsymbol{v_{wall}}$ Flow velocity at the wall

$\boldsymbol{v}, v$ Total velocity (vector, scalar)

$\boldsymbol{v}_{sol}^{'}$ Particle velocity in the solid

Δt Transit time difference between upstream and downstream traveling waves

$\Delta t_{i,0}$ Transit time difference for zero flow for a path i

$\Delta V(j)$ Volume of a mesh cell j

$\dot{m}$ Mass flow

A Cross-sectional area or signal amplitude

A_{ref} Cross-sectional area at a reference position

B Differential operator

B_s Adiabatic bulk modulus

c Speed of sound

c_l Longitudinal wave velocity

c_p Specific heat capacity at constant pressure

c_t Shear wave velocity

c_v Specific heat capacity at constant volume

C_μ Constant used in turbulence model

c_{MS} Simulated or measured speed of sound

CFL Courant-Friedrichs-Lewy number

$Crit$ Optimization criterion

D Chord of a sound-path of a flowmeter, diameter of meter body

d Position of a point

d_w Distance from the wall

$dt_{sim,up}$ Upsampled sampling period

dt_{sim} Time-step of simulation or sampling period

dV Infinitessimal volume

dx_{sim} Cell dimension for simulation

$E_{\bar{v}_i}$ Relative standard uncertainty of average flow velocity

E_m Elasticity modulus

F Symbolic solving scheme or Fourier transform

f Frequency

f_c Carrier frequency

G Shear modulus

$G(r_t)$ Gaussian function for a radial coordinate r_t

H Transfer function

i Index indicating path number

$i(t)$ Current in time

k Turbulent kinematic energy

k_a Calibration factor

L Distance between transducers for path i

L Distance between transducers

l Characteristic length of the flow

L_{cav} Length of cavity

M Mach number

N Number of sound paths

n_0 Exponent depending on Re

n_t Temporal discetization, time-steps per period

n_x Spatial resolution of mesh, cells per wavelength

n_{zero} Number of zero-crossings

p, p_0, p' Total pressure, ambient pressure, acoustic pressure

Q Electrical charge in frequency

q Axial volume flow-rate

$q(t)$ Electrical charge in time

q_c, q_m Sources of sound

q_{ref} Reference axial volume flow-rate

R Radius of the meter body

R_{ref} Radius of the reference cross-section

Re Reynolds number

Re_d Reynolds number based on wall distance

s, s_0, s' Total entropy, ambient entropy, acoustic entropy

s_{xx}, s_{yy}, s_{zz} Normal strains

$s_{xy}, s_{yx}, s_{xz}, s_{zx}, s_{yz}, s_{zy}$ Shear strains

SPL Sound pressure level

T Signal period

t Time

t_3 ToF for last of 3 zero-crossings to reach Int1

$t_3, 3$ ToF for last of 3 zero-crossings to travel from Int2 to the receiver

$t_{12,i,0}^{diff}$ Downstream time-delay for diffraction at zero flow for a sound-path i

$t_{12,i,0}^{el,cab}$ Downstream time-delay for electronics and cables at zero flow for a sound-path i

$t_{12,i,0}^{eltr}$ Downstream time-delay for electronics, cables, transducer, diffraction at zero flow for a sound-path i

$t_{12,i,0}^{tr}$ Downstream time-delay for transducers at zero flow for a sound-path i

$t_{12,i,tot}$ Total downstream time of flight for a sound-path i

$t_{12,i}$ Downstream time-of-flight in fluid for a sound-path i

t_{12} Downstream time-of-flight in fluid

$t_{21,i,0}^{diff}$ Upstream time-delay for diffraction at zero flow for a sound-path i

$t_{21,i,0}^{el,cab}$ Upstream time-delay for electronics and cables at zero flow for a sound-path i

$t_{21,i,0}^{eltr}$ Upstream time-delay for electronics, cables, transducer, diffraction at zero flow for a sound-path i

$t_{21,i,0}^{tr}$ Upstream time-delay for transducers at zero flow for a sound-path i

$t_{21,i,tot}$ Total upstream time of flight for a sound-path i

$t_{21,i}$ Upstream time-of-flight in fluid for a sound-path i

t_{21} Upstream time-of-flight in fluid

$t_{cav,i}$ Time-delay in cavity for path i

T_{ij} Stresses in direction i on plane perpendicular to j

$t_{refl,rec}$ ToF for reflection criterion on the receiver

t_{refl} ToF for reflection criterion on the sender

$ToF_{crit}, ToF_{crit,m}, ToF_{crit,sim}$ Convergence criterion based on ToF

$u(\bar{v}_i)$ Standard uncertainty of average flow velocity

u_T Shear velocity

V Voltage

V_1 Voltage-source

V_5 Received open-circuit voltage

$v_5(t)$ Voltage on receiver in time

v_A Axial flow velocity

V_i Volume of cylindrical sound path i

v_T Transversal flow velocity

$v_{0,CFD}$ Flow velocity calculated with CFD for all sound paths

v_{calc} Flow velocity calculated from all sound paths of a flowmeter

$v_{cyl,i,G}$ Gauss-weighted volume average flow velocity in cylindrical sound path i

$v_{cyl,i}$ Volume average flow velocity in cylindrical sound path i

$v_{line,i}$ Line average flow velocity along sound path i

v_{max} Maximum flow velocity

$v_{path,i}$ Average axial flow velocity along a sound path i

v_{path} Average axial flow velocity along a sound path

v_{ref} Average axial reference flow velocity

w_i Weight factor for a sound path i

x, y, z Cartesian coordinates

x_{edge} Edge-length of the mesh cells

$y+$ Dimensionless distance to the wall

Z Electrical impedance

z Acoustic impedance

Chapter 1

Introduction

1.1 Introduction to ultrasonic flowmeters principle and modeling

Flow measurement, i.e. the quantification of the movement of a fluid that passes through a pipe, duct, or open channel [61, 145], has been of great importance for the industry and, especially recently, of even higher importance for the environment. Inaccuracies in the flow measurement can lead to large miscalculations of liquids, gases, or multiphase media and thus, in wrong estimation of their consumption. Flowmeters of different types are used in order to register the flow of a fluid through a pipe, duct, or open channel [61].

The main focus of this work is on ultrasonic flowmeters (USM), and more specifically on ultrasonic transit-time flowmeters (UTTF) and their modeling with the aim of improving the comprehension of their operation. By understanding and analyzing the behavior of UTTF, an improvement of their accuracy can be achieved. The most important components of an UTTF are the piezoelectric transducers, which are used for the generation of acoustic waves in the ultrasonic range, i.e. at frequencies > 20 kHz [117]. The waves are sent in and opposite to the direction of a moving fluid medium and they are received by a receiving piezoelectric transducer [161]. When the waves travel in the direction of the flow, less time is needed for them to reach the receiver and vice-versa. The time-difference between the two directions of propagation is directly proportional to the flow velocity [49]. More details on the principle of operation of UTTF are given in Sec. 1.2.

From this short description of a UTTF and its operation, it is apparent that for its correct modeling, different physics must be simulated in order to take into account the components that comprise a UTTF. More specifically, piezoelectricity needs to be modeled [91, 107] in order to consider the piezoelectric transducers in the simulations. Acoustic wave propagation must be included in the simulations as well [30, 107], due to the ultrasonic waves that propagate through the solid transducers and the moving fluid medium. Finally, due to the medium flowing through the flowmeter, it is essential to model flow with the use of fluid dynamics [58, 72].

As stated, the piezoelectric transducers are the most important components of an UTTF, since they are responsible for the ultrasonic wave generation and reception, and consequently, their adequate description is of high significance. Despite the high complexity of piezoelectricity, an immense amount of work has been performed for their modeling, either with 1-dimensional (1D) models, e.g. in [169, 237, 270, 276], or with the help of the finite element method (FEM) [20, 105, 122, 136]. In the present work, FEM simulations are employed for the description of the piezoelectric transducers. More details on this matter are given in Sec. 2.1.3.

Acoustic wave propagation in solid and quiescent or moving fluid media is one of the main modeling components of an UTTF. Acoustics were systematically studied for the first time by Lord Rayleigh in the 19$^{\text{th}}$ century, who vastly contributed in the understanding and mathematical description of sound propagation in solid and fluid media [211, 212]. The sound propagates in quiescent or moving, and homogeneous or inhomogeneous fluid media, i.e. with uniform or spatially varying ambient properties. The fluid velocity and ambient properties have significant, measurable effects on wave propagation. Blokhintzev was one of the first to derive a set of equations that describe such cases of wave propagation [35]. The linearized equations of fluid dynamics (LEFD) [35] model three-dimensional (3D), and lossless acoustic wave propagation in an inhomogeneous, time-varying, and moving fluid medium in absence of viscosity, heat conduction, and other acoustic relaxation mechanisms. These effects are to be taken into account and have been studied in specific branches of acoustics. In underwater acoustics it is essential to account for the spatial variation of fluid properties such as ambient density, ρ_0, and speed of sound, c, in particular depth variations, stratification, where the oceanic currents can either be neglected [26] or not [81], depending on the underwater application. Atmospheric acoustics is another field where accounting for an inhomogeneous and moving medium is important, including stratification and wind [187, 188]. It is a question of paramount significance, which set of equations is suitable for the description of an UTTF. A number of different equations has been used in literature for this purpose, for example in [30, 31, 32, 152, 179, 231]. The equations used in the present work for the description of acoustic wave propagation and the respective assumptions are described in Sec. 2.2.

Flow is another important component that needs to be modeled when an UTTF is considered. Fluid dynamics is a branch of physics that describes flow of fluids, i.e. gases and liquids [38, 58]. Fluid dynamics find many applications in nature and in industry, such as external aerodynamics, hydrodynamics, biological applications, automobiles, spacecrafts, meteorology and flow measurement [38, 58]. In order to solve problems of fluid dynamics, a system of equations needs to be solved, i.e. mass, momentum, and energy conservation, as well as an equation of state need to be solved [38, 58]. One can find solutions to this system of equations either with an analytical or numerical manner and solve for field properties of the fluid, such as pressure, flow velocity, density, and temperature [58]. However, an analytical approach is limited to basic problems with simple boundary conditions [58], and therefore one must resort to numerical approaches for the solution of real applications [13, 58, 72]. Modeling of flow inside an UTTF is a complex problem, with different inlet conditions upstream of the device, depending on the industrial application and therefore, computational fluid dynamics (CFD) are often employed [84, 94, 195, 196, 264].

CFD use numerical analysis to solve fluid dynamics problems [13, 72]. The most common

numerical method used in CFD is the finite volume method (FVM), as it has been preferred and implemented to most commercial CFD programs. Other methods, such as the finite difference method (FDM) and finite element method (FEM) are also widely applied [72]. In the present work, CFD are extensively used for the purpose of flow modeling inside the flowmeter (cf. secs. 1.3 and 1.4). The models and equations used in the present work for the flow simulations are given in Sec. 2.3. It should be noted that the basic equations of acoustics are derived from the equations of fluid dynamics, as it will be shown in the present thesis, in Sec. 2.2.

It should be noted that the references are organized alphabetically, based on the last name of the first author of a cited document.

The simulated geometries are available online on the personal profile of the author [194] in either 2D or 3D format depending on the type of the simulation.

1.2 Ultrasound and Ultrasonic Flowmeters (USM)

Ultrasound, or ultrasonics, is a field of acoustics with a large number of applications in quiescent or moving fluids and homogeneous or inhomogeneous fluids and solids. Ultrasound is applied largely in medicine for imaging or therapeutic purposes and in industry for ultrasonic range finding (Sonar), nondestructive testing, and ultrasonic flow measurement. The latter application is of particularly high interest for the present work. Ultrasonic flow measurement is only a division of the enormous industry of flow measurement, which uses a number of other principles, such as differential pressure, positive displacement, electromagnetic, Coriolis, vortex, and thermal among others [145]. However, ultrasonic flow measurement is a fast growing principle with high potential for improvement.

There are three main types of USM, the ultrasonic transit-time flowmeters (UTTF), the Doppler shift and the tag cross correlation [145, 161]. The UTTF, which are on the main focus of the current work, have been most widely used and are divided into clamp-on and wetted (or inline).

The clamp-on are completely non-invasive with their transducers being attached on the outside of the pipe[163]. Initially, clamp-on flowmeters were used for measurement of water in large pipes [79, 163]. Efforts have been made through the years to improve the performance of clamp-on flowmeters, in order to compete in terms of accuracy with inline[163]. Such examples are multipath measurements [240] and optimized positioning of the sound paths [75] to minimize the effect of non-axial flow. Other high-end clamp-on devices are guided-wave USM [1], which extend the interrogation field compared to classic inline or clamp-on USM, making use of Lamb waves [256].

For inline flowmeters, the transducers are in direct contact with the fluid, either inside cavities or exposed in the flow, making them minimally intrusive [163]. Inline UTTF achieve accuracies better than 0.5% [163]. Multiple paths were added as well, to minimize the effect of non-axial flow with quadrature integration [73, 218] or other techniques [56]. For low flows, special UTTF emerged, such as the so-called 'sing-around' devices [54, 143].

In Fig. 1.1 a schematic representation of an UTTF in a pipeline (inline) is shown. The flowmeter is single-path, i.e. it comprises one diagonal sound-path in the middle yz plane of the meter-body. T1 and T2 are the upstream (US) and downstream (DS) transducers

respectively, which can serve as both transmitters (senders) and receivers when voltage is applied on them or when they are mechanically excited respectively. L is the distance between the transducers, which also represents the length of the sound path. θ is the angle between the transducer main axis and the axial direction of the pipe and $\boldsymbol{v_0}(x, y, z, t)$ represents the flow-velocity vector in the fluid domain at a time t. $\boldsymbol{v_0}(x, y, z, t)$ is decomposed

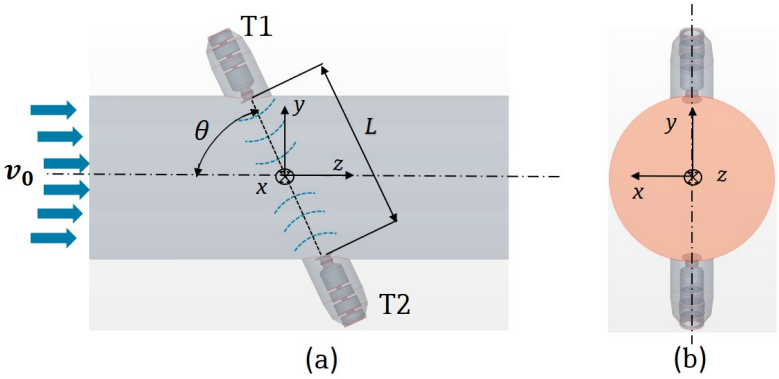

Figure 1.1: A schematic representation of an inline UTTF. (a) Side view and (b) axial view.

into its axial (z) component $v_A(x, y, z, t)$ and its transversal component $v_T(x, y, z, t)$. At a fixed cross-section $z = z_0$ =constant and at fixed time, t_0, the average axial flow velocity is given [155]

$$v_{ref} = \frac{1}{A_{ref}} \iint_{A_{ref}} v_A(x, y, z_0, t_0)\, dx\, dy, \tag{1.1}$$

where $A_{ref} = \pi R_{ref}^2$ is the cross-sectional area at a reference position, with R_{ref} the radius of the reference cross-section, which is usually located inside the meter body of the flowmeter. However, due to continuity [58], this reference cross-section can be located in a different position inside a closed pipeline where the flowmeter is installed, while it is allowed to be of different radius compared to the cross-section of the flowmeter, [66] $A = \pi R^2$, where R is the radius of the meter body of the flowmeter. Therefore, the reference axial volume flow-rate, q_{ref}, [m/s^3] is given as [155]

$$q_{ref} = A_{ref} v_{ref}. \tag{1.2}$$

For a circular cross-section, as shown schematically in Fig. 1.2, the average axial flow velocity along a chord D at lateral position x, is given as [155]

$$v_{path}(x) = \frac{1}{D(x)} \int_{-D(x)/2}^{D(x)/2} v_A(x, y, z_0, t_0)\, dy, \tag{1.3}$$

where $D(x) = 2\sqrt{R^2 - x^2}$ is the chord of the sound path at a position x as shown in Fig. 1.2.

Piezoelectric transducers are typically used for the generation of pulses in the ultrasonic range [91]. When electric voltage with high frequency is applied on a piezoelectric material, it is transformed into mechanical vibrations; this is the so-called inverse piezoelectric effect.

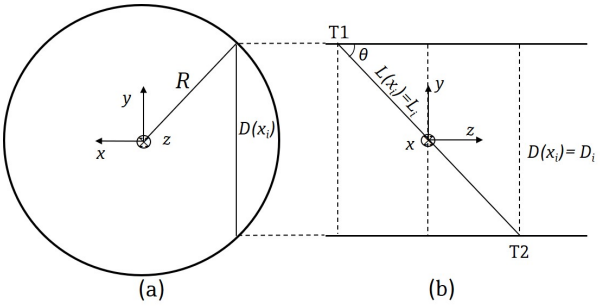

Figure 1.2: A schematic representation of an inline UTTF. (a) Axial view and (b) cut of side view on the plane of the sound path. The chord $D(x)$ of a sound path on a yz plane is shown.

The effect can serve for the purpose of a sending transducer in an ultrasonic flowmeter. When the waves are sent downstream (from T1 to T2), it takes less time, t_{12}, for them to travel compared to the time t_{21}, when they are sent upstream. It should be highlighted that t_{12} and t_{21} refer to the time-of-flight (ToF) inside the fluid medium [155]. The sound waves travel first inside the solid structure of the sending transducer, then in the fluid medium, and finally in the receiving transducer. The mechanical vibrations in the receiving transducer are transformed into electric voltage; this is the so-called direct piezoelectric effect. The downstream and upstream ToF, $t_{12,i}$ and $t_{21,i}$, respectively, for a sound path i of length L_i, in an inclination angle θ_i as shown in Fig. 1.2 with a speed of sound c_i, are given as [30, 155, 176]

$$t_{12,i} \simeq \frac{L_i}{c_i + v_{path,i} \cos\theta_i}, \tag{1.4}$$

$$t_{21,i} \simeq \frac{L_i}{c_i - v_{path,i} \cos\theta_i}. \tag{1.5}$$

A number of approximations is needed for the derivation of eqs. (1.4) and (1.5) [155]

- a ray tracing approximation, i.e. high-frequency approximation of geometrical acoustics,
- the acoustic wavelength is small compared with the acoustic beam width, which is small compared with the pipe diameter,
- uniform axial flow velocity profile,
- no transversal flow,
- low Mach numbers that do not strongly affect the inclination angle θ [155].

A simple relation between the ToF, $t_{12,i}$ and $t_{21,i}$, geometrical elements of the flowmeter and the calculated flow velocity along the sound path i, $v_{path,i}$ is derived when solving the system of Eqs. (1.4) and (1.5) [155, 176], which is given as

$$v_{path,i} \simeq \frac{L_i}{2\cos\theta_i} \frac{t_{21,i} - t_{12,i}}{t_{12,i} t_{21,i}}. \tag{1.6}$$

The approximations made for the derivation of $t_{12,i}$ and $t_{21,i}$ are also valid for Eq. (1.6) [155]. In USM, the approximation is made [155]

$$v_{path}(x) \simeq v_{path,i}. \tag{1.7}$$

This means that the average axial flow velocity over the chord D_i is averaged over an axial distance z_i, of the order of D_i typically, and over a small time-interval, which is a complete cycle of shots over all paths [155]. Consequently with the approximation of Eq. (1.7) it is implied that the flow velocity is constant over z_i and stationary over a small time interval [155]. A lengthier version of Eq. (1.6) is given in Sec. 2.5 as well, which takes into consideration the geometrical parameters of an UTTF, practical matters during measurement, and their consequences on Eq. (1.6).

In the case of multipath UTTF, the flow velocity calculated for all the sound paths is given as [155]

$$v_{calc} = \sum_{i=1}^{N} w_i v_{path,i}, \tag{1.8}$$

where w_i are the weight factors for each path i and $v_{path,i}$ is the calculated flow velocity in each interrogation path i [176]. The value of w_i depends on the path configuration and the integration technique [155, 176]. In order to correlate the calculated axial flow velocity along the sound paths, v_{calc}, with the average axial flow velocity at a fixed cross-section, v_{ref}, a calibration factor must be defined [159]

$$k_a = \frac{v_{ref}}{v_{calc}}. \tag{1.9}$$

Optimization criteria for k_a and remarks for its derivation, as also suggested in [94, 159], are

- its independence from flow effects, i.e. it remains constant irrespectively of the flow in the interrogation paths
- its value should be close to 1
- a function of Reynolds number, Re [58], dependency is derived.

When combining eqs. 1.2 and 1.9, one can derive

$$q = A\ k_a\ v_{calc}, \tag{1.10}$$

which is the axial volume flow-rate based on the axial flow velocity calculated in the sound paths.

The fluid medium inside the pipe is usually moving, inhomogeneous and the flow field varies depending on the application (medium, installation effects, laminar or turbulent flow). For the description of the acoustic wave propagation inside the fluid medium, suitable models have to be used that take these conditions into account, such as the one from Blokhintzev [35] or others derived and implemented later (Sec. 2.2). The flow field itself plays a big role

on the performance of a flowmeter and can be described either analytically or with the use of computational fluid dynamics (CFD) [72]. Numerical simulations and high-performance computing (HPC) in parallel processors are often employed for the numerical modeling of these equations in complex domains.

1.3 Objective and Aim of the Work

1.3.1 Objective and Motivation

The objective of this research work is the development of a hybrid FEM/FVM numerical method, which couples piezoelectricity, wave propagation in solid structures, acoustic wave propagation in moving fluid media and CFD for the purpose of 3D simulations and study of physical phenomena that affect the UTTF behavior. The method is tailored for gas-flow in a pipe with transducers' cavities included, however it is the intention of the author to test it for clamp-on UTTF with liquid flows as well. Moreover, it can be expanded to other applications, where acoustics and flow need to be modeled and coupled, such as atmospheric or underwater acoustics, external flows and internal pipe flows with general complex domains.

A method is developed with the **motivation** to utilize it for design of devices with improved performance, with regard to accuracy and linearity, and to shortening the development cycle of UTTF. It is the first work, to the author's knowledge, that combines CFD with wave-acoustics for the simulation of a full 3D geometry of an UTTF.

Why is it so important to strive for accurate simulations of UTTF? The use of ultrasonic flowmeters has been steadily increased the last decades. In the recent years, the growth is indeed higher compared to other flow measurement principles according to Lynnworth [163]. Some of the most important reasons for the fast growth of the UTTFs are the:

- price to performance ratio
- accuracy
- low impact of the flow field regime on the measurement
- high turndown
- ease of installation
- low maintenance
- bidirectional measurement capability
- non-invasive way of measurement
- low pressure drop
- adoption of Internet of Things (IoT), which gives further insight, diagnostics and measurement of additional parameters
- high data-acquisition frequency
- broad spectrum of applications for many industrial markets.

UTTF are popular in a large amount of industries such as food and beverage, air, water and waste-water, oil and gas, chemical, pharmaceutical, medicine, as they can be applied

to gases, liquids and limited multiphase fluids. Despite their commercial use since the 1950s [127], they still have a large potential technologically and are partially unexplored. The technological developments in terms of more accurate and sophisticated numerical simulations and higher computational power can give an extra push to their research and development (R&D). With numerical simulations, systematic studies can be conducted in order to quantify physical phenomena that affect the flowmeter performance and gain insight of their operation. Since huge quantities of flowing media are transported, measured and sold between parties, even small % differences (of the order of <1%) are often translated to millions of US dollars.

Numerical methods [85] have been broadly used to find approximate numerical solutions to mathematical problems. High computational power gives the opportunity and the **motivation** to use methods for certain applications, which previously were not possible to be used. In Fig. 1.3 the rapid growth of the fastest supercomputer peak speed per year, from the late 1960s to 2019 is shown [249]. Such a computer is not used in the present work but the diagram gives an indication regarding the trend of conventional computers and HPC. This growth helps immensely to solve large domains numerically. Numerical methods

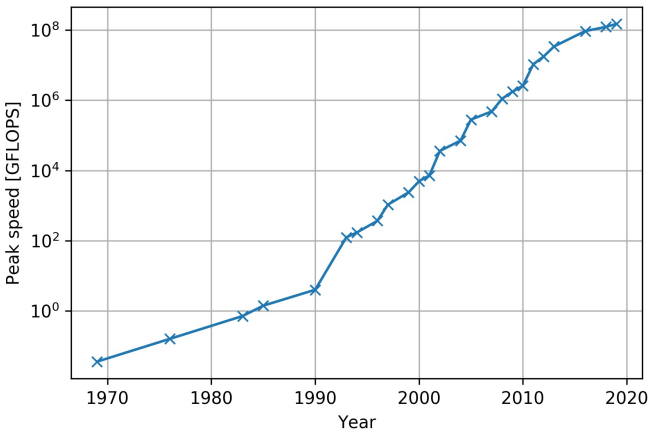

Figure 1.3: Process peak speed of the fastest supercomputer in the world per year (Source [249]).

such as the finite element method (FEM), finite volume method (FVM), or finite difference method (FDM) demand high computational power especially for complex problems as the one of a UTTF.

Let us consider the example of a gas flowmeter for air measurement, at a typical frequency of the order of 100 kHz at normal room temperature ($\simeq$ 20 °C). For these conditions, the wavelength is $\simeq$ 3.43 mm. Typically, for a wavelength to be numerically resolved, depending on the solver of course, at least 20 linear elements/wavelength would be needed. This discretization number is in accordance with similar published results, such as Øyerhamn et al. [277], where 5 second-order elements are used for the wave propagation in air, when the FEM solver 'FEMP' is used [122]. Similarly, 12 linear elements per wavelength are used

by Bezděk [30] when the FEM solver CAPA [137] is employed, which is the predecessor of NACS [183]. For the FVM solver of Star-CCM+®, 20 elements/wavelength is considered a sufficient discretization [116, 229, 235]. For a medium sized device of 100 mm diameter and of axial length of 2 diameters, this means that a couple of millions of elements would be needed for the discretization of the three-dimensional (3D) domain in order to solve the acoustic wave propagation in the fluid. This poses already a challenge for HPC in terms of number of cores and RAM memory. A typical maximum value of supported RAM by a workstation nowadays is $\simeq 2$ TB [243]. Due to these performance and complexity limitations, often indirect ways and hybrid methods should be considered for the simulation of an UTTF and for the connection of the discussed relevant physics.

1.3.2 Problem Description

The main problem posed for the simulation of a UTTF is its multiphysics nature. A simulation of an UTTF is indeed possible to be achieved with the use of CFD only, with the respective assumptions made [195, 196], however for a more realistic, precise, and complete simulation [197], it is essential to model and couple [30]

- Piezoelectricity
- Wave propagation in the solid parts of the transducers
- Wave propagation in the meter-body of the flowmeter, which is however omitted in the present thesis
- Wave propagation in fluid
- Flow
- Combination of flow with wave propagation in fluid

The creation of interfaces for the coupling among the physics is necessary, while the effect of the models on each other has to be either identified or neglected (cf. Ch. 3).

Piezoelectricity is modeled because of the piezoelectric elements used in the sending and receiving transducers. The transformation of electrical voltage to mechanical vibrations is modeled in the sending transducer and the transformation of mechanical vibrations to electrical voltage in the receiving one. Thus, a voltage-to-voltage simulation of the UTTF is possible, with the assumption of a voltage-driven transmitter and an open-circuit voltage detection on the receiver [89].

Wave propagation in solid materials must be modeled, as the waves travel inside the solid parts of the transmitter, the receiver, the meter-body and any other solid part that has to be taken into account. It should be mentioned that the meter-body walls are modeled as rigid walls [117] in the cases investigated in the thesis. When rigid walls are specified, the wave is reflected with no reduction in amplitude and no change in phase, while the normal particle velocity at the boundary is zero [117]. Due to the omission of the pipe walls, pipe-borne crosstalk [100, 162, 163, 278], i.e. the reception of signals that do not propagate through the fluid medium but through the solid pipe, is not investigated in the current work. The

mechanical waves travel from the solid parts of the transmitter and, through the solid-fluid surface, propagate into the fluid. A suitable interface has to be created for the transition of the waves from the solid to the fluid domain. Similarly, a suitable interface has to be created on the receiver side, for the transition of the acoustic waves from the fluid domain to the solid parts of the receiver.

Wave propagation in moving fluids must be properly modeled for the fluid inside the pipe with the effect of flow on acoustics to be considered [30, 203]. An important matter is the assumptions made, depending on the chosen equation or set of equations and their applicability to USM. Such assumptions, studied in literature, are the linearity of acoustics, spatial and temporal variation of ambient properties, losses in the medium, and the effect of turbulence on acoustics [35, 48, 68, 203, 229]. This matter is further discussed in Secs. 1.4.2.3 and 2.2. It should be noted as well that the acoustic waves propagating in the flow reflect on the considered rigid walls of the meter-body.

The flow could be either described with an analytical model or more suitably it should also be numerically modeled with the help of CFD. When CFD are used, several and more detailed flow effects, such as installation and cavity effects, can be studied compared to a theoretical/analytical flow profile. The effect of flow on acoustic wave propagation has to be modeled and a one-way coupling takes place, since it can be assumed that low-power acoustics, as in the case of an UTTF, do not have an effect on the flow field. The effect of turbulence [58] on the acoustic wave propagation in a moving fluid is another aspect to be considered in the case of UTTF modeling, and it is further discussed in Sec. 1.4.2.7.

Another major challenge that has hindered researchers from solving a 3D geometry of an UTTF is the large numerical mesh needed for its simulation [30, 179]. Computational limitations are discussed in the present section and a typical example of a gas UTTF is given, as well as the required mesh (cf. Subsec.1.3.1). In the present work, it was possible to simulate a 3D geometry of an UTTF, due to the utilization of a highly CPU parallelized FVM method [116, 229] and the computation on a HPC cluster.

1.3.3 Solution Method

A solution is proposed with the introduction of the '(Sim)ulations of (P)iezoelectricity, (A)coustics, (C)oupled with (C)FD' (SimPAC^2) method. The hybrid nature of the method means that not only one solver or solution technique is used but different methods are coupled.

A pragmatic approach is adopted for the 3D simulation of acoustics in moving fluid media. Existing equations in the literature that combine acoustics with flow [68, 116, 203, 204] are used (cf. Sec. 2.2.3) in order to model the combined flow-acoustic effects [197]. These equations have been implemented in commercial programs that use either FVM [235], or FEM [183], while they have been already extensively used in literature [30, 31, 32, 60, 116, 203, 229].

More specifically, the piezoelectric, structure, acoustic, flow problem is divided into four parts:

(I) The sending transducer with a portion of fluid

(II) The fluid domain for acoustic wave propagation in flow

(III) The receiving transducer with a portion of fluid

(IV) The fluid domain for the flow simulation

In Fig. 1.4 the division of the device in parts for the simulation is shown. T1 is the sending

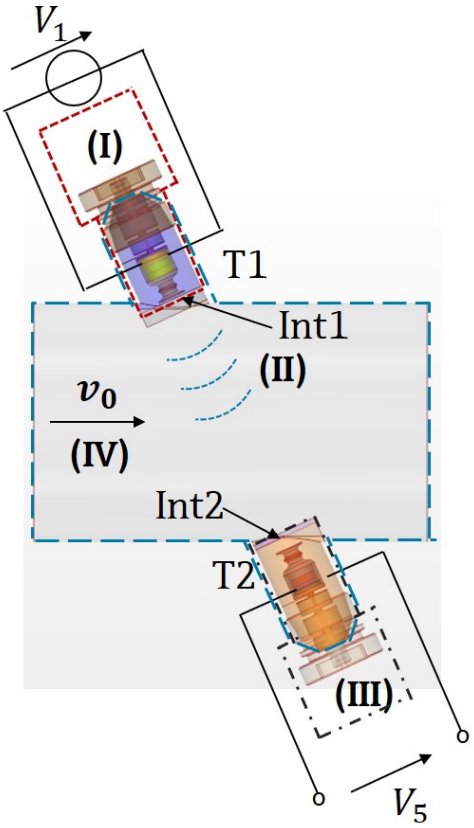

Figure 1.4: Schematic representation of flowmeter and division into parts for simulation. Part **(I)** transmitter with portion of fluid, part **(II)** fluid domain for acoustic wave propagation, part **(III)** receiver with a portion of fluid, and part **(IV)** fluid domain for the flow simulation.

and T2 the receiving transducer. On T1 a voltage-source V_1 is applied and on T2 an open-circuit voltage V_5 is recorded. The load of electronics or a signal generator and cables is not taken into account in the simulation, however an easy way for them to be considered, would be a Thevenin circuit. The black continuous lines around part **(I)** indicate the application of V_1 directly on the piezolectric element of T1. Respectively, the black continuous lines around part **(III)** indicate the measurement of of an open-circuit voltage V_5 directly on

the piezoelectric element of T2. The sending transducer with a portion of fluid in the short-dashed red frame **(I)**, and the receiving transducer with a portion of fluid in the long dash-dot black frame **(III)** are solved with the FEM solver NACS [183]. Parts **(I)** and **(III)** can be interchanged as transmitters and receivers so that the signal is sent in both directions. In the present work, the flow direction is changed and T1 and T2 keep their roles as sender (transmitter) and receiver, respectively. Acoustic wave propagation in the fluid domain in the long-dashed blue frame **(II)** is solved with the FVM acoustic solver of STAR-CCM+® [229, 235]. The meter-body of the UTTF is not considered, since STAR-CCM+®cannot treat solid-fluid interfaces for acoustic wave propagation. Part **(IV)**, also enclosed in the blue dashed lines, represents the fluid domain for the flow (CFD) simulation. Parts **(II)** and **(IV)** do not have to necessarily coincide. More details regarding the simulation strategy are given in Sec. 3.2. It has to be noted that the CFD simulation is performed separately with the FVM solver of STAR-CCM+® [229, 235] in part **IV**, schematically shown in Fig. 1.4. Part **IV** includes the whole 3D fluid domain in the meter-body and the cavities. The effect of flow on acoustics is 'offline' one-way coupled either with NACS for the fluid parts of **(I)** and **(III)** or with the acoustic solver of STAR-CCM+® for part **(II)**. Therefore, Part **IV** is not simulated after parts **I, II, III** but separately and is given as input to parts **I, II, III**.

NACS [183] and Star-CCM+® [235] need to be coupled so that the multiphysics simulation of an UTTF is made feasible (Sec. 3.2). Interfaces are built between the FEM-based solver of NACS [183] and the FVM-based solver of Star-CCM+® [235] in order to transfer the information from the FEM to the FVM mesh. Data are exported from NACS on a surface, Int1, of the domain in space and time, in a form suitable to be used in Star-CCM+® as a boundary condition for the acoustic solver (cf. Sec. 3.2.2). Similarly, data are exported from Star-CCM+® [235] on a surface, Int2, of the FVM mesh in space and time, for the purpose of using them on the FEM mesh of NACS [183] (cf. Sec. 3.2.4). However, the data are not directly usable by NACS [183] and thus, python™ [206] is employed to transform the information from the 3D space of every time-step of Star-CCM+® to the 3D space and time used in NACS. A more detailed description regarding interface Int1 between parts **(I)** and **(II)** and interface Int2 between parts **(II)** and **(III)** and the developed SimPAC^2 method is given in Sec. 3.2.

Approximations are made for the derivation of the implemented equations. Slow variation of ambient quantities in space and time, in comparison with the length and time scales of the acoustic waves is assumed, while second and higher order derivatives of the ambient quantities with respect to space and time are neglected [68, 116, 203, 229]. Further details regarding the models and the related approximations are given in Sec. 2.2. Wave propagation in the solid parts of the transducers together with the piezoelectric elements are taken into account [197] (cf. secs. 2.1, 3.2), however the meter-body is not simulated. Rigid walls [117] and complete reflection on the pipe walls are assumed instead, which can be a reasonable approximation due to the impedance difference between the gaseous medium and the solid walls of the meter body [69, 117]. Therefore, crosstalk phenomena [49, 161, 163] are not captured in the showcases investigated in the thesis (secs. 4, 5, 6). However, the method gives the possibility to include the meter-body of the flowmeter as well and therefore, the capturing of crosstalk is possible.

1.4 Literature Review and State of the Art

Numerical simulations [85] have faced a fast development along with the fast growth of the computational power (see Fig. 1.3) and therefore, they have become an essential part in the development cycle. The purpose of simulations is mainly to gain insight during the R&D, discover physical phenomena, interpret them, and quantify them. Simulations can replace measurements to some extend during R&D and produce models that are closer to the final and optimum design.

The simulation of an USM system dictates that the main focus of the present research is given to modeling each of the relevant physics/subsystems i.e. piezoelectricity, wave propagation in solid materials, wave propagation in fluid media, fluid dynamics and their potential connection.

Therefore, initially a literature review is presented regarding the numerical simulation approaches used here and several applications. Afterwards a more specific literature review is made regarding simulations and modeling approaches of USMs and of the relevant physics/subsystems.

1.4.1 Numerical Simulations and Applications

Two simulation approaches are on focus in the present work, namely FEM and FVM. Each of the approach was used for the simulation of different parts of the flowmeter.

FEM theory and first implementations date back to many decades [289], while the first paper that paved the way and set basic ideas is believed to be the one from Courant [50]. The general principle and approach of the FEM shall be described. The partial differential (PDE) to be solved, with the necessary boundary conditions, are multiplied by weight functions and afterwards integrated over the domain. The weak formulation of the of PDE is obtained with a partial integration. The simulation domain is approximated with a finite number of elements, in which the nodes are defined, where the unknown quantities are to be calculated. and afterwards the algebraic equations are derived with the application of Galerkin approximation method [97, 107, 122]. The method has been implemented to many fields such as structural mechanics [87], electromagnetics [103], electrostatics [53], piezoelectrics [20, 122], acoustics [55, 108, 200, 248], aeroacoustics [109, 201], heat transfer [140, 175], CFD [22, 43, 80], coupled systems and many others [97, 107]. An immense amount of work has been undertaken on the further development of FEM on many different levels [37]. A number of FEM techniques has emerged, such as the scaled boundary finite element method (SBFEM) [234], the finite element discontinuous Galerkin (DG) [45, 90], the smoothed finite element method (S-FEM) [279], and the coupled FEM-BEM [83]. An important aspect of FEM is the discretization method used, where there have been advances on multrigrid methods and non-conforming meshes [107, 108, 216].

With the FVM, the domain to be solved is divided into a finite number of control volumes (cells). The integral form of the PDE, which is used in FVM, is transformed into algebraic equations. The resulting surface and volume integrals are approximated with quadrature formulae, in order to transform the integral form of the PDE to algebraic equations [72, 254]. The computational nodes, on which the equations are solved, are defined inside the

cells [72, 177]. The method is mostly used in CFD as it presents certain advantages compared to the FEM. Indicatively, it can be highly parallelized computationally (in terms of number of computer cores) [133], while its utilization with arbitrary, unstructured meshes is possible and straightforward to implement [72, 126]. Conservation of the field parameters is reassured, as fluxes between neighboring volumes are balanced, and consequently FVM is suitable for large, abrupt gradients in the field [126, 170, 72]. A great effort has been made for the generation of computationally efficient meshes for complex geometries [71, 72, 266]. Another field that needs to be mentioned, as a great amount of research has been dedicated to it, is the solution of the Navier-Stokes (N-S) equations and turbulence modeling approach. A popular approach of modeling turbulence are the Reynolds-Averaged-Navier-Stokes (RANS) models [11], which deliver reasonable results for typical engineering applications [177]. Another approach is the scaled-resolving simulation (SRS), where at least a part of turbulence is resolved, and not modeled, in space and time [173]. Such models include the Large Eddy Simulations (LES), where turbulence is resolved but the smallest length scales are ignored [138], as well as the Detached Eddy Simulations (DES), where large eddies are resolved away from the walls and RANS are used for the boundary layer [173]. The matter is discussed further in Sec. 2.3.2, and in more detail in literature [72, 138, 173, 267]. A direct numerical simulation (DNS) is another approach of turbulence solution, where all the turbulence scales are resolved directly in space and time [222, 267]. However, such an approach is still unrealistic for typical flow problems, due to the high computational demands [222, 267]. Historically, the first paper to introduce the basics of FVM is believed to be the one from McDonald [172] in 1971. The interested reader is referred to modern books that offer a large number of FVM techniques and applications, especially on the topic of CFD [13, 71, 72, 177, 254, 267].

1.4.2 Modeling and Design Aspects of USM

The study of piezoelectricity, wave propagation in solid materials, wave propagation in fluid media, and fluid dynamics is relevant for ultrasonic transmit-receive systems with or without the presence of flow. When these physics/subsystems are simulated and combined, the whole ultrasonic transmit-receive system with or without the presence of flow can be studied. This subsection is organized according to each physics to be modeled or combinations of them, which enable us to simulate an USM device. At the end of the subsection, two special topics are chosen for a bried literature review, i.e. the effect of turbulence on sound propagation for the case of UTTF, as well as the effect of cavity geometries, in which the ultrasonic transducers are located, for the case of inline UTTF.

1.4.2.1 Wave Propagation in Solids and Interfaces

The study of wave propagation in solids is essential due to the presence of the solid transducers and the meter body of an USM [30] (cf. Fig. 1.4). Simulations of structural mechanics and wave propagation in solids with FEM are already established for many decades, as it was initially developed for that purpose [87, 289]. The part of wave propagation in solids is well known [107] and its simulation has been achieved in the past with FEM for USM [1, 30, 31].

The treatment of wave propagation through a solid-fluid interface (cf. Fig. 1.4), especially

when the fluid is moving, is a crucial part of the simulation of an USM that needs special attention. The interface treatment has been investigated in several research works and modeled with the use of either FEM [28, 30, 107] or other methods [152, 268, 280]. In [27] a number of derivations of the weak formulations of equations and FEM techniques are shown for the treatment of solid-fluid acoustic interaction. In the present work, the interfaces' treatment is documented in length in Subsecs. 2.4 and 3.2.

1.4.2.2 Piezoelectricity

Piezoelectricity is more complex to be simulated compared to structural mechanics, as the interconnection between electrostatics and mechanics, as well as the anisotropic nature of the materials must be modeled [91].

Piezoelectric transducers were already modeled successfully with 1D models in the late 1940s by Mason [169] when the piezoelectric disk vibrates on the thickness-extensional (TE) mode, with the use of equivalent electrical circuits. The wave propagation not only in the sending/receiving transducers but also in the fluid is possible to be modeled. These models are often used as a design tool for measurement systems combined with uniform piston [158, 237, 255, 270] or plane wave [88, 191, 269, 276] types of radiation in a fluid. Among the limitations of the Mason or other equivalent models [88, 154, 158, 169, 191, 237, 255, 269, 270, 276] are the incapability to describe non-uniform, axisymmetric, radial-mode vibration of the transducer with the resulting sound radiation [277].

FEM has been well established in the modeling of piezoelectricity, with the first FEM simulation in the field being performed in 1970 by Allik and Hughes [12]. In 1979, Kagawa et al. [105] used FEM for the simulation of composite piezoelectric ultrasonic transducer. Bao et al.[23] presented a FEM-equivalent circuit method to compute the performances of vibration and acoustic radiation of piezoelectric transducers. In the late 1980s, Lerch [135] used FEM for the simulation of piezoelectric transducers with the wave propagation in the ambient medium included. Jeng et al. [102] made a FEM eigenmode analysis for a 1-3 type piezoelectric composite transducer including the effect of fluid loading and internal losses. In 1989, Tzou [252] made a robot end-effect using polymeric piezoelectric bimorph wit the aid of FEM.

In 1990, Challande [40] made optimization studies on ultrasonic transducers with the use of FEM. Kunkel et al. [128] made a series of simulations on piezoelectric ceramic disks with diameter-thickness ratio variation for the determination of series and parallel resonance frequencies, with the modal displacement fields shown. Lerch [136] simulated piezoelectric media and made a quantitative comparison with theoretical and experimental data. Friedrich et al. [76] simulated piezoelectric Lamb-wave delay lines with and without acoustical absorbers and compared with experimental results. In 1993, Hwang et al. [98] used FEM to simulate a laminated plate with piezoelectric sensors/actuators, where various geometries are investigated. von Jena et al. [258] used FEM for the simulation and design of broadband piston-shaped transducers of the radius-to-thickness conversion type for an ultrasound gas flowmeter for household applications. Kagawa et al. [104] simulated, with a FEM approach, 3D piezoelectric actuators in time-domain. Saravanos et al. [219] developed FEM formulations for quasi-static and dynamic analysis of smart composite structures containing piezoelectric layers. In 1998, Abboud et al. [3] used FEM for modeling and design of ultraso-

nic transducers, as well as for coupling piezoelectricity with acoustics. In the work of Abboud et al. [3] different FEM formulations are discussed, i.e. frequency-domain and time-domain, as well as modeling aspects such as implicit and explicit solvers, linear and nonlinear problems, discretization, attenuation, and boundary conditions. In 1999, Simkovics et al. [230] presented a FEM method that takes into account both material and geometric nonlinearities. The resonance frequency shifts due to nonlinearities were measured and simulated.

In 2000, a survey was made by Benjeddou [25] on the advances in piezoelectric FEM of adaptive structural elements. In the late 1990s and early 2000s Kocbach et al. presented several works [122, 123, 125, 124], in which FEM formulations were developed, while simulations were made of piezoelectric transducers coupled with wave propagation in a fluid medium. The effect of geometry and material parameters of the ultrasonic transducers on the vibrational modes and the radiational field were assessed. In 2004, Akasheh et al. [9] used FEM to model, design and optimize piezoelectric micromachined ultrasonic transducers (pMUT) in an operating range of 2-10 MHz and compared to measurements. In 2006, Bezdek [30] used FEM, implemented in the CAPA code [137] to simulate 3D ultrasonic transducers, used for USM. In 2007, Loveday [149] used 3D FEM for the simulation of piezoelectric transducers and 2D FEM for the infinite constant cross-section waveguides. On 2008, Abdullah et al. [4] used FEM to simulate high power piezoelectric ultrasonic transducers and compared with experiments. In 2008, Lahmer et al. [131] proposed a 3D FEM combined with an exact Newton or nonlinear Landweber iterative scheme for the precise reconstruction of piezoelectric material parameters from electric impedance and mechanical displacement measurements for two piezoelectric materials and tested its performance. In 2009, Rupitsch et al. [217] used an alternative method for the parameter estimation, an extended Inverse Method, to minimize the deviation between measurements and simulations for the electrical and mechanical behavior of the investigated actuator.

In 2012, Aanes et al. [2] used FEM for the simulation of piezoelectric transducers immersed in water and the transmission of waves in a water-immersed steel plate, for which the results are compared with 3D angular spectrum method (ASM) and measurements. Lowe et al. [150] illustrated the importance of the consideration of piezoelectric transducers coupled with ultrasonic guided waves in an aliminium rod. Smyth et al. [233] derived an analytical Mason equivalent circuit for a pMUT and validated it with experiments and FEM simulations. In 2017, a stack of two piezoelectric discs with varying thickness were measured, simulated with FEM and theoretically solved, to conclude that the natural frequencies of the radial modes of the transducer were not affected by the stack and thickness of the discs, while the frequencies of the thickness modes were affected [202]. In 2018, Øyerhamn et al. [277] simulated transmitting and receiving transducers and their radiation in air for radial modes and compared with measurements. In 2019, Mahbaz et al. [165] used measurements and FEM for the calibration of piezoelectric transducers in seismic tests, such as ultrasonic non-destructive testing (NDT). In 2018, Mousavi et al. [180] used FEM to design ultrasonic transducers at desired driving frequency and to maximize the transmitted and received voltages. In 2020, Papathanasiou et al. [197] used NACS for a transient simulation of piezoelectric transmitter and receiver coupled with moving fluid for an application of USM, where the effect of different flow fields was assessed. FEM piezoelectricity has been implemented to commercial FEM programs, such as NACS [183], COMSOL Multiphysics®[47], and Ansys®[17].

From the amount of work done in the field, one can state that FEM is the standard method to be used for the simulation, characterization of piezoelectric materials and design of piezoelectric transducers that have a wide range of applications. As reviewed in the present work, solutions have been achieved in frequency-domain and time-domain, for harmonic analyses or transient problems, for 2D and 3D structures in vacuum, or coupled with solid or fluid non-moving and moving media.

1.4.2.3 Acoustic Wave Propagation in Fluid Media

Acoustic wave propagation in quiescent and especially in moving fluid media has been an ongoing topic of investigation [35, 187, 204]. A number of equations have been derived, with different assumptions applied in the course of their derivation, and numerically implemented. Several numerical techniques have been employed, such as ray tracing [204], the boundary element method (BEM) [174, 213], FEM [289], FVM [126], finite difference (FD) [139], discontinuous Galerkin (DG) [45]. For the purpose of simulation of acoustic wave propagation in moving fluid media, the LEFD [35] have been implemented in the FEM solver of COMSOL [47, 48], the Pierce equation (PE) [203] has been implemented in the FEM solver of NACS [183] and the convected acoustic wave equation (CAWE) [68, 116] has been implemented in the FVM solver of STAR-CCM+® [229, 235]. In the present work, the main focus is given on the simulation of acoustic wave propagation in fluid media particularly for the field of UTTF.

FEM Studies for Acoustic Wave Propagation in fluid media have been performed in the field of UTTF. In 1996 and 1998, Eccardt et al. [59, 60] used FEM to show the effect of flow on acoustics for UTTF and compared with geometrical acoustics, i.e. ray-tracing. Laminar and turbulent flow profiles were given as an input and the effect of the flow on the acoustic signal is shown when the wave travels upstream or downstream relative to the flow. In 2003, Lunde et al. [154] simulated acoustic wave propagation in a quiescent medium together with the geometry of a piezoelectric transducer for an axisymmetric domain in order to introduce a diffraction correction for UTTF. In the early 2000s, Bezdek et al. [30, 31, 32] FEM was used for part of the acoustic wave propagation in an UTTF for moving fluid media. In 2020, Mousavi et al. [179] used the FEM solver of COMSOL Multiphysics® [47] to simulate 2D acoustic wave propagation in an UTTF with the effect of CFD generated flow considered. Commercial programs have made available FEM simulations of acoustics in the presence of flow, however the computational demands are still high [47, 183].

Ray-tracing methods are well-established for acoustic wave propagation in moving fluid media and are based on assumptions of geometrical acoustics (waves of very high frequency) [204, 257]. The main assumptions are the invariance of the wave amplitude along the wavefront and that the radius of the wavefront curvature is much larger than the wavelength. The latter assumption implicates that simple ray tracing methods, typically cannot model sound diffraction, however depending on the sophistication of the model such effects can be implemented when extended or combined with other models [30]. One of the main advantages of the method is the low computational demands. McCartney et al. [171] derived a ray tracing method for sound wave propagation in uniform axial flow profile. In 2000, Köchner

et al. [111] applied ray tracing for an ultrasonic gas flowmeter, where the transducers are not taken into account, and combined it with a Monte Carlo statistical technique. In 2001, 2D ray tracing was presented by Frøysa et al. [77] combined with flow data from CFD. This facilitates the investigation of flow effects on acoustics, such as laminar and turbulent flow effect and installation effects. In 2002, Ioos et al. [99] also used a ray tracing method to investigate flow profile and fluid turbulence uncertainties on UTTF for inhomogeneous moving media. The method was applied on two-dimensional (2D) geometries, while temperature and velocity fluctuations are considered in a stochastic framework. In 2003, Kupnik et el. [129] applied a ray tracing method in combination with measurement data for the simulation of an UTTF in high temperature gas flows. Weber [263] combined ray tracing with data from measurements in order to examine the effect of flow turbulence on sound waves. Beždek also used ray tracing in combination with boundary integral techniques for the simulation of acoustic wave propagation in moving media [30] as part of the simulation of the whole system. The combination of ray tracing and boundary integral methods, accounts for diffraction effects for quiescent media and limits its validity to cases where diffraction for moving fluid media is not significant and for Mach number $(M) \ll 1$. In 2007, Franchini et al. [74] determined the effects of trajectory shifts on the velocity measured by the sonic anemometer for one-directional horizontal and vertical shear flows, and mixed with a uniform horizontal flow. An analytical expression for the deviations of the calculated speed from the nominal speed was obtained. In 2010, Reyes et al. [215] used the Helmholtz integral ray tracing method of Beždek [30] to simulate wave propagation between two transducers of an USM. The simulation results were validated with an air USM operated in a calibration rig. In 2013 Li et al. [142] used ray tracing for the simulation of wave propagation in acoustic paths of a clamp-on flowmeter. Nonlinear effects of the flowmeter were investigated for high-speed gas flow measurement. In 2016, Zheng et al. [284] used ray tracing for wave propagation in moving media for gas ultrasonic flowmeters. The propagation time, path length, and path angle are calculated and based on this analysis, a corrected velocity measurement is proposed.

Ray tracing methods describe sound propagation in a simplified way due to the geometrical acoustics approach, i.e. the high-frequency approximation [204, 257]. In order to take into account diffraction effects and finite beam interaction with the flow, other approaches such as wave acoustics [154] or the "simplified finite element diffraction correction method" [238] are more suitable. Moreover, ray tracing methods usually need to be combined with other methods, e.g. FEM [30, 154] for the inclusion of the solid transducers.

Alternative Methods for acoustic propagation in moving media are presented through the years. In 1982, an analytical method was presented by Hemp [89], where the technique of reciprocal operation of an UTTF is described and a relation between the voltage and currents on the receiver and the flow velocity is given. Willatzen developed a semi-analytical method to describe the sound propagation in moving media in confined cylindrical walls with monofrequency excitation using the Frobenius power series expansion method[271]. Depending on the model that was used, different assumptions apply on the flow profile. Another alternative method was published in 2019 by Zheng et al. [285] where the Gaussian beam was used in order to identify aspects of the acoustic field in an UTTF and describe it.

Another approach for modeling the acoustic wave propagation in UTTF is the combina-

tion of simulations and measurements, where measurement data are given as input for the part of the UTTF to be simulated. In 2018, Hu et al. [96] measured the velocity distribution on a circular transducer and used it as a boundary condition (BC) for the simulation of the acoustic field in quiescent, homogeneous and inhomogeneous medium. It has to be noted that the chosen simulated fluid domain was 2D and open, which is not the case for an UTTF, but it can be used as a base for further studies as it delivers results in the fluid domain and on the receiver frontal surface. Zhao et al. [282] somewhat extended the method of Hu et al. [96] to 3D moving fluid media with the inclusion of the receiving transducer. Similarly, useful information is obtained for the acoustic field, however the obtained simulated voltage on the receiver needs the respective measured one for its evaluation. The predicted, simulated voltage is essentially a test of the correct implementation of the transfer function of the receiver and the inverse Fourier transform for the calculation of the received voltage. Consequently, any differences between the measured and predicted voltages would only stem from the Fourier transforms.

1.4.2.4 CFD

CFD studies have been extensively utilized to predict and understand the effect of solely the flow field on the performance of an UTTF. They are mostly used to eliminate undesirable flow effects that cause inaccurate measurements, such as installation effects or the effect of the transducers' position, i.e. protruded, flush, and recessed in the cavities of the meter-body, and for the derivation of calibration factors, k_a as defined in Eq. (1.9). Examples of such studies are given in the present section.

In 1995, Holm et al. [94] made CFD simulations for an UTTF with three different pipe configurations in order to determine the calibration factors. The results were compared with analytical expressions and experimental data. In 1996, Hilgenstock and Ernst [92] made CFD to investigate installation effects on UTTF and compared with experiments. They found out that a better agreement is achieved when more advanced turbulence models are used. In 2002, Hallanger et al. [84] performed CFD simulations for an UTTF installed either in a straight pipe or downstream of bends, evaluated flow data, compared simulated and measured flow profiles and obtained a deviation curve of the flowmeter from CFD. In 2002 O'Sullivan and Wright [189] measured and simulated with CFD two configurations of gas UTTF with broadband ultrasonic transducers. The calibration factors and flow velocity were calculated, measured and compared. In 2004, Temperley et al. [242] conducted axisymmetric CFD studies for a coaxial, ultrasonic transducer housing in a cylindrical cross-section metering duct and compared to laser Doppler velocimetry (LDV) and results were compared with experiments near the duct walls with the aim of improving the UTTF performance.

In 2009, Sheng et al. [225] used CFD in order to identify the sound path optimum position and define k_a for an UTTF with a square-shaped meter-body. In 2011, Zheng et al. [286] investigated the effect of the position of the transducers for an inline UTTF, compared with measurements and described the effect of the flow field for protruded and recessed transducers. In 2011, Martins and Ramos [168] the correction factors were calculated with the help of CFD for single-path UTTF downstream of typical flow disturbances. In 2012, Wang et al. [260] used CFD to study the transducer position effect for a multipath UTTF for different path numbers and pipe diameters. In 2013, Tawackolian [241] made an extensive

study of the flow field, with the use of CFD for an UTTF for a number of different inlet conditions and compared with particle image velocimetry (PIV) measurements. In 2015, Zhao et al. [281] presented a systematic investigation of the influence of complex flow on a multipath UTTF. In 2016, Qin et al. [207] made CFD simulations in order to develop a flow profile identification with multipath transducers. In 2016, Weissenbrunner et al. [264] used CFD in conjunction with a generalized non-intrusive polynomial chaos method in order to estimate the systematic errors for UTTF due to installation effects, as a function of the distance from a disturbance. In 2017, Belligoli et al. [24] used a Bayesian calibration of a model based on CFD in order to predict the flow rate based on certain parameters. In that way, uncertainty of UTTF under non-ideal conditions is calculated and therefore, no recalibration is needed.

In 2019, Papathanasiou et al. [196] performed steady and transient CFD simulations for an UTTF used in custody transfer heat metering applications. The device was simulated and measured for a reference straight pipe and the challenging case of a swirl generator installed upstream. The flow velocity in the virtual cylindrical sound paths was evaluated and was weighted with a Gaussian function to imitate the acoustic field in the sound paths. The flow field and flow profiles were evaluated with different turbulent models. The deviation curves of the flowmeter were calculated with the use of a method called 'CFD-Non-Acoustic' or 'Only CFD-CNA' (CFD Non-Acoustic-Only CFD) or 'CNA', described in the present dissertation, while a comparison with measured deviation curves took place with its use. In 2021, Martins et al. [167] calculated the profile factor of USM and studied the effect of various modeling parameters, such as mesh, boudary conditions, turbulence modeling, and integration scheme. In 2022, Papathanasiou et al. [195] utilized and further automated the Only CFD-CNA method for the simulation of clamp-on UTTF. The so-called 'Flow disturbance compensation' (FlowDC) function was developed for the compensation of flow errors introduced due to disturbed flow conditions and for the automated generation of flow correction factors. With the use of FlowDC the inlet run was significantly reduced i.e., a clamp-on UTTF with 2 sound paths, can be mounted, without rotational position restrictions, as close as 2 diameters downstream of a flow disturbance. The generated flow correction factors were directly implemented in the UTTF for the compensation of the error in the field [65].

1.4.2.5 Analytical and Experimental Studies

Analytically and experimentally, a great amount of research has been done in the field of UTTF in order to define the path configuration and the related calibration factor, k_a, as well as the weight factor, w_i, of each sound path i. It is not the scope of this work to define k_a or w_i, however some work in this field is mentioned indicatively, since it is an important aspect of UTTF R&D. In 1979, Lynnworth [160] gave an overview regarding ultrasonic flowmeters and the different path configurations, with a midradius chord or multiple chords. In 1985, Lynnworth and Lynnworth [159] analytically derived k_a for nondiametrical paths in ultrasonic flowmeters. Depending on the integration technique along the sound paths and their configuration, different weight factors are calculated [176]. Integration techniques that are used for the calculation of the flow velocity in an interrogation path, for different configurations of sound paths, are quadrature, Gaussian, Tchebycev, Tailored, or

others [56, 73, 176, 190, 218]. In 2000, Moore et al. [176] calculated k_a for theoretically defined asymmetric profiles, as well as for different multipath UTTF configurations in order to gain understanding of the behavior of UTTF and the change of k_a depending on installation effects for each path configuration. In 2006, Raisutis [209], experimentally investigated the local flow velocity components using invasive flow sensors in recesses of an UTTF. The flow velocity in the recesses of the downstream transducer is a few times larger than the upstream. In 2006, Kurniadi and Trisnobudi [130] proposed a modified multipath configuration for a tomographic ultrasonic flowmeter, while simulations were performed for asymmetric flow and comparisons were made for diametrical and quadrature configurations. The flow velocity profile for air was reconstructed and was compared to experimental data. In 2014, Chen et al. [41] presented a multipath UTTF, where the acoustic path arrangement with the Tailored integration, ultrasound emission and reception, measurement module, and software were designed systematically. In 2018, Zhou et al. [287] proposed an averaging method for the determination of the reference wave in order to improve the repeatability of ToF for an air six-path UTTF. In 2018, Leontidis et al. [134] developed an UTTF for cryogenic applications for measuring flow rate fluctuations in the range of 0 to 70 Hz, which was validated experimentally for unsteady flows.

Analytical and experimental methods are a paramount pillar in the R&D of UTTF and therefore, their combination and comparison with numerical simulations, which give further insight and flexibility in the studies, is essential for the investigation of physical phenomena and further research.

1.4.2.6 Multiphysics Methods

Multiphysics methods with the coupling and inclusion of relevant physics in order to model either single-path or multi-path UTTF in one concise method have been the goal for many researches since decades already. In 1987, Lygre et al. [158] simulated a single-beam ultrasonic flowmeter, using the program "*FLOSIM*", which takes into account signal generator, matching electrical network for the transmitting transducer, transmitting and receiving transducers, the flowing medium, matching/filtering circuits for the receiver and network termination. A Mason type 1D model [169] is used for the transducers and a uniform flow profile is taken into account. The sound field is calculated by a a model for the far-field sound pressure from a piston source affected by a uniformly moving fluid. In 2003, Lunde et. al [156] extended *FLOSIM* [158] and replaced the modules of the transmitting transducer, fluid medium and receiving transducer with FEM simulations [122, 124, 123, 125]. With the use of FEM, these modules can be described in a more sufficient and accurate manner. Results for a high-precision custody transfer flowmeter of natural gas and oil were presented with both *FLOSIM* and a combination of FEM with *FLOSIM* in order to highlight the capabilities of the newly proposed method. In 2003, Lunde et al. [154] used two different approaches for modeling of USM with the aim of quantifying transient diffraction effects for volumetric, mass and energy flow measurement of natural gas. The first approach is a simplified 1D Mason model for the description of the transducers [169] for a uniform plane piston mounted in an infinite rigid baffled [117] with Williams' diffraction correction [272] combined in the system model FLOSIM [158]. The second approach is based on the method presented in [156]. The importance of accurately calculating the diffraction time delay is

highlighted in relation to different 'dry calibration' methods and its consequences on the USM accuracy. In the beginning of 2000s Bezdek et al. [30, 31, 32] developed the 'HIRM' method, which was applied to a 3D geometry of a clamp-on UTTF. It is a hybrid method combining FEM for piezoelectricity and wave propagation in the solid parts of the device, and BEM with ray tracing for the acoustic wave propagation in the fluid. Flow is included but the profiles are given in an analytical way and not with CFD. The calculated and measured voltage signals on the receivers are compared and several effects are studied such as the effect of temperature and sensor distance on the received signal. This method is closest to a complete simulation of an UTTF, however its limitations are documented and known [30]. Due to the use of ray tracing, diffraction effects and shade zones, e.g. for transducers inside cavities such as the application of inline UTTF, cannot be adequately modeled. Moreover, the non-utilization of CFD data for the flow restricts the flexibility of the method regarding the investigation of flow effects on acoustics.

In 2010 a useful review was made by Reyes et al. [214] on modeling and simulation of ultrasonic flowmeters. In the mid-2010s, Luca et al. developed a code for the purpose of modeling clamp-on UTTF as well, with a direct approach [152, 153, 151]. The nodal discontinuous Galerkin (nodal DG) method is employed for the modeling of wave propagation in solids and moving fluids, which is implemented on graphical processing unit (GPU) for high parallelization and speed-up. Flow data are given from CFD and the received signals for shear and Lamb waves are obtained and compared. The method is applied to 2D geometries and piezoelectricity is not included, while in [151] the obtained results from simulations are compared with experimental results obtained from a gas test rig. In the late 2010s, Simurda et al. [231, 232] developed a Fourier collocation approach for the simulation of UTTF. Fourier collocation is used for the spatial derivatives and FD for the time marching. The method is applied to a clamp-on and an inline test case, while the effect of multiphase flow on the device accuracy is investigated. The method is applied to 2D geometries, CFD are not included and piezoelectricity is not simulated. In 2018, Sun et al. [239] developed a hybrid method for the simulation of UTTF. FEM, ray tracing, wave acoustics, and CFD are combined. The method is applied to a 2D geometry, where the piezoelectric transducers are not included but a piston source transducer is assumed. Results regarding the acoustic field and the effect of the flow field on it are presented and the simulations are compared with measurements. Similarly, in 2019, Zheng et al. [283], based on the method applied in [239] investigated effects of non-ideal flow field on acoustic field for gas ultrasonic flowmeters. In 2020, Mousavi et al. [179] presented a semi 3D-simulation of an ultrasonic flowmeter for the generation of flow profile correction factors (FPCF). In the work of Mousavi et al. [179] a 3D flow was considered, while the ultrasonic transducers were simulated in 3D and simplified to a piezoelectric element, matching layer and casing. The wave propagation in the moving fluid was simulated as 2D. In 2020, in another publication, Mousavi et al. similarly used FEM for the simulation of a Lamb wave clamp-on UTTF and compared with analytical and experimental results [178]. In that approach of Mousavi [178], the CFD simulation was performed in 3D, while the wave propagation in the solid and fluid parts was simulated in 2D and the transducers were ommited.

In 2019, Kiefer et al. [115] applied a spectral collocation scheme for the solution of Lamb waves propagation in a plate interacting with an inviscid fluid. A change of variable transforms the problem from non-linear to linear and as a result, an equivalent fourth-order

polynomial eigenvalue problem is solved in order to obtain the phase velocity dispersion diagram and attenuation curves that are of high importance for the design of a Lamb wave UTTF and other applications, such as non destructive testing (NDT). The presented method of Kiefer et al. [115] was further developed in 2022 in [113, 114], where a software tool was developed, namely the 'Elastodynamic Acoustic Toolbox' (EDAT). For the Lamb wave propagation in flat plates loaded with fluid, a Chebysev spectral collocation method was developed and used [113, 114]. For the propagation in the flowing fluid, a ray-tracing method was implemented, based on the equations given by Pierce [204]. Verifications of the obtained results was realized with measurements and FEM simulations. The method was used for the analysis of a Lamb wave based flowmeter and the evaluation of error sensitivity due to temperature and flow-rate changes. With the use of EDAT, the effect of temperature on Lamb wave based UTTF was studied, while the simulation and analysis of Lamb wave UTTF was enabled reliably and in a systematic manner. However, it should be noted that the transducers were not taken into account in the simulations, whereas pressure was given as a boundary condition instead [113, 114]. Moreover, the simulations were performed in 2D and the flow profiles were analytical i.e., depended only on the lateral dimension, with the assumption of homogeneous and laminar flow [113, 114].

1.4.2.7 Special topics of turbulence and cavity effects on UTTF

Turbulence occurs in internal pipe flows typically for a critical Reynolds number, $Re_{cr} > 2300$ [38]. A question that arises is whether turbulence has a significant effect on the acoustic wave propagation in a moving fluid medium in the turbulent regime, specifically for UTTF applications, since the flow field fluctuates in time and space. Turbulence can have an effect on the received signals and volume flow error (cf. Eq. (2.98)) for an UTTF as shown in [99, 263], however usually mean values of the flow are taken into account e.g. in [30, 152, 158]. Weber [263] showed that for a specific application of upstream and downstream propagation of an ultrasonic pulse in a measured turbulent channel flow, the scatteting of Δt can be up to 5%, while guidelines were given regarding the optimum inclination angle, θ, of the transducers. Ioos and Lhuillier [99, 141] used ray tracing and a Gaussian beam summation method to simulate the wave propagation in moving inhomogeneous random media. More specifically, Ioos et al. [99] quantified the deviation of an UTTF in 2D domain, due to mean profile velocity and temperature profiles, as well as thermal and kinematic turbulence effects for different cases of velocity profiles. They found out that the volume flow error can be overestimated up to 2% for the investigated cases.

The effort and complexity is largely increased when the effect of transient CFD simulations is coupled with 3D simulations of acoustic wave propagation in a moving fluid medium [116, 229]. In the present thesis, steady flows are considered, i.e. mean values of turbulence. The present work and developed method can be the foundation for inclusion of turbulence in 3D simulations and the quantification of its effect on UTTF measurements.

Cavity effects on the acoustic wave propagation in an UTTF have been studied in literature as well, either experimentally or with the aid of simulations. Løland et al. [146, 147] used mainly experiments but also 2D CFD for the estimation of the effect of the flow in cavities of UTTF. A correction was introduced due to the vortex created inside the cavity. It was

found out that the effect was different for each of the upstream and downstream cavities, while the introduced deviation was higher for higher Re, and that the mean cavity velocity was increased linearly with the pipe flow. These results are in agreement with the findings of the present work. In 2002, Kažys et al. [110] made an experimental investigation of gas flow in pipes with recess of ultrasonic transducers, where it is shown, similarly to the present work, that different velocities are observed in the upstream and downstream recessed transducers, while the flow velocity changes differently with the distance from the transducer for the upstream and downstream recesses. As mentioned in Subsec. 1.4.2.5 as well, in 2006, Raišutis [209] experimentally investigated the local flow velocity components using invasive flow sensors in recesses of an UTTF. The flow velocity in the recesses of the downstream transducer is a few times larger than the upstream. As mentioned in the present subsection, Zheng et al. [286] investigated with CFD the effect of the position of the transducers for an inline UTTF, compared with measurements and described the effect of the flow field for protruded and recessed transducers. The results of the study seem feasible, however the analysis and conclusions made is not fully comprehensive and should be read carefully. The negative volume flow errors are expected for recessed transducers, while they can be corrected (cf. Eq. (6.8)). It is commonly known that the linearity of a flowmeter is of importance, i.e. fairly constant value of volume flow error for a range of Re and not its value for a specific Re. In 2012, Wang et al. [261] also simulated the cavity effect by investigating recessed, protruded and half-protruded transducers in the flow, where they concluded that transducers installation has an effect on the flow especially for shorter paths. In 2014, Qin et al. [208] used CFD to simulate recessed, protruded and half-protruded transducers for a range of velocities and different inlet disturbances. Similarly to Zheng et al. [286] protruded transducers are advised to be installed, which is not necessarily an optimum global design, as shown in the present thesis. Protruded transducers are not necessarily preferred in industry either [64]. The reader should handle the conclusions drawn from [208, 261, 286] regarding protruded, recessed or flush transducers with caution. Sun et al. [239] used a mentioned hybrid method for the analysis of the acoustic field and the effect of flow on it. In the present work, the studies made concerning the flow profile effect on acoustics, upstream and downstream ToF, and the performance of an ultrasonic flowmeter shows similarities to the work of Sun et al. [239]. More specifically, the effect on acoustic wave propagation and on the received signal varies with the flow-field type, e.g. uniform, turbulent. Sun et al. [239] also showed the different effect of an upstream and a downstream cavity, as it is shown in the present work and by Løland [146, 147].

Indicatively, other effects that affect the behavior of an USM are diffraction effects that should be corrected or crosstalk i.e., wave propagation through the solid pipe instead of the fluid medium. The systematic investigation of these effects is out of the scope of this work. However, the effect of diffraction is shortly discussed in Subsec. 1.4.2.3 and 1.4.2.6, while the interested reader is referred to [154, 156, 158, 238]. The crosstalk effect is shortly discussed in Subsec. 1.3.2, while the interested reader is referred to [100, 162, 163, 278].

1.4.3 Literature Summary

One can state that a large amount of work has been done in the field of numerical simulation of UTTF, however there are several topics to be further investigated in the field. From

the presented literature, it is evident that the topic of simulation of the whole system of UTTF or parts of it, is an ongoing topic by researchers. Modeling of some parts such as wave propagation in solids is more straightforward than others, such as piezoelectricity, wave propagation in moving fluid media, and CFD. Therefore, there is strong potential for either improvement of the simulation methods or for investigation of, so far, unknown effects, which will be clarified in the course of this thesis.

The connection between the different models mentioned in Subsec. 1.3.2 is a substantial challenge. In each of the presented studies, either a part of the simulation is missing or considerable assumptions had to be made. For example, often piezoelectric transducers are not included [151, 152, 153] and a piston source model or measurements are used instead [96, 113]. CFD are often not part of the whole system as well and analytical flow profiles are given instead [30]. Wave propagation in moving fluid media is usually simulated either with ray tracing [74, 77, 89, 99, 111, 113, 129, 142, 171, 284, 257, 263] techniques, i.e. geometrical acoustics with the inherent assumption of propagation with very high frequencies, or when wave acoustics are used, then the model is reduced to 2D because of high computational demands [179]. The effects of the cavity or of the position of the transducers, i.e. recessed, protruded, flush, which are thoroughly investigated in the present work, have been previously studied as well e.g. in [146, 147, 208, 208, 261, 239, 286] but not for 3D simulations, where the piezoelectric transducers are included, simulated, and coupled with 3D acoustics in moving media, and CFD.

1.5 Ambition and Limitations of SimPAC^2 Method

The ambition and purpose of the SimPAC^2 method is to fill these gaps insofar as it is possible with the aim of giving answers to effects occuring in UTTF devices affecting their accuracy. A full 3D simulation is performed, where the real geometries of piezoelectric sensors are fully 3D modeled inside the cavities of an UTTF. Sophisticated 3D CFD models are used to describe the flow in the pipe and inside the cavities, where 3D vortices are present. Wave propagation is modeled with the help of wave acoustics in the full 3D fluid domain of an UTTF for moving fluid media with the use of two different equations [116, 204] depending on the solver used [183, 235]. For a part of the fluid near the transmitter and the receiver, a FEM solver is utilized [183] but for the largest part of the fluid a FVM solver is employed [235], as described in Sec. 3.2. The inclusion of such a FVM solver is crucial for the successful 3D simulation of acoustic wave propagation in moving fluid media for a fluid domain of a typical volume of a UTTF device. The main reason is that such a FVM solver can be highly parallelized and therefore, it is possible and affordable to model an air UTTF of 80 mm nominal diameter, as the one considered in the present thesis in secs. 6.2 and 6.3.

3D modeling of piezoelectricity, flow, wave propagation in solid materials and moving fluid flow, as well as their interconnection enables a simulation of the real 3D geometry of an UTTF to be performed. More understanding is gained regarding the operation of the device, as simulations facilitate acquisition and visualization of data anywhere in the 3D domain. Systematic studies with real flow data from CFD are carried out for different flow profiles and positions of the transducers, while combined effects of acoustics and flow are visualized and quantified. Such an example is the consideration of a fully-developed flow profile with zero

velocity inside the cavities and of a 'real' CFD flow profile with vortices inside the cavities. In that way, the cavity effect on the signal is calculated, i.e. the effect of the geometry of the cavity, on the flow and acoustic fields, as well as the final summed up effect on the flowmeter performance and linearity. Moreover, the effect is quantified for the '%deviation' of v_{calc} (Eq. (1.8)) from v_{ref} (Eq. (1.1)) for an UTTF with the consideration of these two different flow-fields, while the importance of taking into account CFD is highlighted. The effect of 3D flow in the transducers' cavities of an UTTF has not been systematically investigated before, to the author's knowledge.

The SimPAC² method presents its own limitations and simplifications, which are summarized in the next paragraphs of the present section.

- The modules of electronics for the signal generation on the transmitter side and for signal acquisition on the receiver side are not taken into account. A voltage-source and an open-circuit are modeled for the transmitter and the receiver, respectively. If the exact characteristics of electronics are known, then simple models can be utilized and they can be linked with the use of transfer functions [277].
- For the wave propagation in the moving fluid medium, the considered equations [116, 183, 204, 203, 235] are derived with the approximation of slow variation of ambient properties in relation to the acoustic properties, which is a good approximation for the application of UTTF [31, 203].
- The solid pipe or meter body of the UTTF is not modeled in the current work. A rigid wall is considered instead, which is a reasonable approximation for an interface between air and a solid material such as stainless steel. For clarification, the SimPAC2 method is able to model the solid pipe; it is chosen for the current application not to model it. Due to the approximation of a rigid wall instead of a solid pipe, crosstalk phenomena, which might be of importance especially for gas USM [100, 162, 163, 278] are not simulated.
- Due to the hybrid nature of the method, the linkages betweem the FEM and FVM solvers have to be treated with care. Different meshes are used for each solver and therefore, the data interpolation on the interfaces between the FEM and FVM domains can be a possible source of error. This topic is discussed and investigated in Subsec. 4.3.2.2, through the comparison of the acoustic pressure on the interface between the meshes used in FEM and FVM.
- Due to the 3D nature of the method and the large amount of elements needed to model the 3D geometry, a long time is needed on a HPC machine for the calculation of the received voltage signal. Indicationally, for a UTTF with 100 mm nominal diameter, $\simeq$30 hours of computational time are needed.

It should be noted that the main focus of the present work is on the voltage-to-voltage simulation of UTTF, from a voltage-source of a transmitter on the piezoelectric element to an open-circuit voltage on a receiver, with parts **(I)-(IV)** included and modeled, as shown in Fig. 1.2. The method can be applied either to single-path or to multi-path UTTF. However, it is not the scope of this work the investigation of integration techniques or calculation of weight factors, w_i for multi-path UTTF. The method SimPAC² itself or even the 'CNA-Only CFD' can be used in the future for the extraction of such weight factors of multipath UTTF and for the investigation of optimum sound path position.

1.6 Outline of the Thesis

The present work is organized in 7 chapters.

In the present chapter, an introduction to UTTF, their applications, operating principle, and modeling is given. The motivation and main objective of the work, as well as a short description of the simulation method (SimPAC^2) are described. The state of the art and relevant publications to the topic of simulating UTTF or parts of it are given, while it is pointed out why the need to develop the SimPAC^2 method is evident.

In the second chapter, the theory and relevant equations are given for the description of the physics involved with an UTTF. Wave propagation in solid isotropic and anisotropic materials, piezoelectricity, wave propagation in quiescent and moving fluid media, flow and CFD are described in separate subsections. Finally, flow measurement with an UTTF, its principle, assumptions, and important aspects are given.

In the third chapter, the simulation methods, which are used and developed in this research are described. First, it is the CNA method, where no acoustics are included but only CFD to model the flowmeter. Then, SimPAC^2, which is the main method used and developed for the evaluation and modeling of UTTFs is described in length. Each of the subparts of the method (transmitter, receiver, flow, acoustics) and their connections are illustrated and details are given.

In the fourth chapter, verification and several comparisons of the program NACS, CNA and SimPAC^2 methods take place. The CNA method is compared with measurements of an UTTF for a reference straight pipe and an asymmetric flow disturber installed upstream of the device. NACS' optimum parameters are obtained with convergence studies and with the comparison with already published measurements [277] for two piezoelectric elements used as transmitter and receiver at zero flow. SimPAC^2 is compared with NACS for two different cases, piezoelectric elements in zero flow and in uniform flow parallel to the acoustic wave propagation.

In the fifth chapter, simulations of a simple flowmeter take place, with two piezoelectric elements in oblique angle relative to the flow. Two different geometries are considered, one 'with cavity' and one 'without cavity'. With the use of both the CNA and the SimPAC^2 methods, the effect of the presence of cavity on several parameters of the flowmeter such as the ToF and its deviation from a reference velocity is quantified. Furthermore, for the case 'with cavity' a number of different flow-fields is considered, such as uniform, fully developed and CFD generated flow-fields. The effect of different flow-fields on the flowmeter is investigated as well. At the end of the chapter, a study of the position of the interfaces between NACS and Star-CCM+ ®is performed.

In the sixth chapter, the main results of real flowmeter geometries are presented. Initially the piezoelectric material parameters are determined in order to assure that the simulated piezoelectric elements represent the measured ones. Real transducers are introduced for an inline UTTF with one diametrical sound path. The transducers are shifted to different positions, recessed, flush, and protruded and the effect of the position change as well as the cavities' effect on the signal are identified for different flow velocities. A real two-path UTTF is finally measured and simulated. The setup of the measurements and the simulations is given in detail. Analysis of the results takes place and their agreement is demonstrated.

In the seventh chapter, the main conclusions made during the development of the method and the analysis of results are given, while future work and further development is suggested.

Chapter 2

Theoretical Background

In this chapter, the theory and relevant equations are given for the description of the physics involved with an UTTF i.e. wave propagation in isotropic and piezoelectric solids, in moving, inhomogeneous, fluid media, and flow and computational fluid dynamics (CFD). The theory should be treated as of general use, with the assumptions made, to describe the respective physics and not only for the purpose of modeling an UTTF. At the end of the chapter, theoretical aspects are given regarding flow measurement with UTTF.

2.1 Wave Propagation in Elastic Solid Materials

Elastic solid is a deformable solid continuum, which suffers no energy loss when it goes back to its undefined equilibrium form [52]. Waves propagate in elastic solid materials when forces are applied to their particles, which are subsequently displaced from their initial positions. Elastic solid materials have the ability to restore their volume and shape when external forces are applied to them and therefore, longitudinal and shear waves travel through their matter. Longitudinal waves propagate due to the compression and rarefaction of material particles. In this case, the waves propagate in the direction of the particles' displacement. For shear or transversal waves on the other hand, the deformations in the medium are shear, which means that such waves propagate in a direction perpendicular to the direction of the particles' displacement from their initial positions at rest [5, 52, 107].

Solid materials are divided into isotropic and anisotropic. Their main difference is that the isotropic materials' properties are independent of the direction, while anisotropic materials' properties are dependent on it. In this research, both cases are studied, since the system of UTTF comprises both kinds of materials.

It is assumed that all solid materials investigated in the present work follow linear elasticity, meaning that the relation between stresses and strains is linear [5, 52, 107]. This is valid for a low power UTTF considered here, as displacements are small in comparison with the solid domain, the strain tensor is assumed to be linear and therefore the linear law of elasticity [5, 52, 107, 288] is valid.

2.1.1 Solid Isotropic Materials

One concise wave equation is derived for wave propagation in solid isotropic materials. For the derivation of this equation, let us consider a cartesian coordinate system (x, y, z) and an elementary volume $dxdydz$ [184] as shown in Fig. 2.1. T_{ij} are stresses acting on the surfaces

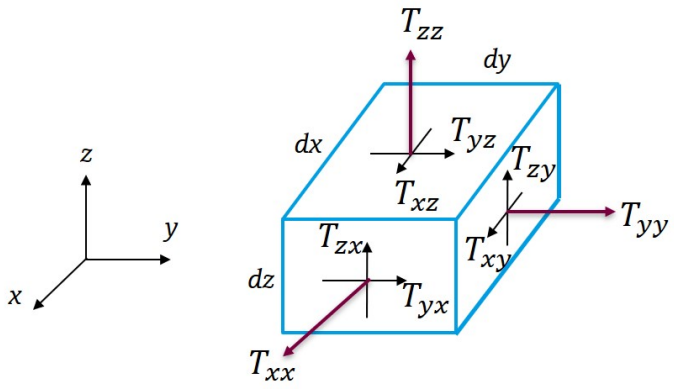

Figure 2.1: Elementary volume with stressing acting on it, for a Cartesian coordinate system.

of the elementary volume $dxdydz$, with i=x, y, z and j=x, y, z, where i denotes the direction of stresses and j the direction perpendicular to the plane that stresses act. T_{xx}, T_{yy}, and T_{zz} are normal stresses and $T_{xy}, T_{yx}, T_{xz}, T_{zx}, T_{yz}$ and T_{zy} are tangential stresses, as shown in Fig. 2.1. It is valid that $T_{xy} = T_{yx}, T_{xz} = T_{zx}$ and $T_{yz} = T_{zy}$ [5, 107, 184]. The balance of forces applied on the elementary volume $dxdydz$ are equal to the product of mass and acceleration per Newton's second law [5, 184]. The balance in directions (x, y, z) for an elementary volume $dxdydz$ that is not subjected to external body forces, is expressed as [5, 184]

$$\rho_0 \frac{\partial^2 u_x}{\partial t^2} = \frac{\partial T_{xx}}{\partial x} + \frac{\partial T_{xy}}{\partial y} + \frac{\partial T_{xz}}{\partial z}, \tag{2.1a}$$

$$\rho_0 \frac{\partial^2 u_y}{\partial t^2} = \frac{\partial T_{yx}}{\partial x} + \frac{\partial T_{yy}}{\partial y} + \frac{\partial T_{yz}}{\partial z}, \tag{2.1b}$$

$$\rho_0 \frac{\partial^2 u_z}{\partial t^2} = \frac{\partial T_{zx}}{\partial x} + \frac{\partial T_{zy}}{\partial y} + \frac{\partial T_{zz}}{\partial z}, \tag{2.1c}$$

where ρ_0 [kg/m^3] is density, $u_i(x, y, z)$ [m] are mechanical displacements in direction i=(x, y, z). The vector of the mechanical displacement

$$\boldsymbol{u} = \boldsymbol{d_1} - \boldsymbol{d_0} \tag{2.2}$$

is the distance that a point has moved from an initial to a deformed configuration of a body Ω_0 and Ω_1, respectively [5, 107], as shown in Fig. 2.2. $A_0(x_0,y_0,z_0)$ is an arbitrary point of

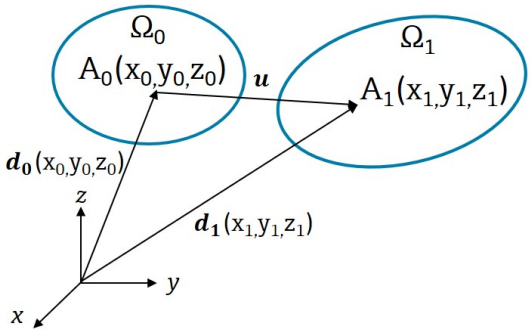

Figure 2.2: Initial and deformed configuration Ω_0 and Ω_1 of a volume body and displacement vector $\boldsymbol{u}$ from initial to deformed configuration.

the initial configuration Ω_0 at a position $\boldsymbol{d_0}$ and $\mathrm{A_1(x_1,y_1,z_1)}$ is the respective point of the deformed configuration Ω_1 at a position $\boldsymbol{d_1}$.

Now that the displacement vector $\boldsymbol{u}(x, y, z)$ is introduced, the three equations (2.1) can be combined into one and express the equation of motion [107]

$$\rho_0 \frac{\partial^2 \boldsymbol{u}}{\partial t^2} = \nabla \cdot [\boldsymbol{T}], \tag{2.3}$$

or equivalently in Einstein's summation convention [5, 122]

$$\rho_0 \ddot{u}_i = T_{ij,j} \tag{2.4}$$

where $[\boldsymbol{T}]$, or T_{ij} in the case of Einstein's summation convention, is the mechanical stress tensor, also called the Cauchy stress tensor [107],

$$[\boldsymbol{T}] = \begin{bmatrix} T_{xx} & T_{xy} & T_{xz} \\ T_{yx} & T_{yy} & T_{yz} \\ T_{zx} & T_{zy} & T_{zz} \end{bmatrix}. \tag{2.5}$$

When stresses are applied on a solid elementary volume, the particles are deformed in the direction of the stresses. The dimensionless deformation of two points of the body from their initial position is called strain. The relationship between strain and displacement can be geometrically derived [107] by considering an infinitessimal, small rectangular element, as shown in Fig. 2.3, for an initial and a deformed state. The terms $u_x(x + \Delta x, y), u_x(x, y + \Delta y), u_y(x + \Delta x, y)$, and $u_y(x, y + \Delta y)$ are expanded in a Taylor series and higher order terms

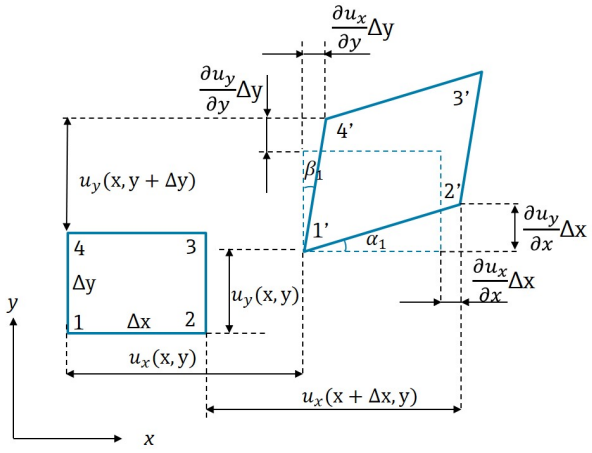

Figure 2.3: Initial and deformed state for an infinitesimal, small rectangular element.

are neglected [5, 107]. Therewith, it is derived that

$$s_{xx} = \frac{\partial u_x}{\partial x}, \tag{2.6a}$$

$$s_{yy} = \frac{\partial u_y}{\partial y}, \tag{2.6b}$$

$$\tag{2.6c}$$

which are the normalized elongations of the elastic body in the x and y directions and are called normal strains. Similarly, and by considering the angles α_1 and β_1 small, it is derived that

$$\frac{1}{2}(\alpha_1 + \beta_1) = \frac{1}{2}(\frac{\partial u_y}{\partial x} + \frac{\partial u_x}{\partial y}) = s_{xy}, \tag{2.7}$$

where s_{xy} is called the shear strain.

In order to derive a general relation between mechanical displacement and strain, the change of a line element between two neighboring points for an initial and a deformed three-dimensional configuration is considered. For more detailed information on this derivation, the interested reader is referred to [107]. Therefore, the strain tensor, which relates mechanical displacement and strain, is [5, 19, 52, 107]

$$[\boldsymbol{S}] = \frac{1}{2}(\nabla u + \nabla u^T), \tag{2.8}$$

The strain tensor has the form

$$[\boldsymbol{S}] = \begin{bmatrix} s_{xx} & s_{xy} & s_{xz} \\ s_{yx} & s_{yy} & s_{yz} \\ s_{zx} & s_{zy} & s_{zz} \end{bmatrix} = \begin{bmatrix} \frac{\partial u_x}{\partial x} & \frac{1}{2}\left(\frac{\partial u_x}{\partial y} + \frac{\partial u_y}{\partial x}\right) & \frac{1}{2}\left(\frac{\partial u_x}{\partial z} + \frac{\partial u_z}{\partial x}\right) \\ \frac{1}{2}\left(\frac{\partial u_y}{\partial x} + \frac{\partial u_x}{\partial y}\right) & \frac{\partial u_y}{\partial y} & \frac{1}{2}\left(\frac{\partial u_y}{\partial z} + \frac{\partial u_z}{\partial y}\right) \\ \frac{1}{2}\left(\frac{\partial u_z}{\partial x} + \frac{\partial u_x}{\partial z}\right) & \frac{1}{2}\left(\frac{\partial u_z}{\partial y} + \frac{\partial u_y}{\partial z}\right) & \frac{\partial u_z}{\partial z} \end{bmatrix} \tag{2.9}$$

when non-linearities are not considered [5, 107]. The generalized Hooke's law for isotropic materials states that stress and strain are linearly related and is well know as [5, 19, 52, 107, 184]

$$[\boldsymbol{T}] = \Lambda \ \mathrm{tr}([\boldsymbol{S}])[\boldsymbol{I}] + 2\mu[\boldsymbol{S}], \tag{2.10}$$

where Λ and μ are the Lame constants, $\mathrm{tr}([\boldsymbol{S}])$ is the trace of $[\boldsymbol{S}]$, i.e. the summation of the diagonal elements of $[\boldsymbol{S}]$, and $[\boldsymbol{I}]$ is the identity matrix. The generalized Hooke's law is equivalently written in Einstein's summation convention as

$$T_{ij} = \delta_{ij}\Lambda S_{ij} + 2\mu S_{ij}, \tag{2.11}$$

where δ_{ij} is the Kronecker delta [5]. Other parameters often used in practical problems instead of the Lame constants are the elasticity modulus [30, 107, 184]

$$E_m = \frac{\mu(3\Lambda + 2\mu)}{\Lambda + \mu}, \tag{2.12}$$

the shear modulus $G = \mu$, and the Poisson ratio [30, 107, 184]

$$\nu = \frac{\Lambda}{2(\Lambda + \mu)}. \tag{2.13}$$

One may see from eqs. (2.12) and (2.13), how the Lame constants, the elasticity and shear moduli, as well as the Poisson ratio are related.

If the stresses in terms of strains (Eq. (2.11)) are substituted in Eq. (2.3), the equation is obtained [30, 107, 184]

$$\rho_0 \frac{\partial^2 \boldsymbol{u}}{\partial t^2} = (\Lambda + \mu)\nabla(\nabla \cdot \boldsymbol{u}) + \mu\nabla^2 \boldsymbol{u}, \tag{2.14}$$

which describes wave propagation in solid, homogeneous, isotropic media in the absence of external forces and is called Navier equation [30, 107, 184].

In general, a vector field can be decomposed into a solenoidal and an irrotational part, according to Helmholtz decomposition [107]. For the displacement, it is therefore valid that

$$\boldsymbol{u} = \boldsymbol{u_l} + \boldsymbol{u_t} = \nabla\Phi + \nabla \times \boldsymbol{\Psi}, \tag{2.15}$$

where $\nabla \times \Phi = \nabla \cdot \boldsymbol{\Psi} = 0$ and therefore, $\boldsymbol{u_l} = \nabla\Phi$ is the irrotational part for a scalar potential Φ and $\boldsymbol{u_t} = \nabla \times \boldsymbol{\Psi}$ is the solenoidal part for a vector potential $\boldsymbol{\Psi}$ [5, 107, 184]. When substituting Eq. (2.15) into the wave equation for isotropic solid materials (Eq. (2.14)), two equations are obtained for the scalar and vector potential Φ and $\boldsymbol{\Psi}$ [5, 19, 30, 107, 184]

$$\frac{\partial^2 \Phi}{\partial t^2} = \frac{\Lambda + 2\mu}{\rho_0} \nabla^2 \Phi, \tag{2.16a}$$

$$\frac{\partial^2 \boldsymbol{\Psi}}{\partial t^2} = \frac{\mu}{\rho_0} \nabla^2 \boldsymbol{\Psi}. \tag{2.16b}$$

These equations express waves for a solid propagating with different velocities c_l of longitudinal nature and c_t of shear nature. From equations (2.16a), (2.16b) the longitudinal and shear wave velocities are defined respectively as

$$c_l = \sqrt{\frac{\Lambda + 2\mu}{\rho_0}}, \tag{2.17a}$$

$$c_t = \sqrt{\frac{\mu}{\rho_0}}. \tag{2.17b}$$

From eqs. (2.17), the ratio between the longitudinal and shear wave velocities is

$$\frac{c_l}{c_t} = \sqrt{\frac{\Lambda + 2\mu}{\mu}}, \tag{2.18}$$

which means

$$c_l > \sqrt{2} c_t, \tag{2.19}$$

i.e. the longitudinal waves travel faster than the shear ones. The interested reader may find detailed theory and derivation of the equation of wave propagation in solid isotropic materials in several textbooks [5, 19, 52, 107, 184].

2.1.2 Solid Anisotropic Materials

For the consideration of anisotropic materials, the tensor of elasticity moduli $\boldsymbol{c}$ is introduced for the linear relation between stresses and strains. [30, 52, 107]

$$[\boldsymbol{T}] = [\boldsymbol{c}][\boldsymbol{S}], \tag{2.20}$$

or in Einstein's summation convention [5, 107, 122]

$$T_{ij} = c_{ijkl} S_{kl}. \tag{2.21}$$

For the tensor components c_{ijkl} it is valid that [107]

$$c_{ijkl} = c_{ijlk} = c_{jikl} = c_{klij}. \tag{2.22}$$

When Eq. (2.20) (or Eq. (2.21)) is substituted in Eq. (2.3), the equation is obtained [107]

$$\rho_0 \frac{\partial^2 \boldsymbol{u}}{\partial t^2} = B^T [\boldsymbol{c}] B \boldsymbol{u}, \tag{2.23}$$

which describes wave propagation in solid anisotropic materials, where

$$B = \begin{pmatrix} \frac{\partial}{\partial x} & 0 & 0 & 0 & \frac{\partial}{\partial z} & \frac{\partial}{\partial y} \\ 0 & \frac{\partial}{\partial y} & 0 & \frac{\partial}{\partial z} & 0 & \frac{\partial}{\partial x} \\ 0 & 0 & \frac{\partial}{\partial z} & \frac{\partial}{\partial y} & \frac{\partial}{\partial x} & 0 \end{pmatrix}^T. \tag{2.24}$$

is the differential operator.

2.1.3 Piezoelectric Materials

The piezoelectric effect was firstly discovered by Pierre and Jacques Curie in 1880. It appears on crystals that have no center of symmetry when strong electric field in high temperatures is applied on them. As a result, the individual crystals that comprise the polycrystal are aligned, the material obtains piezoelectric properties and polarization takes place [91]. The crystals investigated in this research are piezoelectric ceramics and mostly the lead zirconate titanate i.e. PZT [95]. In Fig. 2.4 a piezoelectric element is shown schematically at rest and for the different states of the direct and inverse piezoelectric effects. The different states shown in Fig. 2.4 are indicative, while the displacement and force magnitudes are not realistic but exaggerated for understanding purposes.

Piezoelectric materials are typically used for generation and reception of pulses in UTTF. The inverse piezoelectric effect is used for the sending transducer when alternating current (AC) voltage on high frequency is applied, which is transformed to mechanical vibrations. The piezoelectric effect is used for the receiving transducer when mechanical vibrations due to the acoustic waves received, are transformed into high frequency AC voltage. Depending on the AC frequency applied, different modes are excited resulting to different displacement of the piezoelectric element[78, 122, 124, 210].

A system of equations and a number of assumptions are needed in order to model piezoelectric materials [15]. The strain for linear piezoelectric materials has the same form as Eq. (2.9). The equation of motion is similarly expressed as for solid linear materials in equations (2.3) or (2.4).

For piezoelectric materials the coupling between mechanics and electrics should be additionally expressed, compared to solid elastic materials. The constitutive equations for piezoelectric media are [15, 30, 122]

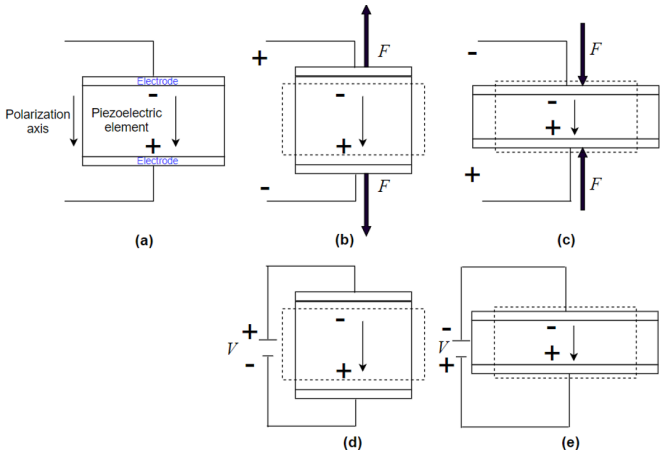

Figure 2.4: Piezoelectric element with electrodes. (a) At rest. (b) Direct piezoelectric effect. Force F applied on element, stretching it, results into voltage V with opposite polarity. (c) Direct piezoelectric effect. Force F applied on element, compressing it, results into voltage V with the same polarity as the polarization axis of the element. (d) Inverse piezoelectric effect. Voltage V with opposite polarity to the polarization axis, results into stretching of the piezoelectric element. (e) Inverse piezoelectric effect. Voltage V with same polarity as the polarization axis results into compressing of the piezoelectric element.

$$[\boldsymbol{T}] = [\boldsymbol{c}^{\boldsymbol{E}}][\boldsymbol{S}] - [\boldsymbol{e}]^T \boldsymbol{E}, \tag{2.25}$$

$$\boldsymbol{D} = [\boldsymbol{e}][\boldsymbol{S}] + [\boldsymbol{\epsilon}^{\boldsymbol{S}}]\boldsymbol{E}, \tag{2.26}$$

where [15, 30, 122]

$\boldsymbol{E}$ is the electric field vector $[V/m]$,

$\boldsymbol{D}$ is the electric displacement vector $[C/m^2]$,

$[\boldsymbol{c}^{\boldsymbol{E}}]$ is the tensor of elasticity moduli determined in constant electric field $[N/m^2]$,

$[\boldsymbol{e}]$ is the piezoelectric constant tensor $[C/m^2]$,

$[\boldsymbol{\epsilon}^{\boldsymbol{S}}]$ is the dielectric constant tensor determined in constant strain $[F/m]$,

Maxwell's equations are used for the description of electromagnetic fields in the piezoelectric materials on a macroscopic level and their relation to the microscopic average properties of the material [19, 122, 224]. When there are no free charges per unit volume in the material, i.e. the material insulates, the electric field is described with [19, 30, 122]

$$\nabla \cdot \boldsymbol{D} = 0 \tag{2.27}$$

or in Einstein's summation convention $D_{i,i} = 0$ [122]. With the introduction of the quasistatic

approximation the electric field is described as [19, 30, 122]

$$\boldsymbol{E} = -\nabla\psi, \tag{2.28}$$

where ψ is the electric potential $[V]$. Eq. (2.28) is written in Einstein's summation convention as $E_i = -\psi_{,i}$ [122].

With the use and combination of the introduced equations (2.4), (2.25), (2.26), (2.27), and (2.28), elastic piezoelectric materials without losses are modeled. For the inclusion of elastic, piezoelectric, and dielectric losses, complex values are introduced in the tensor of elasticity moduli $\boldsymbol{c}^E$, piezoelectric constants $\boldsymbol{e}$, and dielectric constants $\boldsymbol{\epsilon}^S$, respectively [93]. Alternatively, an artificial, numerical damping is included, such as the Rayleigh damping [30, 42]. In the present work, a Rayleigh damping is considered for the inclusion of losses, as it is described in Sec. 6.1.

2.2 Acoustic Wave Propagation in Quiescent and Moving Fluid Media

Sound propagates in fluid media in the form of longitudinal acoustic waves in antithesis to solid media where sound propagates in the form of longitudinal and shear waves [107, 117, 132, 204]. Propagation of sound in quiescent (flow velocity $\boldsymbol{v_0} = 0$) and moving media is described with a set of equations or a concise acoustic wave equation. The derivation of these equations and the underlying assumptions are described in the present subsection. For their derivation, the basic equations of fluid dynamics are presented.

It is important to note that in general a total field quantity of pressure, density, specific entropy, and velocity is expressed as a summation of an ambient field variable and a comparably small acoustic quantity. Therefore, for each of the introduced quantities it is valid that

$$p = p_0 + p', \qquad \rho = \rho_0 + \rho', \qquad s = s_0 + s', \qquad \boldsymbol{v} = \boldsymbol{v_0} + \boldsymbol{v}'. \tag{2.29}$$

Several definitions for the characterization of the fluid are useful for the understanding of this chapter and avoidance of misconceptions. When ambient properties vary with space, the medium is called inhomogeneous, while in the case of non-variation of these properties, the medium is called homogeneous. Furthermore, variation of the ambient properties with time, means that the medium is transient (or unsteady, or time-varying), while non-variation means that the medium is stationary [132]. A fluid is incompressible when the ambient density ρ_0=const throughout the domain, while a flow is incompressible when the density ρ is constant in an infinitesimal volume of the fluid through the flow, with the consequence that $\nabla \cdot \boldsymbol{v} = 0$ [72, 132].

2.2.1 Fluid Dynamics Equations

The basic equations of fluid dynamics are presented, as they are needed for the derivation of acoustic wave equations for quiescent and moving fluid media [117, 132].

The conservation of mass is described as the equality between the net rate with which mass flows into a control volume $dV = dxdydz$ fixed in space (Eulerian description) through its surface, and the rate at which the mass within the volume increases. It is represented with the continuity equation [13, 58, 72, 117, 132]

$$\frac{\partial \rho}{\partial t} + \nabla \cdot (\rho \boldsymbol{v}) = 0, \tag{2.30}$$

which is valid for both viscous and inviscid fluid media. $\rho = \rho(x, y, z, t)$ and $\boldsymbol{v} = \boldsymbol{v}(x, y, z, t)$ are the total field quantities of density and fluid velocity, respectively, which are time and space dependent.

The conservation of momentum is the balance of the net force on a moving element $dV = dxdydz$ (Lagrangian description) that accelerate it according to Newton's 2^{nd} law. It is represented with Euler's equation [13, 58, 72, 117, 132]

$$\rho \left(\frac{\partial \boldsymbol{v}}{\partial t} + (\boldsymbol{v} \cdot \nabla)\boldsymbol{v} \right) = -\nabla p, \tag{2.31}$$

which is valid for lossless fluids, and with the assumption that the effect of gravity is negligible. $p = p(x, y, z, t)$ is the total field quantity of pressure, which is a function of space and time. Eq. (2.31) is used for the derivation of the acoustic wave equations for quiescent and moving media in Sec. 2.2, while for the description and simulation of flow with CFD, the Navier-Stokes equations are used, which are presented in Sec. 2.3.

2.2.2 Quiescent Fluid Medium

Propagation of sound in quiescent, lossless media is described with a well-known linear acoustic wave equation, which is derived from the general equations of fluid dynamics, with the respective assumptions. Since the fluid medium is non-moving, it is valid that $\boldsymbol{v_0} = 0$. The process is nearly isentropic (adiabatic and reversible) [117] and therefore the adiabatic equation of state is considered [117]

$$\frac{p}{p_0} = \left(\frac{\rho}{\rho_0} \right)^{\gamma}, \tag{2.32}$$

where $\gamma = c_p/c_v$ is the ratio of specific heat capacities for constant pressure c_p [J/(kg·K)] and for constant volume c_v [J/(kg·K)]. The equation of state can be written as a function of density, $p = p_0(\rho)$ for an isentropic process. Linearization takes place, with expansion

through a Taylor series and neglecting terms of 2^{nd} order or higher, resulting to [117]

$$p' \simeq B_s \acute{s}, \tag{2.33}$$

where $B_s = \left(\rho_0 \frac{\partial p}{\partial \rho}\right)_{\rho_0}$ is the adiabatic bulk modulus, and $\acute{s} = \frac{\rho - \rho_0}{\rho_0}$ is the condensation [-]. Neglecting 2^{nd} and higher order terms means that the acoustic fluctuations are small [117].

Therefore, the linearized equation of state for isentropic processes can be rewritten as

$$p' = c^2 \rho', \tag{2.34}$$

with $c^2 = B_s/\rho_0$ being defined as the thermodynamic speed of sound [117] and for propagation of sound in fluids with phase speed c.

The continuity equation (2.30) is linearized [117] with the use of condensation $\acute{s}$ and by replacing density $\rho = \rho_0(1 + \acute{s})$, with ρ_0 being a weak function of time, resulting to

$$\rho_0 \frac{\partial \acute{s}}{\partial t} + \nabla \cdot (\rho_0 \boldsymbol{v'}) \simeq 0. \tag{2.35}$$

If ρ_0 is a weak function of space as well, then it is obtained

$$\frac{\partial \acute{s}}{\partial t} + \nabla \cdot \boldsymbol{v'} = 0. \tag{2.36}$$

Similarly, the Euler's equation (2.31) is linearized [117] by assuming small acoustic fluctuation amplitudes and that $\mid (\boldsymbol{v} \cdot \nabla)\boldsymbol{v} \mid \ll \mid \frac{\partial \boldsymbol{v}}{\partial t} \mid$, resulting to

$$\rho_0 \frac{\partial \boldsymbol{v'}}{\partial t} \simeq -\nabla p' \tag{2.37}$$

When the time derivative $\frac{\partial}{\partial t}$ of the linearized continuity equation (2.35) is taken and the divergence$\nabla\cdot$ of the linearized Euler equation (2.37), it is derived that

$$\rho_0 \frac{\partial^2 \acute{s}}{\partial t^2} \simeq \nabla^2 p'. \tag{2.38}$$

Elimination of $\acute{s}$ is possible with the use of equation of state (2.33). Therefore, an acoustic wave equation in terms of acoustic pressure is derived

$$\frac{1}{c^2} \frac{\partial^2 p'}{\partial t^2} = \nabla^2 p' \tag{2.39}$$

for quiescent, lossless fluid media and small acoustic fluctuations, where B_s and ρ_0 are weak functions of time but have no restriction requirement for space in the course of this derivation

and therefore Eq. (2.39) is valid for propagation in media with sound speed $c = c(x, y, z)$, which is a function of space [117].

A similar wave equation can be derived in terms ś by using Eq. (2.33) and assuming that B_s and c are weak functions of space. It is derived that [117]

$$\frac{1}{c^2}\frac{\partial^2 \acute{s}}{\partial t^2} = \nabla^2 \acute{s}, \tag{2.40}$$

which shows that p' and ś satisfy the same wave equation and therefore they are in phase and propagate with phase velocity c.

On the other hand, particle velocity $\boldsymbol{v'}$ does not obey the same wave equation as p' and c. A velocity potential ϕ is defined as [117]

$$\boldsymbol{v'} = \nabla\phi, \tag{2.41}$$

implying that $\boldsymbol{v'}$ is irrotational, which is a reasonable and good approximation for most acoustic processes. Particle velocity $\boldsymbol{v'}$ can be rotational next to boundaries or inside cavities, however the effect is very small [117]. By replacing Eq. (2.41) into Eq. (2.31) an equation between p' and ϕ is obtained

$$p \simeq -\rho_0 \frac{\partial \phi}{\partial t}. \tag{2.42}$$

By replacing Eq. (2.42) into Eq. (2.39) a wave equation in terms of ϕ is obtained [30, 117]

$$\frac{1}{c^2}\frac{\partial^2 \phi}{\partial t^2} = \nabla^2 \phi, \tag{2.43}$$

which has the requirement that ρ_0 is more than a gradual function of space [117]. Therefore, ϕ satisfies the same type of wave equation as p' and ś.

The linear acoustic wave equations for quiescent, lossless fluid media used in the present work are Eq. (2.39) in Star-CCM+® [235] and Eq. (2.43) in NACS [183]. To summarize, the assumptions of the acoustic wave equations (2.39) and (2.43) are

- linear acoustics,
- lossless fluid media,
- wave propagation in fluid with varying properties spatially, i.e. inhomogeneous, and therefore, suitable for homogeneous as well,
- ambient properties B_s and ρ_0 that are weak functions of time
- for Eq. (2.43) only it should be satisfied that v' is irrotational, which could be problematic in the cavities of an USM, however the effect is very small [117].

The assumptions above do not affect the applicability of the equations to modeling of USM for the case of $\boldsymbol{v_0} = 0$ [30, 60, 59, 197].

2.2.3 Moving Fluid Medium

In UTTF applications, the fluid is moving in most of the cases and therefore an acoustic wave equation or a set of equations is needed, in order to take the effect of ambient velocity, $\boldsymbol{v_0}$, into account.

Two different equations for moving fluid media are used in the present work, the Pierce equation (PE) [203] and the convected acoustic wave equation (CAWE) [116, 229] derived from the acoustic perturbation equations (APE) [68]. Nonetheless, more equations or sets of equations are presented through the course of their derivation and a corrected version of the CAWE is given.

2.2.3.1 The Pierce Equation

Let us start by introducing the general, lossless, nonlinear equations of fluid dynamics for a compressible fluid of uniform composition in the absence of dissipation and without the effect of gravitational force [203]

$$D_t\rho + \rho\nabla\cdot\boldsymbol{v} = 0, \tag{2.44}$$

$$D_t\boldsymbol{v} + \frac{1}{\rho}\nabla p = 0, \tag{2.45}$$

$$D_t s = 0, \tag{2.46}$$

$$p = p(\rho, s), \tag{2.47}$$

which are the continuity equation, the momentum equation, the condition of adiabatic motion and the equation of state respectively, with $D_t \equiv \frac{\partial}{\partial t} + \boldsymbol{v_0}\cdot\nabla$ being the material derivative related to the ambient medium (flow) velocity. Equations (2.44), (2.45) are consistent with (2.30) and (2.31) respectively and are rewritten in this form for convenience.

Pierce derived a concise wave equation, from now on called Pierce equation (PE), for unsteady, inhomogeneous fluid media [203]. For the derivation, linearization of the general equations (2.44)-(2.47) is achieved by expressing each field quantity as a summation of an ambient and an acoustic quantity, e.g. $p = p_0 + p'$ in the case of pressure. The resulting linearized set of equations, from which the PE is derived, constitute the the Linearized Equations of Fluid Dynamics (LEFD) for a one-component medium, first derived by Blokhintzev [35] and described in several textbooks and articles [187, 188, 204, 203]

$$D_t\boldsymbol{v'} + \boldsymbol{v'}\cdot\nabla\boldsymbol{v_0} + \frac{1}{\rho_0}\nabla p' - \frac{\rho'}{\rho_0^2}\nabla p_0 = 0, \tag{2.48a}$$

$$D_t\rho' + \boldsymbol{v'}\cdot\nabla\rho_0 + \rho'\nabla\cdot\boldsymbol{v_0} + \rho_0\nabla\cdot\boldsymbol{v'} = 0, \tag{2.48b}$$

$$D_t s' + \boldsymbol{v'}\cdot\nabla s_0 = 0, \tag{2.48c}$$

$$p' = c^2\rho' + \frac{\partial p_0}{\partial s_0}s', \tag{2.48d}$$

when body forces and mass sources are not considered [35, 203]. Here, $\boldsymbol{v'}(\boldsymbol{r}, t)$, $\rho'(\boldsymbol{r}, t)$

$p'(\boldsymbol{r},t), s'(\boldsymbol{r},t)$ are the particle velocity, density, pressure and specific entropy of the acoustic wave fluctuations, and $s_0(\boldsymbol{r},t)$ is the ambient specific entropy. $\boldsymbol{r}$ is the position vector. The ambient properties $\boldsymbol{v_0}$, ρ_0, p_0 are also dependent on space and time.

From combination and mathematical manipulation of the LEFD, the PE is derived [203]

$$\frac{1}{\rho_0}\nabla\cdot(\rho_0\nabla\phi) - D_t(\frac{1}{c^2}D_t\phi) = 0. \tag{2.49}$$

The relation between p' and ϕ for the PE (2.49) is

$$p' = -\rho_0 D_t\phi. \tag{2.50}$$

Certain assumptions and simplifications are made for the derivation of the PE. The ambient medium quantities $\boldsymbol{v_0}(\boldsymbol{r},t)$, $\rho_0(\boldsymbol{r},t)$, $p_0(\boldsymbol{r},t)$, $s_0(\boldsymbol{r},t)$, and $c(\boldsymbol{r},t)$ are assumed to be slowly varying in space and time, as compared to the length and time scales of the acoustic waves i.e., the wavelength and oscillation period of the acoustic signal, respectively. Second and higher order derivatives of $\boldsymbol{v_0}$, ρ_0, p_0, s_0, and c with respect to space and time are neglected, as well as the products of first order derivatives.[203]

2.2.3.2 The Linearized Acoustic Equations

The Linearized acoustic equations (LAE) is another set of equations also derived from the LEFD, given as [47, 48]

$$D_t\boldsymbol{v'} + \boldsymbol{v'}\cdot\nabla\boldsymbol{v_0} + \frac{1}{\rho_0}\nabla p' - \frac{\rho'}{\rho_0^2}\nabla p_0 = 0, \tag{2.51a}$$

$$D_t\rho' + \boldsymbol{v'}\cdot\nabla\rho_0 + \rho'\nabla\cdot\boldsymbol{v_0} + \rho_0\nabla\cdot\boldsymbol{v'} = 0, \tag{2.51b}$$

$$p' = c^2\rho'. \tag{2.51c}$$

Derivation of the LAE given by Eqs. (2.51a)-(2.51c) is indicated in the documentation of COMSOL Multiphysics®.[47, 48]. A derivation from the LEFD can be made as follows [47, 48]. By (i) discarding the specific acoustic entropy fluctuations, s', and (ii) ignoring the remaining part of the condition of adiabatic motion (i.e., ignoring $\boldsymbol{v'}\cdot\nabla s_0 = 0$, that decouples from the remaining equations for $\boldsymbol{v}, p$, and ρ), Eqs. (2.48a)-(2.48d) reduce to Eqs. (2.51a)-(2.51c).

2.2.3.3 The CAWE Model

The CAWE is another equation suitable for modeling sound propagation in moving media. It is derived from the APE, which are given as Eqs. (47)-(48) by Ewert and Schröder,[68]

$$\frac{\partial p'}{\partial t} + \bar{c}^2 \nabla \cdot \left(\bar{\rho}_0 \boldsymbol{v} + \bar{\boldsymbol{v}}_{\mathbf{0}} \frac{p'}{\bar{c}^2} \right) = \bar{c}^2 q_c, \tag{2.52a}$$

$$\frac{\partial \boldsymbol{v'}}{\partial t} + \nabla \left(\bar{\boldsymbol{v}}_{\mathbf{0}} \cdot \boldsymbol{v'} \right) + \nabla \left(\frac{p'}{\bar{\rho}_0} \right) = q_m, \tag{2.52b}$$

where q_c and q_m represent sources of sound, and are given by Eqs. (49)-(50) in Ref.[68], and the bar above the parameters indicates time-averaging. q_c and q_m both account for sound generated by turbulence fluctuations and entropy inhomogeneities, while q_m additionally accounts for sound due to acoustic/mean-vorticity interaction. The APE have been derived by applying a source-filtering technique on the linearized Euler equations (LEE), and taking into account only the vortical and not the acoustic source terms, as explained in [68]. The source term q_c was set to zero and q_m was simplified by Eqs. (51) and (52) in Ref. [68] and as a result, the reduced APE are subject to an assumption of incompressible flow[229] for Mach number, $M = v_0/c \ll 1$ (cf. page 377 in Ref. [68]) and slow variation of the ambient medium quantities in space and time [68, 229].

The CAWE is given as Eq. (3471) in the STAR-CCM+®Documentation[229] and as Eq. (1) by Kierkegaard et al. [116],

$$\begin{aligned} \frac{1}{c^2} \left[\frac{\partial^2 p'}{\partial t^2} + 2\bar{\boldsymbol{v}}_{\mathbf{0}} \cdot \nabla \frac{\partial p'}{\partial t} + (\bar{\boldsymbol{v}}_{\mathbf{0}} \cdot \nabla)(\nabla \cdot \bar{\boldsymbol{v}}_{\mathbf{0}} p') \right] - \nabla^2 p' = \\ -\frac{1}{c^2} \left[\frac{\partial^2 P'}{\partial t^2} + 2\bar{\boldsymbol{v}}_{\mathbf{0}} \cdot \nabla \frac{\partial P'}{\partial t} + (\bar{\boldsymbol{v}}_{\mathbf{0}} \cdot \nabla)(\nabla \cdot \bar{\boldsymbol{v}}_{\mathbf{0}} P') \right], \end{aligned} \tag{2.53}$$

where an artificial and numerically motivated damping parameter used by Kierkegaard et al. [116] (in the $\nabla^2 p'$ term) has been set to zero. Here, P' are the ambient pressure fluctuations. The derivation of the CAWE is done by taking the material derivative of the reduced Eq. (2.52a) and the divergence of the reduced Eq. (2.52b), and combining the resulting equations [229]. The CAWE is then derived in terms of acoustic pressure [229].

However, a closer look at Eq. (2.53) reveals an inconsistency. The 3rd term on the left-hand side of Eq. (2.53) can be written as

$$\bar{\boldsymbol{v}}_{\mathbf{0}} \cdot \nabla(\nabla \cdot \bar{\boldsymbol{v}}_{\mathbf{0}} p') = \bar{\boldsymbol{v}}_{\mathbf{0}} \cdot \nabla(\underbrace{\nabla p' \cdot \bar{\boldsymbol{v}}_{\mathbf{0}}}_{\mathbf{I}} + \underbrace{p' \nabla \cdot \bar{\boldsymbol{v}}_{\mathbf{0}}}_{\mathbf{II}}), \tag{2.54}$$

and similarly for the 3rd term on the right-hand side of Eq. (2.53). Term **II** of Eq. (2.54) contains $\nabla \cdot \bar{\boldsymbol{v}}_{\mathbf{0}}$, which according to the assumption of incompressible flow underlying the CAWE (see above) is to be set to zero. This term should therefore have been discarded. By discarding the two relevant terms at the left and right-hand sides of Eq. (2.53), a more

consistent version of CAWE takes the form

$$\frac{1}{c^2}\left[\frac{\partial^2 p'}{\partial t^2} + 2\bar{\boldsymbol{v}}_{\mathbf{0}} \cdot \nabla \frac{\partial p'}{\partial t} + \bar{\boldsymbol{v}}_{\mathbf{0}} \cdot \nabla(\bar{\boldsymbol{v}}_{\mathbf{0}} \cdot \nabla p')\right] - \nabla^2 p' = -\frac{1}{c^2}\left[\frac{\partial^2 P'}{\partial t^2} + 2\bar{\boldsymbol{v}}_{\mathbf{0}} \cdot \nabla \frac{\partial P'}{\partial t} + \bar{\boldsymbol{v}}_{\mathbf{0}} \cdot \nabla(\bar{\boldsymbol{v}}_{\mathbf{0}} \cdot \nabla P')\right]. \tag{2.55}$$

Eq. (2.55) will be referred to as the Modified CAWE II. In situations for which P' can be neglected (i.e., the flow induced sound is ignored), Eq. (2.55) reduces to

$$\frac{1}{c^2}\left[\frac{\partial^2 p'}{\partial t^2} + 2\bar{\boldsymbol{v}}_{\mathbf{0}} \cdot \nabla \frac{\partial p'}{\partial t} + \bar{\boldsymbol{v}}_{\mathbf{0}} \cdot \nabla(\bar{\boldsymbol{v}}_{\mathbf{0}} \cdot \nabla p')\right] - \nabla^2 p' = 0, \tag{2.56}$$

which will be referred to as the Modified CAWE I.

In the present work, the equation that is used among equations (2.53), (2.55), (2.56) is the Modified CAWE I (2.56). In Star-CCM+®eq- (2.53) is implemented, however due to absence of turbulent fluctuations and flow compressibility in the considered simulations, Eq. (2.53) is reduced to Eq. (2.56). Turbulent fluctuations' frequency is of the order of $<$ 10 kHz, [236, 267] while typical frequencies of gas UTTF are $>$ 100 kHz [57, 155, 163]. Therefore, no interaction between turbulence fluctuations and ultrasonic waves is assumed, because of the order of magnitude difference, and consequently a steady flow is considered. Maximum flows for gas UTTF present typically values of $M < 0.3$ [163]. For such values of M, density does not change due to flow velocity, i.e. the change of density is less than 5%, for which the accepted convention is made that the flow incompressibility assumption is valid. For more information on the topic of flow incompressibility, the interested reader is referred to e.g. [58, 72].

2.3 Fluid Dynamics

Flow inside an UTTF varies heavily depending on the application and conditions and thus, it is crucial that it is modeled correctly.

Ambient flow velocity, $\boldsymbol{v_0} = \boldsymbol{v_0}(\boldsymbol{r}, t)$, can vary significantly, as the flow profile, for internal pipe flows, varies with the Reynolds number [34, 58, 132],

$$Re = \frac{\rho_0 v_{ref} l}{\mu}, \tag{2.57}$$

where l [m] is the characteristic length of the flow, e.g. for pipe flow it is the diameter, μ [Pa $\cdot$ s] is the dynamic shear viscosity, while v_{ref} is given by Eq. (1.1) in the case of a circular pipe. In Fig. 2.5 a schematic representation of velocity flow profile for internal pipe flow is shown. Fig. 2.5 **(a)** shows a parabolic flow profile for laminar flows occurring for a critical $Re \lesssim 2300$. Fig. 2.5 **(b)** shows a turbulent flow profile for turbulent flows occurring typically typically for $Re \gtrsim 4000$. Transition takes place between the laminar and turbulent

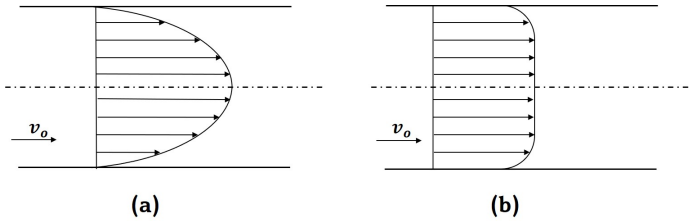

Figure 2.5: Schematic representation of velocity flow profile for internal pipe flow. (a) Laminar flow profile, (b) Turbulent flow profile.

regimes, however the distinction among these is not always straightforward and therefore it is a highly discussed topic in literature [34, 70, 132].

Moreover, the flow profile is not necessarily fully-developed [58, 132, 236] but varies depending on the upstream conditions (e.g. bends, contraction, expansion, obstacles etc.) [106], while in the case of inline UTTF, vortices are created in the cavities, where the transducers are placed [196, 239].

2.3.1 The Navier-Stokes Equations

The Navier-Stokes (N-S) equations describe the complex flow field in several applications (external aerodynamics, internal pipe flows, oceanic currents, atmospheric currents etc.) and therefore they are used for the application of UTTF, which belongs to internal pipe flows. In the present work, incompressible flows are solved ($M \lesssim 0.3$) [72], however the equations for both compressible and incompressible flows are presented. For compressible flows, the continuity equation takes the already presented form of Eq. (2.30), while for incompressible flows, it is simplified to [58, 72, 132]

$$\nabla \cdot \boldsymbol{v_0} = 0, \tag{2.58}$$

or in Einstein's summation convention

$$\frac{\partial v_{0i}}{\partial x_i} = 0. \tag{2.59}$$

The momentum equation i.e. N-S equation for viscous compressible flows takes into account the shear viscous stresses as well, which were neglected in the already presented Euler equation ((2.31)), and takes the form [58, 72, 132]

$$\frac{\partial \rho_0 \boldsymbol{v_0}}{\partial t} + \nabla \cdot (\rho_0 \boldsymbol{v_0} \boldsymbol{v_0}) = -\nabla p_0 + \nabla \cdot \boldsymbol{\tau}, \tag{2.60}$$

where $\boldsymbol{\tau}$ is the viscous (deviatoric) stress tensor [58, 72]

$$\boldsymbol{\tau} = 2\mu \boldsymbol{D_s} - \frac{2}{3}\mu \nabla \cdot \boldsymbol{v_0}, \tag{2.61}$$

where

$$\boldsymbol{D_s} = \frac{1}{2}(\nabla \boldsymbol{v_0} + \nabla \boldsymbol{v_0^T}) = \begin{bmatrix} d_{xx} & d_{xy} & d_{xz} \\ d_{yx} & d_{yy} & d_{yz} \\ d_{zx} & d_{zy} & d_{zz} \end{bmatrix} = \begin{bmatrix} \frac{\partial v_{0x}}{\partial x} & \frac{1}{2}\left(\frac{\partial v_{0x}}{\partial y} + \frac{\partial v_{0y}}{\partial x}\right) & \frac{1}{2}\left(\frac{\partial v_{0x}}{\partial z} + \frac{\partial v_{0z}}{\partial x}\right) \\ \frac{1}{2}\left(\frac{\partial v_{0y}}{\partial x} + \frac{\partial v_{0x}}{\partial y}\right) & \frac{\partial v_{0y}}{\partial y} & \frac{1}{2}\left(\frac{\partial v_{0y}}{\partial z} + \frac{\partial v_{0z}}{\partial y}\right) \\ \frac{1}{2}\left(\frac{\partial v_{0z}}{\partial x} + \frac{\partial v_{0x}}{\partial z}\right) & \frac{1}{2}\left(\frac{\partial v_{0z}}{\partial y} + \frac{\partial v_{0y}}{\partial z}\right) & \frac{\partial v_{0z}}{\partial z} \end{bmatrix} \tag{2.62}$$

is the rate of strain tensor. The N-S equation can also be written in Einstein's summation convention as [58, 72]

$$\frac{\partial \rho_0 v_{0i}}{\partial t} + \frac{\partial \rho_0 v_{0j} v_{0i}}{\partial x_j} = -\frac{\partial p_0}{\partial x_i} + \frac{\partial \tau_{ij}}{\partial x_j}, \tag{2.63}$$

where

$$\tau_{ij} = 2\mu D_{s\,ij} - \frac{2}{3}\mu \frac{v_{0j}}{\partial x_j}, \tag{2.64}$$

with $D_{ij} = \frac{1}{2}\left(\frac{\partial v_{0i}}{\partial x_j} + \frac{\partial u_{0j}}{\partial x_i}\right)$.

When incompressible flows are considered, the respective terms are vanished from the N-S equation (eq. (2.60)) i.e., no spatial or temporal change of density and $\nabla \cdot \boldsymbol{v_0} = 0$. Thus, the N-S equation gets slightly simplified, [58]

$$\rho_0 \frac{\partial \boldsymbol{v_0}}{\partial t} + \rho_0 (\boldsymbol{v_0} \cdot \nabla)\boldsymbol{v_0} = -\nabla p_0 + \nabla \cdot \tau_{inc}, \tag{2.65}$$

where

$$\boldsymbol{\tau_{inc}} = 2\mu \boldsymbol{D_s}, \tag{2.66}$$

which is simplified compared to Eq. (2.61), as its second term is zero, because of the continuity equation (2.58) for incompressible flow. The N-S equation for incompressible flows with Einstein's summation convention is given as

$$\rho_0 \frac{\partial v_{0i}}{\partial t} + \rho_0 \frac{\partial v_{0j} v_{0i}}{\partial x_j} = -\frac{\partial p_0}{\partial x_i} + \frac{\partial \tau_{inc,ij}}{\partial x_j}, \tag{2.67}$$

where

$$\tau_{inc,ij} = 2\mu D_{s\,ij}. \tag{2.68}$$

Detailed derivations of the continuity and N-S equations for incompressible and compressible flow can be found in several textbooks [13, 14, 58, 72, 132].

In the present work, incompressible flows are considered (M<0.3) and therefore, eqs. (2.58) and (2.65) are used for the flow modeling.

2.3.2 Solution Approach to Navier-Stokes Equations

In order to solve the N-S equations and the chaotic nature of turbulence, different turbulence approaches are used. The Reynolds averaged Navier-Stokes (RANS) [11, 72, 267] and scaled-resolving simulation (SRS) [173, 267] are such typical approaches. It has to be noted that when the flow is laminar ($Re \lesssim 2300$), turbulence models are not needed, since turbulence is not present and therefore, the N-S equations may be directly computed and solved with the provided assumptions and boundary conditions [58, 72, 220].

In RANS approach, the unsteady part of the flow is averaged out and is part of the turbulence. In general, a variable w is written as a sum of a time-averaged value and a fluctuation

$$w_0(x_i,t) = \bar{w}_0(x_i) + w_0'(x_i,t), \tag{2.69}$$

where $\bar{w}_0(x_i) = \lim_{T\to\infty} \frac{1}{T}\int_0^T w_0(x_i,t)dt$. By using this convention, the variables in continuity and N-S equations are replaced with the summation of the time-averaged value and the fluctuation, having in mind that in general $\bar{w_0'}(x_i,t) = 0$. For compressible flow, the averaged continuity and N-S equations are derived [11, 72]

$$\frac{\partial \rho_0 \bar{v}_{0i}}{\partial x_i} = 0, \tag{2.70}$$

$$\frac{\partial \rho_0 \bar{v}_{0i}}{\partial t} + \frac{\partial \rho_0 \bar{v}_{0i}\bar{v}_{0j}}{\partial x_j} = -\frac{\partial \bar{p}_0}{\partial x_i} + \frac{\partial \bar{\tau}_{ij}}{\partial x_j} - \frac{\partial}{\partial x_j}\left(\rho_0 \overline{v_i' v_j'}\right), \tag{2.71}$$

where $\bar{\tau}_{ij} = \mu\left(\frac{\partial \bar{v}_{0i}}{\partial x_j} + \frac{\partial \bar{v}_{0j}}{\partial x_i}\right)$ is the averaged viscous stress tensor, and the last term of Eq. (2.71) are the unknown Reynolds stresses, which appears during the derivation of the RANS equation [72]. In order to achieve closure, the Reynolds stresses can be defined in terms of the mean quantities of the flow, and therefore the turbulence models are introduced. There are numerous developed models, which are classified in zero-, one-, two-, stress-equation, and algebraic-stress models, depending on the equations that are used to model the Reynolds stresses [11].

For the eddy-viscosity type of models, eddy-viscosity μ_T or kinematic eddy-viscosity, $\nu_T = \mu_T/\rho_0$ is introduced to model the Reynolds-stresses

$$-\rho_0 \overline{v_i' v_j'} \equiv \tau_{ij}^t = \mu_T\left(\frac{\partial \bar{v}_i}{\partial x_j} + \frac{\partial \bar{v}_j}{\partial x_i}\right) - \frac{2}{3}\rho_0 \delta_{i,j} k, \tag{2.72}$$

where τ_{ij}^t is the Reynolds stresses tensor, $k = \frac{1}{2}\overline{v_i' v_i'}$ is the turbulent kinetic energy. The eddy-viscosity, μ_t, can be calculated in different ways depending on the turbulence model [11, 72]. The mostly used turbulence model is the two-equation k-ε model, where two transport equations are solved, one for the kinetic energy k and one for the dissipation rate ε to calculate the eddy-viscosity $\mu_T = \rho_0 C_\mu \frac{k^2}{\varepsilon}$, where C_μ is a constant that commonly takes the value 0.09 [72]. In the present work, the realizable k-ε (RKEPS), which is an improved version of the standard k-ε model, is used for the majority of the simulations [227].

The elliptic blending Reynolds-stress model (EBRSM) [33, 229] is used in the present

research as well. The Reynolds-stress models (RSM) [11, 72, 267] in general are more suitable for 3D flows with swirl, separation, recirculation etc. For the RSM the ratio between the Reynolds stresses and the mean strain rate is anisotropic (varying in different directions) in antithesis to the eddy-viscosity models, where isotropy is assumed (Eq. (2.72)) [267]. More particularly, $\rho_0 \overline{v_i' v_j'} \equiv \tau_{ij}^t$ is determined by directly solving six transport equations for the Reynolds stresses, which are derived from the N-S equations. The interested reader is referred to [205, 267]. For the closure of the EBRSM one needs to also solve a transport equation of the turbulence dissipation rate ε. The EBRSM, unlike other turbulence models, distinguishes between viscous and non-viscous effects in near-wall regions as mentioned by Manceau and Hanjalic [166]. By considering the improvement of EBRSM functions over existing RSM or eddy-viscosity models, EBRSM performs well in swirling flow as it was also indicated by Ashton and Stoellinger [18]. Billard and Laurence [33] proposed a slightly modified model for the EBRSM, which is implemented in STAR-CCM+[235] and used in the present study [196].

When the SRS models are employed for the solution of N-S, at least a part of the fluid and a part of the turbulence spectrum are resolved in space and time, while the rest is modeled (e.g. by RANS models) [173]. The transient improved delayed detached eddy simulations (IDDES), which belongs to the class of the SRS, is a hybrid RANS-large-eddy simulation (LES) from Shur et al [228]. More specifically, with the IDDES approach, turbulent structures are solved both in temporal and spatial space, while only small-scale turbulent structures, which are smaller than the mesh size, as well as turbulence next to the wall are modeled.

Summarizing, in the present work the RKEPS model [227, 229] is used for all the CFD simulations, which are part of the SimPAC^2 method. For the CNA method, where only CFD is taken into account, the RKEPS model [227, 229], EBRSM [18, 33, 166] and IDDES [228, 229] are used.

2.4 Interfaces Treatment

Piezoelectric, solid, and fluid domains comprise the whole system of an UTTF. In order to transfer the information between adjacent domains, special conditions and treatment of the interfaces are needed.

2.4.1 Solid-Solid Interfaces

In order to examine the information transfer between two solid domains, let us consider two solid bodies 1 and 2 as depicted in Fig. 2.6. It is valid that in general for two solid bodies [10]

$$\boldsymbol{u_1} = \boldsymbol{u_2}, \tag{2.73}$$

$$\boldsymbol{n_1} \cdot [\boldsymbol{T_1}] = \boldsymbol{n_1} \cdot [\boldsymbol{T_2}], \tag{2.74}$$

where $\boldsymbol{u_1} = \boldsymbol{u_1}(x, y, z), \boldsymbol{u_2} = \boldsymbol{u_2}(x, y, z)$ are displacements in body 1 and body 2, respectively, $\boldsymbol{n_1}, \boldsymbol{n_2}$ are unit normal vectors to the interface and $[\boldsymbol{T_1}], [\boldsymbol{T_2}]$ are the stress tensors for bodies 1 and 2 respectively. Eq. (2.73) means that the components of displacement between two

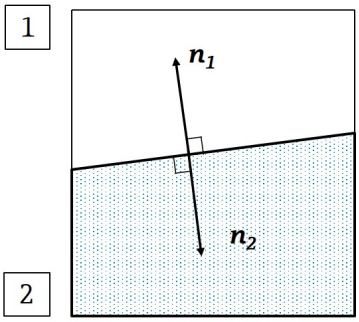

Figure 2.6: Schematic representation of two adjacent solid bodies 1 and 2 with the respective unit normal vectors to their interfaces $\boldsymbol{n_1}, \boldsymbol{n_2}$ depicted.

solid bodies is continuous and Eq. (2.74) that continuity of traction, $\boldsymbol{t(n)}$, is satisfied as well [10]

$$\boldsymbol{t_1(n_1)} = \boldsymbol{n_1} \cdot [\boldsymbol{T_1}] = \boldsymbol{n_1} \cdot [\boldsymbol{T_2}] = \boldsymbol{t_2(n)}, \tag{2.75}$$

where $\boldsymbol{t_1(n_1)}$ and $\boldsymbol{t_2(n_1)}$ is the traction on the solid-solid interface for body 1 and body 2, respectively. In the present thesis, the displacement $\boldsymbol{u}$ is calculated with the implementation of Eq. (2.14) in the FEM program NACS [183] and the satisfaction of eqs. (2.73) and (2.74).

2.4.2 Solid-Fluid Interfaces

The interface between solid body and moving fluid needs to be treated as well, since waves travel from the solid bodies of the UTTF to the quiescent or flowing medium and vice versa. When an inviscid fluid is considered, as in all the cases of the present work for wave propagation in fluid media, it is valid that the normal particle velocity is continuous [30, 107, 181], i.e. the normal component of the mechanical surface velocity of the solid must coincide with the normal component of the particle velocity of the fluid. It should be noted that the terms 'particle velocity' and 'acoustic particle velocity' and 'acoustic velocity' have the same meaning when used in the thesis, as well as in other textbooks [107, 117]. Additionally, for the interface between a solid and an inviscid medium, there is continuity of the normal stresses, in the same way as described in Subsec. 2.4.1, while it is valid that the shear stresses on the interface are zero [10]. However, the effect of viscosity is not neglected in the case of flow, as it would result in a significantly different flow-field [58, 72] and therefore, all the CFD simulations in the present work, with the resulting ambient properties, are performed with the consideration of flow. In Fig. 2.7 two adjacent bodies, a fluid and a solid are shown schematically, with $\boldsymbol{n}$ being the unit normal vector to the interface pointing into the fluid.

2.4.2.1 Quiescent Fluid

For the case of solid and quiescent, inviscid, fluid media the continuity of normal particle velocity on the interface between a solid and a fluid medium is satisfied [30, 107, 181]. Let

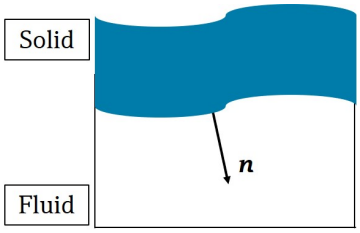

Figure 2.7: Schematic representation of two adjacent bodies, a fluid and a solid with $\boldsymbol{n}$ being the unit normal vector to the interface pointing into the fluid.

us introduce the particle velocity in the solid, $\boldsymbol{v}'_{sol} = \boldsymbol{v}'_{sol}(x, y, z)$, which is expressed as the partial time-derivative of mechanical displacement u

$$\boldsymbol{v}'_{sol} = \frac{\partial \boldsymbol{u}}{\partial t}, \tag{2.76}$$

while for the acoustic particle velocity in fluid it is already introduced that $\boldsymbol{v'} = \nabla\phi$.

Therefore, one can express the continuity of the normal component of particle velocity on the interface between solid and fluid as [30, 107, 181]

$$\boldsymbol{n} \cdot \boldsymbol{v'} = \boldsymbol{n} \cdot \boldsymbol{v}_{sol}{}', \tag{2.77}$$

or in terms of mechanical displacement for the solid

$$\boldsymbol{n} \cdot \boldsymbol{v'} = \boldsymbol{n} \cdot \frac{\partial \boldsymbol{u}}{\partial t}. \tag{2.78}$$

When the acoustic particle velocity in the fluid is expressed in terms of acoustic velocity potential ϕ then Eq. (2.78) becomes

$$\boldsymbol{n} \cdot \nabla\phi = \boldsymbol{n} \cdot \frac{\partial \boldsymbol{u}}{\partial t}, \tag{2.79}$$

which in turn may be expressed as [30, 107]

$$\frac{\partial \phi}{\partial \boldsymbol{n}} = \boldsymbol{n} \cdot \frac{\partial \boldsymbol{u}}{\partial t}. \tag{2.80}$$

Eq. (2.80) couples the Navier equation (2.14) and the acoustic wave equation for quiescent media (Eq. (2.43)) in terms of potential.

The normal mechanical stress vector $\boldsymbol{T_n} = [\boldsymbol{T}] \cdot \boldsymbol{n}$ that acts on the solid surface, because of the acoustic fluctuations in a quiescent fluid has to be taken into account. Therefore, the

continuity of normal mechanical stress on the interface is given as [107]

$$\boldsymbol{T_n} = -\boldsymbol{n}p', \tag{2.81}$$

or in terms of acoustic velocity potential

$$\boldsymbol{T_n} = \boldsymbol{n}\rho_0 \frac{\partial \phi}{\partial t}. \tag{2.82}$$

The coupling is expressed in terms of acoustic velocity potential, since the acoustic wave equation in terms of potential (2.43) is used in NACS [183] to solve wave propagation in quiescent fluid media adjacent to solids. For more details on the coupling of mechanics and acoustics on the interface between a solid and a quiescent fluid, as well as the numerical implementation in FEM, the interested reader is referred to chapter 8 of [107].

2.4.2.2 Moving Fluid

In a similar way, continuity of normal particle velocity and the expression for the stress acting on the solid surface because of the fluid are also valid for the case of an interface between a solid and a moving fluid, as shown in [30, 181].

The continuity of normal particle velocity is given in terms of acoustic velocity potential as [30]

$$\frac{\partial \phi}{\partial \boldsymbol{n}} = \left(\frac{\partial}{\partial t} + \boldsymbol{v_0} \cdot \nabla \right) (\boldsymbol{n} \cdot \boldsymbol{u}) - (\boldsymbol{n} \cdot \boldsymbol{u}) \boldsymbol{n} \cdot \frac{\partial \boldsymbol{v_0}}{\partial n}. \tag{2.83}$$

Another condition that is satisfied is that the shear stresses on the interface between the solid and the moving fluid are zero, as viscosity is not considered in the case of acoustic wave propagation [10].

The normal stress acting on the solid surface $\boldsymbol{T_n}$, because of the acoustic fluctuations in a moving fluid, is expressed as in Eq. (2.81), or in terms of acoustic velocity potential (cf. Eq. (2.50))

$$\boldsymbol{T_n} = \boldsymbol{n}\rho_0 D_t \phi. \tag{2.84}$$

The interested reader is referred to [203] regarding the detailed assumptions of Eq. (2.50), which is used in the derivation of Eq. (2.84). If the term on the right-hand side is expanded, then it is obtained

$$\boldsymbol{T_n} = \boldsymbol{n}\rho_0 \left(\frac{\partial}{\partial t} + \boldsymbol{v_0} \cdot \nabla \right) \phi. \tag{2.85}$$

Although viscosity is not taken into account for acoustic wave propagation in the present work, it is considered in the case of flow with regard to ambient properties, as it is highlighted in the beginning of Sec. 2.4. Consequently, the no-slip condition is valid on the interface between a solid and a moving fluid, i.e. $\boldsymbol{v_0} = 0$ [58, 72]. This leads to a simplification of the coupling boundary conditions (BCs) (2.83) and (2.85) to (2.80) and (2.82), respectively, as it can be easily derived. In NACS [183], the Eqs. derived in the Subsecs. 2.4.2.1 and 2.4.2.2 are used for the treatment of interfaces between solid and quiescent or solid and moving

fluid, respectively.

2.4.3 Fluid-Fluid Interfaces

Two fluid bodies 'Fluid 1' and 'Fluid2' are considered neighboring on the surface 'Int', as shown in Fig. 2.8. The two fluids can be either both quiescent or both moving for the cases considered in the thesis.

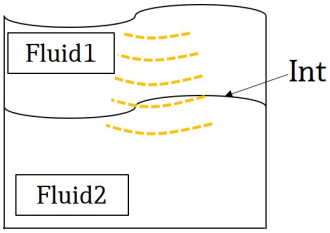

Figure 2.8: Schematic representation of two adjacent fluid bodies, 'Fluid1' and 'Fluid2' with an interface 'Int'. Waves depicted schematically with orange dashed lines, propagating from 'Fluid1' to 'Fluid2'.

In the case of quiescent fluid media, two different equations are used in the present work. Eq. (2.43) in terms of acoustic velocity potential, ϕ, implemented in NACS [183] and Eq. (2.39) in terms of acoustic pressure, p', in STAR-CCM+® [229, 235]. Let us assume that NACS with Eq. (2.43) in terms of ϕ and Star-CCM+® with Eq. (2.39) in terms of p' are used for the simulation of wave propagation in Fluid1 and Fluid2, respectively, which are sequentially solved, i.e. first Fluid1 and next Fluid2. When waves propagate, ϕ is calculated on 'Int'. For the coupling of the two wave equations on a quiescent fluid-fluid interface 'Int', Eq. (2.42) is used, in order to calculate p' from ϕ. Therefore, p' is made available for Eq. (2.39), in which it is replaced for the location of interface 'Int'. From 'Int' the waves propagate further to 'Fluid2'. This resembles the case of the connection between Part **(I)** and Part **(II)**, as they are depicted in Fig. 1.4 and as it will be further examined in Sec. 3.2.

In the case that waves propagate from 'Fluid2', which is solved with Star-CCM+® to 'Fluid1', which is solved with NACS, a coupling on Int must take place as well. The waves are solved in 'Fluid2' and on 'Int' in terms of p'. The information of wave propagation has to be made available on 'Int' in terms of ϕ so that it is made available for Eq. (2.43). Eq. (2.42) is used as well to replace p' with ϕ on 'Int'. ϕ is made available for eq. (2.43), in which it is replaced for the location of interface 'Int'. From 'Int' the waves propagate further to 'Fluid1'. This resembles the case of the connection between Part **(II)** and Part **(III)**, as they are depicted in Fig. 1.4 and as it will be further examined in Sec. 3.2.

In the case of moving fluid media, two different Eqs. are used in the present work. Eq. (2.49), referred to as PE, in terms of acoustic velocity potential ϕ implemented in NACS [183] and Eq. (2.53), referred to as CAWE, in terms of acoustic pressure p' in STAR-CCM+® [229, 235]. For the coupling of the two Eqs. (2.49) and (2.53) on a fluid-fluid interface 'Int' for moving fluid media, Eq. (2.50) is used. The same process as for quiescent fluid media, is followed for moving fluid media as well. However, eqs. (2.43), (2.39), and

(2.42), should be replaced by Eqs. (2.49), (2.53), and (2.50), respectively. Regarding the inconsistency of Eq. (2.53) and its correct version (2.55) the interested reader is referred to Subsec. 2.2.3.3.

Such fluid-fluid interfaces are used in the present thesis and are further described in Sec. 3.2.

2.5 Flow Measurement with Ultrasonic Transit Time Flowmeters (UTTF)

2.5.1 Measurement Principle and Definitions

A schematic representation, through Fig. 1.1, and the general principle of measurement of UTTF are already presented in Sec. 1.1. In this section, more details are given regarding the principle of measurement and the assumptions made.

Eqs. (1.4), (1.5), and (1.6) summarize the general and simplified principle of measurement of t_{12}, t_{21} and the flow velocity v_{path}, as given by Eq. (1.3) and approximately by (1.6), with the respective approximations given in Sec. 1.2 [155]. However, due to complexity of the measurement, these equations become lengthier in order to take into account several measurement effects. In Fig. 2.9 a schematic representation of an UTTF is shown, where in comparison to Fig. 1.1, the dimension L_{cav} and a point b are shown. Instead of 'real' industrial transducers as in Fig. 1.1, piezoelectric disks are shown for the sake of simplicity, with their exact properties and parameters not being important for the general principle description made in this subsection. However, real transducers T1 and T2 can be considered as well. z is defined as the axial direction of the UTTF throughout the thesis, y is the direction of a cross-section of the meter body and x is consequently perpendicular to y and z. L_{cav} is the length between the center of the front face of the transducer and the imaginary cutting point b between the transducers' axis and the edge of the meter body for radius R. L_{cav} is usually the same for transducers opposite to each other and therefore it is depicted only once in Fig. 2.9. An UTTF can however, have more than two transducers and therefore more than one ultrasonic paths in several positions and consequently it is called multipath UTTF [155].

As already described in Sec. 1.2, it is reminded that the average axial flow velocity on a cross-section, A_{ref}, is given by Eq. (1.1) and the reference axial volume flow rate is given by Eq. (1.2).

It is known that $\Delta t_i = t_{21,i} - t_{12,i}$, which is the time difference between the upstream and downstream traveling sound waves, is proportional to the flow velocity in a sound path i, $v_{path,i}$, as given in Eq. (1.6) [30, 155, 176]. A more detailed equation for the measurement/calculation of $v_{path,i}$ in a sound path for an inline UTTF with cavities is derived i.e., presented based on previous literature, cf. [63, 155], for which the approximations made for the derivation of Eq. (1.6) [155] in Sec. 1.2 are also valid. The flow velocity along a sound path i for such a flowmeter is corrected in order to consider effects that are described further in the present section.

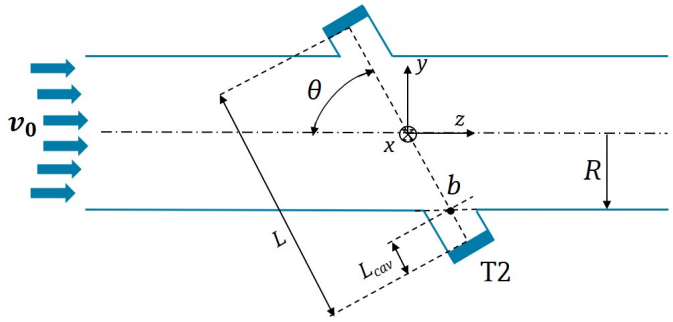

Figure 2.9: A schematic representation of an UTTF with the coordinate system defined and the dimension L_{cav}, which is the length between the center of the front face of the transducer and the imaginary cutting point b between the transducers' axis and the edge of the meter body for radius R.

It is reminded that $t_{21,i}$ and $t_{12,i}$ are the upstream and downstream ToF in the fluid medium only, i.e. the ToF from the frontal face of T2 to the frontal face of T1, and vice-versa, in the interrogation path L_i, with the assumption of plane waves. In reality, $t_{21,i}$ and $t_{12,i}$ cannot be directly measured and therefore other measurable ToFs are used, which have to be corrected, as it is described in the present section, based on [155].

The time-difference between wave propagation from T2 to T1 and from T1 to T2 at zero flow for a sound path i is given as [155]

$$\Delta t_{i,0} = t^{eltr}_{21,i,0} - t^{eltr}_{12,i,0}, \tag{2.86}$$

where $t^{eltr}_{21,i,0}$ and $t^{eltr}_{12,i,0}$ are time-delays for wave propagation at zero flow in the upstream and downstream directions, respectively. The time-delays for zero flow are more specifically given as [155]

$$t^{eltr}_{21,i,0} = t^{el,cab}_{21,i,0} + t^{tr}_{21,i,0} + t^{diff}_{21,i,0}, \tag{2.87}$$
$$t^{eltr}_{12,i,0} = t^{el,cab}_{12,i,0} + t^{tr}_{12,i,0} + t^{diff}_{12,i,0}, \tag{2.88}$$

which means that the 'electronics/cables/transducer/diffraction' delays are determined at dry calibration conditions [155] with the subscript '0' for zero flow. $t^{el,cab}_{21,i,0}$, $t^{tr}_{21,i,0}$, and $t^{diff}_{21,i,0}$ are the time delays in the electronics/cables of the sender and the receiver, the wave propagation in the sender and the receiver, and the diffraction effect for upstream propagation and $t^{el,cab}_{12,i,0}$, $t^{tr}_{12,i,0}$, $t^{diff}_{12,i,0}$ the respective delays for downstream propagation, for zero flow. The interested reader may find a more detailed description of each delay in [155]. In the present thesis, in the case of measurements, $t^{eltr}_{21,i,0}$ and $t^{eltr}_{12,i,0}$ are directly measured for zero flow with the zero-crossings technique, as it will be described in the present section.

For simulations, it can often be assumed that $\Delta t_{i,0} = 0$ when the opposite transducers are considered to be identical. In reality, two opposite transducers are practically never identical. In the present work, $\Delta t_{i,0} = 0$ is assumed for simulations, since the transducers

are considered as identical when simulated. Moreover, in the simulations, the voltage-to-voltage system is considered from transmitter to receiver, as shown in Sec. 1.3 and Fig. 1.4 and therefore, the cables and electronics are not simulated. Thus, it is assumed for the simulations that $t_{21,i,0}^{el,cab} = t_{12,i,0}^{el,cab} = 0$.

Similarly, by subtracting $2L_{cav,i}$, the effect of cavity is considered, inherently implying that it is the same for both transducers T1 and T2, while $v_0 = 0$ in both cavities [63].

It is obvious that especially for measurements, $t_{21,i}$ and $t_{12,i}$ cannot be easily accessed. When flow is present, it is valid that [155]

$$t_{21,i} = t_{21,i,tot} - t_{21,i,0}^{eltr} - t_{cav,i} + \Delta t_{i,0} \tag{2.89}$$

$$t_{12,i} = t_{12,i,tot} - t_{12,i,0}^{eltr} - t_{cav,i}, \tag{2.90}$$

where $t_{21,i,tot}, t_{12,i,tot}$ are the measured ToF directly from the UTTF for upstream and downstream wave propagation, respectively. In a case of real UTTF, this value includes time-delay in electronics, cables, transducers, as measured for zero-flow $t_{21,i,0}^{eltr}$ and $t_{12,i,0}^{eltr}$, as well as ToF wave propagation in the fluid, $t_{21,i}$ and $t_{12,i}$. $t_{cav,i} = 2\frac{L_{cav,i}}{c_i}$ [155] is the time-delay inside the cavity in front of the transmitting and receiving transducers for a for a path i, a distance $L_{cav,i}$, as defined in Fig. 2.9 and speed of sound c_i, which is directly measured with the use of a formula, which will be presented in the present section. By using this $t_{cav,i}$ one assumed no flow in the cavities along path i and that the average sound speed in the the two cavities of path i is equal to the average sound speed along the whole path i [155] and that $L_{cav,i}$ has the same value in front of the transmitting and the receiving transducer. Therefore, considering the described analysis based on [155] one can rewrite Eq. (1.6) as

$$v_{path,i} = \frac{L_i - 2L_{cav,i}}{2(t_{21,i,tot} - t_{21,i}^{eltr} - t_{cav,i} + \Delta t_{i,0})(t_{12,i,tot} - t_{12,i}^{eltr} - t_{cav,i})\ \cos\theta_i} \Delta t_i. \tag{2.91}$$

Under the same assumptions as for the derivation of Eq. (2.91), an equation for the calculation of c_i was derived [155]

$$c_i = \frac{L_i \sqrt{(t_{12,i} + t_{21,i})^2 \cos^2\theta_i + (t_{12,i} - t_{21,i})^2 \sin^2\theta_i}}{2t_{12,i}t_{21,i}\cos\theta_i}. \tag{2.92}$$

The exact technique of zero-crossings used in the present work for the determination of ToF at zero-flow, $t_{21,i,0}$ and $t_{21,i,0}$, and ToF with flow $t_{21,i}$ and $t_{21,i}$, which are needed in Eq. (2.91) and (2.92), for the determination of flow velocity and speed of sound in a sound path i, respectively, is presented in this section. An example of indicative signals on a sender is shown in Fig. 2.10(a), on a receiver placed at distance L_i for zero flow is shown in Fig. 2.10(b) and for flow in Fig. 2.10(c). In Fig. 2.10(b), the measured ToFs on the receiver, $t_{21,i,0}^{eltr}$ and $t_{12,i,0}^{eltr}$ for upstream and downstream propagation, respectively and the time-difference $\Delta t_{i,0}$ for zero flow are depicted. For the determination of $t_{21,i,0}^{eltr}$ and $t_{12,i,0}^{eltr}$, three zero-crossings are taken towards the beginning of the received voltage-signal. More specifically, the 5^{th}-$7th$ zero-crossings are taken, when the first zero-crossing is considered

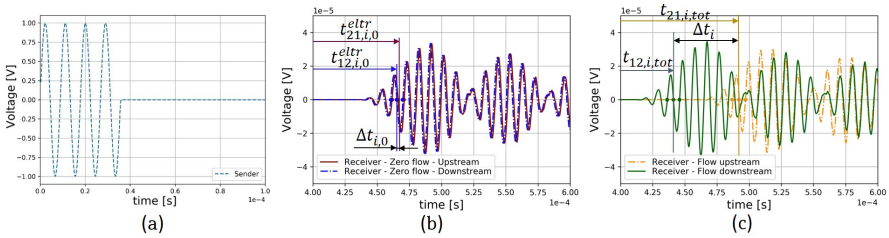

Figure 2.10: Indicative voltage signals (a) on sender, (b) on receiver for two transducers placed in distance L_i for zero flow, and (c) on receiver for two transducers placed in distance L_i for flow different from zero.

to be the one before the peak, which has a value $\geq 2\%\max(V_5)$, where V_5 is the received voltage, as shown in Fig. 1.4. As already presented the time-difference for zero flow, $\Delta t_{i,0}$, is calculated with Eq. (2.86). If $t^{eltr}_{21,i,0,m}$ and $t^{eltr}_{12,i,0,m}$ are the described measured time-delays for zero flow, related to the zero-crossing m, then for the calculation of the time delays, it is used [155]

$$t^{eltr}_{21,i,0} = (t^{eltr}_{21,i,0,5} + t^{eltr}_{21,i,0,6} + t^{eltr}_{21,i,0,7})/n_{zero} \tag{2.93}$$
$$t^{eltr}_{12,i,0} = (t^{eltr}_{12,i,0,5} + t^{eltr}_{12,i,0,6} + t^{eltr}_{12,i,0,7})/n_{zero}, \tag{2.94}$$

where n_{zero} is the number of zero-crossings considered. In this case, $n_{zero} = 3$. The time of a zero-crossing is determined through the linear interpolation between two consecutive values of voltage with signal change. For the calculation of $t^{eltr}_{21,i,0}$ and $t^{eltr}_{21,i,0}$ eqs. (2.93) and (2.94) are used in this thesis, unless stated otherwise.

In Fig. 2.10(c) the measured ToFs on the receiver, $t_{21,i,tot}$ and $t_{12,i,tot}$ for upstream and downstream propagation, respectively and the time-difference Δt_i with flow are depicted. In a similar way the described 5^{th}-$7th$ zero-crossings are considered. If $t_{21,i,tot,m}$ and $t_{12,i,tot,m}$ are the described measured ToFs for upstream and downstream propagation with flow, related to the zero-crossing m, then for their calculation, it is used [155]

$$t_{21,i,tot} = (t_{21,i,tot,5} + t_{21,i,tot,6} + t_{21,i,tot,7})/n_{zero} \tag{2.95}$$
$$t_{12,i,tot} = (t_{12,i,tot,5} + t_{12,i,tot,6} + t_{12,i,tot,7})/n_{zero}. \tag{2.96}$$

For the calculation of $t_{21,i,tot}$ and $t_{21,i,tot}$ eqs. (2.95) and (2.96) are used in this thesis, unless stated otherwise.

In order to obtain the flow velocity and volume flow-rate based on all sound paths of a multipath UTTF, eqs. (1.8) and (1.10) are used. The '%deviation' of the calculated flow velocity v_{calc} from the reference velocity v_{ref} is used for the evaluation of an UTTF. Here, it is defined as

$$\%\text{deviation} = \frac{v_{calc} - v_{ref}}{v_{ref}} \cdot 100 \tag{2.97}$$

Another evaluation parameter is the 'Volume Flow Error [%]', defined as

$$\text{Volume Flow Error}[\%] = \frac{Av_{calc} - A_{ref}v_{ref}}{A_{ref}v_{ref}} \cdot 100 = \frac{Av_{calc} - q_{ref}}{q_{ref}} 100. \tag{2.98}$$

Eqs. (2.97) and (2.98) provide essentially the same information. It is important to note that both eqs. (2.97) and (2.98) give the uncorrected flow velocity and volume flow deviations, respectively, which are used in the present work. For the corrected deviations, one would have to use

$$\%\text{deviation}_{\text{corr}} = \frac{k_a\ v_{calc} - v_{ref}}{v_{ref}} \cdot 100. \tag{2.99}$$

or

$$\text{Volume Flow Error}_{\text{corr}}[\%] = \frac{k_a A v_{calc} - A_{ref}v_{ref}}{A_{ref}v_{ref}} \cdot 100 = \frac{q - q_{ref}}{q_{ref}} \cdot 100. \tag{2.100}$$

2.5.2 Signal-Processing Uncertainty

It is important to provide uncertainty information regarding the obtainment of the measured or simulated ToFs [86, 155] when the presented signal-processing is used. Depending on the frequency of the input voltage signal V_1 a different sampling rate is chosen. An example of a typical simulation carried out in this work will be indicatively given in this respect. It is not the purpose of this example to give accurate values of uncertainty but to describe the order of the errors made, due to the considered signal-processing.

For a simulation with an input carrier frequency $f_c = 100$ kHz of V_1, a time-step, $dt_{sim} = 3.75 \cdot 10^{-7}$ s, which may also be called sampling period, was chosen. The received signal V_5 was upsampled by a factor of 1000. Thereby, the upsampled sampling period of the received signal V_5 is $dt_{sim,up} = 3.75 \cdot 10^{-7}/1000$ s$=3.75 \cdot 10^{-10}$ s. The maximum error that may be made in the choice of a specific zero-crossing is

$$\text{Error}_{\text{zero-cross}} = dt_{sim,up}/2, \tag{2.101}$$

which would be the maximum distance between the zero-crossing calculated and the real zero-crossing. In the case of the presented simulation, this would give a value of $\text{Error}_{\text{zero-cross}} = 1.875{\cdot}10^{-10}$ s.

A very small and the most demanding value that has to be calculated is Δt for low flow-velocities, where high sampling rate is needed for an accurate calculation. Typical values for low flow-velocities, e.g. for an UTTF with meter-body diameter 80 mm, are of the order of $\Delta t = 5{\cdot}10^{-5}$ s. Therefore, the uncertainty added, because of the signal-processing technique in this typical case is

$$\frac{\text{Error}_{\text{zero-cross}}}{\Delta t} \cdot 100 = 0.000375\%,$$

which is acceptable, since it is much smaller than typical deviation specifications for state-of-the-art inline gas UTTF, such as the Prosonic Flow G 300, for which it is specified $\%\text{deviation}_{\text{corr}}{=}\pm 1\%$ for standard operation [64].

In this subsection, it was analyzed and described how the related ToFs, $t_{21,i,0}^{eltr}, t_{12,i,0}^{eltr}, t_{21,i,tot}$, and $t_{12,i,tot}$ with or without flow, are measured and how the ToFs, $t_{21,i}, t_{12,i}$, and $t_{cav,i}$ as well as the time-differences Δt_i and $\Delta t_{i,0}$, needed for the calculation of $v_{path,i}$ (Eq. (2.91)) and c_i(Eq. (2.92)), are obtained. The specific zero-crossing signal processing technique was also presented.

Chapter 3

Simulation Approach and Methods

In the present chapter, three different methods for the simulation of the system of UTTF or parts of it, are presented. In Sec. 3.1, the 'CFD - Non-acoustic' method is presented, also referred to as 'CNA' or 'Only CFD', models the flow field of an UTTF and enables us to extract a deviation curve, i.e. the diagram of v_{ref} against %deviation or Volume Flow Error[%], of the flowmeter only from CFD. Furthermore, valuable, quantifiable information is gained regarding the flow field. In Sec. 3.2, the SimPAC^2 method is presented, which combines the physics of piezoelectricity, wave propagation in solids and moving fluids, as well as CFD, with the aim of simulating and including these mentioned relevant physics for the modeling of an UTTF. Deviation curves, as well as quantifiable information regarding the relevant, combined physical effects are gained and presented in the next sections. The Proline Prosonic Flow G 300 [64], which is measured and simulated in Sec. 6.3, is used as an example in order to present the methods.

3.1 The 'CFD-Non-acoustic' (CNA) Method

Simulation of an UTTF can be achieved with the use of the CFD-Non-acoustic (CNA) or 'Only CFD' method. Of course, physics such as piezoelectricity, acoustic wave propagation in solids and fluids are not included and therefore, an indirect way shall be found in order to obtain useful results with the CNA method. On the other hand, the advantage of such a method is that the flow effects can be quantified and separated from the rest of the effects, which means that the flow field in the UTTF can be optimized. Furthermore, it is a seemingly simpler and faster simulation method compared to more complete methods and consequently, more designs can be quickly evaluated in order to achieve a first estimation of a UTTF design.

Initially, a 3D CFD simulation is conducted, taking into account the fluid domain in the meter body, upstream, and downstream of it, with the commercial program Star-CCM+®[235] using the FVM solver. Steady and transient simulations are performed with the FVM flow solver, where the respective N-S and continuity equations are solved [198, 229]. A typical 3D flow domain of a two-path inline UTTF, spatially discretized in volume cells

with the cartesian mesher of Star-CCM+®, is shown in Fig. 3.1. In this chapter, guidelines are provided for the execution of such a CFD simulation of a 3D UTTF device. Geometrical details are given for the geometry of Fig. 3.1 so that the reader puts the CNA method into context and relates it with a typical, real UTTF, such as the Proline Prosonic Flow G 300 [64]. The diameter of the meter body of the UTTF is D=97 mm, while the parts of the pipe upstream and downstream of it, have the same diameter D. The length from the 'Inlet' surface to the beginning of the meter-body is $L_{inlet=}$450 mm and the length from the end of the meter body to the 'Outlet' is L_{outlet} =1000 mm. The length of the meter-body is L_{body} = 196.6 mm, the centerlines of the two sound paths are located not centrally but towards the sides i.e., they are not diameterical, at x=-23.5 mm and x=23.5 mm, and the inclination angle is θ_i=65^o. Regarding the z position, the paths are located in the axial middle of the meter body i.e., the axial middle of the sound paths coincides with the axial middle of the meter body. The distance between two opposite transducers is L = 103 mm.

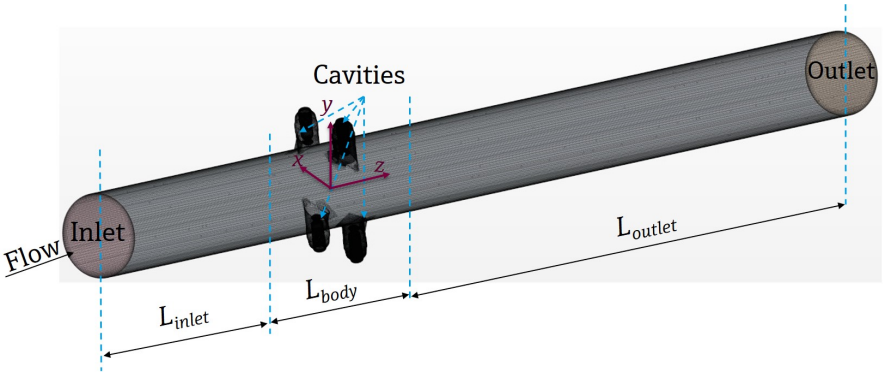

Figure 3.1: Typical flow domain of a two-path inline UTTF simulated with the CNA method

Part of the meshed fluid in the meter body and the meshed area of the cavity are shown in Fig. 3.2. One can see and reconfirm that for the CNA method, only the fluid domain is meshed and simulated, since the solid parts are not taken into account. The mesh that is used is cartesian [229], as the one shown in Fig. 3.2. More geometrical details regarding the transducers used are given in Sec. 6.2. It should be highlighted that the shown mesh is used for the CFD simulation.

For the mesh of figs. 3.1, 3.2 and of the cases presented in Sec. 6.2, certain settings are given in Star-CCM+®. A Cartesian, or 'trimmed cell mesher' [229], is used, with a maximum cell edge-size of x_{edge}=2 mm, as depicted more clearly in Fig. 3.2(b). The trimmed cell mesher is used for the core of the fluid domain, i.e. far from the walls. Cell-edges that are half and a quarter of the largest ones, i.e. 1 mm and 0.5 mm, are used as it is shown in Fig. 3.2(b). For the fluid-domain near the walls, a boundary-layer mesher is used with a maximum number of layers n_{bl}=15, a width of the cell adjacent to the wall $x_{bl} = 5 \cdot 10^{-5}$ mm and a stretching factor between adjacent mesh layers sf=1.17 [229]. With the presented settings, meshes are generated with $y+ < 1$ [72, 229] for the calculated Re numbers. $y+ = \frac{y u_T}{\nu}$ is the dimensionless distance to the wall, where y [mm] is the distance from the wall, ν [m^2/s] the kinematic viscosity, and $u_T = \sqrt{\tau_w/\rho_0}$ [m/s] is the shear velocity,

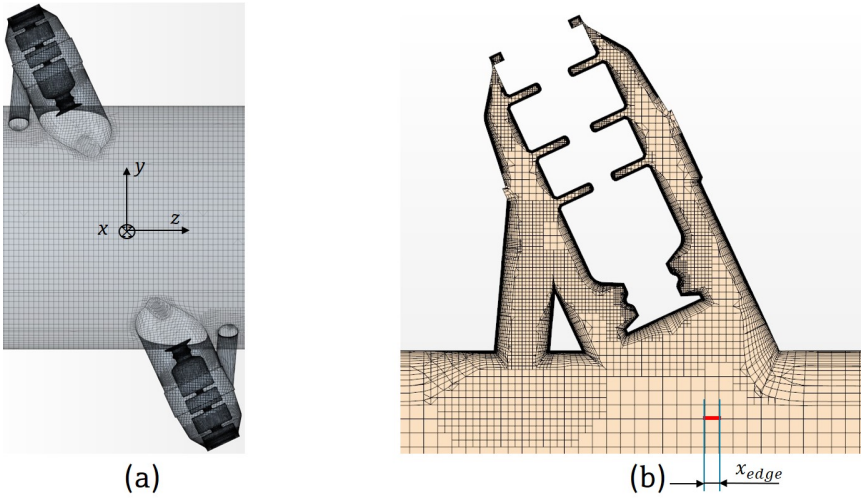

Figure 3.2: Meshed fluid-domain shown for areas of interest. (a) Mesh of the fluid-domain in the meter body and the cavities, (b) mesh on the yz plane section for x=25.3 mm zoomed in a cavity.

where τ_w [Pa] is the shear stress. In general, these settings are used for all the meshed fluid-domains for the purpose of CFD simulations in the present work, unless stated otherwise. For more information on $y+$ and meshing strategies in CFD, the interested reader is referred to [13, 72].

For a reference case of a straight pipe upstream of the meter body, a fully-developed flow profile [58, 132] is specified on the inlet surface, and as result the domain upstream of the meter body does not need to be long for the flow profile to develop. In order to ensure a high-precision fully-developed profile, a separate CFD simulation is performed. In Fig. 3.3 a typical simulation domain is shown, discretized with a Cartesian mesh for the obtainment of a fully-developed profile. A short slice of a pipe is discretized with the same mesh settings as for the CFD simulation of the UTTF. The pipe diameter is equal to the inlet diameter of the UTTF simulation, i.e. D=97 mm and of length L_{slice}=10 mm. The contour of the flow-profile in terms of normalized velocity, v_0/v_{ref}, is shown in Fig. 3.3 as well. The steady N-S equations are solved for an incompressible, viscous flow (cf. 2.3) [58, 72]. A mass flow, $\dot{m}_{S1}$, is specified on surface $S1$, with

$$\dot{m}_{S1} = \rho_0 \boldsymbol{v_{ref}} \cdot \boldsymbol{A}_{S1} = \rho_0 v_{ref} A_{S1} \cos 0^o = \rho_0 v_{ref} A_{S1}, \tag{3.1}$$

where A_{S1} is the area [m^2] of surface $S1$. A fully-developed boundary condition is specified on $S1$ [229], which prescribes that the tangential flow-velocity on $S1$ is zero, and therefore

$$\boldsymbol{v_0} = v_0 \boldsymbol{e_z} \tag{3.2}$$

on surface $S1$, where $\boldsymbol{e_z}$ is the unit vector in the axial z direction. Additionally, a periodic

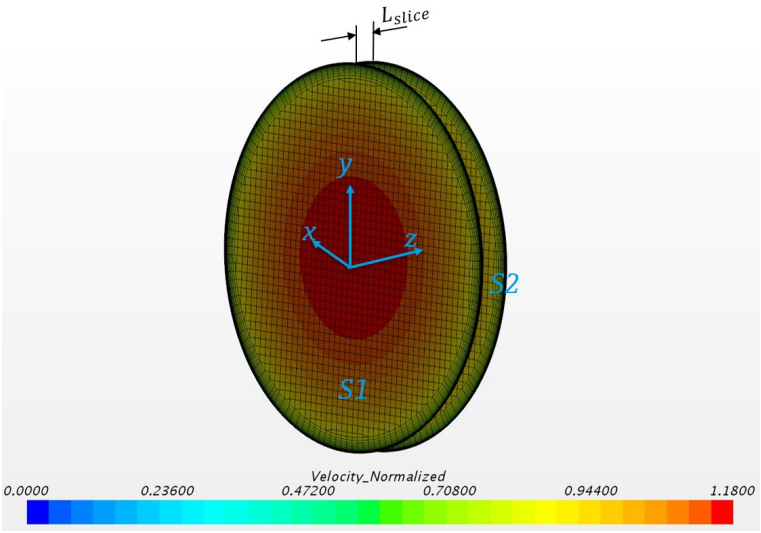

Figure 3.3: CFD simulation for the obtainment of a fully-developed flow profile, with the normalized velocity depicted (v_0/v_{ref}).

interface [229] is specified for surfaces $S1$ and $S2$. "The periodic interface represents a cyclic repeat of information across the boundaries, so fluxes that cross one boundary are transformed and applied to the other." [229]. In the case of the presented simulation of Fig. 3.3 it is valid that

$$\boldsymbol{v_0}(x, y, z_0) = \boldsymbol{v_0}(x, y, z_0 + L_{slice}), \tag{3.3}$$

$$k(x, y, z_0) = k(x, y, z_0 + L_{slice}) \tag{3.4}$$

$$\varepsilon(x, y, z_0) = \varepsilon(x, y, z_0 + L_{slice}) \tag{3.5}$$

where $z = z_0$ on surface $S1$ and $z = z_0 + L_{slice}$ on surface $S2$, k [m^2 s^{-2}] is the turbulent kinetic energy and ε [m^2 s^{-3}] is the turbulent dissipation rate [72, 229].

Indicatively, a fully-developed velocity profile is calculated in the turbulent regime, i.e. for Re >2300 [34, 70, 132], and more specifically here for Re=63000, as shown in Fig. 3.3.

The fully-developed profile simulated in the described simulation separately from the simulation of the UTTF, is given as an input to the inlet of the UTTF simulation. The input data are mapped with the nearest neighbor technique [29] either from surface $S1$ or from surface $S2$ to the 'Inlet' surface of the UTTF simulation as shown in Fig. 3.1. The flow-profile on surfaces $S1$ and $S2$ is identical due to the periodic boundary condition [58, 229]. It is highly important to note, that not only the velocity components are given as a boundary condition on the inlet but also the turbulent kinetic energy k and dissipation rate ε. In that way, a fully calculated boundary condition is given at inlet and not just an approximation or a guess for an internal pipe flow. Furthermore, as it can be seen, the outlet, downstream of the meter body, is relatively long, as shown in Fig. 3.1, since a reference constant pressure

boundary condition is applied on the outlet surface [229]. It has to be ensured that a non-distorted flow profile is achieved on the outlet and that no errors propagate from the outlet to the upstream region [58, 72, 229].

The acoustic paths of the flowmeter need to be modeled as well; unlike other methods presented in literature, where the acoustic paths are modeled as straight lines between the transducers [84, 207, 286], cylinders are used in order to include a larger part of the fluid, where the acoustic waves propagate in reality [30, 77]. The sound paths, in fact, follow neither a line nor a cylinder [30, 77], however this approximation may be used to enable the simulation of UTTF with the inclusion of only CFD.

One may use the approximation of radiation from a plane circular piston mounted on a flat rigid baffled of infinite extent to imitate the sound path acoustic field distribution [118]. In order to imitate this propagation, the approximation of a Gauss function is used to weight the flow-velocity more towards the center of the cylindrical sound path compared to its 'edges', as it will be shown in the present subsection. .

The axial and the side views of the fluid domain of the meter body of an UTTF with the cylinders that imitate that sound paths are shown in figs. 3.4(a) and 3.4(b).

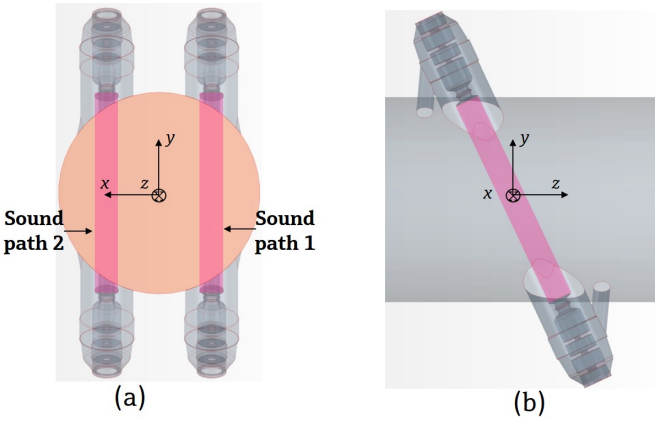

Figure 3.4: Geometry of the fluid domain in the meter body of a two-path inline UTTF. (a) Axial view, (b) side view with the two axially-shifted sound paths depicted.

It should be highlighted that a cartesian coordinate system is used in the present thesis for all cases. The center of this system is always in the center of the meter-body, the z-axis is always in the axial direction of the meter-body, and the y-axis is parallel to the sound paths, as shown in Fig. 3.4. Even when the coordinate system, is shown to be placed elsewhere in the case of other figures in the thesis, it is only indicative of the *axis-directions*. The reason is practical, since when zoomed parts of the UTTF are displayed, the coordinate system real position would be often far away from these parts. Therefore, the above statements regarding the coordinate system are valid throughout the thesis are valid, unless stated otherwise.

The volume average velocity in a cylindrical sound path, i, as shown in Fig. 3.4, is given as

$$v_{cyl,i} = \frac{1}{V_i} \iiint_{V_i} v_{0,i} dV, \tag{3.6}$$

where $v_{0,i} = v_{0,i}(x, y, z,)$ is the flow velocity in an infinitesimal volume dV in the cylindrical sound path i and V_i is the volume of the cylindrical sound path i. $v_{cyl,i}$ is independent of time, since either steady-state CFD simulations are performed or the time-average velocity is taken if a transient simulation is performed. For a volume-cell discretized domain, meshed with the settings described in the present section, $v_{cyl,i}$ may be expressed as

$$v_{cyl,i} = \frac{1}{V_i} \sum_{j=1}^{n} v_{0,i}(j) \Delta V(j), \tag{3.7}$$

where $v_{0,i}(j)$ is the flow velocity in a cell j of the discretized cylindrical sound path, n is the number of cells discretizing the cylindrical sound path, and $\Delta V(j)$ is the volume of cell j. The Gaussian function for the weighting of the volume average velocity in a cylindrical sound path is given as

$$G(r_t) = \sqrt{e^{-r_t^2/a}} \tag{3.8}$$

where r_t is the radial coordinate along a circular cross-section of the cylindrical sound path i, ($r_t = 0$ in the center of the circular cross-section and $r_t = r_0$ is the radius of the circular cross-section) and a is a parameter changing the shape of the Gaussian function. It should be noted that the distribution of the Gaussian function in the cylinder is axisymmetric. The analytical Gaussian function is mapped, with the nearest-neighbor method [29], on every cell j of the numerical mesh that comprises the cylindrical sound path and its distribution is shown in Fig. 3.5. The weighted volume average velocity in a sound path, i, on the

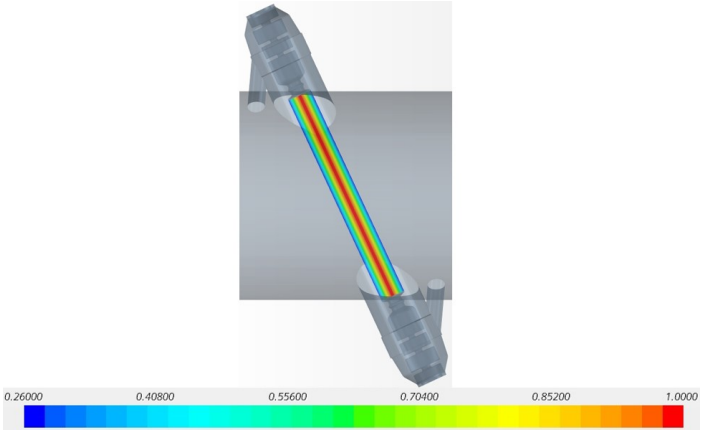

Figure 3.5: Gaussian function distribution along a cylindrical sound path.

discretized domain, is given as

$$v_{cyl,i,G} = \frac{1}{V_i} \frac{1}{\frac{1}{V_i} \sum_{j=1}^{n} G(j) \Delta V(j)} \sum_{j=1}^{n} G(j) v_{0,i}(j) \Delta V(j) = \frac{\sum_{j=1}^{n} G(j) v_{0,i}(j) \Delta V(j)}{\sum_{j=1}^{n} G(j) \Delta V(j)}, \tag{3.9}$$

where $G(j)$ is the value of the Gaussian function in a cell j. In that way, the velocity towards the center of the cylindrical sound path is weighted more compared to the velocity towards the edges of the cylinder. In Fig. 3.6, the velocity field in a sound path, i, is shown. In Fig. 3.6(a), indicatively the normalized flow velocity, $v_{0,i}(j)/v_{ref}$, on the center

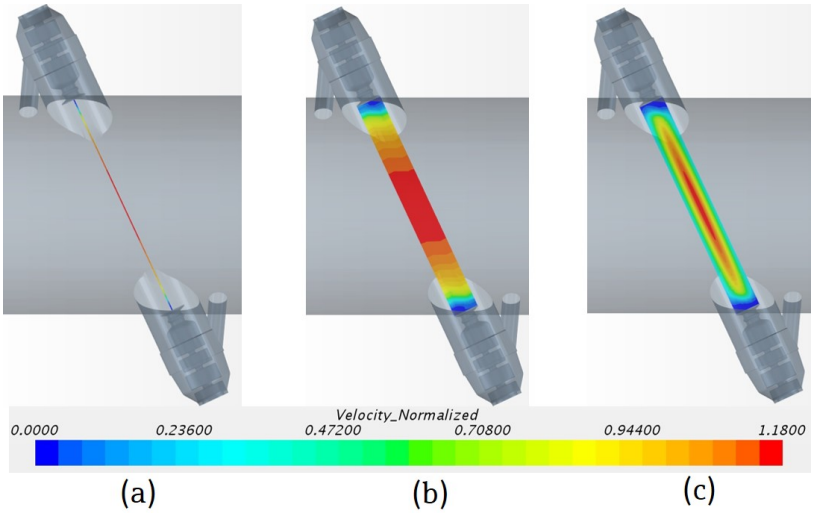

Figure 3.6: Velocity in sound paths of an UTTF, modeled with different methods. (a) Line integral, (b) volume integral unweighted, (c) volume integral weighted with a Gaussian function.

line of a sound path is shown. For the depiction of the line and for the facilitation of the reader, a cylinder with small radius $r_0 = 0.5$ mm is shown, however in the simulation, a line integration is used in this case. In Fig. 3.6(b), the normalized flow velocity, $v_{0,i}(j)/v_{ref}$, in a sound path, i, with radius $r_0 = 5.75$ mm equal to the radius of the front face of the transducers, is shown. In Fig. 3.6(c), the weighted, with a Gaussian function, normalized flow velocity, $v_{0,i}(j)/v_{ref}$, in a sound path i, with radius, $r_0 = 5.75$ mm, equal to the radius of the front face of the transducers, is shown. It is obvious that when only a line is considered, then only a small portion of the relevant fluid is considered. This is not as representative of reality, while the small number of values considered can lead to less physical results because of the mapping. When a cylinder of radius r_0 is taken into account, a larger portion of the relevant fluid is examined, where the sound actually propagates. When a weighted distribution in the cylindrical sound path is considered, a larger portion of the fluid is examined as well, with the advantage that towards the center of the cylinder, the more relevant flow velocity values are weighted more. It should be mentioned that the CNA method does not, obviously, account for beam-deflection, which might be of importance, especially for high M numbers [30, 77, 197].

The final calculated flow velocity for all sound paths N is given as

$$v_{0,CFD} = \sum_{i=1}^{N} w_i v_{cyl,i,G}, \tag{3.10}$$

and is compared with a reference velocity, v_{ref}, which is the value of the surface-average velocity on the inlet of the fluid domain. If an unweighted volume integral is used instead, then in Eq. (3.10) $v_{cyl,i,G}$ is replace with $v_{cyl,i}$ and if a line integral is used, then it is replaced with

$$v_{line,i} = \frac{1}{L_i} \int_{L_i} v_{0,i} dL, \tag{3.11}$$

where dL is an infinitesimal distance in the sound path i. For a volume-cell discretized domain, meshed with the settings described in the present section, $v_{line,i}$ may be expressed as

$$v_{line,i} = \frac{1}{L_i} \sum_{j=1}^{n} v_{0,i}(j) \Delta L(j), \tag{3.12}$$

where $v_{0,i}(j)$ is the velocity in a cell j of the discretized line, n is the number of cells discretizing the line, and $\Delta L(j)$ is the length of cell j in the direction of the sound path. The value of v_{ref} was calculated with the CFD simulation for the obtainment of a fully-developed flow profile, described in this section and shown in Fig. 3.3. Therefore, the deviation of the UTTF from the reference velocity is given as

$$\%\text{deviation}_{CFD} = \frac{v_{0,CFD} - v_{ref}}{v_{ref}} \cdot 100. \tag{3.13}$$

The 'Volume Flow Error [%]' is in general given by Eq. (2.98), while for the case of CNA, v_{calc} in Eq. (2.98) is replaced by $v_{0,CFD}$ as given by Eq. (3.10), and therefore

$$\text{Volume Flow Error}_{\text{CFD}}[\%] = \frac{A v_{0,CFD} - A_{ref} v_{ref}}{A_{ref} v_{ref}} \cdot 100 = \frac{A v_{0,CFD} - q_{ref}}{q_{ref}} \cdot 100. \tag{3.14}$$

Studies have been made for a gas UTTF as the one shown in Fig. 3.1, where line, volume, and Gauss-weighted volume integrals were used [192] in order to assess the approximation effect of every method on the deviation of the device. It was found that for $v_{ref} = 5$ m/s, %deviation for line integral is 0.18% higher than the Gauss-weighted cylindrical paths and 0.28% higher than the volume integral [192]. The highest differences are expected between the line and unweighted volume integral results, since they are the two 'extreme' cases [192].

The CNA or 'Only CFD' method can be summarized in the diagram of Fig. 3.7

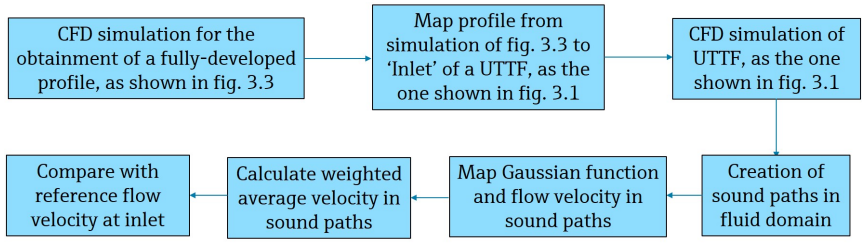

Figure 3.7: CNA method, steps summarized in a diagram.

3.2 The 'Simulations of Piezoelectricity Acoustics Coupled with CFD' (SimPAC^2) Method

3.2.1 SimPAC^2 Method Overview

As the name of the method 'SimPAC^2' implies, modeling of piezoelectricity, acoustic wave propagation is solids and fluids, as well as CFD and coupling among the different physics occurs. This method is obviously more complete compared to the CNA method described in Sec. 3.1 and attempts a more complete simulative approach of the UTTF system. Because of the inclusion of the mentioned physics components, holistic physical effects taking place in the simulated domain can be visualized, explained and quantified.

The method is called 'hybrid' as two different solvers (or programs), a FEM [183] and a FVM [229], are used and combined. The system of an UTTF is simulated from voltage on the sending transducer to voltage on the receiving one, as explained in Sec. 1.3. Assumptions are made for the derivation of the respective modeled equations (cf. Sec. 2) or slight simplifications need to be made in the complex geometries. As different models need to be combined and acoustic wave propagation is solved numerically for high frequencies, the challenge arises that large models need to be solved with short time-steps in the time-domain. To overcome this challenge, HPC is mobilized. The SimPAC^2 method is shortly described in Sec. 1.3, however in this section more technical details and descriptions are given.

The idea of the SimPAC^2 method and the workflow can be described with a diagram in Fig. 3.8. In order to demonstrate the method, a geometry of an UTTF is used as an example [62, 64], which is further measured and simulated in Sec. 6.3. Each component **(I)**, **(II)**, **(III)**, and **(IV)** to be simulated is in accordance with Fig. 1.4. A more detailed description of each component and the connections between them, is given in the rest of Sec. 3. The dashed arrows in Fig. 3.8 connote the hybrid nature of the method, when information is passed between solvers.

The parts to be simulated are shown schematically in Fig. 3.9 for more clarity. A summary of the main components is given with the help of the schematic representation of Fig. 3.9. It is important to notice that for Part **(I)** the fluid domain is divided in two volume regions 'Fluid in cavity' and 'Fluid towards the sender'. The purpose of the separation of the fluid in the two regions, is the creation of an interface of great importance between them, 'Int1', which is used as a surface, where the acoustic pressure is recorded and given as an input in Part **(II)**. Both 'Int1' and 'Fluid towards the sender' are present in Part **(II)** as well. Part **(II)** consists additionally of the volume regions of 'Main fluid', 'Fluid towards the receiver', and 'Fluid for absorption'. The acoustic waves propagate from 'Int1' into the volume regions of 'Fluid towards the sender', the 'Main fluid', the 'Fluid towards the receiver', and on the interface 'Int2', which is used as a surface to record the acoustic pressure. The waves travel further into the volume region of 'Fluid for absorption', which is made large with the purpose of absorbing the acoustic waves propagating up to the outer surfaces of it, where absorbing boundary conditions are defined, as it is further explained in Subsec. 3.2.3. The 'Fluid towards the receiver' and 'Int2' are present in Part **(III)** as well. The acoustic waves are given as an input on 'Int2' of Part **(III)** and propagate in both directions i.e.,

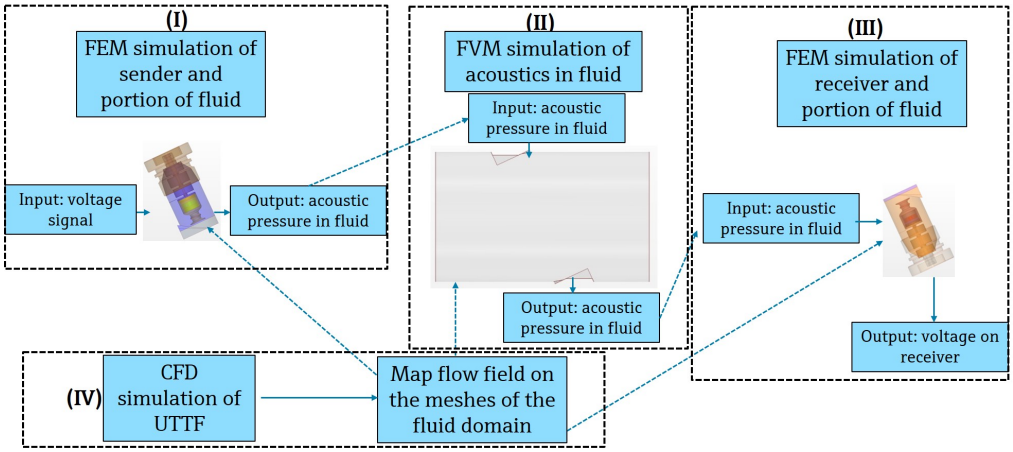

Figure 3.8: SimPAC² method, components and workflow summarized in a diagram. **(I)** Sender with a portion of fluid solved with FEM, **(II)** acoustics in fluid solved with FVM, **(III)** Receiver with a portion of fluid solved with FEM, and **(IV)** CFD simulation of fluid domain of UTTF, as the one shown in Fig. 3.1.

in the direction of the receiver and away from it. In order to avoid unnecessary reflections, absorbing boundary conditions are set on the outer surface of the 'Fluid towards the receiver' as it is further described in Subsec. 3.2.4. The waves that travel in the direction of the receiver, propagate in the 'Fluid in cavity2' and finally in the solid part of the receiver, where voltage is generated with the inverse piezoelectric effect. The reason for the existence of the volume region 'Fluid towards the receiver' is the creation of the interface 'Int2'. The operation of 'Int2' in Part **(II)** is the recording of the acoustic pressure, while in Part **(III)** the input of acoustic waves. Part **(IV)** is omitted in Fig. 3.9. It consists of the complete fluid volume, where a separate CFD simulation is made in order to give the flow velocity as an input to all the fluid regions in parts **(I)**, **(II)**, **(III)**, as it is explained in Subsec. 3.2.5. Thus, in all the fluid regions the fluid can be flowing. A more detailed description of the parts, their dimensions, scope, and operation follows in Subsec. 3.2.2, 3.2.3, and 3.2.4.

For the description of the SimPAC² method in the present section, the geometry of the flowmeter Proline Prosonic Flow G 300 [64] is used. This specific flowmeter is measured and simulated, with its results being shown in Subsec. 6.3.

3.2.2 Part (I): Sender in Fluid

The method starts with the simulation of the sending transducer, namely sender or transmitter, and a portion of fluid. The 3D geometry to be simulated [62, 64] is shown in Fig. 3.10, where 3.10(a) is the axial view and 3.10(b) is the side view of the 3D geometry, while 3.10(c) is the side cross-section in the middle plane of the transducer. The fluid is represented with blue colors and the solid bodies with gray colors. The separation between fluid and solid is more challenging to distinguish in the 3D representation with transparency of Fig. 3.10(a),(b) but more apparent in the 2D representation of Fig. 3.10(c). The fluid can be

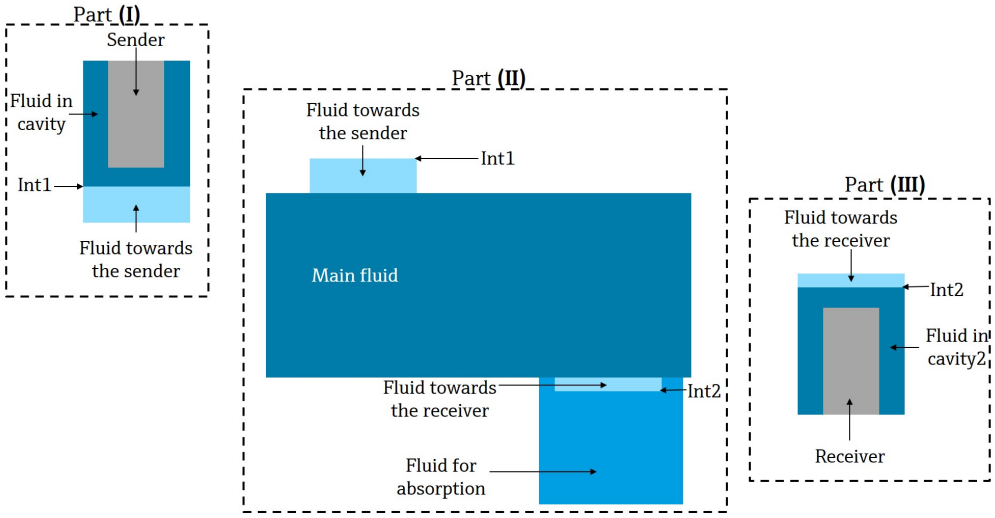

Figure 3.9: Schematic representation of the SimPAC^2 method with main parts **(I), (II), (III)** and their main fluid and solid components.

simulated as either moving or non-moving. The part of the meter-body around the fluid is not included in the simulations of the present work to save computational time however, the simulation of the meter body is possible. Instead, rigid walls are assumed for acoustics [117], as it will be further clarified in this section, and wall no-slip BC for CFD, which is described as zero flow velocity on the walls [58, 72]

$$\boldsymbol{v}_{wall} = 0, \tag{3.15}$$

since the walls are impermeable. This BC is valid due to the fact that viscous fluid sticks to solid boundary [72].

In Fig. 3.11, the view of Fig. 3.10(c) is taken, and information is added regarding each body to be modeled. The domains that are modeled are the mounting, the transducer, which consists of a front and back part, two piezoelectric elements, which transform voltage to mechanical vibrations and a portion of fluid, in which the transducer is emerged. The 'Transducer back' and 'Transducer front' consist of 'Titan grade 2' [36], the mounting consists of Stainless steel - Grade 431 (UNS S43100) [21] from now on referred to as 'stainless steel', the piezoelectric elements of 'PZT5A' [244] and the fluid is air. The exact material parameters of PZT5A are given in Sec. 6.1, where an optimization takes place. The air properties depend on the conditions for each case solved and will be given individually e.g., for the case of Proline Prosonic Flow G 300 presented here, the air properties are given in Subsec. 6.3.1. The air is divided into 'Fluid in cavity' and 'Fluid towards the sender'. The reason for that division is the simulation strategy to be followed. An interface inside the fluid is needed for the assignment of an acoustic pressure boundary condition in the next step of the method, i.e. 'Part (II) Acoustics in fluid'. The acoustic pressure can be recorded

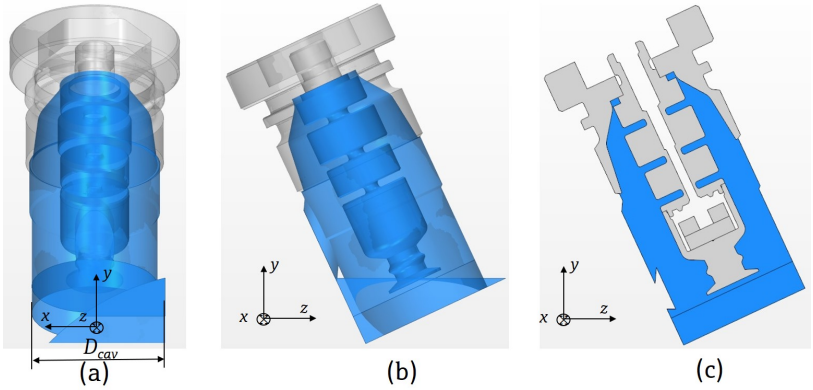

Figure 3.10: Geometry of sending transducer with a portion of fluid. (a) Axial view, (b) side view, (c) side cross-section in the middle plane of the transducer.

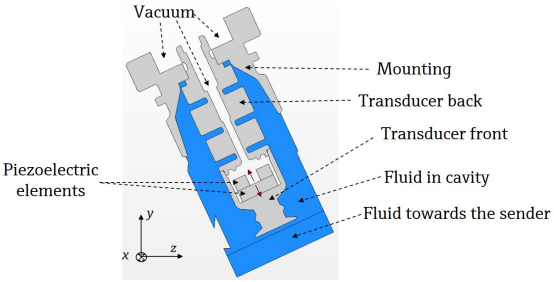

Figure 3.11: Geometry of sending transducer, side cross-section in the middle plane with bodies indicated.

on an interface and therefore, the fluid needs to be divided in the mentioned 'Fluid in cavity' and 'Fluid towards the sender'. The latter works as an extra layer of fluid that absorbs the acoustic waves with the setting of the respective boundary conditions, as it is described further in the present section. More information regarding this interface is given in the present subsection and in Subsec. 3.2.3. In the designated area inside the transducer and outside of the mounting, vacuum is considered as shown in Fig. 3.11. The material properties of Titan grade 2 and stainless steel are given in Table 3.1

For the simulation of all bodies and relevant physics (piezoelectricity, acoustic wave propagation in solids and fluids), the FEM solver of NACS [183] is used. In order to include the flow field on the fluid elements in the cavity, the FVM, CFD solver of Star-CCM+® is used [235]. The calculated velocity components, with the CFD solver of Star-CCM+®, are mapped with the nearest neighbor method [29] from the mesh of the FVM flow simulation to the mesh of the FEM acoustic simulation (cf. Sec. 3.2.5). The flow velocity $\boldsymbol{v_0}$ calculated with Star-CCM+® is given as input to Eq. **(2.49)**, which therefore, takes into account the flow effect on the wave propagation.

The mesh, i.e. discretized domain of the bodies, to be simulated is shown in Fig. 3.12. In

Material	Density ρ_0 [kg/m^3]	Elasticity modulus E_m [Pa]	Poisson ration ν [-]	Longitudinal speed of sound c_l [m/s]	Shear speed of sound c_t [m/s]
Titan grade 2	4510	$1.05{\cdot}10^{11}$	0.37	4825.10	2914.95
Stainless steel	7850	$1.95{\cdot}10^{11}$	0.283	4984.05	3111.39

Table 3.1: Parameters of the materials considered in the simulation.

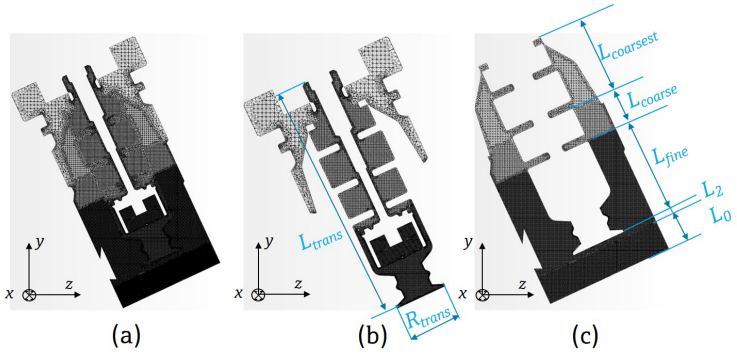

Figure 3.12: Numerical mesh of sending transducer. Side cross-section in the middle plane of (a) solid and fluid numerical mesh, (b) solid numerical mesh, (c) fluid numerical mesh

Fig. 3.12(a) the mesh of both the solid and fluid bodies is shown, in Fig. 3.12(b) the mesh of only the solid bodies and piezoelectric elements is shown, and in Fig. 3.12(c) the mesh of the fluid bodies is shown. In that case, which corresponds the meshing strategy followed in the cases presented in chapters 5 and 6, a 3D tetrahedral mesh of 1^{st} order is used [107] for the discretization of the piezoelectric elements, solid and fluid bodies (cf. Fig. 3.12). The meshing strategy is described separately for the cases of chapter 4. The mesh between interfaces of bodies is conformal i.e. the nodes of adjacent surfaces coincide [148], for all the geometries solved with FEM in this work.

Any meshing software can be used that generates this type of tetrahedral mesh, suitable for NACS, that is described and presented here. An internal program was utilized, the so-called 'mesh2mesh' [250] that enables the conversion of several mesh types. A CGNS [39] file is exported from a meshing software and is converted to a suitable mesh file for NACS, i.e. NACS Mesh Format, 'nmf', on which the interfaces between the domains are conformal [108].

The main dimensions of the transducer, so that an impression is given about its size, are the radius of the front surface, R_{trans} = 5.75 mm and the length, L_{trans}=52.2 mm. A more detailed description of the transducer is given in [62]. The 'Fluid in cavity' extends L_2=1 mm from the front surface of the transducer, while the dimension of the 'Fluid towards the sender' is L_0 = 7 mm. The maximum dimension of the 'Fluid towards the sender' in x-direction as shown in Fig. 3.10(a) is D_{cav} = 25.6 mm. For the meshing of Part **(I)** the tetrahedral mesher of Star-CCM+ is used. As it can be seen in Fig. 3.12, a different cell-size is used for each domain or area of a domain. By 'cell-size', the edge-dimension of a cell is meant, which can be given directly as a setting in Star-CCM+. In Table 3.2, the cell-size for

each domain/area of Part **(I)** is shown. The 'Fluid in cavity-fine', 'Fluid in cavity-coarse', and 'Fluid in cavity-coarsest' are areas of 'Fluid in cavity' with dimensions $L_{fine} = 22$ mm, $L_{coarse} = 7$ mm, and $L_{coarsest} = 16$ mm, respectively, as shown in Fig. 3.12.

Domain/Area	Cell-size [mm]
Fluid towards the sender	0.171
Fluid in cavity-fine	0.171
Fluid in cavity-coarse	0.342
Fluid in cavity-coarsest	0.5
Piezoelectric elements	0.171
Transducer front	0.22
Transducer back	0.35
Mounting	0.88

Table 3.2: Cell-size for each domain/area of Part **(I)**

Equations (2.25), (2.26), (2.27), and (2.28) for piezoelectricity, equations (2.16a), (2.16b) for wave propagation in solid materials, and the PE (Eq. (2.49)) for acoustic wave propagation in moving fluid media are numerically solved with the FEM program NACS [183] in the respective domains, where these physics are involved (cf. Fig. 3.11). For the time-marching of the transient case in time-domain, an implicit time-scheme of 2^{nd} order is employed, solved with the Newmark method [185].

The cross-section view of the geometry of the sending transducer (same as figs. 3.10(c), 3.11) is shown in Fig. 3.13, where information is included regarding the setup and the boundary conditions (BCs) of such a geometry. If two piezoelectric elements are mounted

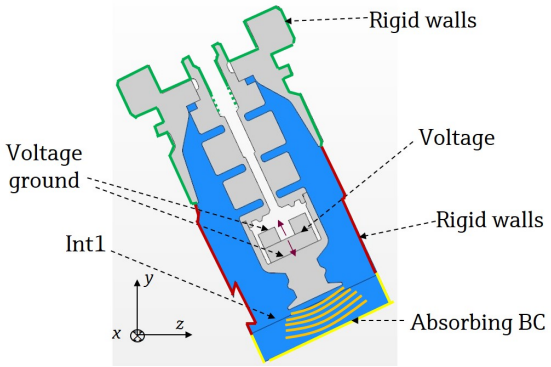

Figure 3.13: Geometry of sending transducer, side cross-section in the middle plane with BCs indicated.

together, as in the geometry of Fig. 3.13, then it is common practice that they are grounded ($V = 0$) on the upper free surface of the upper element and on the down surface of the down element, which is mounted on the solid body of the transducer. The polarization axis of each element is shown with continuous plum arrows in Fig. 3.13. The two elements are polarized in opposite directions. This is also the case for the receiver. AC Voltage is applied

on the interface between the two piezoelectric elements, which causes them to vibrate due to the inverse piezoelectric effect (cf. Sec. 2.1.3). A typical voltage boundary condition for the input voltage is a four-cycle sine burst with a frequency corresponding to the transducer resonance frequency

$$V_1 = A\sin(\omega t), \qquad t \leq 4T, \tag{3.16}$$

where A is the voltage amplitude [V], ω is the angular frequency [rad/s], and T is the signal period [s].

An absorbing boundary condition [107] is indicated in Fig. 3.13, with a continuous yellow line on the outside surface of the region 'Fluid towards the sender'. For an ideal situation, an absorbing boundary condition means that the fluctuations of the acoustic field are not reflected back when they reach a surface with such a BC applied i.e. only outgoing waves can pass the boundary for the ideal case of perpendicular inciding plane waves [44, 67, 82, 107]. It is known that absorbing boundary conditions operate better for acoustic plane waves inciding perpendicular to the surface and they are not fully absorbing for non-perpendicular inciding acoustic waves [44, 67, 82, 107]. In the present work, absorbing boundary conditions are used for the simulation in NACS, as documented in refs. [107, 183] and for the simulation in Star-CCM+ ®, as documented in ref. [229]. In general and ideally for an absorbing boundary condition, only outgoing waves can pass through a surface where an absorbing boundary condition is set. Indicatively, the particle displacement, $u^-(z,t)$ for a wave propagating in the negative z-direction is given by

$$u^-(z,t) = u_0 e^{i(\omega t + kz)}, \tag{3.17}$$

where u_0 is the displacement amplitude, ω the angular frequency, and k the wavenumber. For this wave, it is valid that [107]

$$\frac{\partial u}{\partial t} - c\frac{\partial u}{\partial x} = 0. \tag{3.18}$$

Eq. (3.17) fulfills eq. (3.18) and therefore such a wave will pass through the surface on which the absorbing BC is set. Waves propagating in the positive z-direction on the other hand, given as

$$u^+(z,t) = u_0 e^{i(\omega t - kz)}, \tag{3.19}$$

are completely reflected.

Artificial reflections are expected in the cases investigated here due to non-perpendicular incidence. In Fig. 3.13 typical waves are sketched with orange curved lines, which propagate from the front of the transducer and inside the fluid. It should be highlighted that the waves do not represent reality but a typical, schematic representation of the propagation. Simulated waves will be shown in chapters 4, 5, and 6. It is apparent that the waves are not plane and that they do not impinge in a perpendicular manner the areas, where absorbing boundary conditions are defined and consequently, not full absorption is expected for a large part of the boundary depending on the angle of incidence [44, 67, 82]. A study was made by Bezdek [30] regarding the performance of the absorbing boundary condition

for different angles of incidence, as it was implemented in CAPA [137]. Such a study is not performed in the current thesis, however the performance of the absorbing boundary condition of NACS [183], which is the successor of CAPA, is very similar. Moreover, a test simulation regarding the behavior of the absorbing boundary condition is given in chapter 4, where a test case is simulated.

Additionally, some precautions are taken for the avoidance of such reflections on the 'interesting part' of the signal i.e., the part used to calculate ToF, for the evaluation method presented in Sec. 2.5. The surface indicated as 'Int1' (interface 1) with a black continuous line, (cf. Fig. 3.13), is the interface between the two fluid domains, 'Fluid in cavity' and 'Fluid towards the sender' (cf. Fig. 3.11), which both represent the fluid inside the UTTF. More specifically, regarding the precautions taken, the dimensions L_0 and L_2 are chosen in a way so that the three zero-crossings used for the evaluation (cf. Subsec. 2.5) are recorded on Int1 before any potential reflections from the absorbing boundary conditions, set on the surfaces of 'Fluid towards the sender', arrive back to Int1. If t_3 is the ToF needed for the last of the 3 zero-crossings, described in Sec. 2.5, to propagate to Int1 and t_{refl} the time needed for the waves to propagate to the outer surface of the 'Fluid towards the sender', where an absorbing BC is set, and back, then the criterion for the dimensions' choice is

$$t_3 < t_{refl} \Rightarrow t_3 < (L_2 + 2L_0)/c. \tag{3.20}$$

One chooses the dimensions L_2 and L_0, so that the Eq. (3.20) is not violated. For the choice of L_0 and L_2 with the mentioned criterion, it is assumed, only for that choice and not in general, that $\boldsymbol{v_0}$ is zero in the fluid and that the main reflections, arriving at the shortest time, are expected from the surface opposite to the front surface of the transducer. The criterion is chosen in a pragmatic way, with the aim of saving computational resources, and it is satisfied throughout the simulated cases in the thesis. Int1 is discretized with a tetra mesh, as the rest of the fluid simulated with NACS. Int1 indicates continuity between the domains with the purpose of recording acoustic pressure inside the fluid domain in order to give it as a BC to the next step of the SimPAC² method (cf. Fig. 3.8 and Sec. 3.2.3). It is reminded that for the coupling of NACS and Star-CCM+® Eq. (2.42) is used for the case of quiescent fluid and Eq. (2.50) for moving fluid in order to transform ϕ into p'. The calculated p' on Int1 in each case of quiescent or moving fluid is given to Star-CCM+® in Eq. (2.53).

The coupling between NACS and Star-CCM+ ® is a big task when a transient 3D simulation is performed, as a large amount of data is generated in order to create a BC. Acoustic pressure data are generated for all the nodes on the surface Int1 for every time-step. Because of the high-frequency of the ultrasonic signals, short time-steps are needed for the time-discretization (cf. chapters 4 and 6). Moreover, high frequency implies short wavelength ($c = \lambda f$), which means that small elements are needed in order to discretize spatially the numerical domain (cf. chapters 4 and 6). The acoustic pressure information in the 4-dimensional domain (x, y, z, t) can be exported in several data forms such as standard 'csv' (comma-separated values) or 'CGNS' (CFD general notation system) files and depending on the geometry and discretization, its size can typically vary from several Mega-bytes (MB) to several Giga-bytes (GB). In the cases simulated here, a 'csv' file is used, as it was faster to read for both NACS and Star-CCM+ compared to CGNS. Such simulations are shown in

chapters 4, 5, and 6.

The boundaries indicated in Fig. 3.13 with green and dark red colors for the outer solid and fluid boundaries, respectively, are set to rigid walls, which means that the normal particle velocity on them is zero [117]

$$\boldsymbol{n} \cdot \boldsymbol{v}' = \boldsymbol{n} \cdot \nabla\phi = 0. \tag{3.21}$$

If the green dashed lines, shown in Fig. 3.13, are extended along the inner boundaries of the transducers until they meet each other, with the exception of the surface of the piezoelectric elements, then they define the whole rigid wall boundary. This assumption of rigid walls is made for the scope of the present work, as the difference between the acoustic impedance of the fluid, air, z_{air}, and the acoustic impedance of the solid, steel pipe, $z_{stainless\ steel}$, is orders of magnitude apart

$$z_{stainless\ steel} = \frac{p'_{stainless\ steel}}{v'_{stainless\ steel}} \gg z_{air} = \frac{p'_{air}}{v'_{air}}. \tag{3.22}$$

The issue of crosstalk between sender and receiver through the meter body is known and can influence the flowmeter performance [30, 163, 49]. However it was decided not to include the meter body in the simulations performed in the present thesis but a rigid wall BC instead. It is not the scope of this work to investigate the crosstalk effect or its interference with the main signal received on the receiver from the sender and through the fluid. It should be highlighted that the inclusion of the meter body is possible, however for the purpose of saving computational power, the assumption of rigid walls was made.

The BCs described in in Sec. 2 and in the present section, with the help of the geometry of Fig. 3.13, are in principle applied to the simulated use cases shown in secs. 4 and 6.

3.2.3 Part (II): Acoustics in flowing Fluid

For the largest portion of the acoustic wave propagation in fluid media, the FVM solver of Star-CCM+®is employed, where Eq. (2.53) is solved. For the time-marching of the transient simulation, an implicit time-scheme of 2^{nd} order with the Newmark-Alpha method [274] is utilized [183].

A typical geometry/setup of 3D fluid domain for acoustic wave propagation in moving fluid media in SimPAC^2 is shown in Fig. 3.14. The geometry is slightly different from part **(II)** shown in Fig. 3.8 in order to illustrate more realistically the simulation. The whole fluid domain consists of 3 bodies, a 'Fluid towards the sender', which is the same as the designated fluid shown in Fig. 3.11, the 'Main fluid', which includes most of the domain in the meter body, and a 'Fluid towards the receiver'.

The 'Fluid towards the sender' was included in Part (I) of SimPAC^2, where ϕ was calculated with NACS and recorded on surface Int1. It was transformed into p', as described in Subsec. 2.4.3, in order to give it as an input to Part (II) of the SimPAC^2 method. The region 'Fluid towards the receiver' is similarly defined so that the calculated p' with Star-CCM+® is recorded on the 'down surface', towards negative y-direction, Int2, of the 'Fluid towards the receiver'. The recorded p' on Int2 is transformed into ϕ so that it is used on the next step, Part **(III)**, of the SimPAC^2 method.

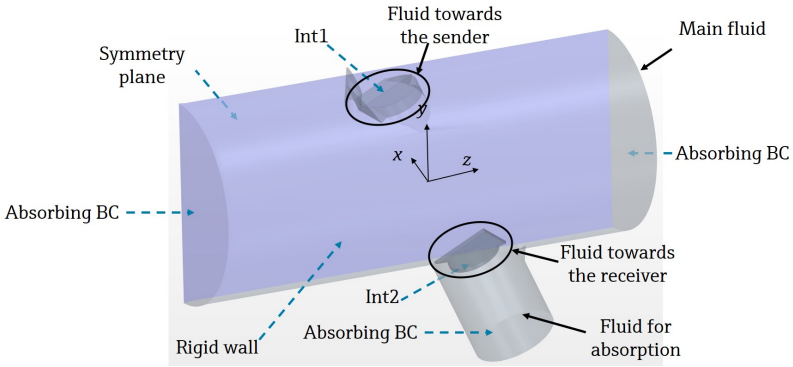

Figure 3.14: Geometry/setup of typical fluid domain for acoustic wave propagation in moving fluid media. 4 fluid bodies indicated with black continuous arrows and BCs (surfaces) indicated with blue dashed arrows

It should be already mentioned that the regions 'Fluid towards the sender' and 'Fluid towards the receiver' as well as the interfaces 'Int1' and 'Int2' are shown magnified in Fig. 3.15, while a the schematic depiction of Fig. 3.9. More details are given in Subsecs. 2.4.3 and 3.2.4 as well. It should be highlighted that the waves propagate unhindered among the 3 designated fluids, since the material is 'air' for all of them and their definition is made only due to simulation strategy reasons and for the definition of surfaces Int1 and Int2, where ϕ and p' are recorded and BCs are provided.

More specifically, and summarizing, ϕ is recorded on Int1 in Part **(I)** of the simulation and subsequently it is transformed into p' to be given as input to Part **(II)**. Similarly, p' is recorded on Int2 and it is transformed into ϕ to be given as input to Part **(III)**; more details about this step are following. The mathematical description of these steps is described in Subsec. 2.4.3.

The bodies are numerically discretized with the use of a Cartesian mesh [6, 229], where all the edges of the elements are parallel to the axes of a Cartesian coordinate system. A typical discretization, with a Cartesian mesh, of the fluid bodies shown in Fig. 3.14, is presented in Fig. 3.15. The two smaller bodies indicated as 'Fluid towards the sender' and 'Fluid towards the receiver are shown magnified on the right of Fig. 3.15. It can be seen that the region in which it is more important to resolve correctly, i.e. the region between the sending and receiving transducer, is discretized with a finer mesh. In all the fluid regions, the fluid can be either quiescent or flowing depending on the settings of the user and the case to be solved.

Meshing and geometrical details are given for the discretized bodies shown in figs. 3.14 and 3.15, which depict a typical case simulated in the present work. A side and an axial view of the refined area of the mesh together with the 'Fluid towards the sender', 'Fluid towards the receiver', and the 'Fluid for absorption' are shown in Fig. 3.16. The 'Fluid towards the sender' is the area with dimensions L_0 and L_3 and the 'Fluid towards the receiver' with L_5 and L_6. The region 'Fluid for absorption' is enclosed by the continuos yellow line. The 'Fluid towards the sender', the 'Fluid towards the receiver', the 'Fluid for absorption', and

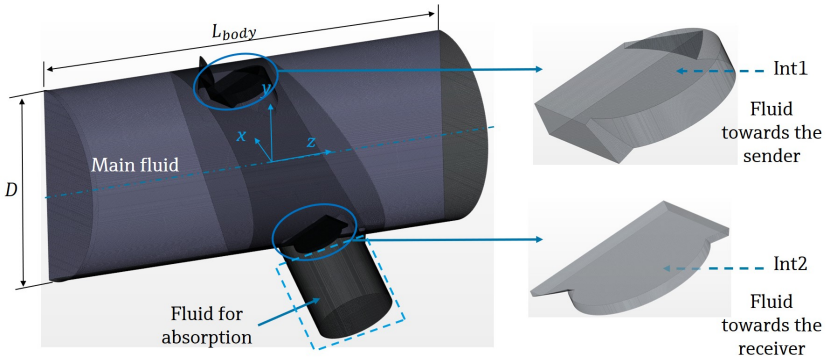

Figure 3.15: Cartesian mesh of 4 fluid bodies 'Main fluid', 'Fluid towards the sender', 'Fluid towards the receiver', and 'Fluid for absorption'. The 'Fluid towards the sender' and the 'Fluid towards the receiver' are zoomed on the right-hand side of the figure. Surface Int1 on the upper surface of the Fluid towards the sender and Int2 on the down surface of the Fluid towards the receiver.

the refined area of mesh of the 'Main fluid', between the 'Fluid towards the sender' and 'Fluid towards the receiver' are descretized with 20 cells/wavelength. The rest of the 'Main fluid' is descretized more coarsely with 10 cells/wavelength, as it is an area of less interest for this simulation. The reason for this choice is given based on convergence tests for the SimPAC^2 method in chapter 4. The diameter of the 'Main fluid' is $D = 97$ mm and its length is $L_{body} = 196.6$ mm. Half of the body is simulated since it is symmetric on plane yz. The total number of cells needed for the discretization is 151 million cells.

The axial dimensions of the refined area are L_{fine1}=54 mm and $L_{fine2} = 80$ mm. The angle between the transducer main axis and the axial direction of the meter body is $\theta = 65^o$, the distance between two opposite transducers is $L = 103$ mm, while $L_{cav} = 5.8$ mm, and the rest of the dimensions depicted in Fig. 3.16 are

- L_0= 7 mm
- L_3= 27 mm
- L_5= 2 mm
- L_6= 27 mm
- L_7= 65 mm
- $D_{abs} = 40$ mm
- $R_{rp} = 28$ mm.

A further clarification is made regarding the mentioned dimensions. The dimension D_{abs} is the diameter and L_7 the length of the 'Fluid for absorption', which replaced the receiver in Part **(II)**. The reason for the replacement is that the presence of the receiver would create reflections that would be reflected back and recorded on Int2. Such recording of the reflections is unwanted and a source of error, since it would be an additional artificial source for Part **(III)** of the simulation, where Int2 is used as a source of ϕ in the fluid. Thereby, the

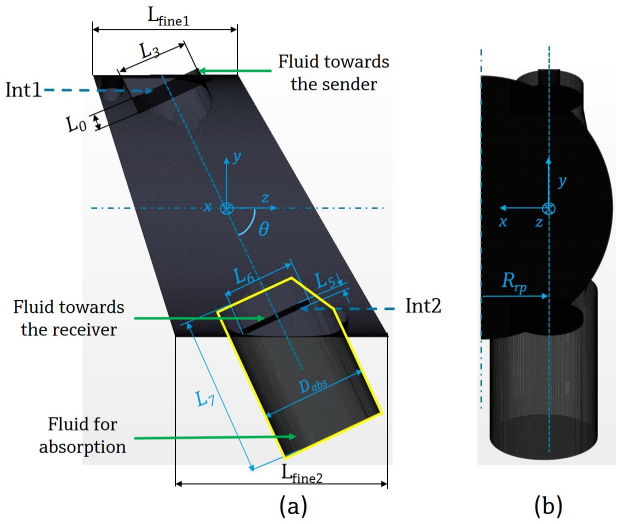

Figure 3.16: Cartesian mesh of the refined area of the 'Main fluid', 'Fluid towards the sender', 'Fluid towards the receiver', and for 'Fluid for absorption' with dimensions shown.

'Fluid for absorption' was created, with the yellow designated absorbing BCs on Fig. 3.16. L_7 was chosen relatively large in order to avoid any unecessary reflections, so that the absorbing BCs are set as far as possible from the interface 'Int2'. For more information regarding the implementation of absorbing BCs, refer to Subsec. 3.2.2 and [229]. R_{dp} is the radial position of the sound paths of the flowmeter, which is for this specific two-path device at $R_{dp} = 0.5 \cdot R$ [176].

The presence of 'Fluid towards the sender' in both Part **(I)** and Part **(II)**, as well as of 'Fluid towards the receiver' in both Part **(II)** and Part **(III)** is necessary, due to recording and imposing the needed BCs inside a fluid domain common in two parts. A similar strategy with the utilization of different methods is followed by Bezdek [30].

The surface Int1 is located on the upper surface, towards the positive y-direction, of the 'Fluid towards the sender'. The acoustic pressure is defined and given on Int1 in the current step of SimPAC², in the way that it is described in subsecs. 2.4 and 3.2.2. Int1, as well as the 'Fluid towards the sender' are included in both Part **(I)** and Part **(II)** of SimPAC², however different meshes and solvers are used, as already clarified. In part **(I)** a tetrahedral mesh and FEM solver are used, while in part **(II)** a Cartesian mesh and FVM solver are used. Therefore, the acoustic pressure, already calculated in part **(I)**, is mapped with the nearest neighbor method [29, 229] from the tetrahedral to the Cartesian mesh of part **(II)**. More information regarding the accuracy of the mapping is given in subec. 4.3.2 for the case of mapping on Int1 from part (I) to part (II) for a tetrahedral mesh.

The surface Int2 is located on the 'down surface', towards the negative y-direction, of the 'Fluid towards the receiver'. The acoustic pressure is recorded on Int2 for each time-step. Int2 should be spatially positioned close to the geometry of the receiver, which is not included in Part **(II)**, for the avoidance of reflections as explained. When Int2 is spatially

positioned close to the coordinates of the missing receiver, the relevant acoustic waves that will meet the receiver are captured. More information on the strategy followed to choose the position of Int2, is given in Subsec. 3.2.4.

Absorbing BCs (cf. Subsec. 3.2.2 and [229]) are defined as well on the left-hand (towards the inlet) and the right-hand side (towards the outlet) to avoid reflections of acoustic waves. A rigid wall, as given in Eq. (3.21), is defined on the curvy surface of the Main fluid, where in reality there is an interface with the solid pipe, as shown in Fig. 3.14. For the geometry presented here, which is a two-path inline device, a symmetry plane is defined in order to save computational time and memory [229]. The symmetry BC is expressed as [229]

$$\frac{\partial p'}{\partial \boldsymbol{n}} = \frac{\partial p'}{\partial x} = 0, \tag{3.23}$$

at $x = 0$, for the geometry of Fig. 3.14.

3.2.4 Part (III): Receiver in Fluid

The last step of the SimPAC^2 method is the simulation of the receiving transducer together with a portion of fluid. It should be mentioned that parts of the description in the current section are similar to Sec. 3.2.2, however it is found essential to fully describe the receiving transducer as well. The 3D geometry to be simulated [62, 64] is shown in Fig. 3.17, where

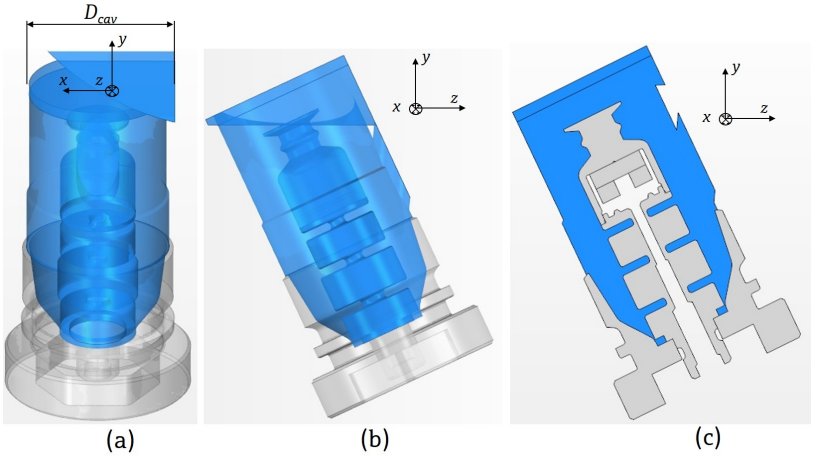

Figure 3.17: Geometry of receiving transducer with a portion of fluid. (a) Axial view, (b) side view, (c) side cross-section in the middle plane of the receiving transducer.

3.17(a) is the axial view, 3.17(b) is the side view, and 3.17(c) is the side cross-section in the middle plane of the receiving transducer. The dimensions of the geometry are given in the present section and in Sec. 6. The fluid is represented with blue colors and the solid bodies with gray colors, as in the case of Part **(I)**. The fluid domain can be, similarly to Part **(I)**,

either moving or non-moving. The part of the meter-body around the fluid is not included. Instead, rigid walls are assumed for acoustics, as described from Eq. (3.21) and wall no-slip BC for CFD [58, 72], as in the case of Part **(I)**.

In Fig. 3.18, the view of Fig. 3.17(c) is taken, and information is added regarding each body to be modeled. The solid bodies, which comprise the receiving transducer, are

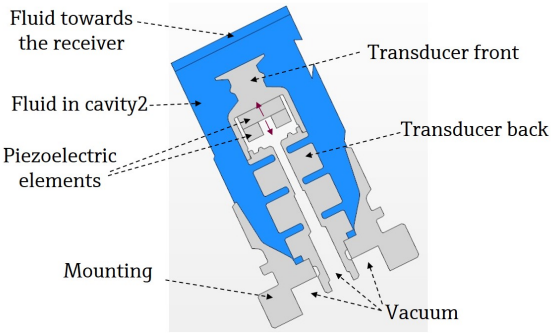

Figure 3.18: Geometry of receiving transducer, side cross-section in the middle plane with bodies indicated.

the same as the ones comprising the sending one. However, the two piezoelectric elements transform mechanical vibrations to voltage (direct piezoelectric effect). The fluid, in which the transducer is emerged, is also of different geometry compared to the fluid in the case of the sender. More specifically, the 'Fluid in cavity2' expands further away from the front surface of the 'Transducer front' compared to 'Fluid in cavity' in Part **(I)** for reasons that follow in the present subsection. The exact dimensions of 'Fluid in cavity2' and 'Fluid towards the receiver' are given in the present subsection as well. The materials used, are described in Subsec. 3.2.2.

Similarly to the sending transducer, the FEM solver of NACS [183] is used for the simulation, while in order to include the flow field on the fluid elements in the cavity, the FVM, CFD solver of Star-CCM+®is used [235]. The calculated velocity components, with Star-CCM+®, are mapped with the nearest neighbor method [29] from the mesh of the FVM flow simulation to the mesh of the FEM acoustic simulation (cf. Sec. 3.2.5). Similarly to Part **(I)**, the flow velocity $\boldsymbol{v_0}$ calculated with Star-CCM+® is given as input to Eq. (2.49), which therefore, takes into account the flow effect on the wave propagation.

The mesh i.e., discretized domain of the bodies to be simulated is shown in Fig. 3.19. In Fig. 3.19(a) the mesh of both the solid and fluid bodies is shown, in Fig. 3.19(b) the mesh of only the solid bodies and piezoelectric elements is shown, and in Fig. 3.19(c) the mesh of the fluid bodies is shown. In that case, simulated in chapter 6, a 3D tetrahedral mesh of 1^{st} order is used [107] for the discretization of the piezoelectric elements, solid and fluid bodies (Fig. 3.19). Star-CCM+ [229] is used for the meshing of the geometry. As it can be seen in Fig. 3.19, the mesh is finer in the areas of interest i.e. fluid in the vicinity of the piezoelectric elements and in front of the frontal surface of the receiver. The same meshing strategy is followed for Part **(III)** as for Part **(I)** (cf. Table 3.2). The main dimensions R_{trans} and L_{trans} of the receiving transducer, are the same as for the sending transducer

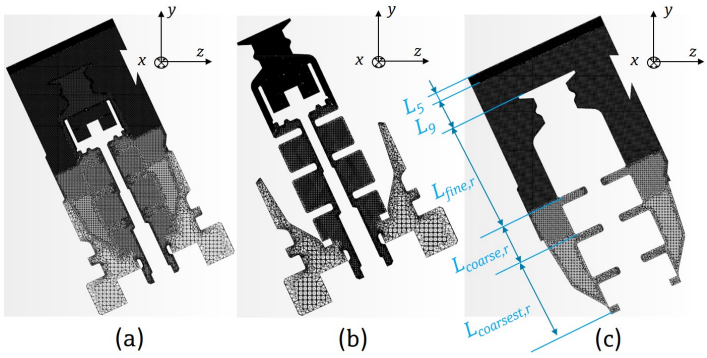

Figure 3.19: Numerical mesh of receiving transducer. Side cross-section in the middle plane of (a) solid and fluid numerical mesh, (b) solid numerical mesh, (c) fluid numerical mesh

shown in Subsec. 3.2.2. The 'Fluid in cavity' extends L_9=6 mm from the front surface of the transducer, while the dimension of the 'Fluid towards the receiver' is $L_5 = 2$ mm. The rest of the dimensions are $L_{fine,r} = 22$ mm, $L_{coarse,r}$ =7 mm, and $L_{coarsest,r}$ =16 mm, with the cell-size dimensions being 0.171 mm, 0.342 mm, and 0.5 mm, respectively, as in the case of Part **(I)**. The maximum dimension of the 'Fluid towards the receiver' in x-direction as shown in Fig. 3.17(a) is $D_{cav} = 25.6$ mm.

The same equations with the same solvers as for the case of the sending transducer are also modeled and solved in the case of the receiving transducer (cf. Sec. 3.2.2).

The cross-section view of the geometry of the receiving transducer (same as figs. 3.17(c), 3.18) is shown in Fig. 3.20, where information is included regarding the setup and the boundary conditions (BCs) of such a geometry. The difference compared to the sending

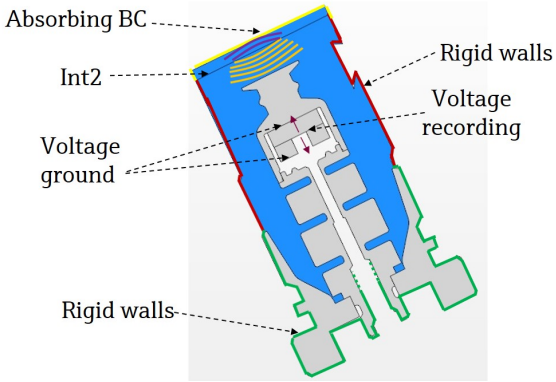

Figure 3.20: Geometry of receiving transducer, side cross-section in the middle plane with BCs indicated.

transducer is that the functioning purpose of the receiver is different, i.e. mechanical vibrations are transformed to voltage, and therefore a number of different BCs are assigned to the

geometry. Voltage is recorded on the surface named 'Voltage recording' in Fig. 3.20, where an equipotential BC, i.e. V_5=constant along the surface, is assigned. An absorbing BC is applied on the yellow designated surface of the 'Fluid towards the receiver', as shown in Fig. 3.20. This absorbing BC is chosen for the surface of 'FLuid towards the receiver' irrespective of it being a wall or part of the fluid domain in order to avoid unwanted reflections from waves that propagate from the source of Int2 and in the direction of the outer surfaces of the 'Fluid towards the receiver'. For more information on absorbing BCs, please refer to Subsec. 3.2.2 and [107, 183]. The polarization axis of the piezoelectric elements is shown in Fig. 3.20 as well. The rigid walls are described in the same way as in Subsec. 3.2.2.

The reason for the division of the domain into 'Fluid in cavity2' and 'Fluid towards the receiver' is the creation of an interface 'Int2'. The surface indicated as 'Int2' (interface 2) is the interface between two fluid domains, 'Fluid in cavity2' and 'Fluid towards the receiver'. Int2 indicates continuity between the domains with the purpose of making it an acoustic potential source inside the fluid domain (cf. Fig. 3.8) in a similar way as for Int1, described in Subsec. 2.5 and 3.2.2, with the utilization of Eq. (2.50) in order to transform p' into ϕ on 'Int2'.

As in Part **(I)**, reflections are avoided on the initial part of the received signal V_5, with the choice of dimensions L_5 and L_9 shown in Fig. 3.19. If $t_{3,3}$ is the ToF needed for the 3 zero-crossings, described in Subsec. 2.5, to propagate from the source of 'Int2' to the frontal surface of the receiver and $t_{refl,rec}$ the time needed for the waves to propagate back to the absorbing BC (distance L_5), get partially reflected, propagate to Int2 (distance L_5) and to the frontal surface of the receiver (distance L_9), then the criterion for the dimensions' choice is

$$t_{3,3} < t_{refl,rec} \Rightarrow t_{3,3} < (2L_5 + L_9)/c. \tag{3.24}$$

The same assumptions apply for the chosen criterion as for Part **(I)**. When 'Int2' is used as a source, waves propagate in two directions, i.e. in the direction of the receiver, as well as in the direction of the absorbing BCs of the 'Fluid towards the receiver', as shown schematically in Fig. 3.20. An investigation that gives a hint of a potential effect of no complete absorption has been carried out in Subsec. 5.5. Moreover, it is assumed that no strong reflections are expected due to incidence close to perpendicular [30]. However, a more complete investigation should be carried out with a systematic approach to quantify the exact effect of reflections. It should be clarified that reflections do not have, by definition, an effect on the source of 'Int2' due to the BC used [30], which will be described in Subsec. 5.5. An effect could be present though due to reflections from the absorbing BCs to the solid bodies of the receiver.

Similarly to the previous steps, a large amount of data is given as a BC on every node of the surface Int2 for each time-step. The acoustic pressure p' recorded on Int2 on the FVM mesh is transformed into ϕ with Eq. (2.50) and mapped on the tetrahedral FEM mesh in the location of Int2 with the nearest neighbor method [29]. The flow velocity $\boldsymbol{v_0}$ calculated with Star-CCM+® is given as input to Eq. (2.49), which therefore, takes into account the flow effect on the wave propagation.

To enable an acoustic pressure or acoustic velocity potential source that will not function as a rigid wall but as a surface that will allow passage of the incident waves on the source, the so-called superposition BC is defined on Int2 [30]. The superposition BC was implemented in CAPA and afterwards in NACS [183], as a result of the research of Bezděk [30]. In

Fig. 3.21, a schematic representation of the receiver with a portion of fluid is given, with the specification of a superposition BC on Int2. Rigid walls, shown with red lines are specified

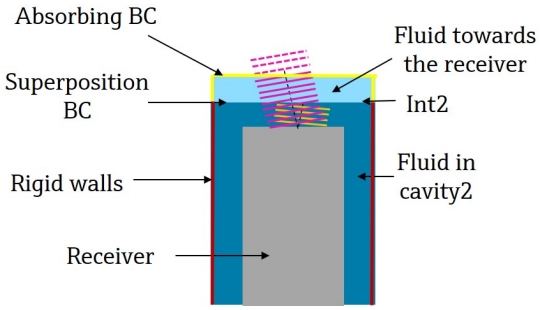

Figure 3.21: Schematic geometry of receiving transducer in fluid with schematic representation of waves traveling. Superposition BC set on Int2 and Absorbing BC on the outer surfaces of the 'Fluid towards the receiver'.

on the outer surfaces of the 'Fluid in cavity2'. An absorbing BC, shown with yellow lines, is specified on the outer walls of the 'Fluid towards the receiver'. The waves shown with orange lines, are sent from Int2. The waves reflected by the receiver, shown with pink lines, propagate towards and through Int2 and into the 'Fluid towards the receiver', due to the superposition BC being able to let them pass through.

The use of the superposition BC is necessary on Int2, due to the mentioned reflections from the receiver, which is in proximity to Int2. In the case that an acoustic pressure source BC is given for example, as on Int1 (cf. Subsec. 3.2.2), then Int2 would act as a rigid wall [30]. As described by Bezdek [30], an acoustic source is analogous to an ideal voltage source in an electric transmission line. Thus, the standard acoustic source formulation leads to an artificial boundary that causes total reflection of the incident waves. Reflections from the near receiver would not pass through Int2 [30] but would reflect on Int2 and impinge the receiver again, which would be an artificial situation.

Regarding the formulation of the superposition BC, an intermediate time-step is introduced that updates the value of the superposition BC before it is given as an input. More specifically, if t is the current time step and F a symbolic solving scheme, then the acoustic velocity potential solution for the next time-step $t+1$ is defined as

$$\phi(t+1) = F[\phi(t)], \tag{3.25}$$

where $\phi(t)$ is the solution provided by the FEM solver of NACS on time-step t [30, 183]. In order to compute the solution for the next time-step $t+1$, while allowing passage of the incident waves, an intermediate time-step is introduced, at which $\phi(t)$ is updated before it enters the solution procedure again [30]. The solution of the acoustic velocity potential on Int2, for that intermediate time-step is [30]

$$\phi^*(t) = \phi(t) + \phi^+(t), \tag{3.26}$$

where $\phi^+(t)$ is the superimposed source of velocity potential on the nodes of Int2. $\phi^+(t)$ is calculated from the transformation of p', which was calculated with the FVM solver of Star-CCM+® in Part **(II)** of the simulation. For that transformation, Eq. (2.50) is used (cf. Subsecs. 2.5, 3.2.2, and 3.2.3). Therefore, the solution for the next time-step of the FEM NACS solver [183] is updated, with the use of the intermediate time-step, as [30]

$$\phi(t+1) = F[\phi^*(t)] \tag{3.27}$$

The reader may find more information on the superposition BC and its verification in the PhD thesis from Bezdek [30].

3.2.5 Part (IV): Flow Field

The flow field is an integral part of an UTTF system and its accurate solution is of great importance for the analysis of a flowmeter [197]. In the present thesis, the flow field is computed with state-of-the-art CFD simulations, as described in Subsec. 2.3. The flow field data are coupled with acoustics, while its respective properties, primarily the flow velocity field, $\boldsymbol{v_0}$, are given to the acoustic wave equations that take flow into account. When coupling occurs with Part **(I)**, i.e. Sender in fluid (cf. Sec. 3.2.2) or Part **(III)**, i.e. Receiver in fluid (cf. Sec. 3.2.4), the flow velocity field, $\boldsymbol{v_0}$, is given to the PE Eq. (2.49), which is solved with the FEM solver of NACS. When coupling occurs with part **(II)**, i.e. Acoustics in fluid (cf. Sec. 3.2.3) the velocity field $\boldsymbol{v_0}$ is given as input to the CAWE Eq. (2.56).

A CFD simulation is important for the completeness of the SimPAC² method, however it should be made clear that its necessity is not demanded, since the flow data are possible to be given otherwise e.g. with an analytical expression. Nevertheless, an analytical expression is not as precise as a high-end CFD simulation, since important effects are not taken into account, e.g. flow inside the cavities and disturbed flows due to inlet conditions. Often, an analytical expression is given as input for the coupling with acoustics [30, 99, 152, 231] instead of CFD data. This approach is problematic for inline UTTF, since zero flow is assumed inside the cavities and around the transducers, where, in reality, $\boldsymbol{v_0} \neq 0$. In other words, if $r_{USM} = \sqrt{x^2 + y^2}$ is the radial coordinate for an USM, as defined in Fig. 1.1 and R the radius of the meter body of the flowmeter, then $\boldsymbol{v_0} = 0$ for $r > R$, when an analytical flow profile is considered. In Fig. 3.22 a schematic depiction of the flow profile in an UTTF is shown for (a) an analytical expression and (b) for a flow profile defined with a CFD simulation. In reality, vortices are generated inside the cavities of the transducers, which is not correctly represented in the case of an analytical flow profile and can therefore lead to error in signal propagation. In this work, both cases are studied in order to quantify this error in Secs. 5.4. 6.2, and 6.3.

An analytical fully-developed profile in a pipe can be expressed with the well-known power-law [226, 253]

$$v_0(r) = v_{max}\left[1 - \left(\frac{r_{USM}}{R}\right)^2\right]^{n_0}, \tag{3.28}$$

where v_{max} is the maximum velocity achieved in the middle of the pipe ($r_{USM} = 0$) and n_0

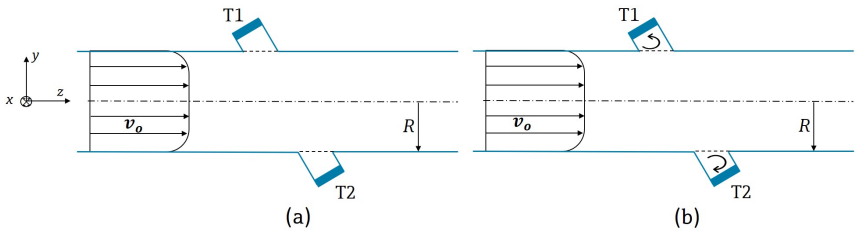

Figure 3.22: Schematic depiction of flow-field in UTTF for (a) analytical flow profile definition, (b) CFD flow profile definition

is an exponent dependent on the Re number

$$\frac{1}{n_0} = 1 + \sqrt[6]{\frac{Re}{50}}. \tag{3.29}$$

In that case, the calculated flow velocity is mapped on the cells of the acoustic mesh, which have the respective coordinates, with the nearest neighbor method.

In the present thesis, instead of an analytical profile, a separate CFD simulation is performed as well, as a more sophisticated method. A fully-developed flow-field is simulated with CFD and with zero velocity inside the cavities for $r > R$. The CFD simulation is performed in the way described in Sec. 3.1 but for a pipe geometry with radius equal to the one of the meter-body of the flowmeter with the absence of cavities. The calculated flow field is mapped from the 'CFD mesh' of the pipe geometry to the respective acoustic mesh of parts **(I), (II), (III)** (cf. Fig. 3.12, 3.15, 3.19) with the nearest neighbor method. The area for $r > R$ is not considered in the CFD simulation. Therefore, inside the cavities when $r > R$, the flow velocity, v_0 is set zero, since there is no v_0 to map from the CFD mesh to the acoustic mesh.

In the case of a real CFD flow-field, the flow field is calculated on the discretized fluid domainof the flowmeter. The CFD simulation is performed in the way described in Sec. 3.1. A typical meshed fluid domain with the assigned BCs is shown in Fig. 3.1. The flow field is mapped from the 'CFD mesh' to the respective acoustic mesh of parts **(I), (II), (III)** (cf. Fig. 3.12, 3.15, 3.19) with the nearest neighbor method as well.

For all the CFD simulations combined with acoustic wave propagation in fluid media, the RANS model realizable k-ε is used [227], as it has been extensively tested [196] and seems to deliver suitable results for the scope of the present work.

Chapter 4

Verification of Methods and Results

The simulation methods presented in Sec. 3 are verified in this section with experimental results and compared with other verified simulations for simple setups. The motivation for this chapter is the comparison and verification of results obtained with NACS [183], CNA, and SimPAC^2 with already published measurements and simulation results [196, 277]. Thus, this chapter serves for the finding of optimum simulation setup for the investigated cases and as a guide for the cases of chapters 5, 6 in order to achieve convergence and obtain reliable results.

For the verification of the CNA method, a flowmeter geometry is used for a variety of inlet conditions and turbulence models. Measurements of a commercial Endress+Hauser UTTF [66] were directly performed at an experimental rig and compared with the simulation results [196]. In this work, gas UTTF devices are on the focus, however a water UTTF is used for the verification of the CNA method. Since only the flow is considered with the CNA method, the Re number plays a major role for the resulting flow field [14, 58]. The Re number range for water and gas UTTF can be of similar range for typical applications [64, 66] and therefore, it is acceptable to test the CNA method with a water UTTF. On the other hand, an issue that arises is the beam deflection which is lower in liquid compared to gas applications [30, 99, 111]. Beam deflection is not considered in the CNA method and can be of importance for higher velocities in gas applications [99].

For the SimPAC^2 method a chain-verification or chain-comparisons take place. SimPAC^2 is compared with the FEM program, NACS, which in turn is compared with experimental results. The method complexity is higher compared to the CNA method and therefore, simple geometries and setups are used with the aim of not introducing unknown factors and of a straightforward explanation and interpretation of the results. Complexity is gradually built, as different flow fields and more geometries are introduced. Initially, a simple case is investigated, namely 'Case 1' of two piezoelectric elements opposite to each other, i.e. a sender and a receiver in zero flow [277]. A comparison is made between measurements [277] and results of the FEM program, NACS [183]. After NACS is compared with measurements for 'Case 1', a similar setup, namely 'Case 2' is considered, of two piezoelectric elements opposite to each other, with the presence of uniform flow. Case 2 is is simulated with NACS [183] and SimPAC^2.

In the subsection of 'Case 1' (Subsec. 4.2) the experimental and simulation setups with NACS are described, while simulations are performed with a 'long' and a 'short' input voltage signal for a 2D axisymmetric case that will be described further in this section. Investigations of spatial and time resolution of the simulation were carried out in order to find the suitable settings for the FEM solver of NACS. Results of the received voltage signal, V_5 in time and frequency domain are presented and compared with measurements.

In the subsection of 'Case 2' (Subsec. 4.3) the simulation setup with NACS and SimPAC^2 is described. The settings used for the NACS setup were derived from 'Case 1', while settings are chosen for Star-CCM+® that produce results, which are in agreement with the results of NACS. The receiver voltage signal, V_5, is calculated with both NACS and SimPAC^2 for a number of uniform flow velocity fields. The %deviation is calculated for this simple UTTF and deviation curves, i.e. %deviation against flow velocity, v_{ref}, are presented and compared for the two methods.

In this section, neither NACS nor SimPAC^2 are combined with 'real', spatially varying flows or flows inside cavities, which are important for the deviation curves extraction of an UTTF [197]. However, such investigations of the flow effect are made in secs. 5 and 6. Furthermore, no real transducers are considered, which will be taken into account in Sec. 6. In both NACS and SimPAC^2, the system of the UTTF from the input voltage on the sender, V_1 to the open-circuit received voltage, V_5, is considered, while the transmitting and receiving electronics are not taken into account.

4.1 'CFD-Non-acoustic' (CNA) Method

The CNA method is compared with measurements [196] for an UTTF geometry. The measurements took place at Endress+Hauser at a dedicated water rig, while the simulations were performed on an internal HPC at Endress+Hauser, due to their size and computational demands. The device used in the present section, for the comparison between the CNA simulation results with experiments, is different from the one presented in Sec. 3.1 and will be further described.

4.1.1 Experimental Setup

The measured and simulated UTTF Prosonic Flow E Heat [66], which is a MI-004 certified flowmeter for liquid custody-transfer heat metering applications [246], is shown in Fig. 4.1.

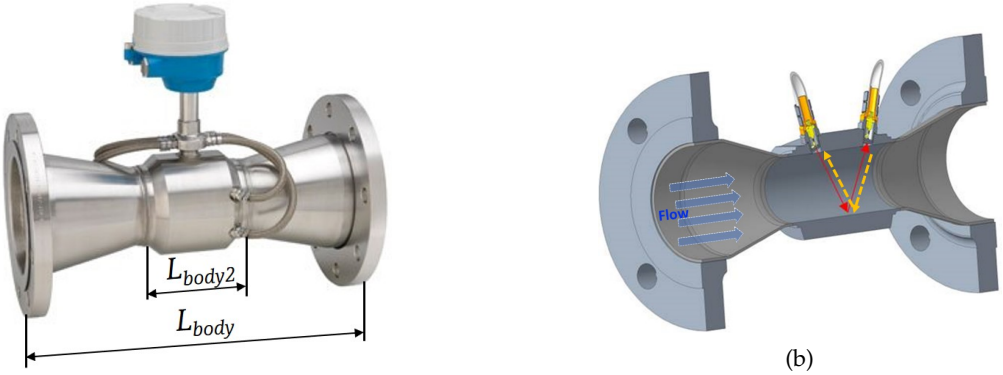

(a) (b)

Figure 4.1: (a) Prosonic Flow E Heat flowmeter and (b) model of the flowmeter cut in the axial middle plane section.

The diameter of the device is 110.3 mm at the inlet and outlet, and 75 mm at the contracted part. The length of the device is L_{body} = 281.16 mm and the length of the contracted part L_{body2} =145 mm. Two transducers with a reflected path are used. The red continuous arrows and the yellow dashed arrows indicate schematically the downstream and upstream sound paths respectively. In reality, the downstream and upstream sound paths should not differ as much as shown in Fig. 4.1(b), in fact they should almost coincide for low flow velocities [263]. However, for the purpose of depiction of both sound paths, they are shown spatially shifted in Fig. 4.1(b). For more information on the device, the interested reader is referred to [66].

In EN1434-4:2015 [46] all technical requirements for devices used in heat metering systems are described in form of tests. One aspect of these tests is the so called "flow disturbance test" according to EN1434-4:2015 Ch.7.22 [46]. Fig. 4.2 shows an asymmetric swirl generator and an out of plane bend as described in the respective norms and shown also by Turiso et al.

[251]. The values of rotation in Fig. 4.2(a) describe the rotational position of the asymmetric

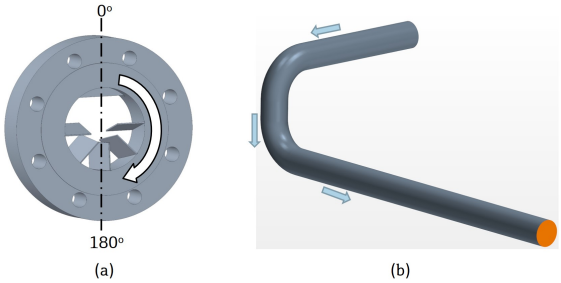

Figure 4.2: (a) Asymmetric swirl generator and (b) out of plane bend.

flow disturber relative to the transducers' location, while the rotational arrow shows the positive rotational direction. The 0^o position is investigated here. The challenging case of the asymmetric swirl generator is chosen to be investigated in order to test the limitations of the CNA method and its consistency with the measurements. The out of plane bend shown in Fig. 4.2(b) is not investigated, however it is shown here, since it is the scope of the asymmetric flow disturber to replace the out of plane bend in the tests, as well as generate the same flow field downstream [251]. In that way, the conducting of measurements is facilitated, since the setup of an asymmetric swirl generator is easier than that of an out of plane bend.

Flow measurements are performed on a dedicated water flow rig, shown in Fig. 4.3 and compared to a 'Swiss Calibration Services' (SCS) [221] calibrated Coriolis reference meter having an accuracy $\pm$ 0.1% (which is a factor of twenty better than the accuracy requirements for a Class 2 flowmeter according to MI-004, which is $\pm$ 2% in the upper flow range). Due to

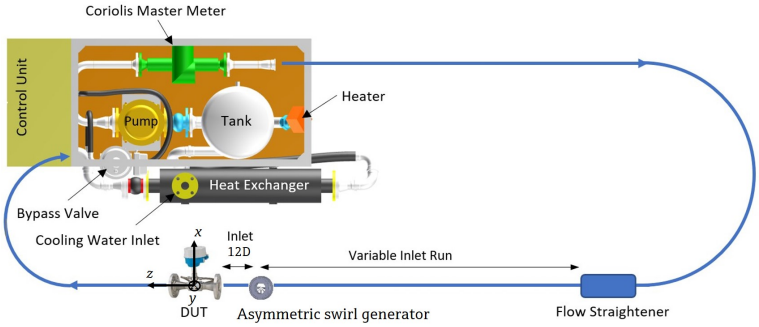

Figure 4.3: Overview of the experimental rig.

bypass valves the rig can deliver stable flows in the range of [0.02, 20] l/s at temperatures of [5, 85]^{o}C, which can be held stable within a range of $\pm$ 0.2 ^{o}C thanks to active heating and cooling systems. Pressures of [0, 6] bar can be applied to the medium. With the use of the described measurement setup, stable conditions are achieved that are used in the simulation

setup as well. Therefore, an effort is made to reassure that deviation curves are generated with the help of either measurements or simulations under the same conditions.

The device under test (DUT) is placed with maximal possible inlet run downstream of the flow straightener. Depending on the size of the device the 'Variable inlet run' shown in Fig. 4.3 may be between 30 pipe diameters, D, (D=110.3 mm in this case) and 90D. It should be highlighted that the coordinate system for this case is different compared to the convention throughout the thesis. More precisely, the coordinate system shown in Fig. 4.3 should be considered with its origin in the middle of DUT.

Measurements are performed with the asymmetric swirl generator placed 12D upstream of the DUT in order to assess its effect on the deviation curves of the UTTF, compared to a reference case of a fully developed flow profile [58]. If z is the axial dimension, with z=0 in the middle of the device, as shown in Fig. 4.3, then 12D=12·110.3 mm = 1323.6 mm is defined as the distance between the most upstream part of the device z=-L_{body}/2=-140.58 mm and the nearest part of the asymmetric swirl generator. The 'Variable inlet run' is set to 50D for the present case when the asymmetric swirl generator is placed 12D upstream of the DUT. All data are read digitally from the DUT and are directly compared to the data of the reference meter. Flow and temperature ramps can be programmed freely within the technical limits.

The measurements are made for a 'reference case' as well, with the absence of the asymmetric swirl generator. For the measurement setup of the reference case, the distance between the flow straightener and the DUT is set to 62D, which is enough to build a fully-developed flow profile [220, 236].

The 'Volume Flow Error [%]' is in general given by Eq. (2.98) and for the case of measurements, q_{ref} is provided directly by the Coriolis Master Meter shown in Fig. 4.3 and described in the present subsection.

The measurements are made for a reference case of a straight pipe without the asymmetric swirl generator, with enough inlet run so that the flow profile is fully developed (Fig. 4.3) and another case, where the asymmetric swirl generator (Fig. 4.2(a)) is placed 12D upstream of the device. The fluid is water with density ρ_0=999.15 kg/m^3 and dynamic viscosity μ=0.0011385 Pa·s. The same density and viscosity, as for the measurements, are considered for the CFD simulations.

4.1.2 Simulation Description and Setup

For all models, before the main CFD simulation of the device, another CFD simulation was performed for several Reynolds numbers in order to calculate the fully developed flow profiles that were specified before the asymmetric swirl generator. The way that the fully-developed flow profiles are obtained is explained in Sec. 3.1 and shown in Fig. 3.3. For the improved delayed detached eddy simulation (IDDES), in addition to the flow profile, synthetic turbulence is generated at the inlet as described by Jarrin et al. [101]. More precisely, the flow velocity components and the Reynolds-stresses are prescribed on the 'Inlet' surface, which correspond to a fully-developed turbulent flow profile [72, 101]. Based on the Reynolds-stress distribution on the Inlet surface, a statistical synthetic turbulence is created spatially, which does not have to be varied temporally and is suitable for large eddy simulations (LES), detached eddy simultions (DES), and IDDES [101]. A turbulence length

scale must be provided as well, which was kept constant [101].

For the wall boundary condition, a two-layer approach was used for the realizable $k-\varepsilon$ (RKEPS) model [227]. The advantage of the RKEPS model over the standard k-ε is that it gives much better results for the large mean strain rate flows. The main difference of the RKEPS model compared to the classic k-ε model [72] is the introduction of new formulations for both the dissipation rate equation and the eddy-viscosity [227]. More specifically, the constant C_μ, as described in Subsec. 2.3.2, which commonly takes value 0.09 for the k-ε model [72], is not constant anymore for RKEPS but it is related to the mean strain rate tensor [227]

$$\bar{\boldsymbol{D}}_{\boldsymbol{mean}} = \sqrt{2\bar{\boldsymbol{D}}_{\boldsymbol{s}}\bar{\boldsymbol{D}}_{\boldsymbol{s}}} = \sqrt{2\frac{1}{2}(\nabla\bar{\boldsymbol{v}}_{\mathbf{0}} + \nabla\bar{\boldsymbol{v}}_{\mathbf{0}}^{\boldsymbol{T}})\frac{1}{2}(\nabla\bar{\boldsymbol{v}}_{\mathbf{0}} + \nabla\bar{\boldsymbol{v}}_{\mathbf{0}}^{\boldsymbol{T}})}. \tag{4.1}$$

For the exact formulation of C_μ and its relation to the mean strain rate tensor, $\bar{\boldsymbol{D}}_{\boldsymbol{mean}}$, and the complete formulation of $RKEPS$ the reader is referred to the publication of Shih et al. [227]. The RKEPS becomes realizable for high mean strain rate flows, in contrast to the standard k-ε, which is non-realizable for such flows. For the standard k-ε model the normal stresses τ_{ii} may become negative and Schwarz' inequality for shear stresses can be violated, when high mean strain rates are present [227]. For the complete model formulation, the interested reader may refer to the work of Shih et al. [227] on the RKEPS model. In general, for the momentum equations no-slip condition was employed at the wall, i.e. $\bar{\boldsymbol{v}}_{\mathbf{0}} = 0$ [58, 72].

The two-layer approach of Wolfstein [273], implemented in Star-CCM+® for the RKEPS model [227], allows to model the flow up to the viscous sublayer with a reasonable accuracy by solving a single equation near the wall. Therefore, in the main flow, where the mean strain rate tensor, $\bar{\boldsymbol{D}}_{\boldsymbol{mean}}$ is not large, the turbulent kinetic energy and turbulent dissipation rate equations are solved [227] but near the wall in the viscous sublayer [72], where the flow is viscosity-dominated, the turbulence dissipation rate equation is replaced by an algebraic length scale, l_ε, [229] to determine the eddy-viscosity, as shown by Wolfstein [273]

$$l_\varepsilon = c_l d_w \frac{Re_d}{Re_d + 5.3}, \tag{4.2}$$

where $c_l = 0.42C_\mu^{-3/4}$, d_w is the distance from the wall, and $Re_d = \frac{\sqrt{k}d_w}{\nu}$ is the wall-distance Reynolds number [229]. Therefore, in the viscous sublayer [72], turbulence dissipation rate is given as [229]

$$\varepsilon = \frac{k^{3/2}}{l_\varepsilon}. \tag{4.3}$$

To model the flow development and hence shear-stresses reasonably well next to the wall, one needs to integrate up to the viscous sublayer, i. e. $y+ < 5$, where $y+$ represents the dimensionless wall distance and is given as [220]

$$y^+ = \frac{d_w v_T}{\nu}, \tag{4.4}$$

where [220]

$$v_T = \sqrt{\tau_w/\rho_0} \tag{4.5}$$

is a reference flow velocity, also called friction velocity [220, 229] and $\tau_w = \rho_0 \left(\frac{d\bar{v}_{0,z}}{dy}\right)_{d_w=0}$ is the shear stress at the wall for $d_w = 0$ [220], if y is the direction normal to the wall and $\bar{v}_{0,z}$ is the mean flow velocity in the axial direction z.

For the EBRSM model, all $y+$ treatment of Star-CCM+® was adopted, meaning that depending on the mesh a low-$y+$ or high-$y+$ treatment may be chosen [220, 229]. A high-$y+$ treatment implies that a wall function is used if the near-wall cell is within the logarithmic region, while a low-$y+$ treatment implies that the near-wall cell lies in the viscous sublayer, preferably at $y+ < 1$ [229], and therefore the viscous sublayer is properly resolved [229].

The IDDES model is operated in Wall-Modeled LES mode (WMLES), where the solver runs in RANS mode only next to the wall and in the core region of the pipe LES mode is active owing to the turbulence content at the inlet boundary. For the RANS part of the computation k-ω SST (Shear-stress transport) model was utilized. For details on this model, readers are encouraged to refer to the work of Shur et al. [228].

The fluid flow RANS equations, as shown in Sec. 2.3, were solved with a segregated iterative flow solver with a SIMPLE (Semi-Implicit Method for Pressure Linked Equations) type of algorithm [199] until the steady-state convergence is achieved for each flow velocity. Re number of the flow is varied between 1000 and 500000. The segregated solver is set to perform 2000 iterations for each Re. In order to avoid numerical error due to spatial discretization, the mesh is kept constant for all flows and the size of the cells are computed based on the highest Re number considered for each set of simulation. The mesh consists of 5.4 Million cells and a part of it is shown in Fig. 4.4 on the xz middle plane section of the UTTF for $y = 0$.

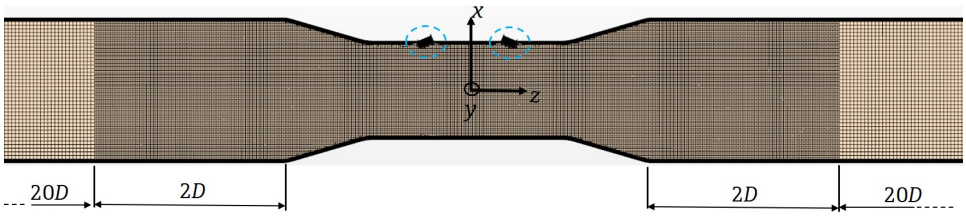

Figure 4.4: Mesh on the xz middle plane-section (y=0) of the Prosonic Flow E Heat UTTF.

The 'trimmed mesher', implemented in Star-CCM+® [229], consists predominantly of hexahedral elements in the core of the domain and of prisms near the walls. The element size is $D/80$ for the finest area, where the flowmeter is located, and $D/40$ for the coarser areas upstream and downstream of the flowmeter (Fig. 4.4). The wall $y+$ is below 1 for all the range of Re numbers. As shown in Fig. 4.4, the finest area of the mesh extends $2D$ upstream and downstream of the flowmeter. The dashed light blue circles indicate the cavity areas near the transducers. It should be noted that the transducers are not included in the CNA simulations. For both the reference case and the case where the asymmetric swirl generator is included, $22D$ of pipe length are simulated downstream of the DUT in order

to ensure a fully-developed flow profile at the 'Outlet', as explained in Sec. 3.1 [72]. The distance between the DUT and the 'Inlet' is $22D$, i.e. $2D$ and $20D$ of fine and coarse mesh, respectively. At the 'Inlet' a fully-developed profile is given as described in Sec. 3.1. For the reference case, the $20D$ of mesh are coarse with $D/40$ up to the 'Inlet' surface. However, in the case of the asymmetric swirl generator, its geometry is included at a distance upstream of the DUT (between the DUT and the 'Inlet'). More specifically, three upstream distances of the asymmetric swirl generator are investigated, i.e. $8D$, $10D$, and $12D$. These distances are defined in the same way as described in Subsec. 4.1.1. The mesh at the position of the asymmetric swirl generator is shown in Fig. 4.5. The coordinate system in Fig. 4.5(a) is not

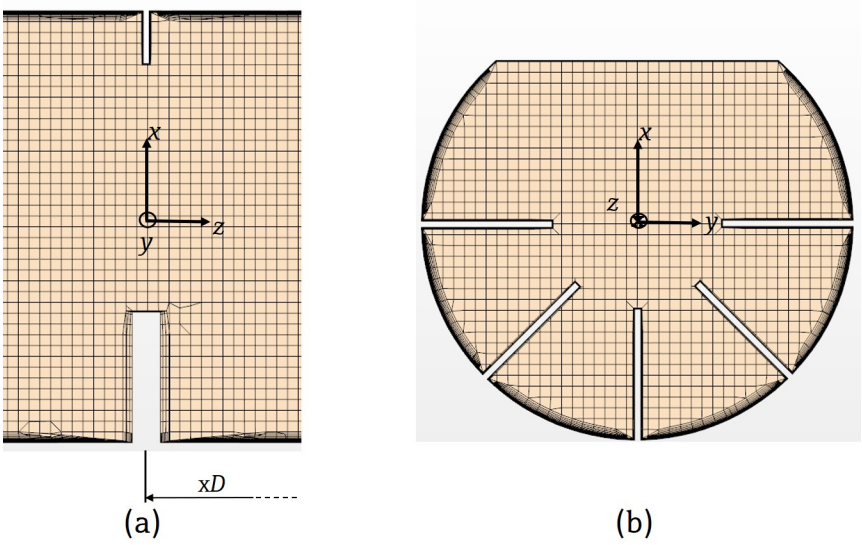

Figure 4.5: Mesh at the position of the asymmetric swirl generator. (a) Side view and (b) axial view.

representative of the origin but only of the directions. The distance xD from the DUT may vary among $8D$, $10D$, and $12D$ depending on the investigated case. In Fig. 4.5(b) the mesh on the middle plane section xy of the asymmetric swirl generator is shown.

For the IDDES as a scaled resolved simulation (SRS) [173, 267], unsteady flow equations need to be solved. For the time-integration, it is ensured that the convective Courant number ($CFL = (U dt_{sim})/dx_{sim}$) [72] is always kept below 1 or in other words, the numerical time-step dt_{sim} should be kept below dx_{sim}/U, where dx_{sim} is the cell size and U the local velocity in the cell. If this condition is not fulfilled, the turbulence is not well resolved regardless of the mesh size. For both temporal and spatial discretization, second order schemes were employed. Time-integration is performed and all flow quantities like velocity components and pressure are averaged for every time-step until the time-averaged flow field does not change in time. For this purpose, approximately 70000 time-steps were required. Owing to large computing time for the IDDES only four Re numbers were computed. The present case is solved on a HPC cluster using 160 cores, which takes about 42 hours for one flow rate for

the whole time-averaging. The time-averaged flow field is used to evaluate the performance of the flow meter.

The CNA method, described in Sec. 3.1, is employed for the calculation of the 'Volume Flow Error$_{\mathrm{CFD}}$ [%]' given by Eq. (3.14). The reference cross-section A_{ref} is located at the Inlet surface of the simulation and v_{ref} is the average axial flow velocity at the Inlet as given by Eq. (1.1).

In the deviation curve diagrams presented in this section, i.e. 'Volume Flow Error [%]' against 'Reynolds number', as a label on the y-axis is written in general 'Volume Flow Error [%]', since it refers to both measurements and simulations. However, the respective method and equations are used for the generation of each of the curves, i.e. eqs. (3.14) and (2.98) for the extraction of the simulation and measurement results, respectively.

4.1.3 Measurement and Simulation Results

4.1.3.1 Reference Straight Pipe

The reference case of a straight pipe (fully developed flow profile), without an asymmetric swirl generator, is measured and simulated with the RANS RKEPS model [227] to ensure that the simulations deliver results in agreement with the measurements, which are repeated three times for each volume flow. In Fig. 4.6 the measured and simulated results of the deviation curves for the reference case of a straight pipe are shown. The dashed blur line shows the theoretical transition between laminar and turbulent flow in a pipe for $Re = 2300$ [58, 61]. Especially for the clearly turbulent region, where $Re > 10000$, the measurements and

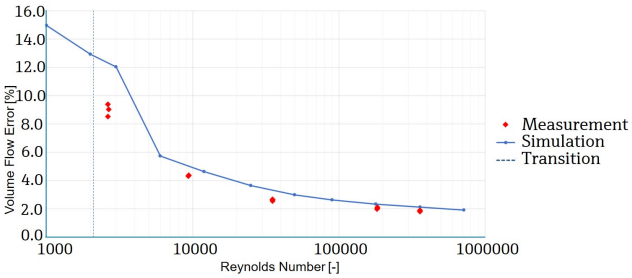

Figure 4.6: Deviation curve for the reference case of straight pipe. Measurements and simulations with the RKEPS model with the aim of estimating the difference between measurements and simulations for the reference case.

the simulations are in better agreement than the region of low Re numbers closer to the transition, i.e. $2300<Re<3000$. For the transition region between laminar and turbulent flow, all turbulent models have difficulties modeling the flow [72, 229]. There is quite a large discrepancy between the lowest measured $Re \simeq 2500$ and the simulation at $Re = 3000$. Transition from laminar to turbulent flow is not deterministic, as there is a nonlinear relation between the disturbance amplitude and the critical (transition) Re [186, 275]. More specifically, transition in pipe flows occurs more easily when higher turbulence fluctuations

are present [186, 275]. In the reference case of a straight pipe, the turbulence model predicts a flow more similar to the laminar for $Re = 3000$ because of low turbulence fluctuations prescribed at the Inlet in form of flow velocity v_0, k, and ε, in contrast to the measurements at Re $\simeq$ 2500, which typically have higher turbulence fluctuations. Therefore, the Volume Flow Error [%] for $Re = 3000$ in the simulations is closer to the results of a laminar case, despite the use of a turbulent model. If $Re = 3000$ is excluded, the maximum deviation for the Volume Flow Error [%] between the measurements and the simulations is <0.4 %. The reason for this discrepancy at Re>3,000, is the possible not exact reproduction of the flow field from the CFD simulation, as well as the CNA method itself, i.e.the absence of acoustic, structural mechanics, and piezoelectric simulations.

In Fig. 4.7, the normalized axial velocity field is shown, i.e. the component of flow velocity in the z direction, $v_z(x, y, z)$, normalized with v_{ref}. The contour is shown indicatively for $Re = 25{,}000$, for the reference case of the straight pipe in the middle plane section xz for $y = 0$. In the legend of Fig. 4.7 this quantity is indicated as '*Velocity_Normalized*'. The central cylindrical reflected sound path, taken into account for the calculation of $v_{0,CFD}$, as given by Eq. (3.10), is depicted in Fig. 4.7 as well. Because of the contraction of the device,

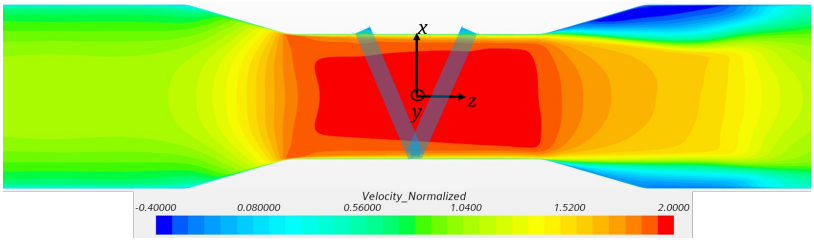

Figure 4.7: Axial velocity field, $v_z(x, y, z)$, in the middle plane section of the device xz, at y=0.

the flow is accelerated, and lower volume flows can be measured more precisely. Because of the flow acceleration, Δt between the upstream and the downstream signals get larger and limitations in resolution can be overcome especially for low flows.

In Fig. 4.7, one can observe an asymmetric flow-field in the contracted part of the flowmeter and downstream of it, owed to the cavities, which is the only geometrical asymmetry in the domain. Hence, even small cavities can create a flow asymmetry inside the flowmeter or downstream of it.

4.1.3.2 Asymmetric Swirl Generator

Measurements are performed with the asymmetric swirl generator mounted $12D$ upstream of the flowmeter and respectively simulations at distance $8D$, $10D$, and $12D$, with a radial orientation at 0^o. In order to gain some insight regarding the deviation curves, especially for the asymmetric swirl generator, the calculated flow field and flow profiles at specific axial z distances downstream of the asymmetric swirl generator are further examined, as shown in Fig. 4.8. It is to be noted that the sound path is parallel to the zx plane, as shown in Fig. 4.7. Especially for $3D$ downstream of the asymmetric swirl generator the flow profiles are still highly distorted for both the yz ($x = 0$) and zx planes, while the IDDES shows

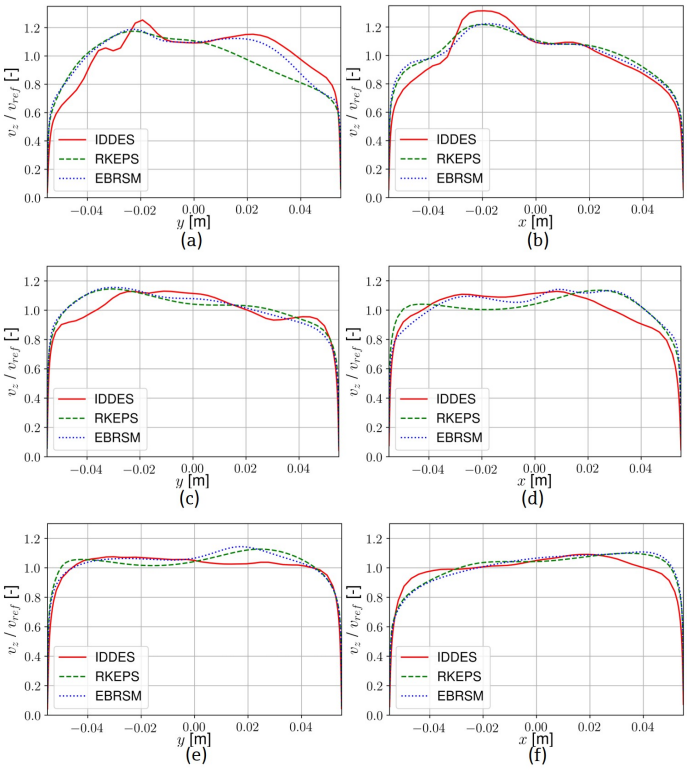

Figure 4.8: Flow profiles simulated with IDDES, RKEPS, and EBRSM models. Axial flow velocity, v_z, normalized with v_{ref}, as given by Eq. (1.1) at $z = 0$, at specific distances downstream of the asymmetric swirl generator, on a line on the yz and the zx planes. Distances downstream of the asymmetric swirl generator considered: (a) $3D$, on the yz plane (b) $3D$, on the zx plane (c) $6D$, on the yz plane (d) $6D$, on the zx plane (e) $10D$, on the yz plane (f) $10D$, on the zx plane.

a stronger distortion compared to the RANS models (RKEPS and EBRSM). It has to be highlighted that despite the difference of the flow profiles for the $3D$ distance, they present a good agreement towards the middle of the pipe ($x = 0$ m or $y = 0$ m). At $6D$ distance, for the flow profiles shown in Fig. 4.8(c),(d), the flow profile is less distorted than the $3D$ distance, shown in Fig. 4.8(a),(b), as expected, while the RANS models show a stronger asymmetry compared to the IDDES model. At $10D$ distance, for the flow profiles shown in Fig. 4.8(e),(f), the flow profile is further developed, and the asymmetries are smoothed out on both the yz and zx planes. The IDDES model shows that the flow profile is more developed and symmetric compared to the delayed flow development of the RANS models (in contrast to the $3D$ distance).

The flow profile in the meter-body of the flowmeter at z=0 and for a line on the yz and zx planes is shown in Fig. 4.9. The flowmeter is placed at a radial orientation of 0^o and $10D$ downstream of the asymmetric swirl generator, with the distance having been defined in subsecs. 4.1.1, 4.1.2 and in Fig. 4.5.. The IDDES, RKEPS and EBRSM are in

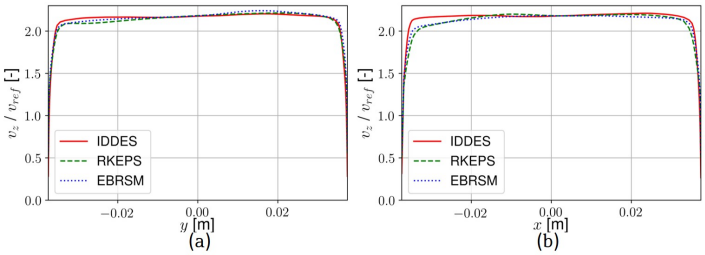

Figure 4.9: Flow profiles simulated with IDDES, RKEPS, and EBRSM models. Axial flow velocity, v_z, normalized with v_{ref}, as given by Eq. (1.1) at $z = 0$, inside the flowmeter. The flowmeter is placed $10D$ downstream of the asymmetric swirl generator at radial position 0^o. Results shown on a line on (a) the yz and (b) the zx plane.

agreement especially towards x=0 and y=0. Therefore, the question could arise: Is it necessary to simulate with the more time-intensive IDDES model for the demanding case of the asymmetric swirl generator? The answer is no, due to the agreement of the results between RANS and IDDES. The reader is referred to [196] for more results of the case and a detailed description. The RANS simulations are accurate enough to model the flow for this case. However, the answer to the question also depends on the level of accuracy that needs to be reached and the balance with the CPU time that can be invested [11, 173].

Concluding, for the scope of this work the observation of no need of transient CFD simulation is expanded to cases simpler from the flow point of view. Thus, cases of flowmeters with fully developed flow profiles defined at the 'Inlet' and with the inclusion of full CFD profile with the presence of vortices in the cavities, will be simulated with the RANS models, and more specifically with the RKEPS model.

Another useful parameter that gives more insight regarding the flow-field downstream of the asymmetric swirl generator is the swirl angle defined as $\theta = arctan\frac{v_T}{v_A}$ and shows the ratio between the tangential velocity component v_T and the axial velocity component $v_A \equiv v_z$ of the flow, as given in Subsec. 1.2. The swirl angle is shown for cross-sections at different distances downstream of the asymmetric flow disturber in fig 4.10. It is obvious that there is a strong swirl downstream of the asymmetric swirl generator and as it is also shown with measurements by Turiso et al. [251]. The swirl angle is gradually reduced for distances further downstream of the asymmetric swirl generator. In Fig. 4.10(c) the swirl angle is shown for a distance of $10D$, exactly at the entrance of the flowmeter. In Fig. 4.10(d) the swirl angle in the axial middle of the contracted part of the flowmeter is shown, i.e. z=0, when it is placed $10D$ downstream of the asymmetric flow disturber. The cross-section in Fig. 4.10(d) is smaller (D = 75 mm) compared to the cross-sections in figs. 4.10(a)–(c) (D = 110.3 mm) but for reasons of consistency it is depicted in the same size. The swirl is significantly reduced inside the flowmeter because of its contracted form. The reason is that inside the contraction, the axial component of the velocity is accelerated more compared to the tangential component.

The sensitivity of the device in terms of axial shift is measured and simulated, as it is often the case that the flowmeter is not placed exactly at the nominal downstream distance. The investigated radial orientation is 0^o. In Fig. 4.11, the measured deviation curve for

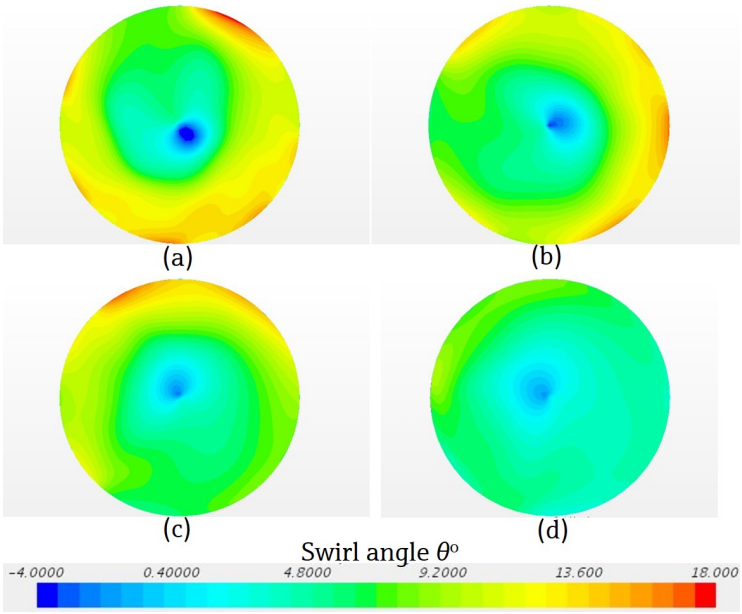

Figure 4.10: Swirl angle θ [^{o}] in cross-sections solved with the RKEPS model downstream of the asymmetric swirl generator at radial orientation 0^o for axial distance (a) $3D$, (b) $6D$, (c) $10D$, and (d) $10D + L_{body}/2 = 10D + 140.58$ mm, i.e. at z=0.

distance $12D$ and the simulated deviation curves for distance $8D, 10D$, and $12D$ downstream of the asymmetric swirl generator are shown. For the $12D$ distance, there is good agreement between measurements and simulations, as only one measurement point deviates compared to the $12D$ simulated case by <0.8 % in terms of Volume Flow Error [%].

Only simulations are made for the investigation of the effect of the axial shift and not measurements. Such investigations are easily set up numerically but not experimentally and this showcases the value of simulations. When the flowmeter is axially shifted at $10D$ distance, the deviation curve is slightly different, especially for the region of Re [20,000, 100,000]. When the flowmeter is shifted at $8D$ distance, the deviation curve is shifted to slightly higher values, with maximum %deviation <1.2 %. The reason for these slight shifts of the deviation curve is mainly the remaining rotation of the flow after the asymmetric flow disturber (Fig. 4.10). In contrast to the reference case (Fig. 4.6), there is a good agreement for the lowest measured Re between the measurements and the simulations. The flow remains turbulent, as the disturbance amplitude is higher downstream of the asymmetric flow disturber [186, 275]. Based on the simulations, it can be stated with confidence that the flowmeter is still robust regarding the axial shift of +/-$2D$, with max. %deviation <1.2 %, despite having only two transducers, due to its contracted part and the V-shaped reflect-mode sound path, which compensates for rotational flow effects [66].

Concluding, the CNA method is tested and compared with measurements for a reference straight pipe and an asymmetric swirl generator. Transient IDDES and steady simulations with the RKEPS and EBRSM turbulent models, as well as distances of the asymmetric swirl

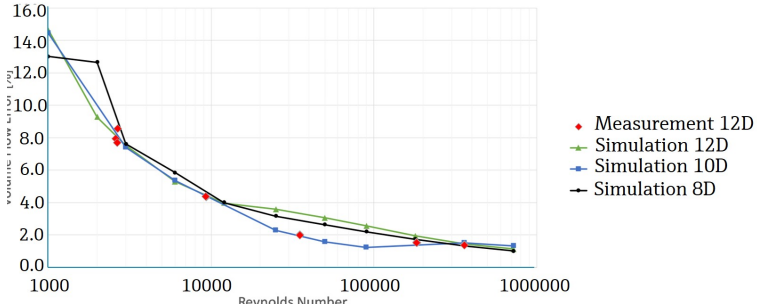

Figure 4.11: Deviation curve for the asymmetric flow disturber. Axial position investigation, measurements and simulations with the RKEPS model with the aim of quantifying the flowmeter's sensitivity in axial shifts.

generator are tested. The method provides realistic results, that represent only the flow part of the flowmeter. It is shown that steady simulations with the RKEPS model are suitable for the simulation of the flowmeter and therefore, no transient simulations are necessarily needed. This knowledge is important, as steady simulations are used as well to provide the flow part in the SimPAC^2 method, when instantaneous turbulence is not taken into account. The importance of the method lies on the capability to quantify the pure flow effects in an UTTF, as described in Sec. 3.1. In other words, the flow effect in an UTTF can be separately quantified, as only flow is considered. This effect may be compared with the results of the SimPAC^2, which considers piezoelectricity, structural acoustics and wave propagation in the moving fluid medium as well.

4.2 Piezoelectric Elements in Air in Zero Flow

The seemingly simple case of two piezoelectric elements opposite to each other in air in zero flow is used in order to verify or compare the FEM program, NACS, with already published measurements [277]. Although the setup seems simple, there are certain aspects, which are described in the present section, that pose difficulties to a highly-precise simulation of this case in time-domain.

4.2.1 Experimental Setup

The experimental setup of two piezoelectric elements in zero flow is shown in Fig. 4.12. The system consists of several modules that are schematically shown in Fig. 4.13

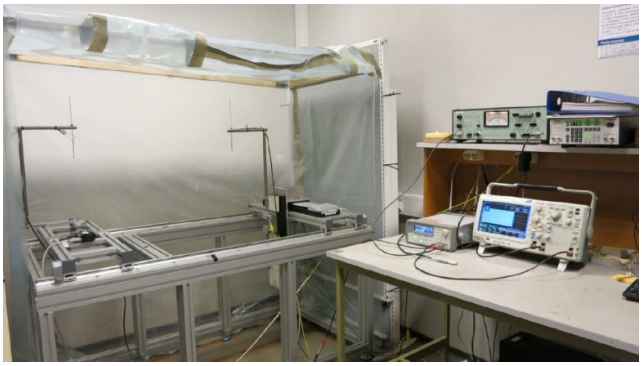

Figure 4.12: Experimental setup of the acoustic measurement with piezoelectric elements [277].

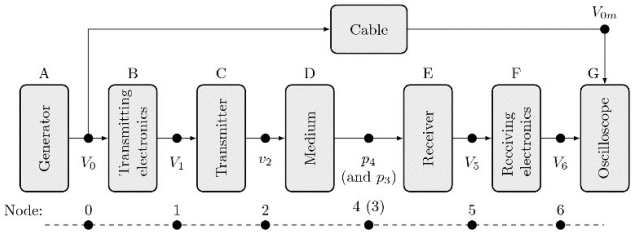

Figure 4.13: System with modules shown A-G and, connected at nodes 0-6 [277].

Module A represents the signal generator, which transmits the Voltage signal through coaxial cables (RG58) to the transmitting electronics, V_0, and to the oscilloscope, V_{0m} (m for measured). The signal generator is an Agilent 33220A with 50 Ω output electrical impedance and sends a continuous-wave tone burst at frequency f_c with constant burst length of 1.4 ms and 25 Hz repetition rate. Module B represents the transmitting electronics (here only a cable) that converts the signal V_0 to input, V_1 to module C representing the sending

transducer i.e. piezoelectric element, which converts voltage signal V_1 to acoustic particle velocity v_2 on the interface between the transmitter and the medium. Module D is the medium, here air, and p_4 is the axial free-field sound pressure at the center of the receiver front surface. Module E is the receiving transducer, here piezoelectric element that converts the acoustic pressure oscillations to voltage signal V_5. Module F represents the receiving electronics, consisted of an amplifier (Brüel & Kjær 2636), a frequency filter (Krohn-Hite 3940A), and two coaxial cables converting V_5 to V_6. Module G represents the oscilloscope (Textronic DPO3012) with a large input impedance. As described in detail by Øyerhamn et al. [277], both the sending and receiving piezoelectric disks are suspended from horizontal bars by electrical wires soldered onto the front and back electrodes, where the wires are fastening to a thin metal rod by heat shrink tubing. The wires are soldered to the electrodes using 5 minutes preheating of the elements to 150 ^{o}C, before using a soldering iron heated to 250 ^{o}C [277]. The wires and the described process are not taken account in the simulations. The interested reader is referred to Øyerhamn et al. [277] for a more detailed description of the experimental setup.

The measurements are made in air, in room temperature and atmospheric pressure. The air properties are $\rho = 1.21$ kg/m^3 and $c = 343$ m/s. The piezoelectric elements consist of PZ27 [31, 277], they are circular, with diameter $D_{p1} = 20.238$ mm and thickness $T_{p1} = 2.035$ mm for the transmitter and diameter $D_{p2} = 20.234$ mm and thickness $T_{p2} = 2.035$ mm for the receiver. The piezoelectric elements are positioned opposite to each other at a distance of 770 mm between their front surfaces. The piezoelectric disks are both grounded on their front surfaces, towards the medium between them. Their polarization axes coincide with the axial direction of the system. The polarization direction for both the sender and the receiver is towards the medium between them, i.e. opposite polarization directions for each disk. The impedance fitting in order to find the correct piezoelectric parameters has been carried out in a previous work by Knappskog [121] for a specific batch of piezoelectric disks and not the one investigated here. The material parameter fitting for the disks used here could improve the results, however a good agreement is already demonstrated between the measurements and finite element simulations by Øyerhamn et al. [277] The results of the simulations in the present thesis, are directly compared with the reference measurements and not the simulations in [277].

In the present work, more focus is given on the nodes 1 and 5, which represent direct input voltage on the transmitter, V_1, and output voltage from the receiver, V_5.

4.2.2 Simulation Setup

The described experimental setup is directly simulated with the aid of the FEM program, NACS, from node 1 to node 5. The simulation setup, schematically shown in Fig. 4.14, can be simulated as a 2D axisymmetric case, since the piezoelectric elements are circular and the fluid can be considered as a cylinder with absorbing BCs for avoidance of reflections. Depending on the simulation program used, one has to specify the respective absorbing boundary condition i.e., for NACS [183] or Star-CCM+® [229]. More information regarding the function of the absorbing BCs and their efficiency is given in Sec. 3.2, as well as in [30, 107, 229]. The piezoelectric parameters of the material of the piezoelectric disks are given in Table4.1 [121, 277].

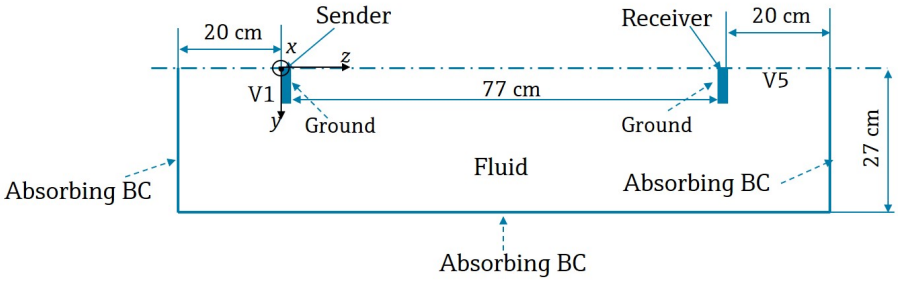

Figure 4.14: Schematic representation of the simulated case with domains of sender, receiver, and fluid of air. Dimensions and BCs included.

Parameter	Unit	Adjusted data set
c_{11}^E	10^{10} Pa	11.875(1+i/95.75)
c_{12}^E	10^{10} Pa	7.430(1+i/71.24)
c_{13}^E	10^{10} Pa	7.425(1+i/120.19)
c_{33}^E	10^{10} Pa	11.205(1+i/120.19)
c_{44}^E	10^{10} Pa	2.110(1+i/120.19)
e_{31}	C·m^{-2}	-5.40(1-i/166)
e_{33}	C·m^{-2}	16.0389(1-i/323.177)
e_{15}	C·m^{-2}	11.20(1-i/200)
ε_{11}^S	pFC·m^{-1}	8.110044(1-i/50)
ε_{33}^S	pFC·m^{-1}	8.14585(1-i/86.28)
ρ	kg·m^{-3}	7700

Table 4.1: Adjusted material data for Pz27 [121, 277].

In Fig. 4.15 the schematic fluid representation of the simulated case is shown, including the path of the shortest possible reflected sound path from an absorbing BC that can reach the receiver. Considering the dimensions of the fluid and the piezoelectric elements, the length of the shortest reflected path from an absorbing BC to reach the receiver is $l_{refl} = 917.839$ mm. When a speed of sound, $c = 343$ m/s is considered, the time needed for the reflections to impinge the receiver is $t_{short} = l_{refl}/c \simeq 2.676$ ms. This value is already relatively late in time, i.e. later than the zero-crossings of interest, in the way they were described in Sec. 2.5 and as it will be further clarified from the results in the present section. Therefore, the reflections do not affect the initial part of the received voltage of interest, V_5.

On the back-side of the sender a voltage signal V_1 is applied, as shown in Fig. 4.14, which travels through the fluid and is received on the body of the receiver in the form of mechanical vibrations that are converted to voltage signal V_5 due to the piezoelectric effect. The received voltage, V_5, is measured on the back-side of the receiver, as shown in Fig. 4.14. V_1 is the voltage between the nodes of the 'Transmitting electronics' and the 'Transmitter' (cf. 4.12), while V_5 is in this case the open-circuit voltage on the receiver. The front-sides of the sender and the receiver are grounded.

The very long distance of 77 cm between the piezoelectric elements poses difficulties to

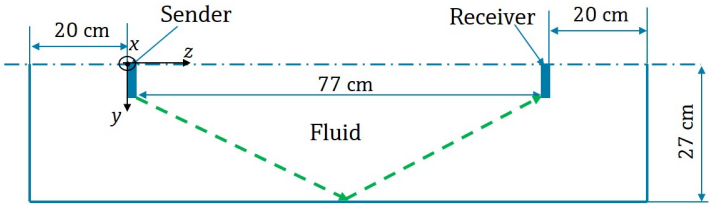

Figure 4.15: Schematic representation of the simulated case with the shortest possible reflected wave that can reach the receiver included.

a good agreement between the ToF of measurement and simulation with the FEM approach used here. The simulation method utilized by Øyerhamn et al. delivered highly accurate results, with deviation of 0.1 dB between the measurements and simulations [277]. In that method [277] a combination of FEM and transfer functions was used, with the benefit of saving computational demands. In the present work, an FEM approach is used containing the sender, the receiver, and the medium and thus, special attention is needed to compromise between accuracy and computational power.

A fine mesh and good time discretization are important to avoid numerical dissipation, ToF and overall signal errors. The fluid domain and the piezoelectric elements are meshed with a 2D quadrilateral, axisymmetric, linear, conformal mesh. A zoomed view of the meshed region of a piezoelectric element emerged in fluid is shown in Fig. 4.16. The piezoe-

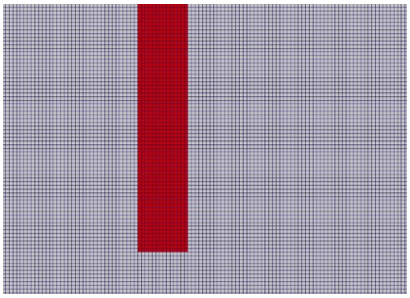

Figure 4.16: Zoomed view of the meshed region of a piezoelectric element, red domain, emerged in fluid, gray domain.

lectric element is depicted with red color and the fluid around it is depicted with light-gray color. The mesh shown in Fig. 4.16 consists of cells with edge-length of 0.15 mm. For a carrier frequency, f_c=112 kHz, the spatial resolution in air is $n_x \simeq 20$ elements/wavelength and in the piezoelectric material with the adjusted parameters [121] it is $n_{x1} = 116$ elements/wavelength for the shear waves with shorter wavelength compared to the longitudinal ones [5]. Convergence tests for the determination of the spatial and temporal resolution of the simulation are made in Sec. 4.2.3. Losses in the fluid are not considered, while losses in the piezoelectric materials are taken into account in the form of two Rayleigh parameters [30, 42, 107] with values a_M=5,000 and $\beta_k = 6.1 \cdot 10^{-9}$. More information regarding the determination of the Rayleigh damping parameters is given in Sec. 6.1.

4.2.3 FEM Simulations and Measurements

4.2.3.1 Long Input Signal

An input voltage signal V_1, shown in Fig. 4.17 is given as input to the sender for both the measurements [277] and the simulations, with a carrier frequency $f_c = 112$ kHz [277]. More specifically, as described by Øyerhamn et al. [277], a continuous-wave tone burst at

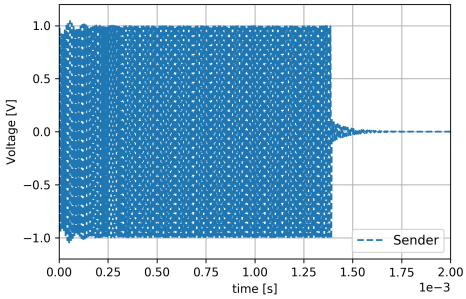

Figure 4.17: Input voltage V_1 for the measurements [277]. The same signal is replicated and given as input to the simulations.

frequency f_c with constant burst length of 1.4 ms and a 25 Hz repetition rate is generated by an Agilent 33220A waveform generator with a 50 Ω output electrical impedance and sent to the transmitting piezoelectric disk, with generator excitation voltages of 1 V [277]. Originally, amplitudes of 1 V and 10 V were used [277] but in the present work, only the 1 V amplitude voltage input signals are considered. Due to the described setup and voltage input, one observes in Fig. 4.17 the initial transition period of the voltage signal until $\simeq 0.2$ ms, the steady phase afterwards until 1.4 ms and the ringing of the signal after 1.4 ms. For more information on the equipment and the measurement details, the reader is referred to [277].

The described signal V_1 is given as an input to the simulations as well. The time-sampling for the measurement i.e., the time-intervals for which V_1 is recorded, is 20 ns. This value is much smaller compared to the simulations, where such a small time-sampling (or time-step) is not affordable. Furthermore, a coupling of time and space is usually present in simulations and therefore, the time-step is chosen in accordance with the spatial discretization or vice-versa, as it is already well-known [30, 72] and will be described further in the present section and through the presented results.

A convergence study is performed i.e., a number of simulations with different discretization in time and space. More specifically, 3 spatial resolutions are chosen, with the number of cells per wavelength as well as the time-steps per period being varied. In table 4.2 the different time and spatial resolutions used for the simulations of the convergence study are shown. n_t is the value of the time-steps per period $T = 1/f_c$ and n_x is the value of cells per wavelength in air for f_c. It should be highlighted that the values respect to the wavelength in air, which is more critical for the space resolution compared to the longer wavelength in

Case	n_t	n_x	Millions of cells
1b	21	15	6.53
1c	28	20	9.91
1d	35.5	25.5	15.5

Table 4.2: Convergence study simulations with different time and spatial resolutions, with air as a reference.

the solid. If such values refer to solid domain, it will be explicitly written. Moreover, it will refer to the shear wavelength due to Eq. (2.19), which implies that shear waves are shorter than the longitudinal ones. The values in table 4.2 refer to the carrier frequency, f_c=112 kHz. The present case is used as a base for comparison with measurements, as well as for detection of the optimum simulation settings i.e. n_t and n_x. For cases 1b -1d the ratio n_t/n_x is $\simeq$1.4.

A convergence criterion is set according to the accuracy needs of a typical 2-path inline gas flowmeter, such as the Proline Prosonic Flow G 300 [64]. To derive this convergence criterion, let us first define the %error for the speed of sound

$$\%error_c = \frac{c_{MS} - c}{c} \cdot 100\%, \tag{4.6}$$

where c is the real speed of sound and c_{MS} is the measured or simulated speed of sound for zero flow velocity. In the case of the Proline Prosonic Flow G 300 it should be satisfied $\%error_c \in [-0.2, 0.2]\%$ [64].

A suitable criterion, related to the flow measurement (cf. Eq. (2.91)) would be based on ToF and not the speed of sound. In the present thesis, Eq. (2.92) is used for the calculation of speed of sound for a specific path i. For zero flow velocity Eq. (2.92) gives $c_i = c_{MS} = L/t_{12}$ if it is assumed that $t_{12} = t_{21}$. The convergence test is conducted on the basis of only 1 path for zero flow velocity. Since length L is known, the accuracy needed for ToF, t_{12}, should be the same as for speed of sound, i.e. it should be in the range [-0.2,0.2] %. Therefore, the difference between t_{12} of two consecutively finer meshes should belong to [-0.2,0.2] % as well. Because of the simplicity of the criterion and in order to ensure that the accuracy demands of a typical respective flowmeter [64] are satisfied, the range of the criterion may have to be shortened, especially for the convergence study. The stringency of the criterion is set to one order higher for the convergence study, in other words

$$ToF_{crit} = \frac{t_{12,fine} - t_{12,coarse}}{t_{12,coarse}} \cdot 100\% \in [-0.02, 0.02]\ \%, \tag{4.7}$$

where $t_{12,fine}$ and $t_{12,coarse}$ are the ToF for a finer and a coarser mesh, respectively, for zero flow velocity. In the present study, the refinement of the meshes is successively increased from Case 1b to 1c to 1d, as shown in tab. 4.2. The subscripts 'fine' and 'coarse' may also refer to a time-step discretization.

In the present convergence study, only the first of the three zero-crossings presented in Subsec. 2.5 is used. In tab. 4.3 the downstream ToF, i.e. t_{12} and ToF_{crit} are shown for the

simulation cases 1b, 1c, and 1d. No ToF_{crit} can be set for Case 1b, since it is the case with

Case	ToF [s]	ToF_{crit} [%]
1b	2.27139e-3	-
1c	2.27111e-3	-0.0123
1d	2.27142e-3	0.0136

Table 4.3: ToF [s] and ToF_{crit} [%] for cases 1b-1d.

the coarsest mesh. One can observe that the $ToF_{crit} < 0.02$ % for both cases 1c and 1d and consequently, their utilization is possible for results' generation. The slightly higher value of ToF_{crit} of Case 1d compared to Case 1c should not be alarming, since the criterion is already overly satisfied.

The acoustic pressure field is shown for Case 1d in Fig. 4.18. In Fig. 4.18(a) the fluid near the sender is shown for t=11.556 μs and in Fig. 4.18(b) the fluid near the receiver for t=2.36024 ms. The arrows in the figures show the 'sender-to-receiver' direction, as a zoom is made near the piezoelectric elements, which are areas of higher interest.

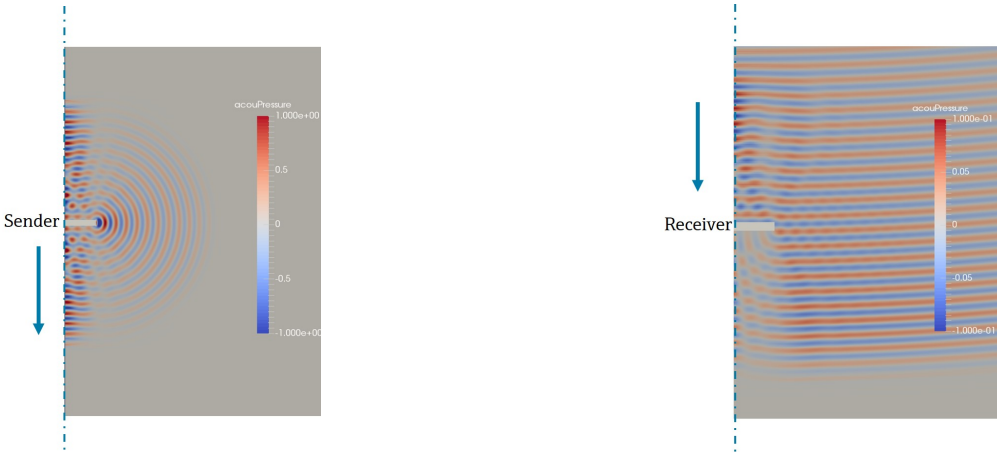

(a) (b)

Figure 4.18: Acoustic pressure field (a) near the sender for t=11.556 μs and (b) near the receiver for t=2.36024 ms. Input signal V_1 with f_c= 112 kHz.

For each of the cases of table 4.2 the recorded signal on the receiver, V_5, is shown in Fig. 4.19. The received signal, V_5, shown in Fig. 4.19 does not include the time-delays before node 1 and after node 5 (cf. Fig. 4.13) for neither the simulations nor the measurements and thus, the signals are directly comparable. In order to quantify the agreement between measurements [277] and simulations, the ToF among them is compared. Only the initial part of the received voltage signal V_5 signal is shown, since it is the signal of interest used in the evaluation of the UTTF in the present work. Moreover, computational time is saved by simulating only the initial part of the received voltage signal V_5. As clarified, the ToF for the present case is calculated by comparing the respective zero-crossings of the received

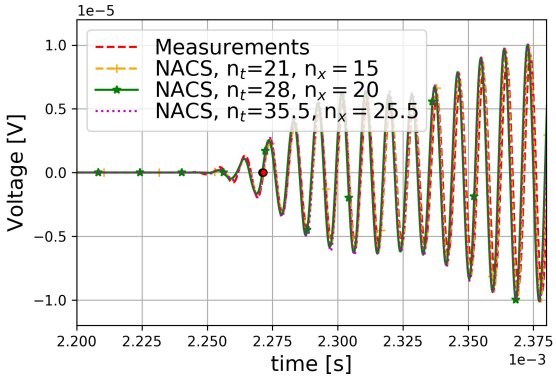

Figure 4.19: Received signal V_5 for measurements by Øyerhamn et al. [277] and simulations.

signal, shown in Fig. 4.19 with a small, red circle for the measurements [277] and a bigger, black circle for the simulations. The two circles almost coincide and are located on top of each other.

Another criterion is set in order to quantify the accuracy of the simulations compared with the measurements. The criterion $ToF_{crit,m}$ is introduced, i.e. the deviation of the measured ToF_{meas} values from the simulated ones, ToF_{sim} for the respective flow velocities. $ToF_{crit,m}$ is given by

$$ToF_{crit,m} = \frac{ToF_{sim} - ToF_{meas}}{ToF_{meas}} \cdot 100 \in [-0.2, 0.2]\%. \tag{4.8}$$

The range of [-0.2,0.2]% is set for the purpose of comparison of the simulations with measurements [277], according to the accuracy needs of a the flowmeter Prosonic Flow G 300 [64]. The values of $ToF_{crit,m}$ are shown in table 4.4. In tab. 4.4, it is shown that all cases are inside

Case	ToF [s]	$ToF_{crit,m}$ [%]
Measurement	2.27159e-3	-
1b	2.27139e-3	-0.00880
1c	2.27111e-3	-0.02113
1d	2.27142e-3	-0.00075

Table 4.4: ToF and deviation $ToF_{crit,m}$ among ToF for measurement and cases 1b-1d.

the specified range. Case 1c is 'worse' compared to case 1b although the latter is calculated with a coarser mesh. However, the criterion is already overly satisfied and therefore, the differences are not alarming.

Although a carrier frequency is given, in this case f_c=112 kHz, the overall signal contains a full spectrum of frequencies. Trying to resolve the very high frequencies would lead to a non-feasible simulation to perform, due to very fine meshes with high computational and

time demands. Therefore, the main focus has been, in the application of UTTF, to resolve the 'important' sending and receiving frequencies.

To examine the underlying input and output frequencies, a Fast-Fourier Transformation (FFT) is made in order to transform the input and output voltages, V_1 and V_5 from the time-domain into $V_1(f)$ and $V_5(f)$ in frequency-domain. More specifically, Welch's method [265] is used for the estimation of the spectral power density (SPD) in python with the scipy module [247]. The inverse of the selected time-step is taken as the sampling frequency. For cases 1b, 1c, and 1d, a number of 12000, 15000, and 18000 is taken respectively. A Hanning window is used with a length of 2046 for cases 1b and 1c and a length of 4096 for Case 1d. The overlap of the window is set to the half of its length. The square root of SPD is equivalent to the magnitude obtained from a FFT. In Fig. 4.20 the magnitude of the measured [277] and simulated input and output voltages, $|V_1(f)|$ and $|V_5(f)|$, over the frequency range [50-300] kHz are shown.

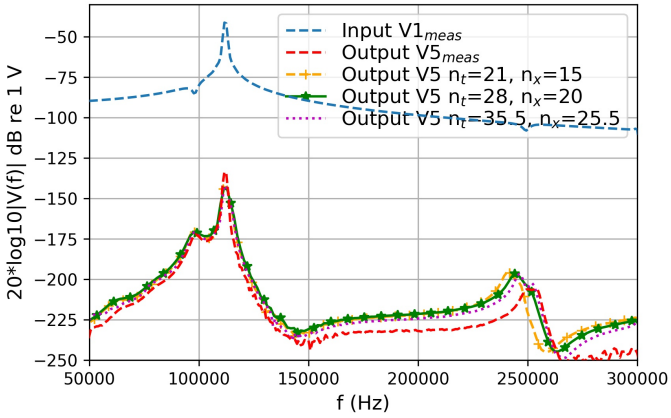

Figure 4.20: Magnitude of Input voltage $|V_1(f)|$ and of output voltage $|V_5(f)|$ in the frequency domain.

The input voltage, V_1 is the same for the measurements [277] and all simulations. One can observe, from the curve of the measured magnitude of input voltage [277], the peak of the carrier frequency f_c=112 kHz. The magnitude of the measured or simulated output voltage presents a pair of maxima in the 100 kHz range. More specifically, the two maxima located at $\simeq$ 98.2 kHz and $\simeq$ 112 kHz are related to the 1st and 2nd peaks of the lower radial mode, denoted R1, of the sender and the receiver respectively [277]. Two more peaks are observed near $\simeq$250 kHz related to the second radial mode, denoted R2. For the scope of this work, the R2 modes are of less interest, however, one can see that for higher n_x, the simulations are getting closer to the measurements' results. In order to sufficiently resolve the 250 kHz frequencies, a value of at least $n_x = 20$ with the respective n_t value should be chosen referred to the 250 kHz, which would require much finer discretization and computational time. Finally, n_x=20 referred to f_c=112 kHz is chosen, as shown in tab. 4.3, in order to satisfy the set convergence criterion.

The magnitude of the voltage-to-voltage transfer function,

$$|H_{15}^{VV}| = \frac{|V_5(f)|}{|V_1(f)|}, \tag{4.9}$$

describing the behavior of the system from node 1 to node 5 (cf. Fig. 4.13), is shown in Fig. 4.21 for cases 1b-1d in the frequency range of [50-300] kHz. The information conveyed

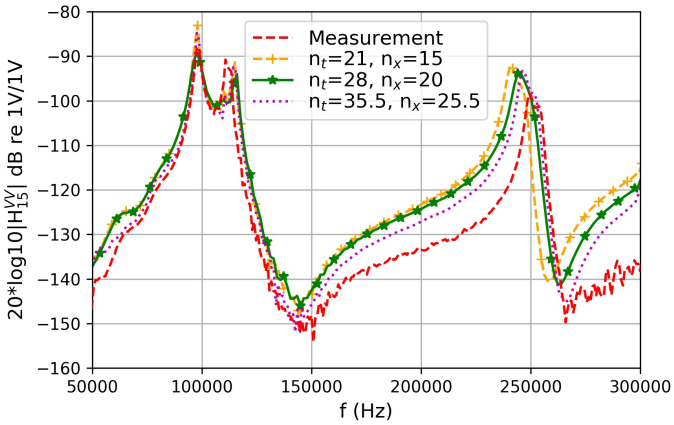

Figure 4.21: Voltage-to-voltage transfer function magnitude $|H_{15}^{VV}|$ describing the system from node 1 to node 5.

from Fig. 4.21 is similar to the one of Fig. 4.20. The peaks of the R1 mode at 98.2 kHz and 112 kHz and R2 mode at ≃250 kHz, related to the overall behavior of the system between node 1 and node 5 are observed. Furthermore, one can see that for higher n_x and n_t values, the simulations are closer to the measurements' results.

In order to further demonstrate the importance of the time and spatial discretization, as well as the coupling between them, cases 1c and 1d are more extensively investigated. The purpose of this study is the finding of the minimum spatial discretization, n_x, for which the ToF does not vary significantly when the temporal discretization, n_t, is varied i.e. the set criterion $ToF_{crit,m}\%$ is satisfied. Furthermore, an equally important goal of the study is the finding of an optimum ratio between n_t and n_x that minimizes the differences between measured and simulated ToF. More specifically, the n_x for each of the cases is kept constant and the n_t is varied. Ideally, there is no variation of the results in such an investigation. However, a compromise should be made for the investigated case, since a very fine temporal and spatial discretization would result into high computational demands. The investigated cases are shown in table 4.5. One can observe that the pairs of cases 1c-1d, 1ci-1di, 1cii-1dii have similar values of n_t/n_x, respectively. The aim is to further investigate the sensitivity of time-step variation for seemingly converged cases according to the set criteria of eqs. (4.7) and (4.8) when the ratio n_t/n_x is varied.

In Fig. 4.22 the received signal V_5 over time is shown for the cases presented in table 4.5.

Case	n_x	n_t	n_t/n_x
1c	20	28	1.40
1ci	20	25	1.25
1cii	20	22	1.10
1d	25.5	35.5	1.392
1di	25.5	31.8	1.247
1dii	25.5	27.9	1.094

Table 4.5: Further time-step investigation of cases with n_x=20 and n_x =25.5.

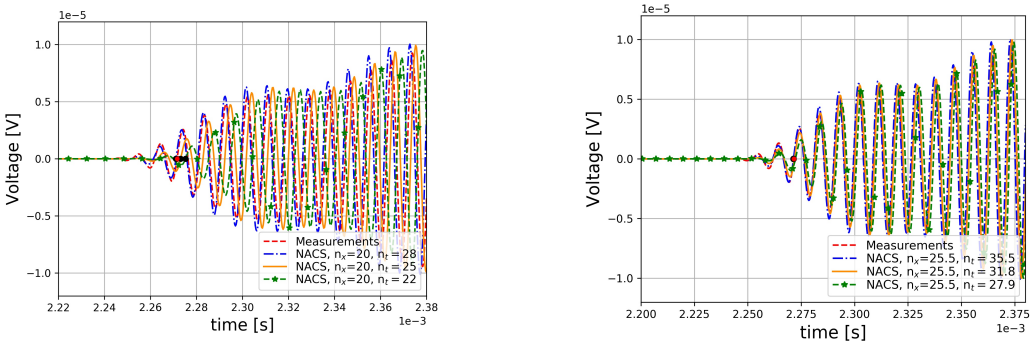

(a) (b)

Figure 4.22: Time-step investigation. Voltage on the receiver V_5 against time, with ToF depicted, for measurements [277] and simulations with NACS, with (a) n_x=20 and varying n_t and (b) n_x=25.5 and varying n_t.

In Fig. 4.22(a), V_5 is shown for the measurements [277], as well as for cases 1c, 1ci, 1cii, with the ToF depicted as a small, red circle for the measurements and as a bigger, black circle for the simulations. Similarly, V_5 and ToF are depicted in Fig. 4.22(b) for measurements [277] and the simulation cases 1d, 1di, 1dii. One can observe that the dependence of ToF on the n_t change is higher for the cases with n_x=20 (Fig. 4.22(a)) compared to the cases with n_x=25.5 (Fig. 4.22(b)), a clear indication that the cases with higher spatial discretization are better converged. Since the exact values of ToF are challenging to be observed in Fig. 4.22, their exact values, as well as $ToF_{crit,m}$ and ToF_{crit} are shown in tab. 4.6. The subscripts 'fine' and 'coarse' of ToF_{crit} (Eq. (4.7)) refer to the time-step in this investigation. Moreover, a dependence of the amplitude of V_5 on the time-step is observed, i.e. longer time-step results in a lower amplitude.

The deviation of ToF between measurements and simulations is shown in a more illustrative way in Fig. 4.23. From this figure, it is obvious that the dependence of ToF on the time-step is still present for n_x=20 but it tends to be weaker for the higher spatial discretization of n_x=25.5.

For n_x=20, the time-step dependence of wave propagation does not exceed the set criterion of Eq. (4.8), $ToF_{crit,m} \in [-0.2, 0.2]\%$ according to tab. 4.6, based on the investigated

Case	ToF [sec]	$ToF_{crit,m}$ [%]	ToF_{crit} [%]
Measurement	2.27159e-3	-	-
1c	2.27111e-3	-0.02113	-
1ci	2.27312e-3	0.06735	0.08850
1cii	2.27527e-3	0.16200	0.09458
1d	2.27142e-3	-0.00075	-
1di	2.27186e-3	0.01189	0.01937
1dii	2.27231e-3	0.03170	0.01981

Table 4.6: ToF for measurement [277] and simulations. $ToF_{crit,m}$ [%] and ToF_{crit} for cases 1c, 1ci, 1cii, 1d, 1di, and 1dii.

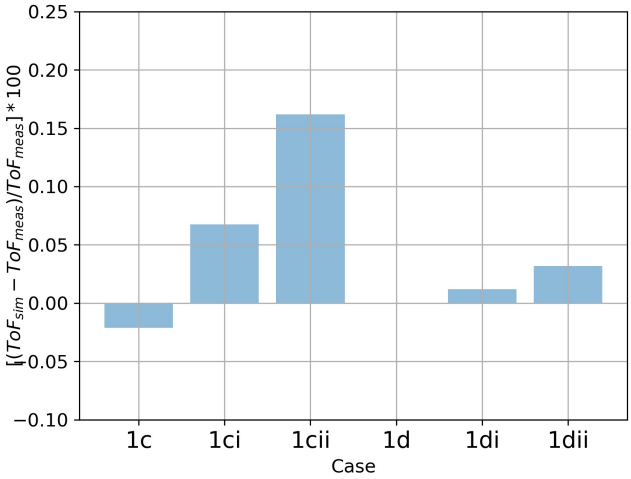

Figure 4.23: ToF deviation between measurements [277] and simulations for n_x=20 (cases 1c, 1ci, 1cii) and n_x=25.5 (cases 1d, 1di, 1dii) with varying time-step.

cases 1c, 1ci, and 1cii. However, the value of $ToF_{crit,m}$ is close to the limit for Case 1cii. It can further be concluded that for longer time-step, i.e. lower values of n_t, the wave tends to propagate slower. For $n_x = 25.5$, the time-step dependence of wave propagation does not exceed, as it is actually much lower than the set criterion of Eq. (4.8) according to tab. 4.6, based on the investigated cases 1d, 1di, and 1dii.

The set criterion of $ToF_{crit} \in [-0.02, 0.02]$ is exceeded for cases 1ci and 1cii, while it is in the acceptable range for cases 1di and 1dii. It should be reminded that ToF_{crit} is very strict, since the accuracy demands are 10 times higher compared to a typical UTTF application investigated in the present work [64]. Therefore, a case may still be used if it exceeds the strict criterion of ToF_{crit}, as long as the limitations are known and if certain precautions are taken, as follows.

Consequently, according to the presented time-step study, a pragmatic but also accurate enough approach, conforming to the set criteria of eqs. (4.7) and (4.8) may be followed. An

optimum value of the ratio n_t/n_x is set, which is located at the value for which Eq. (4.8) is minimized i.e. tends to zero. The trend of ToF is monotonic with the change of temporal discretization and weaker when the spatial discretization is increased. A linear interpolation between the ratios n_t/n_x {1.25,1.4} for cases 1c and 1ci gives an optimum value $(n_t/n_x)_{opt1} = 1.3642$, for which Eq. (4.8) becomes zero. For a linear interpolation between the ratios n_t/n_x {1.247,1.392}, based on the results of the case with n_x=25.5, the optimum value is similarly calculated as $(n_t/n_x)_{opt2} = 1.3834$. The two optima calculated would ideally be identical, however the choice of one or the other would have a very small effect on ToF compared to the set criterion of Eq. (4.8), according to the presented time-step study. Consequently, the choice of one of the two or of a value in between in the present work is acceptable. Meshes with at least n_x=20 are used in the present work, as long as n_t/n_x is close to the optimum value. The mesh settings are described for each case investigated in the following Secs. 4.2.3.2, and 4.3, as well as in chapters 5 and 6. A spatial discretization of n_x=20 is not ideal and not fully converged however, based on the convergence study made in the present chapter, the accuracy limitations are set and known.

The 1-dimensional Courant–Friedrichs–Lewy (CFL) number [51] for acoustics is defined as

$$CFL = c\frac{dt_{sim}}{dx_{sim}}, \tag{4.10}$$

where dt_{sim} is the time-step and dx_{sim} is the cell dimension. It can be shown that n_x/n_t is equivalent to CFL number, and therefore for $n_x = 20$ the optimum value is $CFL_{opt1} = (n_x/n_t)_{opt} = 1/1.3642 = 0.7330$, while for $n_x = 25.5$ the optimum value is $CFL_{opt2} = 1/1.3834 = 0.7229$. CFL_{opt1}=0.7330 is used for the simulation of the cases presented in the thesis with the NACS solver, unless stated otherwise.

4.2.3.2 Short Input Signal

To further investigate the case, a shorter input signal V_1 is given, which is more typical for UTTF. A sinusoidal input signal V_1 is given as an initial condition to the sender with frequency f_c=112 kHz and length of 4 periods.

$$V_1 = Asin(\omega t), \quad t \leq 4T, \tag{4.11}$$

where $\omega = 2\pi f_c$ and $T = 1/f_c$, $A = 1$ V is the amplitude. The resulting transfer function of the system should be similar to the case of the longer input signal (Fig. 4.17), while the ToF should theoretically be identical.

The received signal V_5 is shown for the measured case with the long input signal [277] and the simulated case with the short input signal in Fig. 4.24. The simulated V_5 has a different form compared to the measurements, because of the different input voltage signal V_1 given in the case of the measurements (cf. Fig. 4.17) and the present simulation (cf. Eq. (4.11)). There is an agreement of hte two received signals until ≅2.32 ms and afterwards the simulated V_5 is 'ringing out' and not rising further as in the case of measurements. The reason for this 'ringing out' is the short input voltage signal V_1 of length $4T$. A band of frequencies is excited that rings out faster than the measurements where the receiver is forced to vibrate longer due to the long input voltage signal.

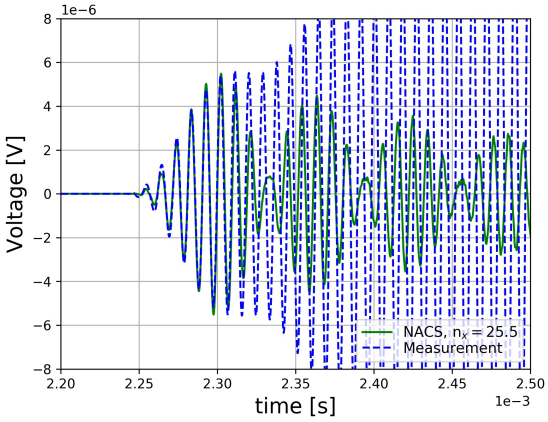

Figure 4.24: Received signal V_5 for measured case with long input signal V_1 and simulated case with short input signal V_1

The first of the three zero-crossings is used for the estimation of ToF, as presented in Subsec. 2.5, and in the same way as utilized Subsec. 4.2.3.1 The calculated deviation is $[(ToF_{sim} - ToF_{meas})/ToF_{meas}] \cdot 100\% = -0.00748\%$, which is highly acceptable based on the set criterion of Eq. (4.8).

Similarly to the already investigated case with the long input signal, a FFT is made in order to obtain $V_1(f), V_5(f)$ and the transfer function H_{15}^{VV}. The magnitudes $|V_1(f)|, |V_5(f)|$, $|H_{15}^{VV}|$ are shown in Fig. 4.25.

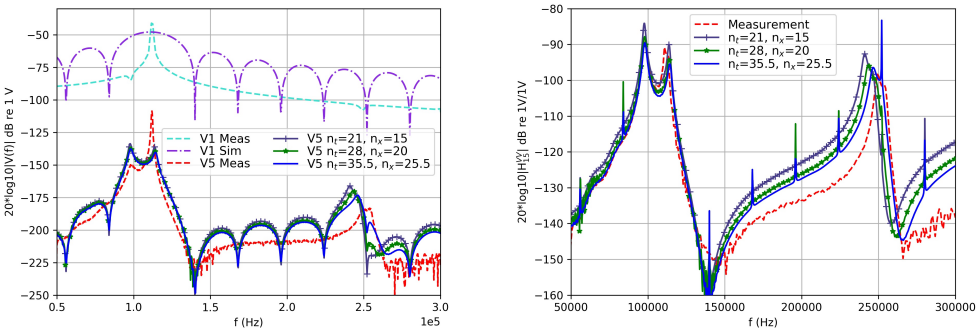

(a) (b)

Figure 4.25: Measurements [277] and simulations. (a) $|V_1(f)|$ and $|V_5(f)|$ and (b) $|H_{15}^{VV}|$.

The FFT magnitude of the short input signal, $|V_1(f)|$, presents, as expected, differences compared to the long input signal. Since the sender is only excited in the transient phase with the short input signal, it does not reach the steady phase and a broader range of frequencies

is excited. Therefore, 'bands' and 'deeps' are present in $|V_1(f)|$, which are not present when a long input signal is given (cf. Fig. 4.20). Due to the short input signal V_1, the value of $|V_5(f)|$ also differs and presents similar bands and deeps as $|V_1(f)|$. An interesting aspect is that the first peak of the R1 mode for $V_5(f)$ at $\simeq 98$ kHz is more pronounced in the case of the short input signal compared to the long input signal, if someone compares figs. 4.20 and 4.25(a). The reason is again that the sender is excited more in its natural R1 mode $\simeq 98$ kHz and is less forced to vibrate at the steady phase at 112 kHz, as for the case of the long input signal.

As expected, the transfer function H_{15}^{VV} remains mostly unchanged, independent of the input signal, while it gets closer to the measurements when the time and spatial discretization are increased. No specific criterion is set for the agreement of the transfer functions, since the purpose is to qualitatively identify the reason for the discrepancies in the time-domain. The peaks appearing in the transfer function are related with the FFT used, i.e. Welch transformation [265], which is consistent with the transformation used in Subsec. 4.2.3.1, however not fine enough in order to highly resolve the abrupt deeps in $V_1(f)$ and $V_5(f)$.

4.3 Piezoelectric Elements in Uniform Flow

Two piezoelectric elements opposite to each other, at 150 mm distance between them, are simulated with NACS and SimPAC^2. The solver of NACS, for which convergence and verification studies were conducuted and comparisons with measurements [277] (cf. Sec. 4.2) is used for the comparison with SimPAC^2. For this case, simulations with uniform flow velocity field are introduced. A case with shorter distance between the piezoelectric elements (150 mm) compared to Case 1 is used for convenience, as it demands lower computational resources. Moreover, the distance of 150 mm is closer to the UTTF simulatted in the present work.

4.3.1 Simulation Setup

4.3.1.1 NACS - FEM Simulation Tool

The setup of the simulated case, denoted from now on in the text as Case 2, is shown in Fig. 4.26. The general setup of the simulation and the BCs applied are the same as for

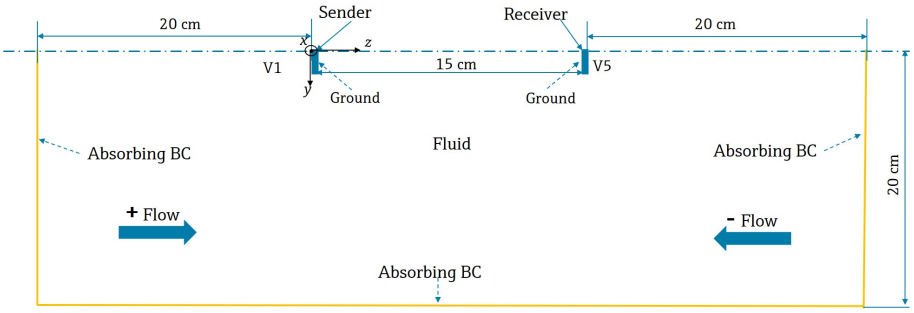

Figure 4.26: Schematic representation of the simulated 'Case 2' with NACS. Domains fluid (air), sender and receiver depicted. Dimensions and BCs are also included.

Case 1 , described in Subsec. 4.2. The fluid is air in room temperature and atmospheric pressure, while the sender and the receiver are identical as the ones described in Subsec. 4.2 as well. It is reminded that the density of air is ρ=1.21 kg/m^3 and the speed of sound c=343 m/s. The dimensions of the sender and the receiver are given at the end of Sec. 4.2.1 and the parameters of the material PZ27 in Table 4.1. The notable difference is the distance between the piezoelectric elements, which is 15 cm instead of 77 cm of Case 1. The width of the domain is 20 cm, instead of 27cm used in Case 1. The reason for the narrower domain of Case 2 is the shorter distance between the sender and the receiver compared to Case 1, meaning that a similar investigation, as the one described in Fig. 4.15, easily shows that the width of 20 cm is long enough for the avoidance of reflections. The distances behind the sender and the receiver are 20 cm for the NACS setup, the same as for Case 1. The most important difference compared to Case 1 is the inclusion of uniform flow. The positive and

negative flow directions are indicated in Fig. 4.26. The piezoelectric elements do not affect the flow-field, for which a constant value is set in all the finite elements of the fluid domain.

A sinusoidal input signal V_1 is given as an initial condition to the sender with frequency f_c=112 kHz and length of 4 periods (Eq. (4.11)). For the simulation with NACS, an axisymmetric 2D mesh is used with $n_x = 20$ and $n_t = 28$ with respect to the fluid (air). The size of the elements is the same for the fluid, the sender, and the receiver. The cells of the mesh are 2D, quadrilateral, depicted in Fig. 4.16. For the reasons described in Subsec. 4.2.3 after the conducted convergence studies, the mesh with n_x=20 and a time-discretization of $n_t = 28$ is utilized. The mesh comprises $\simeq$ 4 Mcells in total.

4.3.1.2 SimPAC^2

The acoustic solver of Star-CCM+®is currently not developed for 2D axisymmetric cases [229] and therefore a 3D simulation is performed instead, which demands more computational power. It should be mentioned, this is one of the reasons for choosing Case 2 to compare SimPAC^2 with NACS and not Case 1 with 77 cm distance between the piezoelectric elements. The sender and the receiver, as well as their material data are the same as in Subsec. 4.3.1.1, which in turn are the same as for Case 1 in Sec. 4.2. In order to reduce computational demands, a quarter of a cylindrical domain is simulated and symmetry is applied. In Fig. 4.27 the simulated domains are shown schematically, with the BCs indicated, as well as the dimensions of the domains. The sender and receiver regions are shown in Fig. 4.27, while

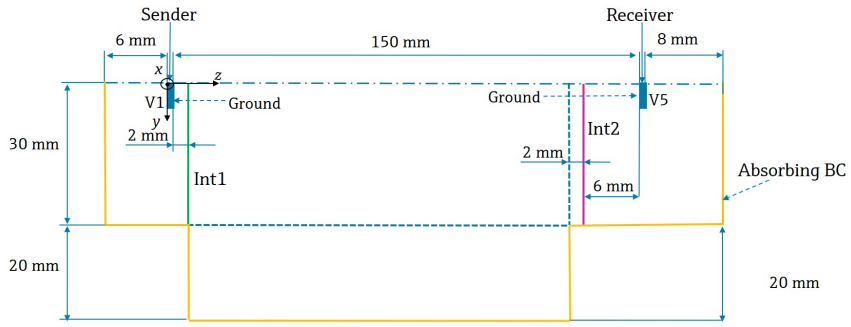

Figure 4.27: Case 2: Simulated geometry with SimPAC^2.

the rest of the domain enclosed in the orange continuous lines represents fluid (air). The division in parts, in the same way as demonstrated in Sec. 3.2 is described further in the present subsection. The dimensions are chosen in a way to avoid reflections, as indicated in Subsec. 4.3.1.1 as well, having in mind the computational time and resources. Int1 and Int2 are shown with continuous green and plum lines, respectively. The operation of Int1 and Int2 is described in Sec. 3.2 through an example of a flowmeter, while it is further explained in the present section for case 2. On the interfaces between the fluid bodies, indicated with blue dashed lines, there is continuity of acoustic pressure, since all the fluid domains consist of air. The division of the geometry is made due to the need of the SimPAC^2 method, in which the fluid domain is divided, as described in Sec. 3.2.

The BCs considerations are the same as for the NACS setup in Subsec. 4.3.1.1. The division in Parts (I), (II), and (III) of the simulation, as generally defined and explained through a flowmeter example in Sec. 3.2.1, is shown in Fig. 4.28. Furthermore, Int1 is shown in both parts (I) and (II), while Int2 is shown in both parts (II) and (III). The operation of Int1 and Int2 is likewise already defined in secs. 3.2.2, 3.2.3, and 3.2.4. The origin of the coordinate system (x, y, z)=(0,0,0) is located in the center of the sender radially and on its back side, as shown in Fig. 4.27. If it is shown in a different place in other figures for Case 2, it only indicates the directions x, y, z, while its origin is still in the center of the sender. According to the coordinate system and due to the fact that one quarter of the domain is simulated, symmetry is defined on planes xz for $y = 0$, and yz for $x = 0$ in terms of acoustic pressure, (cf. Eq. (3.23) in the x-direction and respectively in the y-direction i.e., $\frac{\partial p'}{\partial y} = 0$).

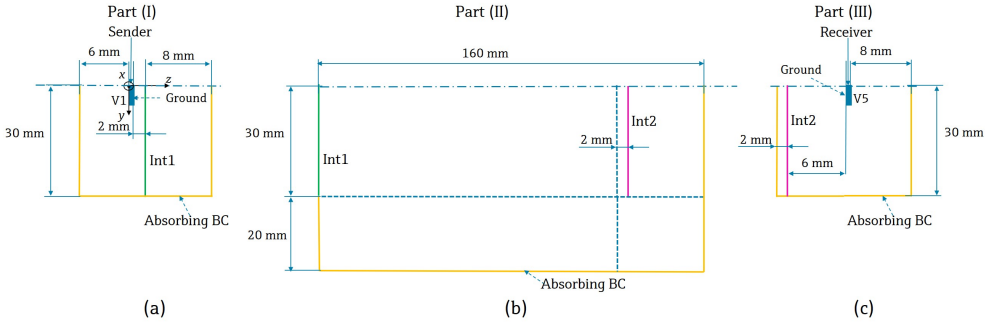

Figure 4.28: Case 2: Simulated geometry with SimPAC^2 divided into parts, geometrical considerations, and BCs. (a) Part (I): sender with portion of fluid simulated in NACS, (b) Part (II): fluid simulated in Star-CCM+®, and (c) Part (III): receiver with a portion of fluid.

One can see in Fig. 4.28 that the dimensions of the fluid domain are smaller compared to the NACS setup (cf. Fig. 4.26), because of the 3D nature of the simulation with SimPAC^2 and the need to save computational power. For parts (I) and (III), which are simulated with NACS [183], a quarter of a cylinder of 30 mm radial dimension is considered, since the needs of the FEM solver in terms of memory are high. As it will be shown through the comparison of SimPAC^2 with NACS, this dimension should be sufficient for part (I), simulated with NACS [183]. Absorbing BCs are applied on the outer surfaces of the fluid, indicated with orange continuous lines in Fig. 4.28(a). Correspondingly, this should also be sufficient for part (III), simulated with NACS [183], when the superposition BC [30], described in Subsec. 3.2.4 and schematically shown in Fig. 3.21, is applied on Int2 for a relatively short time and with absorbing BCs for the outer surfaces of the fluid, as shown in Fig. 4.28(c). For part (II), the radial dimension is 50 mm for the, as much as possible, avoidance of reflections. The waves need to travel for a longer time compared to parts (I) and (III) and therefore, spread more in the radial direction. A simple investigation similar to the one depicted in Fig. 4.15 shows that the width of 50 mm is sufficient. The total length of part (II), simulated with Star-CCM+® [235], is 160 mm, with the receiver being replaced by fluid to avoid artificial reflections being recorded on Int2. On the outer surfaces of the fluid, absorbing BCs are set, indicated with orange continuous lines in Fig. 4.28(b).

The mesh generated for parts (I), (II), and (III) is shown in Fig. 4.29. The mesh of each

(a) (b) (c)

Figure 4.29: Case 2: Mesh generated for the SimPAC^2 method. (a) Part (a), zoomed view near the sending piezoelectric element, (b) fluid, and (c) part (c), zoomed view near the receiving piezoelectric element.

of parts (I) and (III) consists of $\simeq$ 15 million tetrahedral, linear cells. A zoomed view of the mesh of parts (I) and (III) is shown in figs. 4.29(a) and 4.29(c), respectively. The piezoelectric element of the sender is shown with brown color in Fig. 4.29(a) and of the receiver with green color in Fig. 4.29(c). The mesh of part (II) is Cartesian and consists of $\simeq$ 110 Mcells. All meshes for the SimPAC^2 method are generated with Star-CCM+®. The time-step used for all parts is $dt_{sim} = 2.7 \cdot 10^{-7}$ s, which results to $n_t = 33$ for $f_c = 112$ kHz. For parts (I) and (III) simulated with NACS, the tetrahedral cells' edge dimensions are $\simeq$0.125 mm resulting to n_x =24.5 for air and $f_c = 112$ kHz as well. Therefore, n_t/n_x =1.375, which is very close to the optimum value defined in 4.2. For part (II) simulated with Star-CCM+® a value of $n_x = 24.5$ is chosen as well. No systematic convergence study is documented in the thesis for the solver of Star-CCM+® however, the spatial and temporal discretizations were chosen according to the guidelines of the documentation of Star-CCM+® [229]. Furthermore, if an agreement is achieved between NACS and SimPAC^2 inside the set criterion of Eq. (4.8) it will be the proof of well chosen settings for Star-CCM+®.

4.3.2 Comparison between NACS and SimPAC^2

Results are presented in this Subsec. for the described Case 2 with NACS and SimPAC^2 and their agreement is quantified. Initially, the acoustic pressure in the fluid domain and the voltage signal on the receiver obtained with NACS are presented. Afterwards, an investigation regarding the accuracy of the interface Int1 used in SimPAC^2 takes place. Finally, the received voltage signals over time, the ToF and the %deviation obtained with NACS and SimPAC^2 are compared.

4.3.2.1 NACS

In Fig. 4.30 the acoustic pressure field is shown for uniform ambient flow velocities $v_0 = [-20, 0, 20]$ m/s for t = 0.39636 ms. The piezoelectric element operating in $f_c = 112$ kHz (radial mode R1), radiates in all directions, however the acoustic pressure field in the main lobe is much stronger compared to the secondary lobes. One can observe that when the acoustic waves propagate opposite to the flow ($v_0 = -20$ m/s) they are decelerated (Fig. 4.30(a)) compared to the waves traveling in quiescent medium (Fig. 4.30(b)), while they are accelerated for uniform ambient flow in the direction of the propagation (Fig. 4.30(c)).

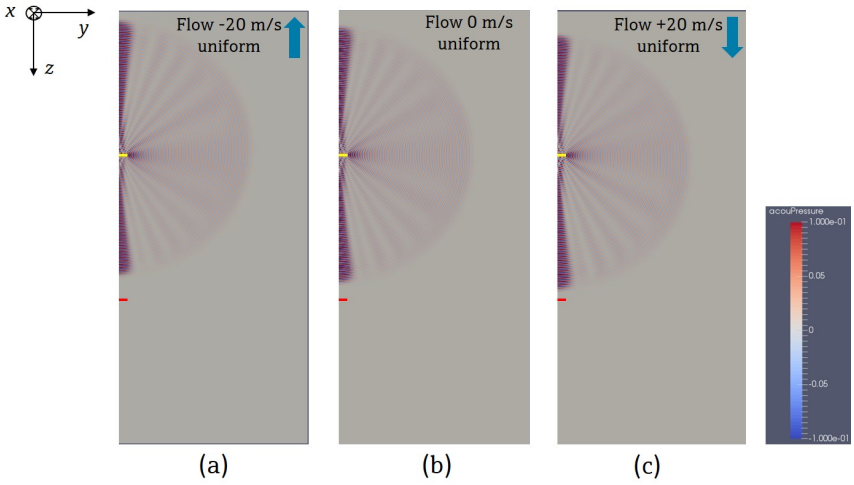

Figure 4.30: Acoustic pressure field solved with NACS, for t= 0.39636 ms, uniform flow velocity in the axial direction (a) $v_0 = -20$ m/s opposite to the direction of the acoustic propagation and (b) $v_0 = 0$ m/s, and (c) $v_0 = 20$ m/s in the direction of the acoustic propagation.

The received signal V_5 is obtained with NACS and it is shown in Fig. 4.31 indicatively for the same fluid velocities as the ones shown in Fig.4.30 (v_0=[-20,0,20] m/s).

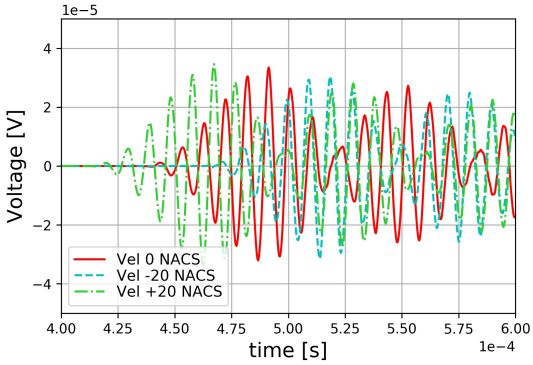

Figure 4.31: Voltage on the receiver V_5 against time, solved with NACS, for uniform flow velocity v_0=[-20,0,20] m/s

It can be observed that obviously also in terms of V_5 the received signal arrives later when the acoustic waves propagate opposite to the ambient flow ($v_0 = -20$ m/s) compared to the signal for quiescent medium ($v_0 = 0$ m/s), while it arrives earlier when the waves propagate in the flow direction ($v_0 = 20$ m/s). Moreover, a 'ringing' of V_5 is observed as the receiver does not achieve a steady state and therefore two frequencies dominate (the R1

sending and receiving radial modes at $\simeq$ 98.2 kHz and 112 kHz respectively). Quantifiable results and the effect of flow on wave propagation are presented in Subsec. 4.3.2.3, where a comparison is shown between the results of NACS and SimPAC^2.

With a FFT, the frequency spectrum of the received signals V_5 is shown for the flow velocities v_0=[-20,0,20] m/s in Fig. 4.32. The magnitude of the received signals $|V_5(f)|$ is

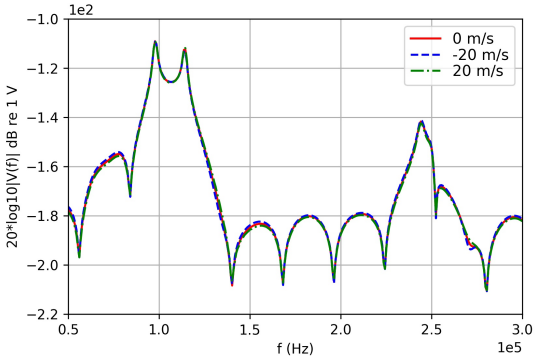

Figure 4.32: Magnitude of output voltage $|V_5(f)|$ in the frequency domain, solved with NACS, for uniform flow velocity v_0={-20,0,20} m/s.

almost identical for the different flow velocities, especially at the areas around the two peaks of R1 mode. However, for the rest of the frequencies, differences are present; the -20 m/s case shows higher amplitude compared to the 0 m/s case, which in turn shows higher amplitude compared to the 20 m/s case. These small differences of amplitude are the result of the interaction of the flow field with the acoustic propagation, since the flow velocity is the only different parameter among the simulated cases i.e., {-20, 0, 20} m/s.

4.3.2.2 SimPAC^2

In order to ensure the validity of the SimPAC^2 method, the error, which is introduced due to the interface Int1, has to be quantified. Int1 belongs to both Part (I) and Part(II) of the simulation. The mesh used on the surface of Int1 for part (I) is shown in Fig. 4.33. In Fig. 4.33(a) the mesh on the whole Int1 of part (I) is shown, while on Fig. 4.33(b) a zoom of the mesh is shown in order to give a detailed view of the tetrahedral finite elements.

Similarly, the mesh used on the surface of Int1 for part (II) is shown in Fig. 4.34. In Fig. 4.34(a) the mesh on the whole Int1 of part(II) is shown, while on Fig. 4.34(b) a zoom of the mesh is shown in order to give a detailed view of the tetrahedral finite elements.

The mesh for Int1 belonging to part (I) is linear tetrahedral [107], as described in Subsec. 4.3.1.1, while it is Cartesian [229] for Int1 belonging to part (II), as described in Subsec. 4.3.1.2.

The acoustic pressure is shown on Int1 in Fig. 4.35 at a random time-step at t=54.27 msec. A visual inspection of the two contours can only give a qualitative comparison of the acoustic pressure on Int1. The acoustic pressure on Int1 of part (I) is calculated on the nodes of

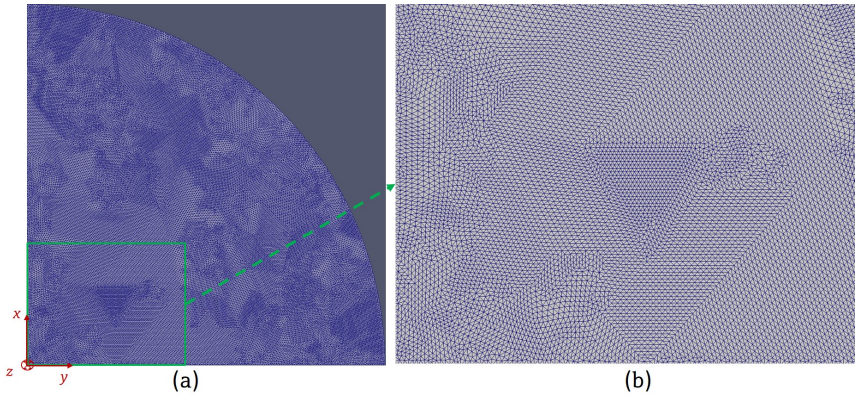

Figure 4.33: Mesh on Int1 for part (I): (a) On the whole Int1 with a designated green area and (b) on a zoomed view of the green area of Int1.

the tetrahedral elements [107, 183], however on Int1 of part (II) the acoustic pressure is calculated on the center of each tetrahedral element [229]. Therefore, it is not possible to directly compare the values of acoustic pressure between the nodes of the elements of Int1 of part (I) and the centers of the elements of Int1 of part (II), since they are not positioned on exactly the same coordinates. It is reminded that the acoustic pressure is mapped from the nodes of the elements of the tetrahedral mesh to the centers of the elements of the Cartesian mesh with the nearest neighbor technique [29], as mentioned in Subsec. 3.2.3.

In order to provide a quantification of the accuracy, the spatially averaged value of the acoustic pressure on Int1, at a random time t=54.27 is calculated for both part (I) and part (II). The spatially averaged acoustic pressure on Int1 for part (I), $p'_{Int1,nodes}$ and for part (II), $p'_{Int1,centers}$, is calculated on the nodes of the tetrahedral elements (FEM) and the centers of the Cartesian elements (FVM), respectively. For the calculation, the program ParaView [119] is employed. More specifically, the generated csv file with the information of the coordinates of either the nodes or the centers is loaded in ParaView [119]. A 'Table To Points' tool of ParaView [119, 120] is used in order to visualize the values of acoustic pressure on either the nodes or the centers. As a next step, a 'Delauny 2D' tool of ParaView [119, 120] is used in order to visualize the acoustic pressure on Int1 as contours, in the way shown in Fig. 4.35. Finally, the 'Integrate Variables' tool of ParaView [119, 120] is used in order to calculate the surface average acoustic pressure over the surface of the interface Int1.

The calculated averaged acoustic pressures at t=54.27 msec are

$$p'_{Int1,nodes} = -3.35631 \cdot 10^{-5} \text{ Pa},$$

$$p'_{Int1,centers} = -3.35487 \cdot 10^{-5} \text{ Pa}$$

The deviation between the two calculated spatially averaged acoustic pressures on Int1 at

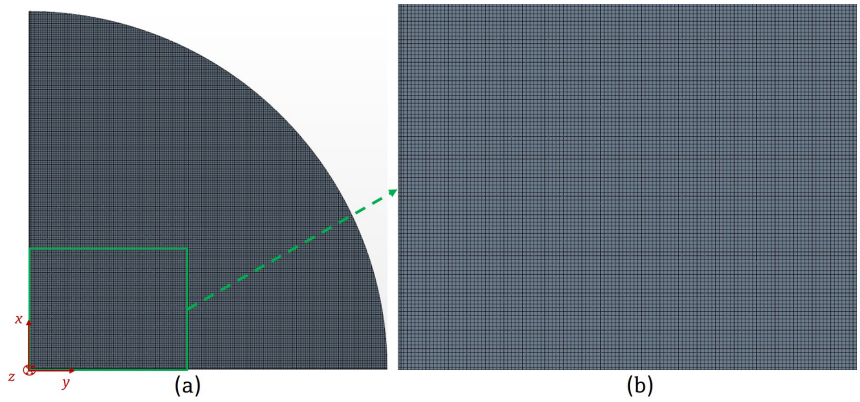

Figure 4.34: Mesh on Int1 for part (II): (a) On the whole Int1 with a designated green area and (b) on a zoomed view of the green area of Int1.

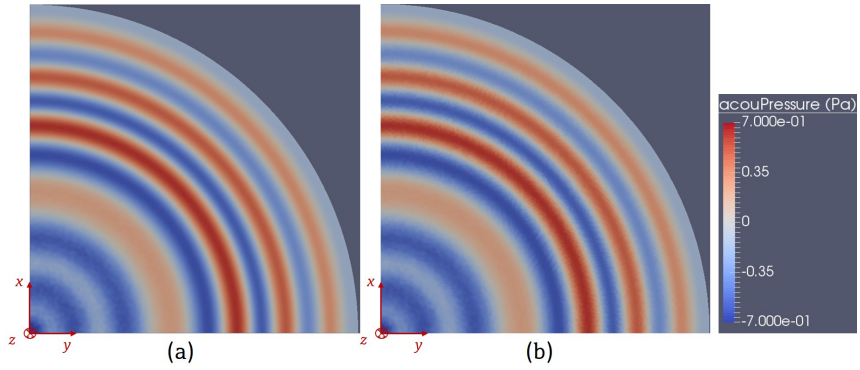

Figure 4.35: Acoustic pressure on Int1 at t=54.27 msec, on Int1 for (a) part (I) solved with NACS and (b) part (II) solved with Star-CCM+®.

t=54.27 msec, is

$$\frac{p'_{Int1,nodes} - p'_{Int1,centers}}{p'_{Int1,centers}} \cdot 100\% = 0.043\%$$

which is not large but significant based on the accuracy criteria set and the destined applications [64]. Thus, it should be kept in mind as a potential small source of error.

The error introduced on Int2 is of similar nature and therefore, no such investigation is conducted for Int2.

The acoustic pressure field is shown in Fig. 4.36 for the 3D domain when simulated with the SimPAC^2 method for $v_0 = [-20, 0, 20]$ m/s, at t = 0.39636 ms. The deceleration or acceleration of the waves is qualitatively observed in Fig. 4.36. To avoid unwanted reflections and to save computational time, the acoustic pressure BC on Int1 is taken from part (I) of the simulation, cf. Fig. 4.28) but it is simulated from t=0 up to t = 0.000162 s

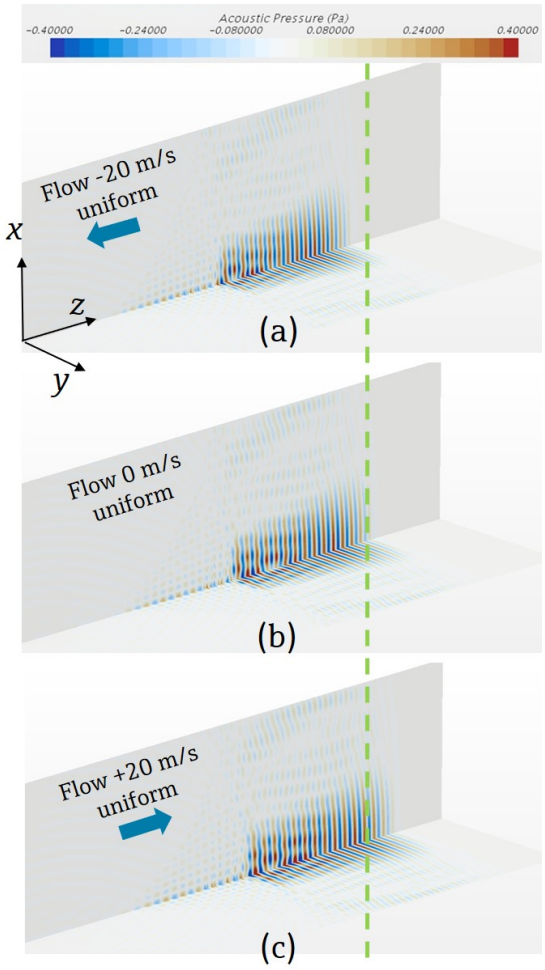

Figure 4.36: Acoustic pressure field solved with SimPAC^2, for t= 0.39636 ms, uniform flow velocity in the axial direction (a) $v_0 = -20$ m/s opposite to the direction of the acoustic propagation, (b) $v_0 = 0$ m/s, and (c) $v_0 = 20$ m/s in the direction of the acoustic propagation.

(600 time-steps), while for the rest of the simulation the acoustic pressure on Int1 is set to zero. As a result, not the whole received signal V_5 is useful but only 0.000162 s after it has reached the receiver. . Acoustic pressure is recorded on Int2 and is given as a BC for part (III) of the simulation.

4.3.2.3 NACS and SimPAC^2

The received signal V_5 is obtained with SimPAC^2 as well and a visual comparison is made between NACS and SimPAC^2 in Fig. 4.37 for $v_{ref} = \{-20, 0, 20\}$ m/s. The SimPAC^2 presents

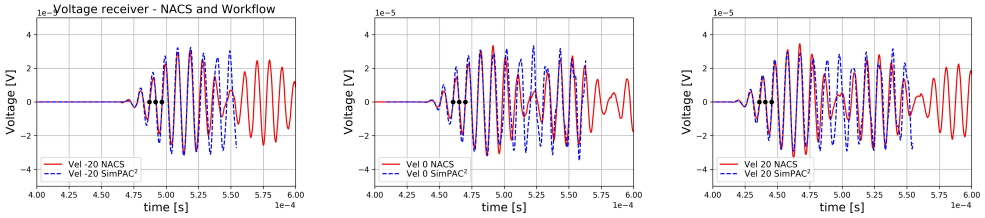

(a) (b) (c)

Figure 4.37: Voltage signal V_5 against time, solved with NACS and SimPAC^2 for different flow velocities, with three zero-crossings depicted (a) v_{ref}=-20 m/s, (b) v_{ref}=0 m/s, and (c) v_{ref}=20 m/s.

problems with capturing the ringing, while it is conjectured that a higher mesh discretization will aid to capture the exact form of the signal. It is reminded that no systematic convergence study was made for the solver of Star-CCM+®, whereas the temporal and spatial discretizations were based on the guidelines of the documentation of Star-CCM+® [229] and on the agreement of ToF between the NACS and SimPAC^2 simulations, shown in the present section. A much higher spatial discretization in 3D, would cost high computational resources and long computational time, in the order of several days for one simulation in one direction of the flow only. This strategy is practically impossible in the frame of the thesis where a large number of simulations was made with SimPAC^2, as documented in chapters 4, 5, and 6. Case 2 should be treated with care, as it cannot be reproduced with an experiment in reality when uniform flow velocity is present everywhere in the fluid domain, even next to the solid surfaces, and its purpose is only the numerical validation of SimPAC^2. However, the ultimate comparison of SimPAC^2 with measurements is additionally made in chapter 6 for an industrial flowmeter geometry.

The geometry of Case 2 (Fig. 4.26, 4.27) can be used as a simple UTTF. Obviously, this is far from a good design of an UTTF [163], however it can operate as one. This means that the ToF and Δt values are calculated for several uniform v_0, for which the flow velocity in the sound path along the z-axis, v_{calc}, is calculated via Eq. (1.8) and the process presented in secs. 1.2 and 2.5. The main goal should be the obtainment of highly-accurate ToF values in accordance with the set criterion of eqs. (4.7), (4.8). The ToF is calculated through the zero-crossings of the signal, as presented in Sec. 4.2. For the calculation of ToF, three zero-crossings of the received signal V_5 are taken into account, as described in Subsec. 2.5 with Eqs. (2.95), (2.96) and Fig. 2.10.

Eq. (2.91) is used for the calculation of the fluid velocity, v_{calc}, with this simple UTTF for uniform v_0. For 1 sound path it is valid that $v_{path,i} = v_{path,1} = v_{calc}$. For the investigated case, $L_{cav} = 0$, $t_{cav} = 0$, because the flow is uniform, $\cos\theta = 1$, due to the direction of the flow parallel to the wave propagation direction and $\Delta t_0 = 0$ (cf. Eq. (2.86)), since the sender and the receiver are identical for the simulation. The distance between the transducers is $L = 150$ mm and the speed of sound is c=343 m/s.

The ToF, t_{12} and t_{21}, are calculated from the average value of all three-zero crossings, with eqs. (2.89) and (2.90). The index i is neglected here, since i=1. For this case, the time-delay $t^{eltr}_{21,0} = t^{tr}_{21,0} + t^{diff}_{21,0}$ is calculated for zero-flow, as described in Subsec. 2.5, while

$t_{21,0} = L/c$ for zero flow. It should be mentioned that the value of $t_{21,0}^{tr} + t_{21,0}^{diff}$ is clumped together and not separate evaluation of each of $t_{21,0}^{tr}$ and $t_{21,0}^{diff}$ is made. The value of $t_{21,tot}$ is directly obtained from the simulation with Eq. (2.95), as described in Subsec. 2.5 as well. The same description applies for downstream propagation of waves and for the evaluation of t_{12}.

The resulting flow velocity, v_{calc}, is compared with the known average axial flow velocity over a cross-section, v_{ref}, given by Eq. (1.1). In this case $v_{ref} = v_0$ because of the uniformity of the flow-field. A deviation is calculated, with the equation already presented as Eq. (2.97) and reminded here again as

$$\%\text{deviation} = \frac{v_{calc} - v_{ref}}{v_{ref}} \cdot 100\%. \tag{2.97}$$

The set criteria of ToF have to be satisfied in this case as well. Previously, this criterion was used for the spatial and temporal convergence study (Eq. (4.7)), as well as for the comparison with measurements (Eq. (4.8)). A similar criterion may also be used here, given by

$$ToF_{crit,sim} = \frac{ToF_{NACS} - ToF_{SimPAC^2}}{ToF_{SimPAC^2}} \cdot 100\% \in [-0.2, 0.2]\% \tag{4.12}$$

for each v_{ref}. The calculated ToF with both NACS and SimPAC^2 is given in tab. 4.7

	v_{ref} [m/s]	t_{12} [ms]	t_{21} [ms]
NACS	0	465.234	465.234
	10	454.048	479.556
	20	442.332	493.468
	30	431.222	508.252
SimPAC^2	0	465.086	465.086
	10	453.020	478.618
	20	441.289	492.639
	30	430.015	507.543

Table 4.7: t_{12} and t_{21} calculated with the three-zero crossings technique. Simulated with NACS and Star-CCM+®.

The values of $ToF_{crit,sim}$ for downstream and upstream wave propagation are given in tab. 4.8. The values of $ToF_{crit,sim}$ slightly exceed the set criterion of [-0.2,0.2] % for downstream propagation, while they are in the set range for upstream propagation. Therefore, the respective uncertainty should be considered for the generated results. It should be reminded though, that for the present comparison, $n_t = 27$ and $n_x = 20$ are chosen for the simulations with NACS, which is the absolute lower limit set. The resulting %deviation is calculated with the use of Eq. (2.97) and shown in Fig. 4.38 for $v_{ref} = \{10, 20, 30\}$ m/s.

For a typical application of an UTTF, such as the Proline Prosonic Flow G 300, it is required %deviation ± 1 % [64] for [3, 40] m/s. Thus, the accuracy criteria should be set well below this value in order to use the simulations within reasonable accuracy for the extraction of useful conclusions. That is the case with the set criteria $ToF_{crit} \in [-0.02, 0.02]\%$,

v_{ref} [m/s]	$ToF_{crit,sim}$ [%] downstream	$ToF_{crit,sim}$ [%] upstream
0	0.032	0.032
10	0.227	0.196
20	0.236	0.168
30	0.281	0.140

Table 4.8: $ToF_{crit,sim}$ for downstream and upstream wave propagation for v_{ref}={0, 10,20,30} m/s. Simulated with NACS and Star-CCM+®.

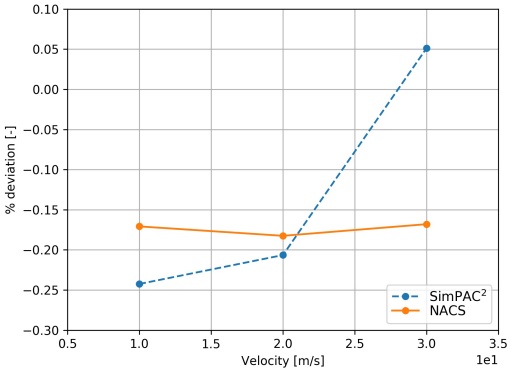

Figure 4.38: %deviation calculated with NACS and SimPAC^2 for $v_{ref} = \{10, 20, 30\}$ m/s.

$ToF_{crit,m} \in [-0.2, 0.2]\%$ and $ToF_{crit,sim} \in [-0.2, 0.2]\%$. The studies made, showed the level of accuracy of NACS and SimPAC^2, as well as the agrement between them in terms of ToF and %deviation and thus, they are used as a guide for the setup of further simulations.

By definition, in the simulation since the sender and the receiver are identical, %deviation $= 0$ for $v_0 = 0$ m/s, which is omitted from the deviation curves. An acceptable agreement between the methods is observed, as the maximum %deviation $\simeq 0.22\%$ for the maximum flow velocity $v_0 = 30$ m/s, which is well below the $\pm$ 1% level of accuracy required [64].

4.4 Summary and Conclusions

In the present chapter, the CNA method is investigated for a number of turbulent models and is compared with already published measurements [196], for a challenging case of an UTTF with an asymmetric flow disturber mounted upstream of it. It is shown that it provides realistic results and despite its limitations, i.e. no simulation of acoustics but only CFD, it can be used as an additional reference simulation or for quantification of flow effects.

The FEM program NACS was compared with highly accurate, already published measurements for two piezoelectric elements in air[277]. The numerical robustness of NACS was tested and optimum parameters were found for the execution of transient acoustic simulati-

ons, i.e. numerical convergence studies were made for the calculation of optimum temporal and spatial discretization.

The SimPAC^2 method is verified with the program NACS for a case of two piezoelectric elements in air for zero and uniform flow. Optimum parameters are found for Star-CCM+® to deliver results in agreement with NACS. The interfaces and communication between NACS and Star-CCM+® are created.

It should be highlighted that Case 1 and Case 2 investigated so far, are highly simplified cases compared to a real industrial UTTF geometry. However, such cases are chosen for initial comparisons and convergence studies in order to identify more conveniently potential numerical sources of errors. Furthermore, the accuracy of the measurements used as reference is well known [277]. They can still serve as test cases, since the main components of an UTTF are present and the geometry is to be divided into parts (I), (II) and (III) for the SimPAC^2 method.

On the other hand, certain aspects are not yet considered in the studies cases, such as realistic flow profiles, angle between the wave propagation and the flow direction $\theta \neq 0^o$, realistic transducers, chordal sound paths, and transducer cavities. These matters are addressed in the next chapters of the present thesis, where complexity is gradually added in order to quantify their effects on the operation of an UTTF.

Chapter 5

Simulations of a Single-path Flowmeter

In this chapter, piezoelectric elements are positioned opposite to each other, in oblique angle relative to the flow direction. This geometry resembles more the classic appearance of an inline UTTF compared to the previous two cases investigated (cf. secs. 4.2, 4.3). The motivation for the investigation of this case is its utilization as an intermediate step before studying the more complex geometries of real transducers. The case is simulated as 3D with the CNA and SimPAC^2 methods, it has one diametrical path, and the fluid is air. More details are given in the present chapter.

The effect of different flow profiles on the wave propagation, the ToF, and the %deviation (Eq. (2.97)) of the flowmeter is investigated. The considered flow profiles are one with uniform v_0 in the domain, a fully-developed one [58, 132] with zero velocity inside the cavities, and one simulated with CFD, where flow is calculated inside the meter-body and the cavities of the transducers. A more thorough description of the flow profiles is given in the present chapter.

A case with a geometrical cavity and one without are studied as well. The definitions of the terms 'with cavity' and 'without cavity' are described through the schematic illustration of Fig. 5.1. The transducer, T1, is depicted as a blue orthogonal shape. The blue continuous

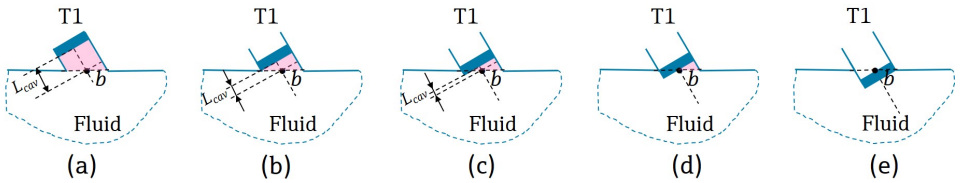

Figure 5.1: Detail of one of the transducers and a portion of fluid from Fig. 2.9. Different positions of a transducer in a flowmeter. Geometries: (a) with cavity, recessed, with $L_{cav} \neq 0$ (b) with cavity, flush, with $L_{cav} \neq 0$ (c) with cavity, protruded, with $L_{cav} \neq 0$, (d) with cavity, protruded, with $L_{cav} = 0$, and (e) without cavity, with $L_{cav} = 0$.

lines represent the walls of the flowmeter. The white area confined among the continuous and dashed blue lines represents the fluid of air inside the meter body and the pink area

the fluid of air inside the cavity. The dashed black lines indicate dimensions only. L_{cav} and point b are defined in Subsec. 2.5. In Fig. 5.1(a) a geometry 'with cavity' is shown, with the transducer recessed in the cavity. In Fig. 5.1(b) a geometry 'with cavity' is depicted with the transducer flush with the walls of the meter body of the flowmeter. If the transducer is shifted slightly more towards the fluid, then it will be protruded, since even a small part of it will be inside the fluid in the meter body. In Fig. 5.1(c) a geometry 'with cavity' is shown with the transducer protruded in the fluid. However, $L_{cav} \neq 0$ must be considered, since the center of the frontal surface of the transducer is still located inside the cavity. In Fig. 5.1(d) the transducer is shifted further inside the fluid and the center of its frontal surface coincides with point b. Thus, from that position and for further protrusion of the transducer in the fluid, one considers $L_{cav} = 0$. Due to the presence of the cavity one names this case still as 'with cavity'. If the transducer is shifted further inside the fluid, there is no cavity anymore as shown in Fig. 5.1(e), while $L_{cav} = 0$ as well. From that position on and for further protrusion the geometry is called 'without cavity'. With the definition of the 5 cases pictured in Fig. 5.1, all the possible cases are covered in respect with the transducer position, in the present thesis. The two geometries studied in the present chapter belong to the categories 'with cavity, flush' and 'without cavity'.

The effectiveness and accuracy of the interfaces between the different parts of the SimPAC^2 is studied. A sensitivity analysis is conducted for Interfaces Int1 and Int2 i.e., they are axially shifted in order to assess their effect on the received voltage signal. It is reminded that a study on the numerical accuracy because of the mapping on Int1 from the mesh of part (I) to the mesh of part (II) is already made in Subsec. 4.3.2.2.

5.1 Model Description - Piezoelectric Elements in Oblique Angle

Two different geometries are modeled, one with cavity, where the piezoelectric elements are flush with the meter-body walls (cf. Fig. 5.1(b)), and one without cavity, where they are directly exposed in the flow (cf. 5.1(e)). The only difference between the two geometries is the presence of cavity or not. Otherwise, the same transducers are used, in the same distance L and in air. Therefore, a comparison of the results of these two geometries, gives purely the quantification of the acoustic effect of the cavity as a geometry. More specifically, regarding the geometry with the cavity, reflections may occur either on the sender or on the receiver side, due to the confined space near the transducers. Such reflections do not occur for the case of the geometry without cavity, because of the absence of such confined spaces. The effect of the presence or not of this confined space, i.e. cavity, is qualitatively and visually studied with the illustration of the acoustic pressure waves in the fluid, as well as quantified with the comparison of the received voltage signal of the two cases. The described effect that causes such differences is called 'cavity effect'.

Once the cavity effect is studied, the case 'with cavity' is further investigated. In particular, different flow-fields are taken into account, such as the mentioned uniform, fully-developed, and CFD ones. The consideration of different flow-fields has consequences on the wave propagation inside the fluid. The acoustic pressure waves are qualitatively and visually

inspected, while the received voltage signal is quantitatively compared among the cases.

The goal of this study is to systematically investigate the effect of the cavity and of the flow-field on the wave propagation and the deviation curve of an UTTF. Such a systematic flow-field investigation i.e., 'flow-effect', with the consideration of piezoelectricity, acoustic wave propagation and CFD has been previously conducted by Papathanasiou et al. [197] as part of this work. Sun et al. [239] used simulations of ray-tracing, CFD, and wave acoustics to calculate the 'flow-effect' for a USM with protruded transducers. Otherwise, the systematic effect of different flow-fields, inlet disturbances, or the transducer position has been studied before, as reviewed in Subsec. 1.4.2.4, mostly with the use of CFD only and without the inclusion of piezoelectricity and wave propagation in solids and fluids, as here. The 'cavity-effect' has been already investigated in an experimental manner in [110, 209], or with the use of CFD and comparison with experiments in [208, 261, 286]. Løland [146, 147] suggested a correction of the 'cavity-effect' with the use of both experiments and 2D CFD. The 'cavity-effect' has not been previously studied in the manner performed in the present thesis i.e., with the 3D simulation of piezoelectricity, CFD, and wave propagation in solids and fluids, to the author's knowledge. A discussion of the results of the 'flow-effect' and 'cavity-effect' takes place compared to the findings of previous works [146, 147, 110, 209, 208, 261, 286] in the present chapter, as well as in Sec. 1.4.2.7 and in chapter 6.

5.1.1 With Cavity

The simulated case of piezoelectric elements in oblique angle with cavities is shown schematically in Fig. 5.2, from now on denoted as 'Case 3'. The geometrical dimensions of the

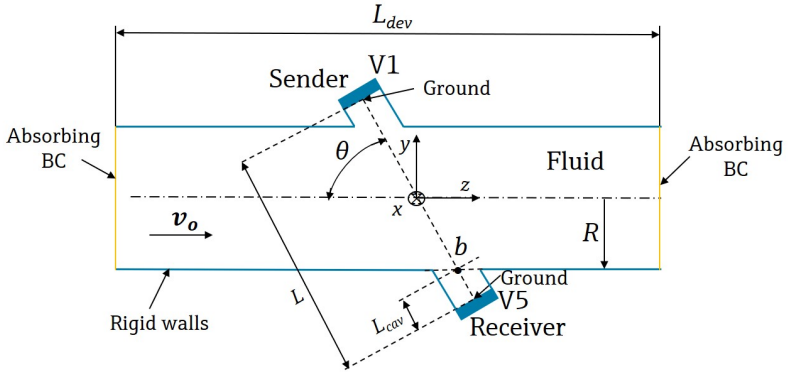

Figure 5.2: Schematic representation of the simulated geometry, denoted as Case 3.

device, shown in Fig. 5.2, are $R = 48.5$ mm, $L = 116.468$ mm, $L_{cav} = 4.719$ mm, $\theta = 65^o$, and the length of the device $L_{dev} = 110$ mm. The fluid is air with $\rho_0 = 1.21$ kg/m^3 and $c = 342.3$ m/s. The piezoelectric elements are the same as the ones of Case 1 and Case 2 described in Subsec. 4.2 and in ref. [277]. The domain is simulated as 3D, and the fluid is confined in the continuous blue and yellow lines. The blue lines denote rigid walls [117] and the yellow lines denote absorbing BCs [44, 107], as defined in Subsec. 3.2.2. The black

lines' purpose in Fig. 5.2 is to solely deliver information regarding the simulated geometry. A sinusoidal signal V_1 is given on the outer surface of the sender (Eq. (4.11)) with $f_c = 112$ kHz, length of 4 periods $T = 1/f_c$, and amplitude 1 V, while a voltage signal V_5 is recorded on the outer surface of the receiver. The electrodes on the outer surfaces of the piezoelectric elements are not considered in the simulation and therefore, the BCs are set directly on the surfaces, as described and denoted in Fig. 5.2 with 'V1' and 'V5' for the input and received signals, respectively. The inner/frontal surfaces of the sender and the receiver are grounded.

The 3D domain of Case 3 is shown in Fig. 5.3. An axial view and a side view are shown in figs. 5.3(a) and 5.3(b), respectively. The piezoelectric elements 'sender' and 'receiver',

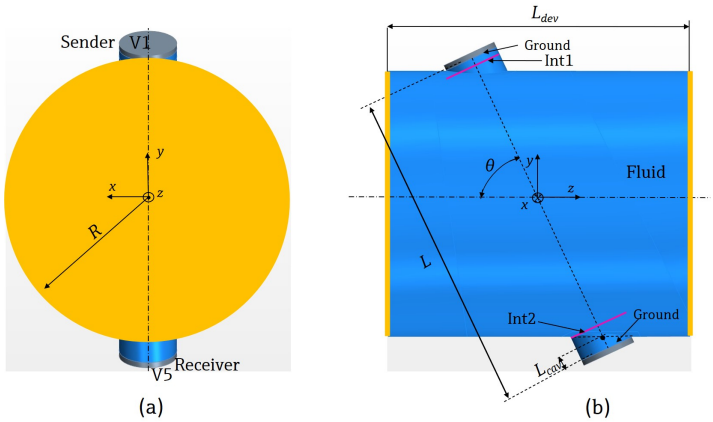

Figure 5.3: Overall 3D simulated geometry of Case 3, with sender, receiver, fluid, and interfaces Int1 and Int2 shown. (a) Axial view and (b) side view.

are shown with gray color and the the fluid domain with blue color. One can observe that the piezoelectric elements are flush with the walls of the meter body, in the same way as explained through Fig. 5.1(c). The meter-body is not simulated here, since the simplification was made to replace it with rigid walls, as shown schematically in Fig. 5.2 as well. Interfaces Int1 and Int2 are indicated inside the fluid as pink lines, in front of the sender and the receiver, respectively. Absorbing BCs are defined on the upstream and downstream surfaces of the fluid domain. In particular, the absorbing BCs are shown with orange color in Fig. 5.3. The upstream surface, on which an absorbing BC is defined, is shown as an orange circle in the axial view of Fig. 5.3(a) and as a line on the left-hand side in the side view of Fig. 5.3(b). Similarly, the other absorbing BC is shown as a line on the right-hand side of Fig. 5.3(b). The rest of the outer fluid surfaces, which are in reality in contact with the walls of the meter body, shown with blue color in Fig. 5.3, are defined as rigid walls [117]. The absorbing BCs [44, 107] and rigid walls are implemented in the way described in Subsec. 3.2.2, as well as more extensively in [107, 183] for NACS and in [229] for Star-CCM+®.

In Fig. 5.4 the actual simulated geometry is shown, divided in parts (cf. Sec. 3.2). The coordinate systems in figs. 5.4(a),(b,(e),(f) indicate only directions, while in figs. 5.4(c),(d) the actual coordinate systems are shown. The absorbing BCs are shown once again with orange lines that confine the respective surfaces or with orange surfaces. Int1 and Int2

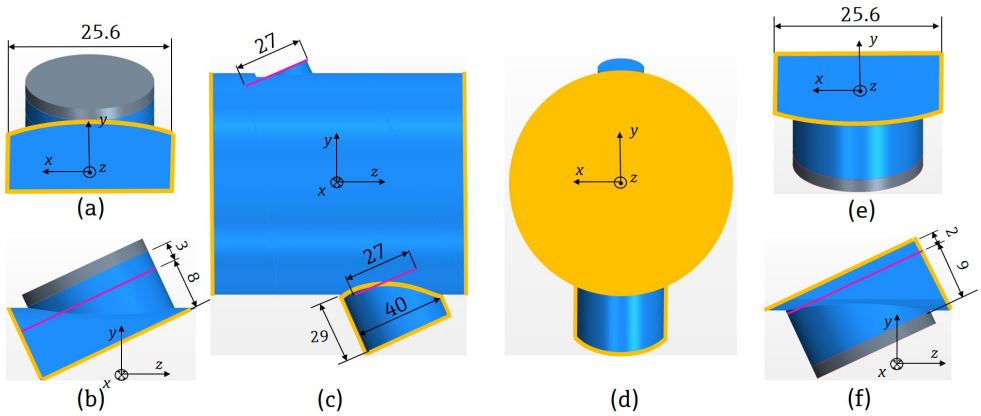

Figure 5.4: Simulated geometry of Case 3 in parts. (a) Part (I) axial view, (b) part (I) side view, (c) part(II) side view, (d) part (II) axial view, (e) part (III) axial view, and (f) part (III) side view.

are shown with lines of pink color. Additional dimensions are given in [mm], necessary for splitting the parts and for the definition of Int1, Int2. By combining the information given in figs. 5.2, 5.3, and 5.4 one can reproduce the 3D simulated geometry. Part (I) includes the sender and a portion of fluid divided in two bodies. Int1 is positioned close to the front surface of the sender, at 3 mm distance, to avoid artificial reflections, in the way described in Subsec. 3.2.2. Part II includes the fluid domain divided into several bodies for functional reasons i.e. connection with parts (I) and (III) and recording of acoustic pressure on Int2, and for meshing reasons, i.e refinement in the areas of interest, as it will be explained in the present subsection. In the vicinity of the receiver, the real geometry of the receiver is replaced by a cylindrical domain to avoid artificial reflections as well, in the way described in Subsec. 3.2.3. Part (III) includes the receiver and a portion of fluid divided in two bodies. Int2 is positioned further from the front surface of the receiver compared to the Int1 from the sender, at a distance of 9 mm, as its purpose is different; unwanted reflections from the rigid walls or the piezoelectric element are avoided when Int2 is positioned further away, in the way described in Subsec. 3.2.4 .

In Fig. 5.5 the mesh for parts (I), (II), and (III) is shown. Parts (I) and (III) are solved as 3D geometries with NACS and consist each of $\simeq$ 16 million tetrahedral, linear cells, with edge-dimension of cells 0.125 mm ($n_x = 24.5$). The value of $n_x = 24.5$ refers to air, since this is the critical material, in terms of spatial discretization, compared to the PZ27 [30, 277] material of the piezoelectric material, i.e. the wavelengths in PZ27 are longer than in air for the same frequency [91, 277]. It should be noted that the time-step is $\Delta t = 2.7 \cdot 10^{-7}$ s for all three parts of the simulation and thus, $n_t = 33$ for $f_c = 112\ kHz$. Part (I), when solved with NACS in 8 parallel cores for 600 time-steps, lasts $\simeq$ 20 hours, while $\simeq$ 380 GB of RAM are needed. Part (III) when solved with NACS in 8 parallel cores for 600 time-steps, lasts $\simeq$ 40 hours. The Cartesian mesh of part (II) consists of $\simeq$ 317 million hexahedral, linear cells, with edge-dimension of cells 0.125 mm ($n_x = 24.5$). Part (II), when solved with Star-CCM+®in 320 parallel cores for 1850 time-steps, lasts $\simeq$ 20 hours. In Fig. 5.5(b), it

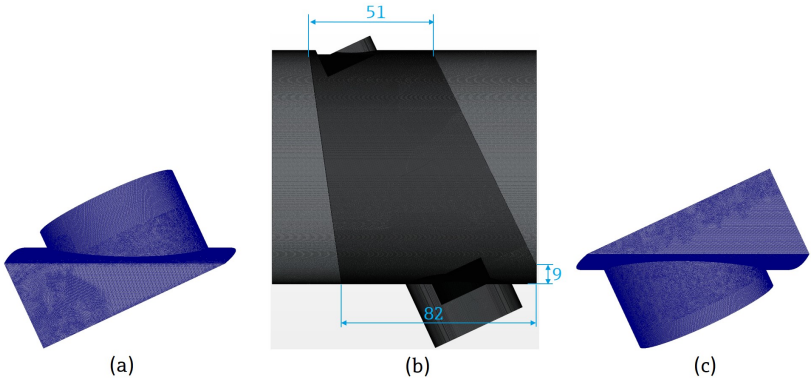

Figure 5.5: Mesh of Case 3 in parts. (a) Part (I), solved with NACS, tetrahedral mesh, (b) part (II) solved with Star-CCM+®, Cartesian mesh, and (c) part (III), solved with NACS, tetrahedral mesh.

is shown that the area of interest between the opposite piezoelectric elements is finer, with $n_x = 24.5$, compared to the rest of the fluid, shown in Fig. 5.5(b), for which $n_x = 12.25$. The dimensions of the refined area of interest are shown in Fig. 5.5(b) as well. The reason for choosing this shape of the refined area is the propagation of the waves always from part (I) to Int1, inside part (II), towards Int2, and finally to part (III). In order to calculate the 'downstream' propagation of the waves, the flow axial direction is z, while for the 'upstream' propagation, the flow axial direction is $-z$. The waves always propagate from the described part (I) toward finally part (III) and thus, they spread further [117] when they propagate towards part (III), while they are additionally deflected either downstream or upstream depending on the given flow-field. Consequently, the refined area of interest is larger close to part (III).

From the case, the mesh and the computational demands presented here, it is obvious that Star-CCM+® is more efficiently parallelized computationally compared to NACS, which is mostly the rule for all FV based solvers in comparison with the FE solvers. A case, such as the one presented here, with more than 300 million cells may be considered as a 'large' one. This would be a representative number of million cells for the simulation of a typical gas UTTF in 3D. Such a mesh would be highly unlikely to be solved with FEM on a typical workstation [243] or a computer cluster as of today [249]. Therefore, the implementation of CAWE in FV, gives the opportunity to solve 'large' problems of acoustic wave propagation in moving fluid media.

5.1.2 Without Cavity

The piezoelectric elements are positioned in the same distance $L = 116.468$ mm as for the case 'with cavity', while $L_{cav} = 0$ mm $\theta = 65^o$. The piezoelectric elements are the same as for the case with cavity and the air has the same properties, $\rho_o = 1.21$ kg/m^3 and $c = 343$ m/s, as the case 'with cavity'. Instead of a geometry of typical fluid in a meter body, a cylindrical

fluid geometry with radius 50 mm is considered, as shown in Fig. 5.6 .

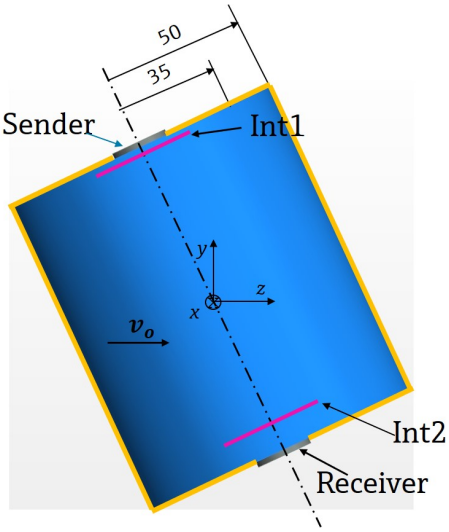

Figure 5.6: Overall 3D simulated geometry of Case 3 without cavity, with interfaces, absorbing BCs, sender, receiver and the direction of uniform flow velocity v_0 indicated.

This case emulates the situation described in Fig. 5.1, in terms of the existence of cavity. However, no rigid walls are defined but only absorbing BCs, as shown in Fig. 5.6 with orange lines, in order to avoid any reflection that would arise from the existence of rigid walls [44, 107]. The inner radius of 35 mm corresponds to the area with the finer mesh of fluid while the radius of 50 mm to the coarser mesh of the fluid body. The radius of 50 mm is large enough according to the criterion set in Sec. 4.2.2 in order to avoid reflections. Absorbing BCs, as described in Sec. 3.2, are defined on all the outer surfaces of the domainindicated with orange lines. The exact simulated geometry is shown in Fig. 5.7, divided in parts, in the way described in Sec. 3.2. The coordinate system in Fig. 5.7(b) is correctly depicted, while in figs. 5.7(a),(c) its purpose is only to indicate the correct directions. Part (I) consists of the sender and two fluid bodies. Int1 is positioned at 3 mm distance from the front surface of the sender, while a layer of 6 mm cylindrical fluid is added. Part (II) consists only of fluid, which is refined for radius $\leq$ 35 mm and is coarser for radius $>$ 35 mm. Part (III) consists of the receiver and two fluid bodies. Int2 is positioned at 6 mm distance from the receiver. The dimensions of the bodies and the position of Int1 and Int2 are chosen in a way to satisfy the criteria set in secs. 4.2.2 and 3.2.4. On all the outer surfaces of the fluid bodies absorbing BCs are defined, indicated with orange lines.

The mesh of parts (I) and (III) consists of $\simeq$ 30 and $\simeq$ 26 million tetrahedral, linear elements, while the mesh of part (II) is Cartesian, consisting of $\simeq$ 232 million tetrahedral cells. For all the bodies $n_x = 24.5$, except for the area of part (II) with radius $>$ 35 mm, for which $n_x = 12.25$. The value of n_x corresponds to air, which is the critical material in terms of spatial discretization, as already described in Subsec. 5.1.1. The time-step for all parts is $\Delta t = 2.7 \cdot 10^{-7}$ s and thus, $n_t = 33$ for $f_c = 112$ kHz.

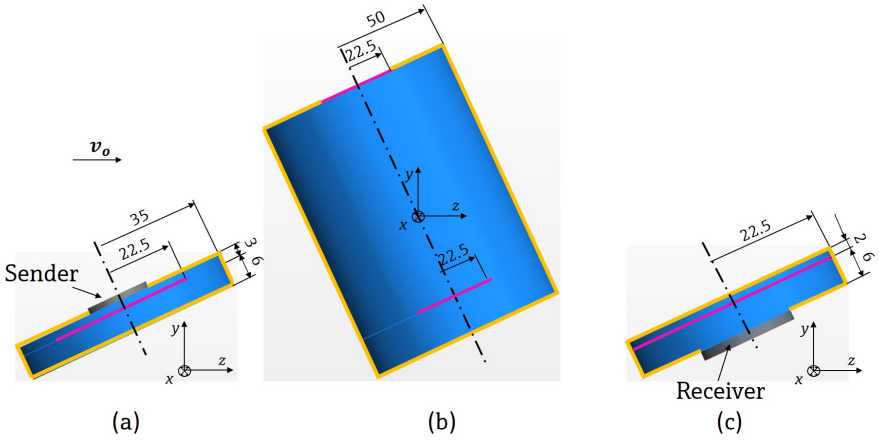

Figure 5.7: Simulated 3D geometry of Case 3 without cavity in parts. (a) Part (I)-sender with fluid, (b) part (II)-fluid, and (c) part(III)-receiver with fluid.

5.2 Computational Matrix

A number of cases is simulated in order to investigate specific effects. Two different geometries are taken into account, as presented in Sec. 5.1, one where the piezoelectric elements are in cavities, denoted as 'with cavity', and one for which they are exposed in the flow, denoted as 'without cavity'. For the 'with cavity' case, a number of different flow fields and flow velocities are considered. More specifically, zero flow, overall uniform (unif.), uniform with zero velocity in cavities (unif.-0), fully-developed with zero velocity in cavities (ful-dev), and CFD flow with the flow-field calculated in the meter and in cavities are taken into account. For the 'without cavity' case, zero and uniform flow are studied. In table 5.1 the computational matrix for Case 3 is presented. It should be clarified that the 'fully-developed' flow profile is generated with the help of CFD as well, in the way described in Subsec. 3.2.5.

	Case	Flow type	Velocities [m/s]
With cavity	3A-0	Zero	0
	3A-1	Uniform	{-30, -20, -10, 10, 20, 30}
	3A-2	Unif.-0	{-30, -20, -10, 10, 20, 30}
	3A-3	Fully-developed	{-30, -20, -10, 10, 20, 30}
	3A-4	CFD	{-30, -20, -10, -5, 5, 10, 20, 30}
Without cavity	3B-0	Zero	0
	3B-1	Uniform	{-30, -20, -10, 10, 20, 30}

Table 5.1: Simulations performed for Case 3. With and without cavity, different types of flow, and velocities considered.

In Fig. 5.8 the different flow types, for the case 'with cavity', are presented for $v_{ref} = 10$ m/s, where the normalized magnitude of velocity, $v_{mag,norm} = v_{mag}/v_{ref}$ is shown. $v_{mag} =$

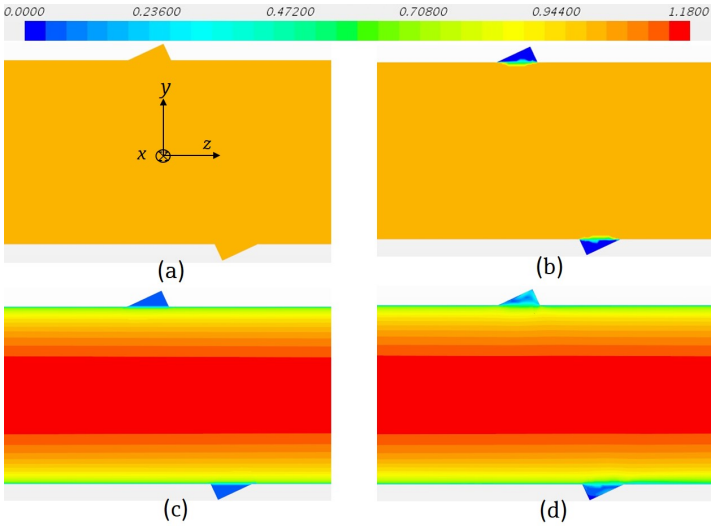

Figure 5.8: Magnitude of flow velocity for different flow types considered for Case 3, shown on the middle plane yz for $x = 0$. (a) Uniform, (b) uniform with zero velocity in cavities, (c) fully-developed with zero velocities in cavities, and (d) CFD with vortices simulated in cavities. The depicted coordinate system only indicates the direction for the 4 considered cases.

$\sqrt{v_{0,x}^2 + v_{0,y}^2 + v_{0,z}^2}$, where $v_{0,x}, v_{0,y}$, and $v_{0,z}$ are the components of flow velocity in the x, y, and z direction, respectively. The range of $v_{mag,norm}$ is set to [0, 1.18]. This normalization is a common practice for the direct comparison of flow-fields for different v_{ref}. A respective figure of the flow-field for the 'without cavity' case is not added, since a uniform flow-field is considered all over the cylindrical fluid domain, as in the case of Fig. 5.8(a).

These flow types are coupled with acoustics for moving fluid media in order to show and quantify the effect on wave propagation. The case of uniform flow is an artificial case, for which even inside the cavities $v_0 = 10$ m/s. Therefore, mass conservation is not satisfied [14], however it is a useful case to study, especially for comparison reasons with the rest of the studied flow-fields. The case of uniform flow with zero velocity in the cavities is a case of special interest, since Eq. (2.91), which is broadly used in UTTF measurement, is derived exactly for such a flow-field [155]. For the cases of uniform velocity and uniform with zero velocity in the cavities, $\boldsymbol{v_0}$ is given directly as an input to the cells of the acoustic mesh. The values of the given $\boldsymbol{v_0}$ are considered in the respective equations, i.e. PE for NACS and CAWE for Star-CCM+®.

The case of fully-developed profile, is the state-of-the-art and the one commonly used in literature as a flow-field in an UTTF, in order to resemble the real flow-field [30]. However, it does not represent reality, since the flow velocity inside the cavities, for $r > R$, where r is the radial coordinate and R is the pipe radius, is set to zero, as described in Subsec. 3.2.5. In the present thesis, the fully-developed profile is not defined in an analytical way, as often considered in literature [30, 226, 253] but it is calculated with CFD, as described in Sec. 3.1 and Subsec. 3.2.5. More specifically, a separate CFD simulation of a pipe geometry without

cavities is carried out. With the use of CFD, a more accurate and consistent result for a fully-developed profile with zero velocity in the cavities is achieved.

The CFD flow-field on the other hand, is closer to reality, as CFD simulations are used for its generation with the whole domain of the UTTF together with the cavities considered. One can see in Fig. 5.8(d) that inside the cavities, the flow velocity is not zero but vortices are present. Because of the cavities, the flow-velocity in the meter-body is different between the cases 'Ful.-dev.' and 'CFD'. A quantified investigation is shown in Subsec. 5.4. A description of the whole process of such a simulation and its mapping on the acoustic mesh is given in Sec. 3.1 and in Subsec. 3.2.5.

Therefore, through the presentation of these 4 'with cavity' subcases one can systematically investigate flow effects, from simple to more complex, on acoustic wave propagation and on the UTTF measurement.

The case 'without cavity' is studied for zero and uniform flow, as its purpose is the comparison with the 'with cavity' uniform case.

5.3 Cavity Effect

For the two domains, with cavity and without cavity, the same flow field is given as input in the simulation i.e., uniform, while the transducers and the distance between them are identical, and the only differences are the cavity geometry and the respective BCs on the outer surfaces (cf. Sec. 5.1). Because of these similarities and differences of the two geometries, it is possible to quantify the acoustic effect of the cavity. The exact geometries, their dimensions, the materials and the whole simulation setup are given in secs. 5.1.1, 5.1.2.

In Fig. 5.9 the acoustic pressure field in the fluid in the vicinity of the sender is shown, for v_{ref} ={-10,10} m/s at $t = 4.455 \cdot 10^{-5}$ s. The sender is shown on the upper part of each of the subfigures as a gray rectangular. The position of the plane section yz, on which the contours are depicted, is at $x = 0$, i.e. on the symmetry plane of the domain. The

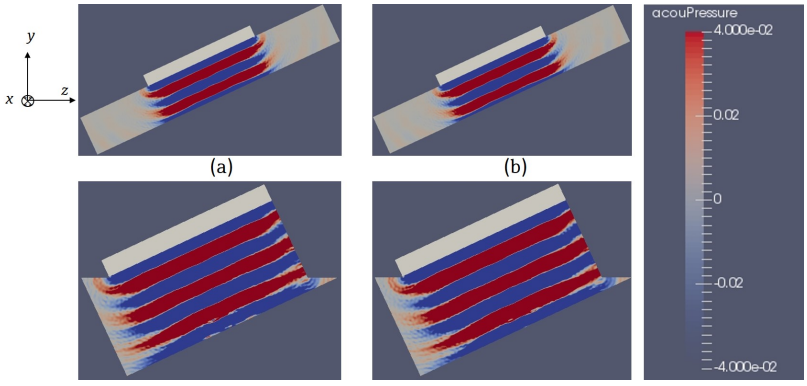

Figure 5.9: Acoustic pressure field for uniform flow in the fluid for part (I): sender and fluid, at $t = 4.4550 \cdot 10^{-5}$ s. (a) Without cavity, $v_{ref} = -10$ m/s, (b) without cavity, $v_{ref} = 10$ m/s, (c) with cavity, $v_{ref} = -10$ m/s, and (d) with cavity, $v_{ref} = 10$ m/s.

coordinate system only indicates directions, while the correct one is given in subsecs. 5.1.1, 5.1.2. It is observed that for such short wave propagation near the sender, the flow field, in that case of uniform flow v_{ref} ={-10,10} m/s does not have a strong effect on acoustics, since the distance the waves have traveled is small (cf. figs. 5.4, 5.7) and the differences are not easily observable through the contours of acoustic pressure. However, the pressure waves already interact with the walls for the 'with cavity' case, in contrast to no interaction with the walls for the 'without cavity' case, which has a consequence on the further propagation of the waves in the fluid domain.

In Fig. 5.10 the acoustic pressure field in the fluid of part (II) is shown for v_{ref} = {-10,10} m/s at $t = 2.8647 \cdot 10^{-4}$ s. Acoustic pressure is given as input on the respective

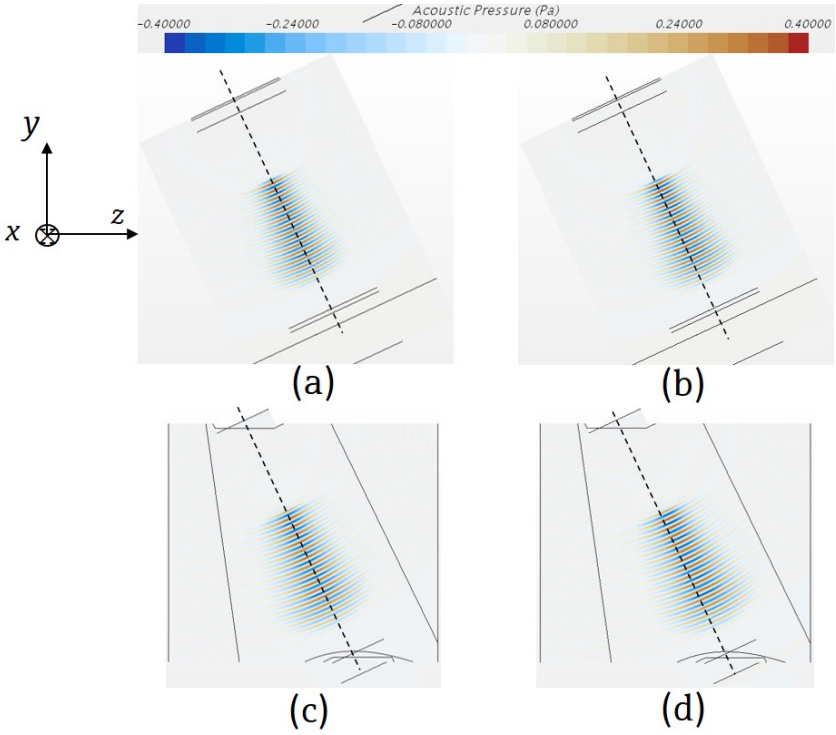

Figure 5.10: Acoustic pressure field in the fluid for part (II) at $t = 2.8647 \cdot 10^{-4}$ s for uniform flow. (a) Without cavity, $v_{ref} = -10$ m/s, (b) without cavity, $v_{ref} = 10$ m/s, (c) with cavity, $v_{ref} = -10$ m/s, and (d) with cavity, $v_{ref} = 10$ m/s.

Int1 surface (cf. figs. 5.3, 5.6). The piezoelectric element structures are not simulated in part (II), as explained in Sec. 3.2.3. The centerline between the center of the sender and the receiver is denoted with a dashed black line. The waves are deflected upstream (-z) for $v_{ref} = -10$ m/s and downstream for $v_{ref} = 10$ m/s. The quantification of the effect of the flow on the waves is made through the ToF comparison between the upstream and downstream propagation in the present subsection.

In Fig. 5.11 the acoustic pressure field for the 3D geometry in part (III), i.e. the fluid near the receiver together with the receiving piezoelectric element, for v_{ref} ={-10,10} m/s for the geometries 'with cavity' and 'without cavity' is shown. The receiving piezoelectric element is shown on the lower part of each of the subfigures as a gray rectangular. The coordinate system indicates the correct directions only, while the correct one is given in subsecs. 5.1.1, 5.1.2. The axial direction of the flow is z (cf. fig 5.2). The acoustic field is shown for the same

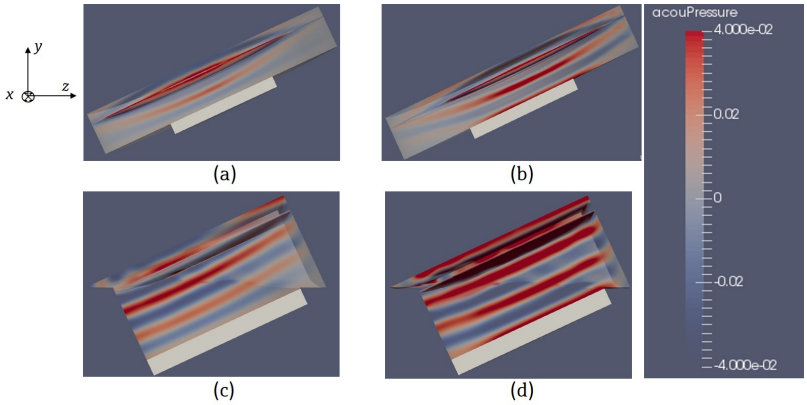

Figure 5.11: Acoustic pressure field in the fluid for part (III): receiver and fluid, at $t = 3.44895 \cdot 10^{-4}$ s for uniform flow. (a) Without cavity, $v_{ref} = -10$ m/s, (b) without cavity, $v_{ref} = 10$ m/s, (c) with cavity, $v_{ref} = -10$ m/s, and (d) with cavity, $v_{ref} = 10$ m/s.

time sample, $t = 3.44895 \cdot 10^{-4}$ s, in all four subfigures of Fig. 5.11. It is apparent that for $v_{ref} = -10$ m/s, the acoustic waves are deflected upstream (-z), while for $v_{ref} = 10$ m/s, they are deflected downstream, as expected. Moreover, for the same time sample, the waves for the upstream cases have hardly reached the piezoelectric element, while for the downstream cases they have already reached it and are reflected back. As described in subsecs. 5.1.1, 5.1.2 and in Sec. 3.2.4, acoustic pressure, which was calculated during the simulation of part (II), is given on Int2 inside the fluid with the so-called superposition BC [30, 183]. The acoustic waves propagate from Int2 in both directions, i.e. towards and away from the receiver, which is not the case in reality, since the acoustic pressure is given as input inside the fluid on Int2. The waves that propagate from Int2 away from the receiver are artificial, meaning that when the acoustic pressure is given as input on Int2 then it will propagate towards and away from the receiver. In other words it is not a numerical error but a known situation that does not represent reality. In order to cancel out these waves propagating from Int2 and away from the receiver, an absorbing BC, as discussed in Sec. 3.2.2, is defined as shown in figs. 5.4, 5.7, which ideally absorbs the incident waves [30, 44].

The received voltage signal against time for zero flow, shown in Fig. 5.12, is compared for the two geometries. From Fig. 5.12(a), the two signals look similar, while the 'with cavity' case seems to be shifted later especially for the later peaks. Additionally, the amplitude for the later peaks of the 'with cavity' case is increased compared to the 'without cavity', since the acoustic waves are reflected by the cavity and directed incident to the receiver. The later the signal is observed, e.g after the maximum voltage is achieved for $t > 4 \cdot 10^{-4}$ s,

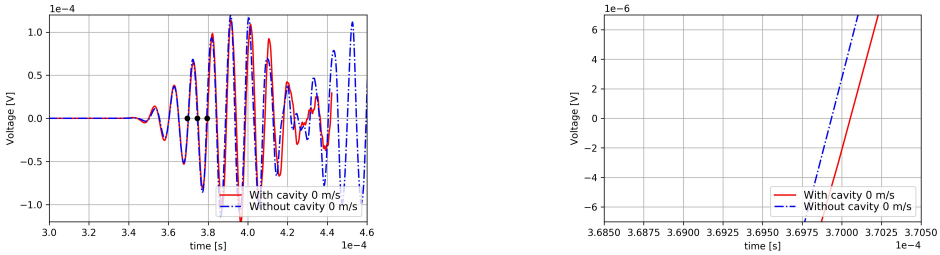

(a) (b)

Figure 5.12: Voltage signal on receiver V_5 against time, solved with SimPAC^2 for 3D geometry, zero flow and two different geometries: 'with cavity' and 'without cavity'. (a) Voltage depicted with three zero-crossings, (b) Zoomed view on the first of the three depicted zero-crossings with black circles.

the higher the differences between the signals of the two geometries, in terms of amplitude and phase-shift, i.e. shift in time, due to the presence of more reflections from the cavity walls. The ToF difference for zero flow, based on the three zero-crossings (cf. Sec. 2.5), between the two geometries is $2.58 \cdot 10^{-7}$ s. The ToF deviation for zero flow between the two geometries is given as

$$\%dev_{ToF,0} = \frac{ToFwith,0 - ToF_{without,0}}{ToF_{without,0}} \cdot 100\% \tag{5.1}$$

where $ToF_{with,0}$ and $ToF_{without,0}$ are the ToF for the geometries 'with cavity' and 'without cavity', respectively, for zero flow. For the case studied here, $dev_{ToF,0} =\simeq 0.07\%$, put it into perspective with a typical UTTF [64] examined with the SimPAC^2 method, this value is compared to the error of speed of sound (Eq. (4.6)) that has to be in the range [-0.2,0.2] %. Consequently, the existence or absence of cavity for zero flow does not exceed the set accuracy criterion of c and thus, neither of ToF but it exceeds the numerical error tolerances (cf. tabs. 4.3, 4.6). Since the differences attributed to numerics are lower compared to the difference of 0.07% observed here, it is safe to attribute this difference to the cavity, knowing that the simulation setup is the same between the two cases. Concluding, the 'cavity effect' on ToF is not large but still present for zero flow. The effect of the cavity is further discussed in the present section, for flow velocity $\neq 0$.

In Fig. 5.13 the received voltage signal against time is shown, for the two geometries and uniform flow v_{ref} ={-10,10,-20,20,-30,30} m/s. Obviously, for higher negative flow velocities (upstream), the signal arrives later, while for higher positive flow velocities it arrives earlier. It is observed that for each flow velocity, the received signals are very similar in the beginning of their arrival but differ later, especially after the maximum voltage is reached. The exact values and differences in terms of ToF and Δt between the cases are shown in the present section (cf. Figs. 5.16, 5.17, and 5.18). The differences are getting larger, particularly after the first 'ringing' part of the received signal. These differences are owed to the effect of reflections, because of the walls in the 'with cavity' case and the absence of them in the

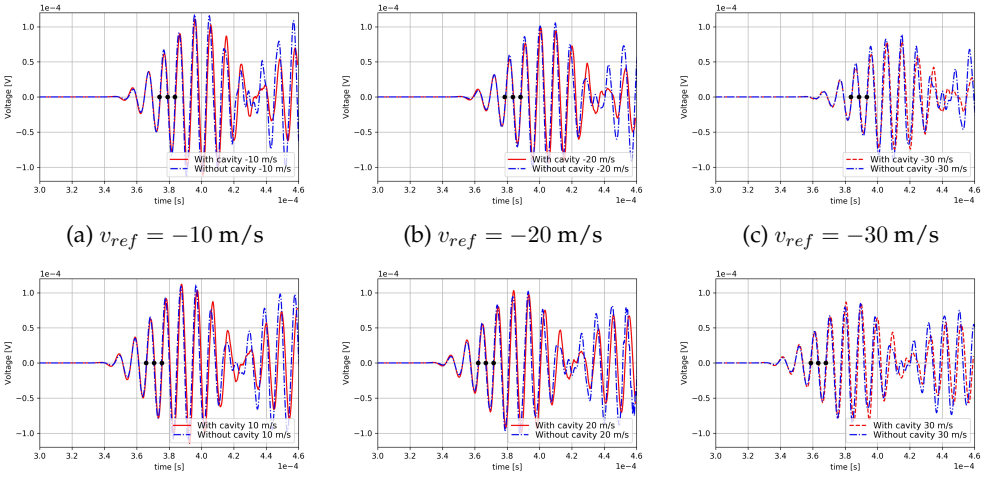

(a) $v_{ref} = -10$ m/s (b) $v_{ref} = -20$ m/s (c) $v_{ref} = -30$ m/s

(d) $v_{ref} = 10$ m/s (e) $v_{ref} = 20$ m/s (f) $v_{ref} = 30$ m/s

Figure 5.13: Voltage signal on receiver V_5 against time, solved with SimPAC^2 for uniform flow and two different geometries: 'with cavity' and 'without cavity', with three zero-crossings depicted, for uniform flow, 3D simulated. (a) $v_{ref} = -10$ m/s, (b) $v_{ref} = -20$ m/s, (c) $v_{ref} = -30$ m/s, (d) $v_{ref} = 10$ m/s, (e) $v_{ref} = 20$ m/s, and (f) $v_{ref} = 30$ m/s

'without cavity' case. Therefore, similarly to the zero flow (cf. Fig. 5.12), this observation encourages to perform signal-processing towards the start of the receiving signal, to avoid dependencies of received signals on the geometry of cavities, which are typically present for inline gas UTTF [64].

In Fig. 5.14, a zoomed view of the received voltage signal against time is shown for the two geometries and uniform flow $v_{ref} = \{-10, 10, -20, 20, -30, 30\}$ m/s. The zoom is performed on the first of the three zero-crossings, depicted in Fig. 5.13. Both upstream and downstream signals are consistently shifted in the same direction, which excludes the effect from being owed to flow (cf. Sec. 5.4), as the flow-field is nonetheless uniform for both cases. Therefore, it can be either a numerical or an acoustic effect.

The demands of accuracy are high, as described in Subsec. 4.2.3 for the speed of sound $\%error_c \in [-0.2, 0.2]\%$, however the only source of numerical deviations is the mesh, which is, by definition, slightly different for the two cases, as the geometries are not the same. A convergence study is not made for the present study, still the convergence results and conclusions of the study made in Subsec. 4.2.1 can be used in order to choose the the discretizations n_x, n_t, with the assessment that the convergence study is related to the solver. Since the n_t and n_x values of the present case are similar to Case 1d (cf. tab. 4.2), the accuracy value $ToF_{crit} = 0.0136\%$ (cf. tab. 4.3) is used as an uncertainty, with some extra tolerance set to $ToF_{crit} = 0.02\%$.

Int1 and Int2, as part of the mesh, could be potential sources of error. Based on the study made in Subsec. 4.3.2.3, a potential error was specified for Int1. This error is expected to be very similar for the two cases, since they are by definition very alike, i.e. similar mesh,

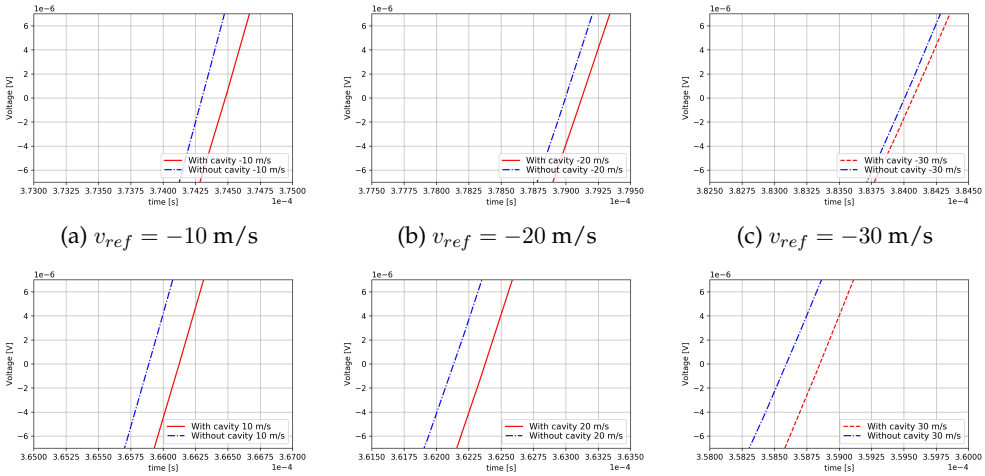

(a) $v_{ref} = -10$ m/s (b) $v_{ref} = -20$ m/s (c) $v_{ref} = -30$ m/s

(d) $v_{ref} = 10$ m/s (e) $v_{ref} = 20$ m/s (f) $v_{ref} = 30$ m/s

Figure 5.14: Voltage signal on receiver V_5 against time, zoomed on the first of the three considered zero-crossings for geometries 'with cavity' and 'without cavity', for uniform flow, 3D geometry simulated with one diagonal path. (cf. Fig. 5.13). (a) $v_{ref} = -10$ m/s, (b) $v_{ref} = 20$ m/s, (c) $v_{ref} = -30$ m/s, (d) $v_{ref} = 10$ m/s, (e) $v_{ref} = 20$ m/s, and (f) $v_{ref} = 30$ m/s.

input signal, piezoelectric elements, and fluid. Another study is performed in Subsec. 5.5, which quantifies the effect of changing the position of Int1 and Int2 on the received signal and the determination of ToF. Moreover, since n_t/n_x is constant for the two geometries, with the same type of elements, one leans towards the explanation of an acoustic effect, due to reflections in the cavities. For the upstream cases, the difference of ToF between the two geometries is reduced for higher negative flow velocities, while for the downstream cases, the difference remains fairly constant for higher positive flow velocities.

An explanation for the different behavior between the upstream and downstream propagation is that the cavities do not interact in the same way with the acoustic waves for each propagation, because of the different paths that the waves follow. A similar situation to the one described here is presented by Sun et al. [239], where the beam deflection, calculated with ray-acoustics, is different for upstream and downstream propagation for a case with cavity, with uniform flow profile, and with one diagonal path in the middle plane of the device. Thus, different interaction may be expected for the upstream and downstream cases and therefore, their effect is allowed to be different for each propagation direction, as shown e.g. also by Mylvaganam [182] and Zheng et al. [284].

Every geometry can have a unique effect, because of the different shape of the cavity and the respective flow field. The SimPAC^2 method gives quantitatively the effect of cavity on ToF, Δt, and subsequently, %deviation but a further investigation needs to be made for the identification of the exact reasons of that behavior. An effort for further explanation is made with the representation of acoustic pressure over time in the center of the interface between the front side of the cylindrical piezoelectric element of the receiver and the fluid, as shown

in Fig. 5.15, for $v_{ref} = \{-10, 10\}$ m/s. The resolution of the results over time is $8.1 \cdot 10^{-7}$s ,

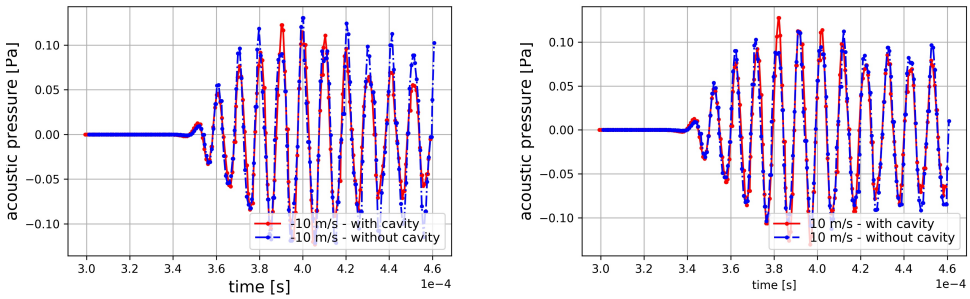

Figure 5.15: Time-parameters against flow velocity for geometries 'with cavity' and 'without cavity'. Uniform flow, 3D geometry simulated with one diagonal path. (a) t_{21} (upstream wave propagation) and (b) t_{12} (downstream wave propagation).

i.e. 3·time-step, and therefore, some peaks might not be shown as accurately as in the case of the voltage in Fig. 5.13. An interesting aspect is revealed, which is in agreement with the voltage over time shown in Fig. 5.13. The acoustic pressure for the cases 'with cavity' initially arrives earlier on the center point of the interface for both $v_{ref} = \{-10, 10\}$ m/s, due to the reflections in cavity walls, which is the only difference in the setup between the two cases. Afterwards though, and already from the first of the three zero-crossings, as shown in figs. 5.13, 5.14, the signal is 'decelerated', or in other words, because of the reflections with the cavities, both the amplitude and ToF of the acoustic pressure is different between the two cases. This is in agreement with the voltage results over time of Fig. 5.14. Moreover, the global maximum of the acoustic pressure for the case 'with cavity' is reached earlier compared to the case 'without cavity'.

The trends of ToF, t_{12} and t_{21}, determined with the three zero-crossings (cf. Fig. 5.13), as well as of Δt are shown in figs. 5.16 and 5.17. Typically, t_{12} is reduced, while t_{21} and as Δt are increased with flow velocity in a linear way. If this is not the case, the deviation curve of the UTTF, i.e. flow velocity deviation against flow velocity, or volume flow, or Reynolds number, presents non-linearities. For t_{12}, as indicated in Fig. 5.16, based on the described three-zero crossings, there is a constant offset between the two cases, independent of flow velocity, while the trend is linear. For t_{21}, also based on the three zero-crossings, the difference between the two cases is reduced with flow velocity and the trend is linear as well. Δt, as shown in Fig. 5.17, is higher for the case without cavity and the difference between the two cases is slightly increased for higher velocities.

To quantify the above remarks regarding t_{12} and t_{21}, the deviation between the ToF of the geometries 'with cavity' and 'without cavity', % $\mathrm{dev}_{\mathrm{ToF}}$ [-] is calculated, which is given by

$$\%\ \mathrm{dev}_{\mathrm{ToF}} = \frac{ToF_{with} - ToF_{without}}{ToF_{without}} \cdot 100, \tag{5.2}$$

where ToF_{with} and $ToF_{without}$ is the ToF for the geometries 'with cavity' and 'without cavity',

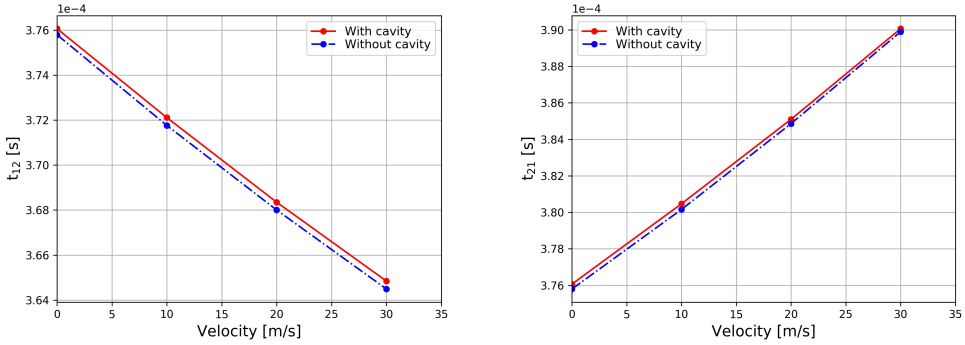

(a) (b)

Figure 5.16: Time-parameters against flow velocity for geometries 'with cavity' and 'without cavity'. Uniform flow, 3D geometry simulated with one diagonal path. (a) t_{12} (downstream wave propagation) and (b) t_{21} (upstream wave propagation).

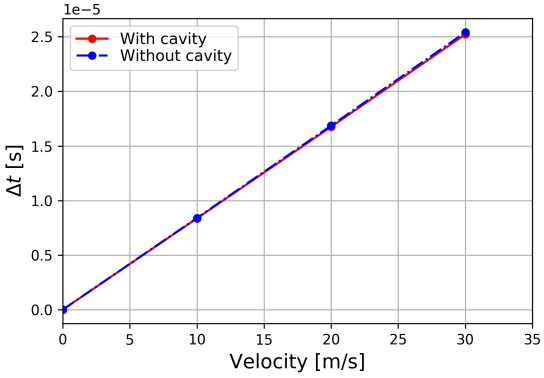

Figure 5.17: $\Delta t = t_{21} - t_{12}$ against flow velocity for geometries 'with cavity' and 'without cavity'. Uniform flow, 3D geometry simulated with one diagonal path.

respectively. Moreover, the deviation between the Δt of the geometries 'with cavity' and 'without cavity', % $\text{dev}_{\Delta t}$ [-] is given by

$$\%\ \text{dev}_{\Delta t} = \frac{\Delta t_{with} - \Delta t_{without}}{\Delta t_{without}} \cdot 100, \tag{5.3}$$

where Δt_{with} and $\Delta t_{without}$ are the Δt for the cases 'with cavity' and 'without cavity', respectively. Eqs. (5.2) and (5.3) give normalized values in % so that the 'cavity-effect' is normalized through the studied range of v_{ref}. Thus, one can directly judge, for which v_{ref} the cavity-effect is stronger. As documented in Sec. 5.4 and in chapter 6, similar versions of

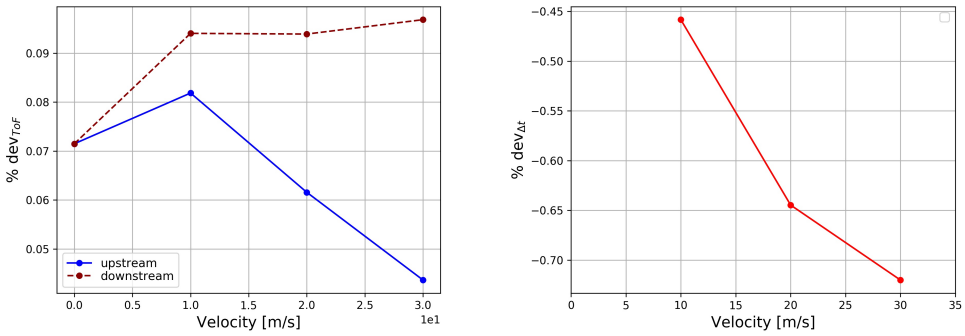

Figure 5.18: Time-parameters against flow velocity for geometries 'with cavity' and 'without cavity'. Uniform flow, 3D geometry simulated with one diagonal path. (a) % dev$_{\mathrm{ToF}}$ [-] and (b) % dev$_{\Delta \mathrm{t}}$ [-]

eqs. (5.2) and (5.3) are used for the quantification of the respective effect. % dev$_{\mathrm{ToF}}$ and % dev$_{\Delta \mathrm{t}}$ against flow velocity are shown in Fig. 5.18.

The uncertainty of ToF in the simulation, due to numerics, was set to $ToF_{crit} \in [-0.02, 0.02]$% due to the set criterion (cf. eq. (4.7)) and the convergence studies conducted in chapter 4. % dev$_{\mathrm{ToF}}$ shown in Fig. 5.18(a) is higher than the set $ToF_{crit} \in [-0.02, 0.02]$% and therefore, it cannot be owed to numerical uncertainties, which are lower than the observed effect according to the convergence studies (cf. Sec. 4.2.3). One observes that the effect for upstream and downstream propagation is different, as already seen in the contours of acoustic pressure (cf. Fig. 5.11) and studied in prior literature for a number of different USM geometries e.g. in [146, 147, 284]. More specifically, Zheng et al. [284] showed with ray-tracing that for a single path DN100 flowmeter with $\theta = 45^o$, the downstream path is further shifted compared to the upstream one. The downstream % dev$_{\mathrm{ToF}}$ presents higher values in the investigated case, as shown in Fig. 5.18(a), because of the different interaction of acoustics with the cavities when propagating in the upstream and downstream direction. Due to the % dev$_{\mathrm{ToF}}$, the % dev$_{\Delta \mathrm{t}}$ presents the respective values shown in Fig. 5.18(b). % dev$_{\Delta \mathrm{t}}$ between the two cases already tells the direction of deviation curves of the flowmeters since Δt is directly proportional to v_{path} (cf. eq. (2.91)). In particular for the cavity-effect studied here, $\Delta t_{without} > \Delta t_{with}$ for $v_{ref} = \{10, 20, 30\}$ m/s, which means that % dev$_{\Delta \mathrm{t}}$<0 for the whole range of $v_{ref} = \{10, 20, 30\}$ m/s, as confirmed also in Fig. 5.18(b). Due to the normalized values of % dev$_{\Delta \mathrm{t}}$, one can see that the cavity-effect is stronger for higher velocities. This is expected, because of the stronger deflection of the acoustic waves and their reflection on the cavity walls.

One can also follow an alternative evaluation [157] of the effect of Δt on the measured flow velocity from an USM. A typical maximum relative deviation from flow calibration of 1% at 3 m/s for an USM Proline Prosonic Flow G 300 [64] is taken into account. The method of the evaluation followed here, is described in more detail in [157]. The Δt_i of a sound path,

i, is approximately given as [157]

$$\Delta t_i \approx \frac{2Dv_{ref}}{c^2}. \tag{5.4}$$

For a simplified uncertainty analysis, when neglecting all other uncertainties other than the uncertainty of Δt_i, the standard uncertainty of Δt_i is then given approximately as [157]

$$u(\Delta t_i) \approx \frac{2D}{c^2}u(\bar{v}_i) = \frac{2D|\bar{v}_i|}{c^2}|\frac{u(\bar{v}_i)}{\bar{v}_i}| = \frac{2D|\bar{v}_i|}{c^2}E_{\bar{v}_i}, \tag{5.5}$$

where $u(\bar{v}_i)$ and $E_{\bar{v}_i}$ are the standard and relative standard uncertainties of the average flow velocity $\bar{v}_i$. For the cases presented in the present chapter, it is $c = 343$ m/s, D =97 mm, $L = 116.468$ mm, and $\theta = 65^o$. According to [157], by assuming a Type B uncertainty, at a 100% confidence level and a rectangular probability distribution with coverage factor $k = \sqrt{3}$, the corresponding relative expanded uncertainty is $2(1/\sqrt{3}\% \approx 1.15\%$ at a 95% confidence level and with a coverage factor $k = 2$. This corresponds to a relative standard uncertainty of 0.575% or by rounding up to $\approx 0.6\%$. A safety factor of 2 is used, because all other uncertainties are neglected and therefore, $E_{\bar{v}_i}$=0.6%/2=0.3%. For the calculated velocities here of {10, 20, 30} m/s it is similarly $E_{\bar{v}_i}$=0.3%.

It is calculated for $\bar{v}_i$=10 m/s and for $E_{\bar{v}_i}$=0.3% that $u(\Delta t_i) = \frac{9710^{-3}\cdot 10}{343^2} \cdot 0.3 \cdot 10^{-2} = 2.5 \cdot 10^{-8}$ s. Similarly, for $\bar{v}_i$=20 m/s, it is $u(\Delta t_i) = 5.0 \cdot 10^{-8}$ s, and for $\bar{v}_i$=30 m/s, it is $u(\Delta t_i) = 7.5 \cdot 10^{-8}$ s.

The $|\Delta t_{with} - \Delta t_{without}|$ is calculated from the simulations (cf. Fig. 5.1), and is compared to the values of $u(\Delta t_i)$. The results are summarized in Table 5.2. One can see that the

v_{ref} [m/s]	$\lvert\Delta t_{with} - \Delta t_{without}\rvert$ [s]	$u(\Delta t_i)$ [s]
10	$3.847 \cdot 10^{-8}$	$2.5 \cdot 10^{-8}$
20	$10.870 \cdot 10^{-8}$	$5.0 \cdot 10^{-8}$
30	$18.290 \cdot 10^{-8}$	$7.5 \cdot 10^{-8}$

Table 5.2: Simulated values of $|\Delta t_{with} - \Delta t_{without}|$ and 'theoretical' standard uncertainties of $u(\Delta t_i)$ for v_{ref}={10, 20, 30} m/s.

simulated values of $|\Delta t_{with} - \Delta t_{without}|$ are higher than the 'theoretical' standard uncertainties of $u(\Delta t_i)$ for the corresponding v_{ref}, which means that the effect of the cavity on Δt is of importance. This conclusion is in agreement with the conclusions drawn from the study of % dev_{ToF}, which was found to be outside the set criterion $ToF_{crit} \in [-0.02, 0.02]\%$. Thus, the 'cavity-effect' on the performance of a typical gas flowmeter [64] is of high importance as well.

In Fig. 5.19 the deviation curves of the two cases are shown, where %deviation [-] is given by Eq. (2.97). The trends of the parameters t_{12}, t_{21}, and Δt, shown in Fig. 5.16, 5.17, in combination with Eq. (2.91) explain the trend of the deviation curves. Because of the linear change of the parameters, the deviation is fairly constant for each case. The offset of the 'without cavity' compared to the 'with cavity' case in a positive direction is owed to the lower values of both t_{12} and t_{21} and higher value of Δt of the first case compared to the latter, due to the cavity presence. Furthermore, since Δt of the 'without cavity' is increased

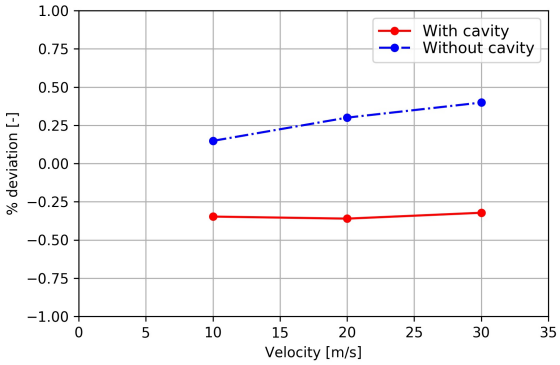

Figure 5.19: Deviation against flow velocity for two different 3D simulated geometries, 'with cavity' and 'without cavity'.

more with flow velocity compared to the 'with cavity' case, the trend of the deviation curve of the first case is positive.

Concluding, the effect of cavity is higher for higher velocities, as shown in prior literature [110, 146] , while it is manifested as a negative deviation compared to the 'without cavity' case. The difference between the deviations of the two geometries for $v_{ref} = 30$ m/s reaches $\simeq 0.7$ %. One may wonder if this effect is a numerical or a real one, due to the reflections on the cavity walls. According to the convergence studies conducted, in terms of ToF, in Subsec. 4.2.3, this value cannot be owed to numerical effects due to the presented results in Fig. 5.18. More specifically, % dev_{ToF} takes values from $\approxeq 0.043\%$ to $\approxeq 0.098\%$, which are higher than the specified range of numerical uncertainty $ToF_{crit} \in [-0.02, 0.02]\%$. Moreover, the only difference between the two studied cases is the existence of cavity or not. The cases 'with cavity' and 'without cavity' are simulated under the same conditions, with the same mesh settings, and with the same materials and therefore, any numerical errors, because of the mentioned settings, are expected to be of the same value.

The difference of 0.7 % between the % deviation of the two cases is of significance when compared with the uncertainty of ±1 % of a typical inline two-path gas UTTF [64], used as a reference here. In real applications, the effect of the cavity should be corrected by calibrating the flowmeter. The quantification of the cavity effect with the SimPAC^2 method may help in the direction of not calibrating the flowmeter but immediately implementing the correction in the model, due to the cavity geometries, as similarly done before [146].

5.4 Flow Effect

Flow-field varies inside a flowmeter, depending on the Re number and upstream conditions, having consequences on its behavior and accuracy. An UTTF should be robust for a variety of flow-fields, however variations do affect it, as flow interacts with acoustics. In this section, a number of flow-fields, i.e. flow-types, are considered in order to quantify their effects on

the flowmeter and its deviation curve (cf. tab. 5.1).

In fig 5.20 the acoustic field in the fluid near the receiver is shown for different flow types and velocities at $t = 3.43545 \cdot 10^{-4}$.

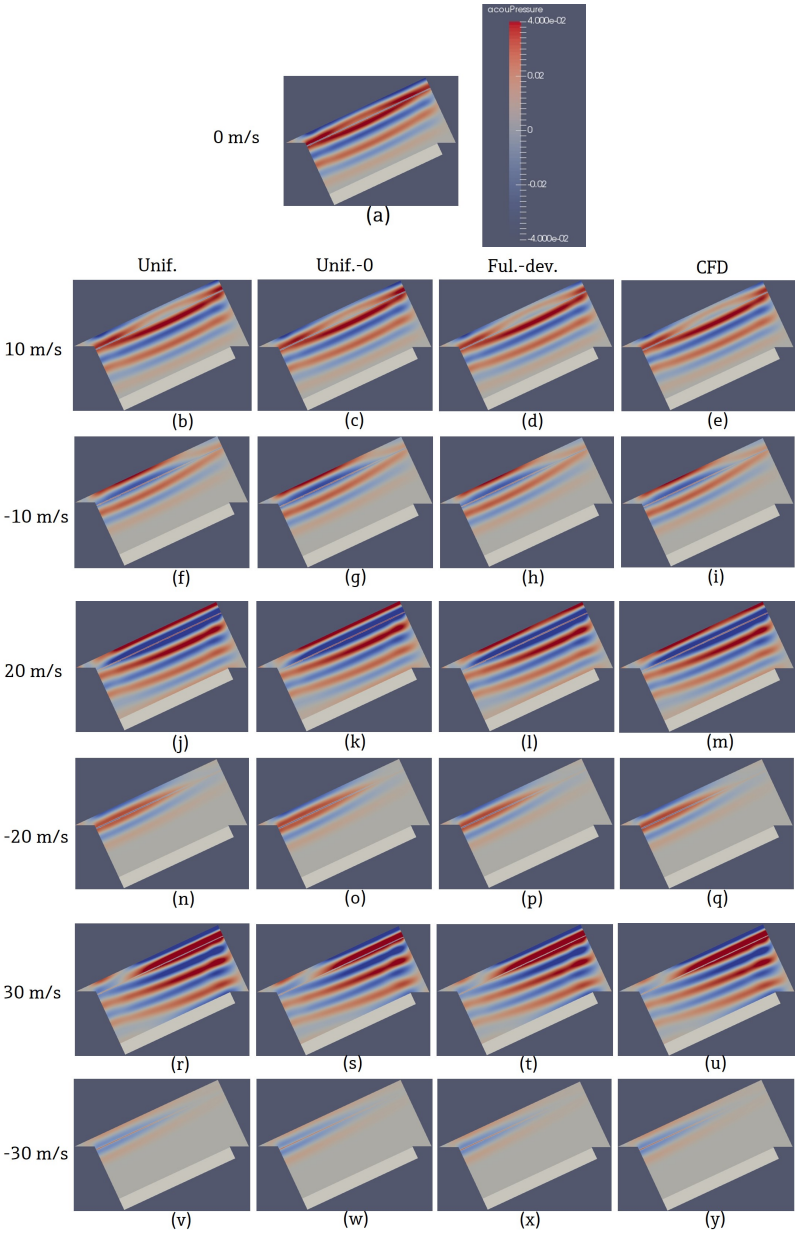

Figure 5.20: Cases 3A-0 to 3A-4. Acoustic pressure field in the fluid for part (III): receiver and fluid, at $t = 3.43545 \cdot 10^{-4}$ s, for (a) $v_{ref} = 0$ m/s, (b),(f),(j),(n),(r),(v) Unif. ; $v_{ref} = \{10, -10, 20, -20, 30, -30\}$ m/s, (c),(g),(k),(o),(s),(w) Unif.-0 ; $v_{ref} = \{10, -10, 20, -20, 30, -30\}$ m/s, (d),(h),(l,(p),(t),(x) Ful.-dev. ; $v_{ref} = \{10, -10, 20, -20, 30, -30\}$ m/s, (e),(i),(m),(q),(u),(y) CFD flow ; $v_{ref} = \{10, -10, 20, -20, 30, -30\}$ m/s, respectively.

The reader should refer to Sec. 5.1.1 for the description of the geometry and to Sec. 5.2 for a reminder and depiction (Fig. 5.8) of the considered cases and flow-fields. In Fig. 5.20(a), the pressure wave contours are shown for zero flow velocity. Each next row of subfigures of Fig. 5.20 contains pressure wave contours for the same flow velocity, while each column for the same flow type. As expected, the pressure waves arrive later for increasing negative, and earlier for increasing positive flow velocity. Furthermore, one can see that the acoustic waves are deflected downstream and upstream for positive and negative flow velocities, respectively. However, the differences of the acoustic pressure fields for a specific flow velocity and a different flow type, i.e. for each row of subfigures, are small and therefore a challenge is posed for their comparison through the contours.

A better quantification is achieved with the voltage signals on the receiver, shown in Fig. 5.21.

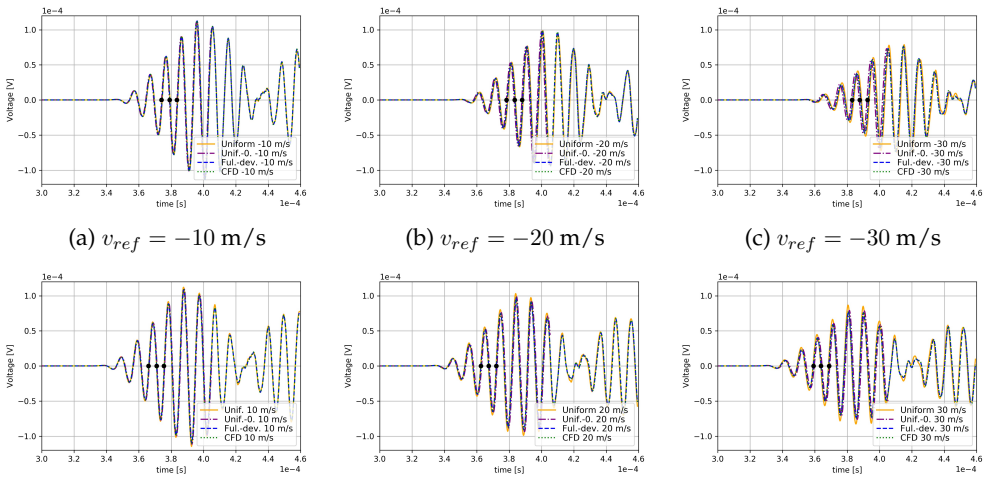

(a) $v_{ref} = -10$ m/s (b) $v_{ref} = -20$ m/s (c) $v_{ref} = -30$ m/s

(d) $v_{ref} = 10$ m/s (e) $v_{ref} = 20$ m/s (f) $v_{ref} = 30$ m/s

Figure 5.21: Voltage signal on receiver V_5 against time, solved with SimPAC^2 for different flow velocities, with three zero-crossings depicted (a) v_{ref}=-10 m/s, (b) v_{ref}=-20 m/s, (c) v_{ref}=-30 m/s, (d) v_{ref}=10 m/s, (e) v_{ref}=20 m/s, and (f) v_{ref}=30 m/s

As expected, and also already observed through the contours of pressure waves (cf. Fig. 5.20) the signals arrive at a different time depending on the flow velocity. However, the ToF differences for different flow-types and for a specific flow velocity are not as large. Unlike the cavity effect, the received signals are not drastically time-shifted at a later time of the signal pattern, such as during the 'ringing' phase or after it.

It is interesting to note that the signal-amplitude is reduced when flow velocity is increased either in negative or positive direction due to beam-deflection, as shown in Fig. 5.20. The major lobe of the pressure waves does not to impinge directly the receiver but either upstream or downstream of it in the case of negative or positive flow velocity respectively, and thereby a reduced voltage signal is observed. The exact maxima for each flow velocity and flow-type are shown in Fig. 5.22. The maximum received voltage, V_{max}, for each flow

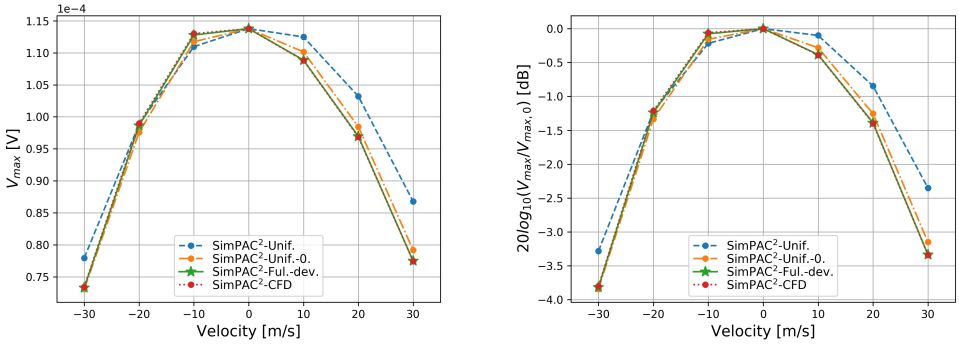

(a) (a) (b) b

Figure 5.22: Maxima of received voltage, V_{max} for each flow velocity and flow-type for the full 3D geometry shown in Fig. 5.4 and described in Subsec. 5.1.1. a) in [V], b) in [dB] relative to the highest maximum for $v_{ref} = 0$ m/s, $V_{max,0}$.

velocity is shown in [V] in Fig. 5.22(a) and in [dB] relative to the highest among the voltage maxima, $V_{max,0}$ in Fig. 5.22(b). The highest among the maxima is observed for zero velocity, since the pressure waves impinge the receiver symmetrically, with their major lobe hitting the center of the receiver (cf. Fig. 5.20).

Another interesting finding is the difference in amplitude between the respective upstream and downstream flow velocity, especially for higher v_{ref}. To quantify this effect, let us consider the case of $v_{ref} = \{-30, 30\}$ m/s, where the effects are larger and more intuitive to investigate. The maximum voltage amplitude is higher for the downstream (30 m/s) compared to the upstream case (-30 m/s). The flow is different in the cavities of the sender and the receiver, i.e. for $r > R$, for the CFD flow only, as similarly seen in prior literature [110, 146]. For each of the rest of the considered flow types, the flow is the same between the cavity near the sender and the receiver. Particularly, for the Unif. flow field, $v_0 = v_{ref}$ for both $r < R$ and for $r > R$, i.e. in the cavity. For Unif.-0 $v_0 = v_{ref}$ for $r < R$ and $v_0 = 0$ for $r > R$. For ful.-dev. v_0 varies for $r < R$ and $v_0 = 0$ for $r > R$. In other words, the flow is symmetric in respect to the xz plane for the flow fields Unif., Unif.-', and Ful.-dev. Therefore, it can be stated that the difference in amplitude between upstream and downstream cases is a purely acoustic effect owed to the cavity walls, which are not 'acoustically-symmetric', as the acoustic pressure waves reflect on them in a different way for the upstream and downstream case before impinging the receiver.

Since the differences in ToF between the flow-types, for a specific flow velocity, are not pronounced, a zoom is made on the first of the three depicted zero-crossings, as shown in Fig. 5.23. A notice that confirms the flow nature of the effect is that for each flow-type and for a pair of negative-positive flow velocities, the earliest ToF for an upstream case is the latest for a downstream one and vice-versa. E.g. the 'Unif.-0' case is always the earliest for negative flow-velocities and respectively always the latest for positive ones. In order to illuminate further the reasons for this behavior, one can analyze further the flow and its effect on the wave propagation. The case for $v_{ref} = 30$ m/s is considered, because the

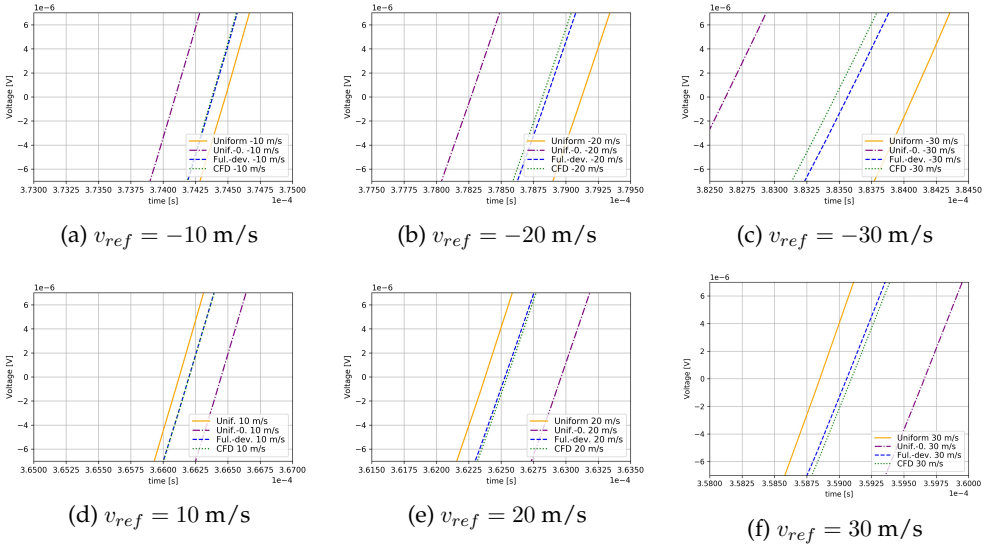

(a) $v_{ref} = -10$ m/s (b) $v_{ref} = -20$ m/s (c) $v_{ref} = -30$ m/s

(d) $v_{ref} = 10$ m/s (e) $v_{ref} = 20$ m/s (f) $v_{ref} = 30$ m/s

Figure 5.23: Voltage signal on receiver V_5 against time, zoomed on the first of the three considered zero-crossings (cf. Fig. 5.21) for different flow types, for the full 3D geometry shown in Fig. 5.4 and described in Subsec. 5.1.1. (a) v_0=-10 m/s, (b) v_0=20 m/s, (c) v_0=-30 m/s, (d) v_0=10 m/s, (e) v_0=20 m/s, and (f) v_0=30 m/s

differences are larger, and the average velocity on a line from the center of the sender to the center of the receiver, V_{line}, is calculated. If the two extreme cases of 'Unif.' and 'Unif.-0' are considered, then for 'Unif.', it is $V_{line} = 30$ m/s, while for 'Unif.-0' it is V_{line}=27.9 m/s. The lower V_{line} for 'Unif.-0' compared to 'Unif.' is a sign that for 'Unif.-0' the wave will reach the receiver later for the downstream propagation and earlier for the upstream one. Further analysis is needed to fully understand the effect. More sophisticated analysis based on the observed flow-field is made in the present section and in chapter 6.

The difference in ToF between the 'Ful-dev.' and 'CFD' cases (here meant SimPAC^2-CFD) is small, due to the very similar flow-fields. However, it is observed that the cases coupled with a real CFD flow arrive earlier for upstream and later for downstream propagation. In Fig. 5.24, the vectors of the normalized velocity fields ($\boldsymbol{v_0}/v_{ref}$) are shown for the CFD flows at $v_{ref} = \{10, 20, 30\}$ m/s. The difference in ToF is owed to the vortices inside the cavities, considered in the SimPAC^2-CFD case. Flow in the upstream direction is observed that decelerate the acoustic wave propagation in the downstream direction (t_{12}) and accelerate it in the upstream direction (t_{21}) compared to the Ful.-dev. case, where zero flow is considered in the cavities. In Fig. 5.24 one can see the different flow field inside the upstream and downstream cavities, as already shown e.g. in [110, 146]. For the real transducers considered in chapter 6, larger differences are expected. The reason is that for the real transducers, the cavities are larger (cf. Sec. 3.2) and subsequently, the generated vortices in the cavities and in front of the transducers are larger and more variable compared to the small cavities of Case 3A. More details are given in chapter 6.

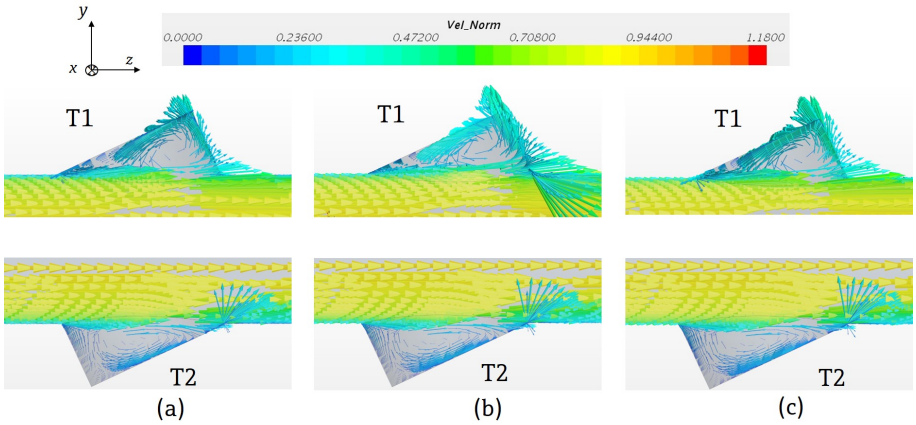

Figure 5.24: Flow fields depicted with vectors near the transducers T1 and T2 for (a) $v_{ref} = 10$ m/s, (b) $v_{ref} = 20$ m/s, and (c) $v_{ref} = 30$ m/s. Simulated full 3D geometry shown in Fig. 5.4 and described in Subsec. 5.1.1.

The case of the 'Unif.' flow field presents higher differences of ToF and Δt compared to the other flow-fields, because of higher flow velocity along the sound path, i.e. uniform velocity inside the cavities as well. As described in Subsec. 5.2, mass conservation is violated for this artificial setup, examined for the purpose of studying the effect of different flow types on the wave propagation. Therefore, due to practically higher volume flow for the 'Unif.' case compared to the rest of the cases, the pressure waves arrive latest for the upstream cases and earliest for the downstream ones.

The values of ToF averaged over three zero-crossings, as well as Δt are shown in Fig. 5.25. The differences of ToF and Δt among the signals, shown in Fig. 5.25, are reflected on the

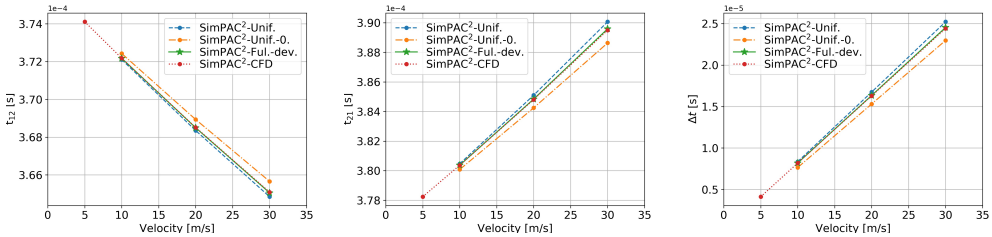

Figure 5.25: Time-parameters against velocity. (a) t_{12} (downstream wave propagation), (b) t_{21} (upstream wave propagation), and (c) $\Delta t = t_{21} - t_{12}$. 3D geometry simulated with one diagonal path.

deviation curves, shown in Fig. 5.26. 'Unif.' and 'Unif.-0' are the two extreme cases in terms of Δt and in terms of % deviation. One can observe in Fig. 5.26 that for the 'Unif.' and 'Unif.-0' cases, linear deviation curves present a large offset between them, which is owed

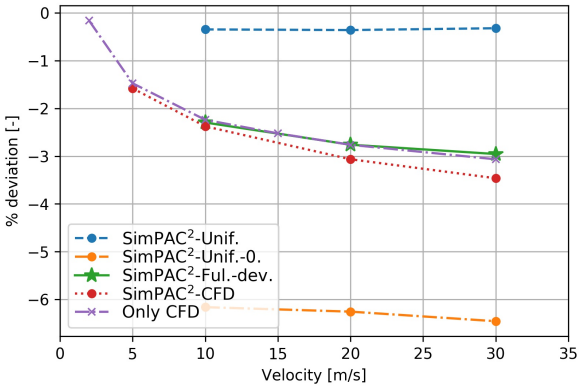

Figure 5.26: % deviation against flow velocity for different flow types and simulations methods. 3D geometry simulated with one diagonal path.

to practically different volume flows, as already noticed. The differences between 'Ful.-dev.' and 'CFD' are reduced, since the the flow differences between them are small but significant (cf. Fig. 5.24). Moreover, the same volume flow is compared between 'Ful.-dev.' and 'CFD' and therefore, their difference is not as large as between the 'Unif.' and 'Unif.-0'., where practically 'Unif.' respects to a higher volume flow along the sound path. Non-linearities appear when a non-uniform flow profile is considered, which are in agreement with the Only CFD (CNA method) case, where acoustic effects are not taken into account (cf. Sec. 3.1). Consequently, it can be stated with confidence that the non-linearities are highly owed to the flow profile. The differences between the 'SimPAC^2-Ful.-dev.' and 'SimPAC^2-CFD' cases, which reach values of 0.505% for $v_{ref} = 30$ m/s (cf. Fig. 5.26), reflect combined flow-acoustic effect due to the zero flow and presence of vortices in the cavities, respectively.

Here, Δt values play a major role for the shifting of the deviation curves. The flow-nature of the effect, i.e. same geometry investigated with different flow-field considered, causes t_{12} and t_{21} to increase and decrease respectively, or vice-versa, in a similar way, making their multiplication remain fairly constant and therefore, having insignificant effect on the calculated flow velocity (cf. eqs. (2.91), (2.97)). In other words, the trend of the calculated flow velocity ((2.91)) and % deviation (2.97) is driven by the Δt values.

This observation is further studied with the calculation of the multiplication $t_{21} * t_{12}$ [s^2] and % dev$_{\Delta t}$ [-] given as

$$\%\ \mathrm{dev}_{\Delta \mathrm{t}} = \frac{\Delta t_{flow-field} - \Delta t_{Unif.}}{\Delta t_{Unif.}} \cdot 100, \tag{5.6}$$

where $\Delta t_{flow-field}$ and $\Delta t_{Unif.}$ are the time-differences Δt for the the investigated flow-field and the 'Unif.' flow-field, respectively. The parameters $t_{21} * t_{12}$ and % dev$_{\Delta t}$ are shown in Fig. 5.27. In Fig. 5.27(a) it is observed that the multiplication has a positive trend for all cases, meaning that for higher flow velocity, t_{21} increases more than t_{12} decreases

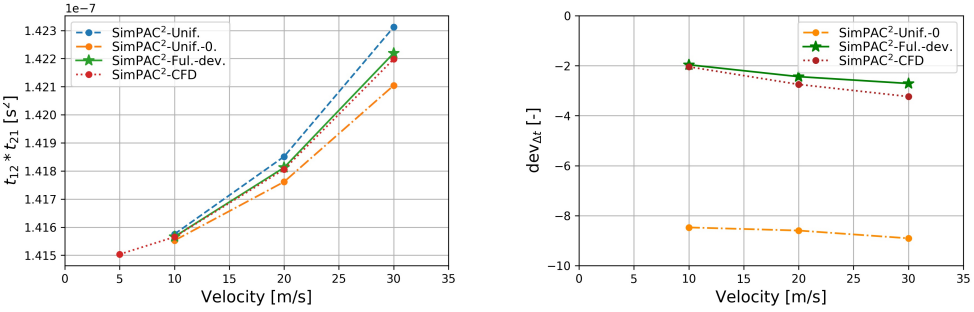

(a) (b)

Figure 5.27: Time-parameters against flow velocity for cases 3A-1 to 3A-4 with different flow-fields considered (cf. 5.1). 3D geometry simulated with one diagonal path. (a) $t_{12} * t_{21}$ [s^2] and (b) % dev$_{\Delta t}$ [-].

for a specific flow velocity. This is in agreement with the results of Zheng et al. [284], where it is calculated that the downstream propagating waves are further shifted than the upstream ones. Consequently, as shown in [284], the waves propagate for a longer distance for downstream compared to upstream propagation for the same v_{ref}. That means as well that t_{21} increases more than t_{12} decreases for the same v_{ref}, which is in agreement with the present study.

The deviation between maximum and minimum $t_{12} * t_{21}$ at maximum and minimum flow velocity, respectively is of the order of $\simeq$ 0.5 %, which means that the $t_{12} * t_{21}$ does not contribute much to the differences among the deviation curves of Fig. 5.26 (cf. eq.(2.91)). The highest difference is observed for the 'Unif.' flow-field, where v_0 is the highest along the path among the cases. A further investigation of the flow-field and its effect on ToF is made in chapter 6. In Fig. 5.27(b), with the 'Unif.' flow field taken as a reference for the calculation of dev$_{\Delta t}$, it is shown that the differences among Δt are much higher compared to the differences of the multiplication $t_{21} * t_{12}$ among the cases, i.e. up to 8.7 %. Consequently, as noticed, the trends of %deviation [-] are driven by the Δt values, due to the different flow-fields as described through Fig. 5.24 and the relevant explanations.

The 'Only CFD', i.e. CNA, case is in good agreement with the 'SimPAC^2-Ful.-dev.' case, as shown in Fig. 5.26, which is believed to be a coincidence for this specific geometry, as it takes into account only flow effects. For larger cavities and different behavior of the flow-field, another behavior of the 'Only CFD', i.e. CNA, method is expected, as shown in chapter 6.

5.5 Interface Investigation

In order to investigate if the current choice of the position of interfaces Int1 and Int2 has an influence on the results, an interface investigation is carried out. Artificial, spurious reflections from the absorbing BCs, as defined in Fig. 5.4, are possible to influence the

received voltage. Part of the pressure waves are reflected back from the absorbing BCs [30] and impinge the receiver. The more challenging geometry, 'with cavity' (Case 3A), in terms of reflections, is chosen. Int1 and Int2, together with the outer surfaces of the fluid, which are parallel to the front surfaces of the piezoelectric elements, are shifted by 2 mm nearer to the sender and the receiver, respectively, relative and parallel to the transducers' front surfaces. Therefore, the dimensions of part (I) denoted in Fig. 5.4(b) as 3 mm and 8 mm, and the dimensions of part (III) denoted in Fig. 5.4(f) as 2 mm and 9 mm ('Standard' geometry) change to 1 mm and 6 mm for part (I) and to 2 mm and 6 mm for part (III) ('Smaller' geometry), respectively.

In Fig. 5.28 the field of acoustic pressure [Pa] in the fluid near the receiver is shown, for $v_{ref} = 0$ m/s at $t = 3.439045 \cdot 10^{-4}$ s, for the two described geometries. One can observe

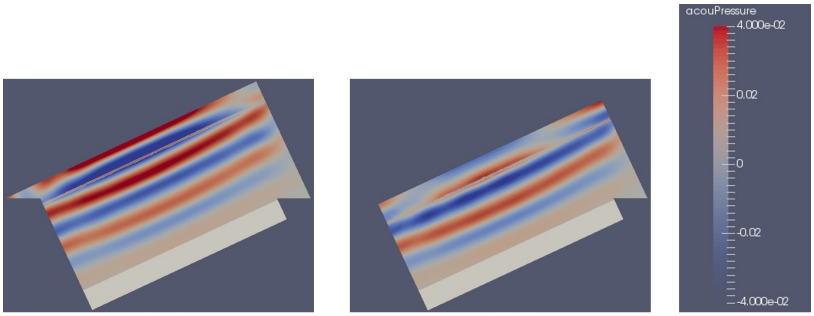

Figure 5.28: Acoustic pressure field in the fluid for part (III): receiver and fluid, at $t = 3.439045 \cdot 10^{-4}$ s, $v_{ref} = 0$ m/s. (a) 'Standard' geometry with dimensions shown in Fig. 5.4) and (b) 'Smaller' geometry, 2 mm ($1.53\lambda_{air}$) smaller fluid geometries. 3D geometry case simulated with one diagonal path.

the qualitative similarity of the two acoustic pressure fields in terms of ToF and amplitude. The wavefronts are located at a similar distance from the receiving piezoelectric element despite the difference of the Int2 location and the smaller size of the geometry of Fig. 5.28. However, one can observe that the acoustic pressure field for the smaller geometry is slightly more distorted, potentially because of artificial reflections from the nearer absorbing BC.

The effect can be better quantitatively investigated through the comparison of the received voltage signals shown in Fig. 5.29.

A criterion was set with Eq. (3.20) regarding reflections in part (I). The criterion is not entirely satisfied for the 'Smaller' geometry, since $t_3 > t_{refl}$, as shown with a vertical dashed blue line in Fig. 5.29. However, it can be said, due to the presented results, that even the last of the three zero points shown with black circles in Fig. 5.29 are not influenced from the artificial reflections. On the other hand, the criterion is clearly satisfied for the 'Standard' geometry, as shown with a vertical dashed red line.

Another criterion was set with Eq. (3.24) to investigate the time at which artificial reflections impinge the receiver for a chosen geometry of part (III). This criterion is not entirely satisfied for the 'Standard' geometry, $t_{3,3} > t_{refl,rec}$, as shown with the dotted red vertical line, which coincides with the blue dashed one. Similarly, it can be said for the 'Standard'

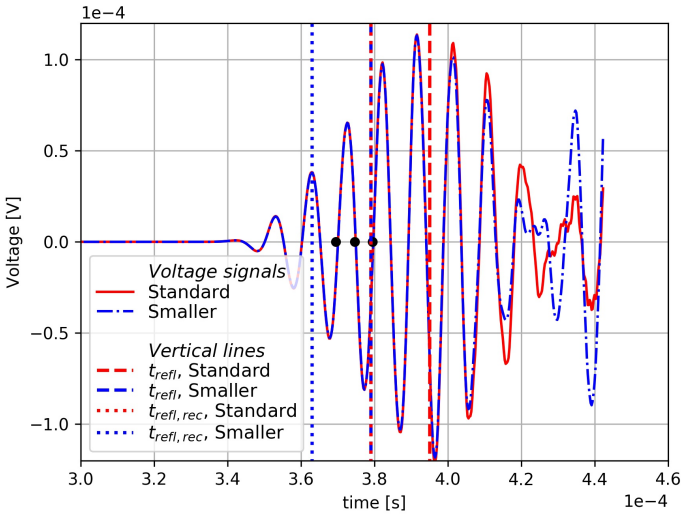

Figure 5.29: Acoustic pressure field in the fluid for part (III): receiver and fluid, at $t = 3.439045 \cdot 10^{-4}$ s, $v_{ref} = 0$ m/s. (a) 'Standard' geometry with dimensions shown in Fig. 5.4) and (b) 'Smaller' geometry with 3 mm smaller fluid dimensions, as described in the present section.

geometry that even the last of the three zero points shown with black circles in Fig. 5.29 are not influenced from the artificial reflections. For the 'Smaller' geometry, the criterion is clearly not satisfied, since $t_{3,3} > t_{refl,rec}$, as shown with the dotted blue vertical line. Consequently, if the absorbing BCs do not absorb 100% of the impinging waves, spurious reflections are expected for times higher than the vertical lines. That is clearly the case for the 'Smaller' geometry, while the last of the three considered zero-crossings is slightly affected for the 'Standard' case.

The comparison of ToF between the two received signals is of high interest in order to evaluate if the effect of the shift of the interface is of importance according to the criterion of ToF_{crit}, which in that case is

$$ToF_{crit} = \frac{ToF_{standard} - ToF_{smaller}}{ToF_{smaller}} \cdot 100\ \% \in [-0.02, 0.02]\ \%, \tag{5.7}$$

where $ToF_{standard}$ and $ToF_{smaller}$ are the ToF calculated with the three zero-crossings for the 'standard' and the 'smaller' geometry, respectively. It is calculated that

$$ToF_{crit} = \frac{3.76061 \cdot 10^{-4} - 3.76085 \cdot 10^{-5}}{3.76085 \cdot 10^{-5}} \cdot 100\ \% = -0.006\ \% \in [-0.02, 0.02]\ \%.$$

Thus, the shift of the inteface has a small impact on the important parameter of ToF, as it satisfies the set criterion (cf. eq. (5.7)).

Due to the satisfaction of ToF_{crit}, one can argue that in the beginning of the signal and up to its maximum at $t \simeq 3.93 \cdot 10^{-4}$ s, the two received voltage signals are identical but after the maximum they start to deviate from each other (cf. Fig. 5.29). The ringing phase is different due to interferences and artificial reflections. Thus, even when the set criteria are not entirely satisfied, the effect on the received voltage signal appears later.

It is shown that the initial part of the signal is not influenced by artificial reflections for the 'Standard' geometry according to the criterion of Eq. (3.20), since even if they are present, they have not reached the receiver yet. The small effect of the shift of the interface is further confirmed from the satisfaction of ToF_{crit} as defined in eq. (5.7). According to the criterion set from Eq. (3.24), not entirely safe conclusions can be drawn. However, it is highly unlikely that spurious reflections in part (III) of the 'Standard' geometry influence the shown zero-crossings as shown in Fig. 5.29, since the reflections have just reached the frontal surface of the receiver $\simeq 10^{-5}$ s earlier than the last of the three zero-crossings. This value is the difference between the vertical line of $t_{refl,re}$ and the last of the three zero-crossings for the standard geometry.

One can notice the similarity of the effect with the real reflections due to the cavity walls in Sec. 5.3, where differences between the voltage signals appear on a later part of the signal (Fig. 5.12, 5.13).

Additionally, it is concluded, that especially for cases, where the sender and receiver domains together with the fluid around them must be small, the initial part of the signal should be preferably used for the signal-processing.

5.6 Summary and Conclusions

SimPAC^2 is used for the investigation of effects that have been of high interest in UTTF. The effect of cavity geometries is studied and compared for a domain without cavities for uniform flow. The cavity walls influence the received voltage signal in a different way for upstream and downstream wave propagation. Moreover, the cavity effect, is owed solely to acoustics, since the compared cases are examined under same flow conditions, i.e. uniform flow profile. The effect is quantified in terms of ToF, dt and %deviation, for a number of flow velocities and is found to be of significance, since for $v_{ref} = 30$ m/s uniform flow, the difference between the deviations of the two cases, 'with cavity' and 'without cavity', reaches 0.7%. Such a study, where the pure 'cavity-effect' is quantified due to the geometrical difference of the cavity, but exactly the same flow-field i.e., uniform, has not been performed to the author's knowledge. Many interesting studies have been conducted regarding the different effect of the upstream and downstream cavities and the shape of the cavity e.g. in [110, 146, 147, 209, 239, 284] or the position of the transducers i.e. recessed, flush, protruded e.g. in [208, 261, 286], but none that quantifies the pure 'cavity-effect', as defined in the present thesis. For all these prior studies, when the geometry of the cavity changes, the flow changes as well, as in reality. The novelty of the present study is the quantification of the effect of the geometry of the cavity purely, since the flow considered is the same for the ' with cavity' and 'without cavity' cases.

The effect of different flow-fields is investigated as well with the aid of SimPAC^2. The considered flow-fields are uniform, uniform with zero flow in cavities, fully-developed with zero flow in cavities and CFD flow. It is found that the 'SimPAC^2-Unif.' and 'SimPAC^2-Unif.-

0' cases deviation curves are highly linear, while the 'SimPAC^2-Ful.-dev.', and 'SimPAC^2-CFD' deviation curves present non-linearities. It is concluded that these non-linearities are caused mainly by the flow-field, as shown before in [197]. A significant difference of up to 0.505% is observed in deviation between the case of a fully developed flow ('SimPAC^2-Ful.-dev.'), and the 'SimPAC^2-CFD' case. The non-linearities are present also in the 'Only CFD' (CNA) case, which is in agreement with the respective SimPAC^2 cases. Similarly to the present study, Løland showed before [146] that the flow inside the cavities should not be neglected, while he suggested a correction due to the flow in the cavities. The different effect of the upstream and downstream cavity described in Sec. 5.4 is in agreement with previous studies e.g. [110, 146, 284]. Moreover, it is shown that t_{21} increases more than t_{12} decreases for the same v_{ref}, which is in agreement with the study of Zheng et al. [284], where it was described that the downstream propagating waves are shifted more compared to the upstream ones.

The effect of the position of interfaces Int1 and Int2, as well as the size of the considered fluid domain near the sender and the receiver are studied. The effect of artificial reflections is more profound for a later part of the signal. It is concluded in the study made in Sec. 5.5 that it is beneficial to use the initial part of the signal for the estimation of ToF.

The consideration of a fully-developed flow profile has been so far the state-of-the-art when combined with acoustics and piezoelectricity for the simulation of a 3D UTTF [30, 31, 32]. A CFD profile in combination with acoustics has been simulated previously [239] but for a 2D geometry without the consideration of piezoelectricity. Recently, Mousavi et al. [179] presented a semi-3D simulation of an UTTF with CFD and piezoelectricity included. The effect of inlet flow conditions or position of the transducers on UTTF has been systematically studied before with simulations, e.g. in [84, 264, 286] but only with the help of CFD. However, there is no such systematic study of flow-effects for 3D UTTF geometry, with the use and combination of piezoelectricity, acoustics, and CFD simulations in 3D, to the author's knowledge. The effect of flow on an UTTF with real transducers is further investigated in chapter 6.

Chapter 6

Simulations and Measurements of an Industrial Flowmeter

In this chapter, real, industrial ultrasonic transducers for UTTF are introduced, simulated and measured. Initially, the curve of impedance over frequency is measured and simulated. Through the fitting of the simulated impedance curve on the measured one, the piezoelectric parameters are estimated. UTTF with one diametrical chord sound path and several insertion-depth positions of the ultrasonic transducers are simulated, i.e. recessed, flush, and protruded. A two-path UTTF is measured and simulated, while the results' agreement is investigated. For the simulations both the CNA and SimPAC^2 methods are used.

6.1 Determination and Optimization of Piezoelectric Parameters

Piezoelectric materials are anisotropic and depending on the class that they belong [15], (Sec. 2.1.3) the structure of the elastic stiffness, piezoelectric and dielectric constant tensors varies. Their complex, anisotropic structure makes the determination of the exact values of their parameters a non-trivial task, while the values given by the manufacturers are often not accurate enough for high-precision simulations. An incorrect set of parameters is a source of errors for a transient simulation of a transducer or an UTTF, especially in the case of direct comparisons between measurements and simulations, where high precision is needed. In the present thesis, such comparisons take place (cf. Sec. 6.3) and therefore, the exact parameters must be set beforehand.

The piezoelectric material of the elements used in the studied cases in the present chapter is Pz27 5A from MEGGiT[244] belonging to the crystal class 6mm [15]. 10 independent

material parameters are given as

$$[\boldsymbol{c}^E] = \begin{pmatrix} c_{11}^E & c_{12}^E & c_{13}^E & 0 & 0 & 0 \\ c_{12}^E & c_{11}^E & c_{13}^E & 0 & 0 & 0 \\ c_{13}^E & c_{13}^E & c_{33}^E & 0 & 0 & 0 \\ 0 & 0 & 0 & c_{44}^E & 0 & 0 \\ 0 & 0 & 0 & 0 & c_{44}^E & 0 \\ 0 & 0 & 0 & 0 & 0 & (c_{11}^E - c_{12}^E)/2 \end{pmatrix}, \tag{6.1}$$

$$[\boldsymbol{e}] = \begin{pmatrix} 0 & 0 & 0 & 0 & e_{15} & 0 \\ 0 & 0 & 0 & e_{15} & 0 & 0 \\ e_{31} & e_{31} & e_{33} & 0 & 0 & 0 \end{pmatrix}, \tag{6.2}$$

$$[\boldsymbol{\epsilon}^S] = \begin{pmatrix} \epsilon_{11}^S & 0 & 0 \\ 0 & \epsilon_{11}^S & 0 \\ 0 & 0 & \epsilon_{33}^S \end{pmatrix}, \tag{6.3}$$

where all properties in the matrices (6.1), (6.2), and (6.3) are real. More information on piezoelectric materials are given in Subsec. 2.1.3.

A cylindrical piezoelectric element is measured and simulated with radius 5 mm and thickness 3 mm for the correct set of the parameters.

An optimization takes place that combines several steps and programs in order to identify the material parameters. A diagram of the process followed for the parameters' definition and optimization is shown in Fig. 6.1.

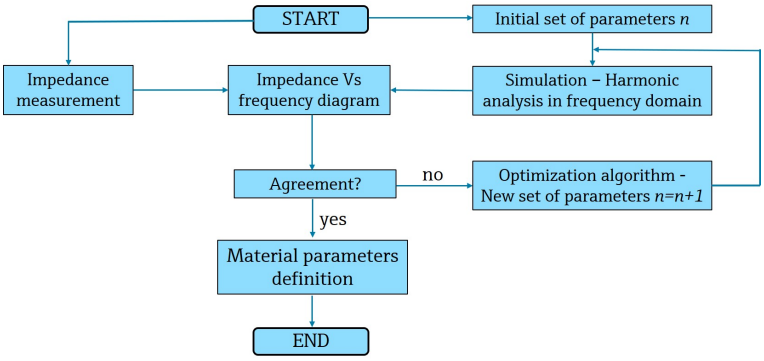

Figure 6.1: Process for the correct definition of the piezoelectric material parameters.

Initially, an impedance measurement with an impedance analyzer is performed for a range of frequencies [10, 500] kHz with a step of 500 Hz. The impedance analyzer is a 'E5100A Network Analyzer' from Keysight Technologies [112], and it is used for both the excitation and recording of the respective impedance of the piezoelectric element over the frequency. The piezoelectric element is excited with a broadband charge $q(t)$. From the measurement, impedance magnitude, $|Z|$ and phase, ϕ_z, versus frequency diagrams are obtained. For the

impedance $Z(j\omega)$ in the frequency domain, with $j = \sqrt{-1}$, it is

$$Z(j\omega) = \frac{V_5(j\omega)}{I(j\omega)} = -\frac{V_5(j\omega)}{j\omega Q(j\omega)}, \tag{6.4}$$

where $I(j\omega) = F\{i(t)\}$, $V_5(j\omega) = F\{v_5(t)\}$, and $Q(j\omega) = F\{q(t)\}$ are the Fourier transforms in the frequency-domain of the current $i(t)$, voltage $v_5(t)$, and charge $q(t)$ in time-domain, respectively [30].

Simulations are performed as well, initially with the initial parameters given by the manufacturer for the Pz27 5A material [244]. More particularly, a harmonic analysis of the axisymmetric piezoelectric element for a range of frequencies [10, 500] kHz with a step of 500 Hz is made, with the FEM program NACS. On one of the flat surfaces of the piezoelectric element, a ground BC is defined, while on the second flat surface, charge, $Q(j\omega)$ and equipotential BCs are applied. For the simulation two additional Rayleigh damping parameters a_M and β_k are defined and optimized [107], since it is not possible to use complex piezoelectric parameters in NACS in that case. The voltage, $V_5(j\omega)$, on the piezoelectric element is obtained and thus, impedance $Z(j\omega)$ is calculated from eq. (6.4).

One can choose a number of strategies and optimization algorithms for the material parameters' definition. A sensitivity analysis is performed prior to the optimization in order to determine the effect of each parameter on the impedance curve and the correlation with the change of the curve. For the sensitivity analysis each of the parameters, $c_{11}, c_{12}, c_{31}, c_{33}, c_{44}, e_{31}, e_{33}, e_{15}, \varepsilon_{11}, \varepsilon_{33}, a_M$, and β_k is varied consecutively by $\pm 50\%$, while the rest pf the parameters are kept constant in order to evaluate the effect of each parameter on the impedance over frequency. The results of this study are not presented here, as it would be out of the scope of this work.

As optimization criterion, the minimization between the measured and simulated values is set, i.e. [30]

$$Crit = min \sum_{i=1}^{M} \sqrt{(20log_{10}|Z_{i,meas}| - 20log_{10}Z_{i,sim})^2}, \tag{6.5}$$

where i is a specific frequency step, M the total number of steps, $|Z_{i,meas}|$ the measured impedance amplitude for a step of frequency, i, and $|Z_{i,sim}|$ the respective simulated impedance amplitude.

The software used for the optimization is optiSLang® [16], which is coupled with NACS for the harmonic analysis FEM simulation and python for additional post-processing and coupling of NACS with optiSLang®. The process is schematically shown in Fig. 6.2. After a sensitivity analysis, the optimization algorithm 'Adaptive response surface method' (ARSM) is used [262], where the parameters $c_{11}, c_{12}, c_{31}, c_{33}, c_{44}, e_{31}, e_{33}, e_{15}, \varepsilon_{11}, \varepsilon_{33}, a_M$, and β_k are taken into account, while the density is set to ρ_{PZT} =7700 kg/m^3 [244], as it is given from the manufacturer company, MEGGiT [245]. The manufacturer parameters for Pz27 5A [244] are shown in table 6.1. The simulated impedance result obtained with the manufacturer parameters and its comparison with the measurement is shown in Fig. 6.3. Such large differences are not acceptable and therefore, more accurate values should be specified for their later utilization on the transient simulation of the UTTF. 500 designs (sets of parameters) are simulated, with the convergence history being shown in Fig. 6.4. More specifically, the

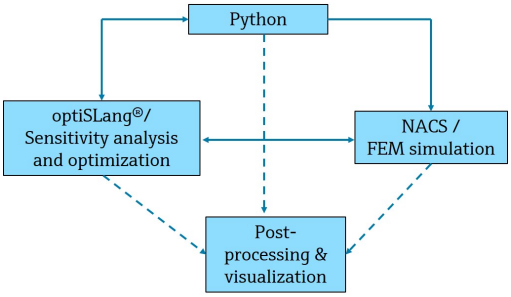

Figure 6.2: Optimization process, software used, and coupling among the programs.

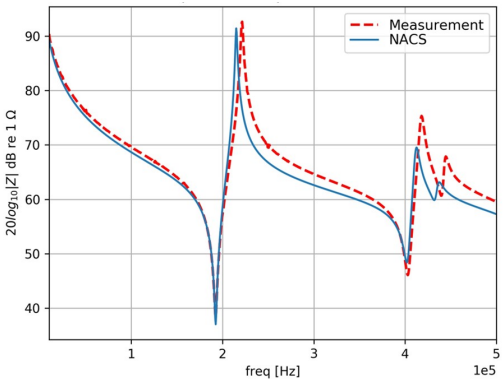

Figure 6.3: Measured and simulated $20log_{10}|Z|$ dB re 1 Ω for the initial material parameters.

value of $Crit$ (eq.(6.4)) on the y-axis against the number of design on the x-axis is shown. It seems that the algorithm converges to a minimum value of $Crit$, with the best design having $Crit = 28.2967$. No specific minimum value was set for the $Crit$ as a goal, however the comparison of the diagram of impedance against frequency from measurements and simulations was observed for each of the 500 designs along with the value of $Crit$. The simulated impedance result obtained with the optimized parameters that give the minimum $Crit$ among the simulated designs and its comparison with the measurement is shown in Fig. 6.5.

The values of the manufacturer as well as the optimized parameters are given in table 6.1. The Rayleigh parameters a_M and β_k are used in the simulation for the introduction of damping in NACS.

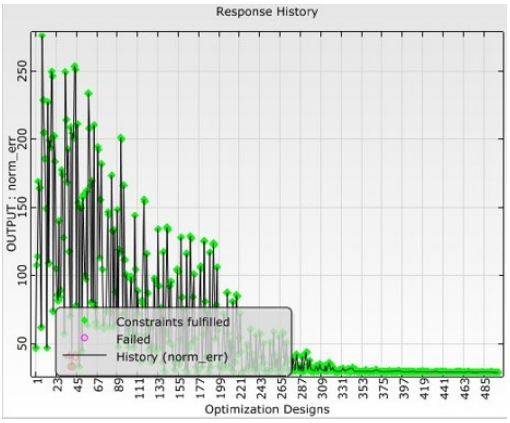

Figure 6.4: Convergence of optimization criterion

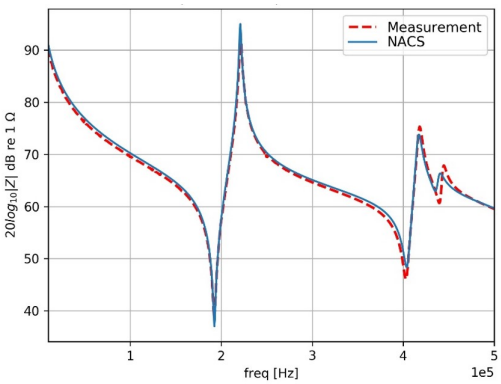

Figure 6.5: Measured and simulated $20log_{10}|Z|$ dB re 1 Ω for the optimized material parameters.

Material parameter	Manufacturer's properties [244]	Optimized properties
c_{11} [N/m^2]	1.47e11	136,819,561,983.709
c_{12} [N/m^2]	1.05e11	7.970e10
c_{13} [N/m^2]	9.37e10	85,044,080,218.915
c_{33} [N/m^2]	1.13e11	120,282,425,103.475
c_{44} [N/m^2]	2.30e10	1.990e10
e_{31} [C/m^2]	-3.09	-3.813
e_{33} [C/m^2]	16.00	15.840
e_{15} [C/m^2]	11.64	10.660
ε_{11} [F/m]	1.59e-8	9.310e-9
ε_{33} [F/m^2]	1.59e-8	1.017e-8
a_M [-]		4000
β_k [-]		5.120e-9

Table 6.1: Manufacturer's and optimized material parameter values for Pz27 5A [244].

6.2 Flowmeter with One Diametrical Path: Introduction of Transducers

A variation of the insertion depth of the transducers is performed with the aim of systematically investigating the effect of cavities on:

- Acoustic wave propagation
- Flow-field
- Interaction between acoustics and flow
- Linearity of the UTTF

Three different insertion depths of the transducers are simulated with the CNA and SimPAC^2 methods, i.e. flush, recessed, and protruded transducers. The reader is referred to 5.1 for a reminder of the definition of the transducer position.

The effect of the position of the transducers has been previously simulated but only with either the help of CFD or experimentally e.g. in [260, 286]. Different conclusions are drawn in the present thesis regarding the transducers' position compared to [286] showing that no general statements can be made regarding the optimum position of the transducers, which is a complex 3D matter interdependent with the whole geometry of the meter body, the path arrangement and the transducer cavities.

For all three transducer positions, the medium is air, at temperature $T_0 = 19.4^o$C, pressure, $p_0 = 1$ bar, and speed of sound, $c = 342.8$ m/s. The carrier frequency used is $f_c = 100$ kHz for a sinusoidal input voltage signal of amplitude $|V_1|$=1 V and length $4T_c$, where $T_c = 1/f_c$.

6.2.1 Flush Transducers

6.2.1.1 Simulation Setup

The case of an UTTF with one diametrical chord and flush transducers is simulated. The geometry of the UTTF is shown in Fig. 6.6. The diameter of the pipe is D=97 mm, the angle between the main axis of the pipe and the sound path is $\theta = 65^o$, the radius of the front face of the transducer is $R_{trans} = 5.75$ mm, the distance between the center of the frontal surfaces of the transducers is L=112.58 mm, while b depicts the intersection between the sound path axis and the imaginary line parallel to the main axis of the pipe at distance R=48.5 mm ($D/2$). The distance between the center of the frontal surface of the transducer and point b is L_{cav}=2.78 mm. The length of the simulated domain is $L_{dev} = 160$ mm and the radius of the cylindrical part of the cavity is D_{cav}=25.6 mm. A more detailed description and depiction of the transducers' geometry, the simulated parts, BCs, and general simulation setup is given in Sec. 3.2. The exact geometry simulated is uploaded online [**?**]

The piezoelectric elements consisting of Pz27 5A [244], used in the simulated UTTF, are shown in Fig. 6.7. *Piezo2* is positioned on the inner surface of the transducer, while '*Piezo1*'

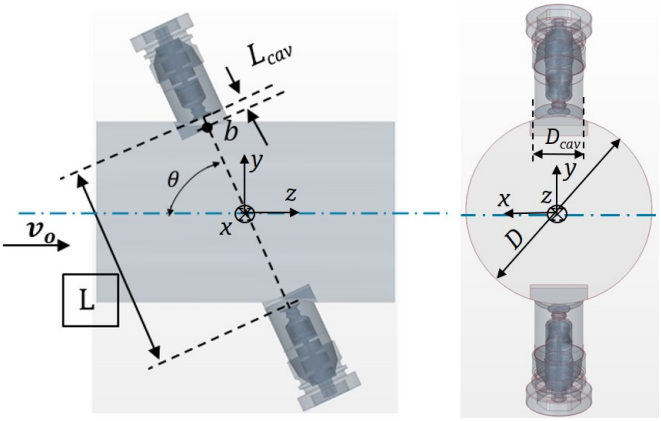

Figure 6.6: 3D geometry of the simulated 'Case 4' with one diametrical chord sound path and flush transducers. Left: side view and right: axial view.

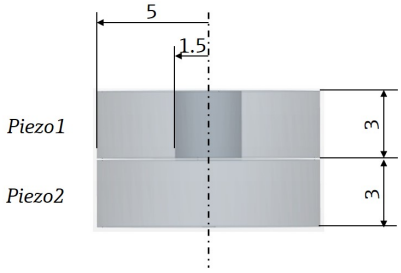

Figure 6.7: Two piezoelectric elements positioned on each other. Upper element, '*Piezo1*', is a ring, while down element, '*Piezo2*' is cylindrical. The dimensions are in [mm].

is positioned on '*Piezo2*'. It is noted that for the optimization of the material parameters in Sec. 6.1, the geometry of *Piezo2* is used.

The domain is split into parts as described in 3.2 and shown in Fig. 6.8. In Fig. 6.8(a), part (I) is shown, i.e. sender with a portion of fluid and in Fig. 6.8(b), part (III) is shown, i.e. receiver with a portion of fluid. The chosen dimensions for the fluid parts are

- L_1=8 mm
- L_2=1 mm
- L_3=27 mm
- L_4=8 mm
- L_5=2 mm
- L_6=27 mm.

For the mesh of parts **(I)** and **(III)** linear tetrahedral cells are used of size $\lambda/20 = 0.1715$ mm ($n_x = 20$) for f_c =100 kHz. It is reminded that ca. 17 million cells are used for each of parts (I) and (III), from which ≃15 million cells belong to the fluid parts and ≃2 million cells to the solid parts. For an impression of the mesh for parts **(I)** and **(III)** the reader is

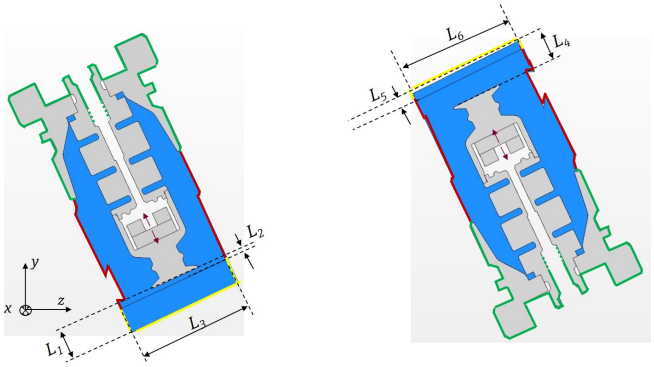

Figure 6.8: Plane section of transducers with a portion of fluid, with chosen dimensions for the fluid depicted. (a) sender, (b) receiver. Flush transducers.

referred to figs. 3.12, 3.19. The time step used is 375 ns, for which $n_t \simeq 26.67$ (time-steps / T_c) for f_c=100 kHz.

For the mesh of part (II), 210 million hexahedral cells (Cartesian mesh) are used, while the mesh is finer in the area of higher interest, which is located in the fluid domain between the sender and the receiver. For this specific area of interest, $n_x = 20$, while for the consecutive coarser areas, n_x is divided by 2 every time. For an impression of the mesh of part (b) the reader is referred to Fig. 3.15. The time-step used is 375 ns as well ($n_t = 26.67$).

For all parts of the simulation, it is calculated n_t/n_x=26.67/20=1.3335, which is in accordance with the guidelines of Sec. 4.2.

6.2.1.2 Computational Matrix

The geometry is simulated with both the CNA and SimPAC^2 methods (cf. Sec. 3). For the CNA method a real CFD flow-field is used, while for the SimPAC^2 two different flow-fields are used in couple with acoustics, i.e. a fully-developed with $v_0 = 0$ for $r > R$, and a real CFD flow-field with flow inside the cavities (cf. Sec. 3.2.5), which is the same as for the CNA. The simulated cases are documented in tab. 6.2.

Velocity v_{ref} [m/s]	CNA (Only CFD)	SimPAC^2-Ful.-dev.	SimPAC^2-CFD
0	✓	✓	✓
2, -2	✓	-	-
5, -5	✓	✓	✓
10, -10	✓	✓	✓
15, -15	✓	✓	✓
20, -20	✓	✓	✓
30, -30	✓	✓	✓

Table 6.2: Computational matrix of Case 4 with one sound path and flush transducers.

For the simulated UTTF, $\Delta t_0 = t^{eltr}_{21,0} - t^{eltr}_{12,i,0} = 0$ (eq. (2.86)) is assumed i.e., the electronics

and cables are not simulated and therefore, $t_{21,0}^{el,cab} = t_{12,0}^{el,cab} = 0$, while the two transducers are identical and therefore, $t_{21,0}^{tr} - t_{12,0}^{tr} = 0$. Moreover, in the simulations of wave acoustics the diffraction is automatically taken into account. For zero flow and identical transducers $t_{21,0}^{diff} = t_{12,0}^{diff}$ Thus, for $v_{ref} = 0$ we have $\Delta t_0 = 0$ (cf. Sec. 2.5) and therefore, $\%deviation = (v_{calc} - v_{ref})/v_{ref}$ (eq. (2.97)) becomes '0' as well.

The comparison between the CNA and SimPAC^2-CFD enables a direct comparison and quantification of the combined acoustic-flow effect of the cavities, since the flow-field considered, is the same for the two cases, while the CNA takes into account only flow and SimPAC^2 both flow and acoustics.

The comparison between SimPAC^2-Ful.dev. and SimPAC^2-CFD enables respectively a quantification of the combined acoustic-flow effect when a fully-developed and a real CFD flow field are considered. This comparison is of significance as an analytical or fully-developed flow-field has been used extensively in literature [30].

The CNA is computationally less demanding and simpler to apply, compared to the SimPAC^2 and therefore, it is of importance to assess which of the two methods shall be used each time, depending on the purpose of the performed investigation.

6.2.1.3 Results

The voltage on the receiver V_5 is calculated with the SimPAC^2 method and presented in figs. 6.9 and 6.10 for upstream and downstream acoustic wave propagation respectively, for the number of cases documented in table 6.2. Not the whole received signal is calculated, as it is not necessarily needed for the UTTF evaluation and extraction of deviation curve.

Obviously, as expected, for increasing negative (upstream) velocities the received voltage arrives later, while for increasing positive velocities (downstream), it arrives earlier. The three zero-crossings, taken into account for the ToF and Δt calculation are depicted in figs. 6.9 and 6.10 with black dots. However, the differences for a specific reference flow velocity, when a CFD or Ful.-dev. flow-field is considered, are of the order of ns, and therefore it is challenging to assess the difference in the scale presented in figs. 6.9 and 6.10.

Consequently, a zoom is made on the first of the three-zero crossings in order to assess the arisen difference due to the flow-field type (CFD or Ful.-dev.). The zoomed diagrams of voltage against time are presented in Figs. 6.11 and 6.12. It should be noted that the x and y axes of these diagrams are of the same range for comparison reasons.

First, let us analyze the consequences of the CFD and Ful.-dev. flow types on the received signal for the upstream flow (Fig. 6.11). The CFD cases arrive consistently later compared to the Ful.-dev. cases. More specifically, the difference between the two cases is gradually increased for increasing flow velocity. This is an indication of a consistent flow effect for the investigated range of flow velocities. Such claims are challenging to fully support and therefore, evidence is brought from the CFD simulation and the calculated flow-field.

In the case of a flow effect, for the CFD cases to arrive later, the acoustic waves should travel through a flow-field of higher flow velocities compared to the Ful.-dev. cases. It should be reminded that for the Ful.-dev. case, the flow velocity $\boldsymbol{v_0} = 0$ for $r > R$, while for the CFD case it is calculated ($\neq 0$) and varies spatially. Therefore, initially, the flow field inside the cavities and near the transducers is visually inspected. An indication that the later arrival of the signal of the upstream CFD cases is owed to flow, would be the presence of vortices with

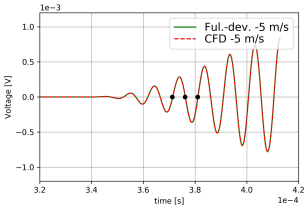

(a) v_{ref} =-5 m/s

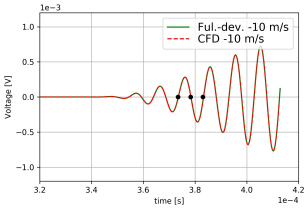

(b) v_{ref} =-10 m/s

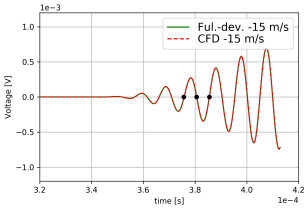

(c) v_{ref} =-15 m/s

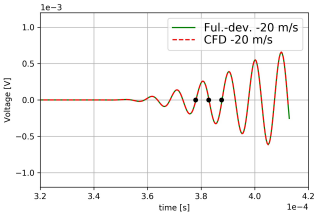

(d) v_{ref} =-20 m/s

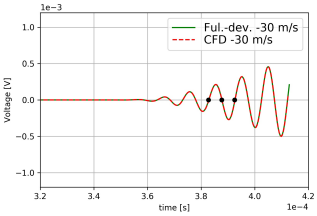

(e) v_{ref} =-30 m/s

Figure 6.9: Voltage signal on receiver V_5 against time, solved with SimPAC^2 for upstream flow velocities, with three zero-crossings depicted (a) v_{ref}=-5 m/s, (b) v_{ref}=-10 m/s, (c) v_{ref}=-15 m/s, (d) v_{ref}=-20 m/s, and (e) v_{ref}=-30 m/s. Flush transducers.

average axial velocity, v_z, in the positive z direction. This would mean local deceleration of the acoustic waves traveling upstream, where the generated vortices are located (always compared to the respective Ful.-dev. case).

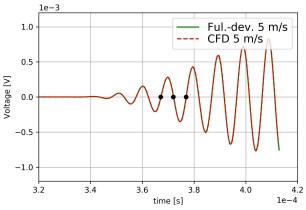

(a) v_{ref} =5 m/s

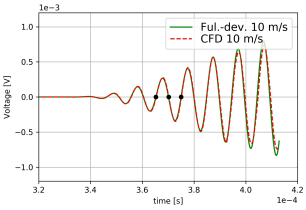

(b) v_{ref} =10 m/s

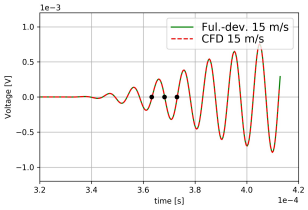

(c) v_{ref} =15 m/s

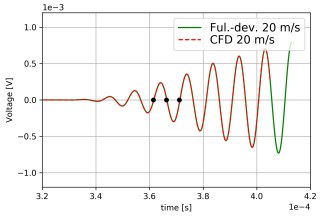

(d) v_{ref} =20 m/s

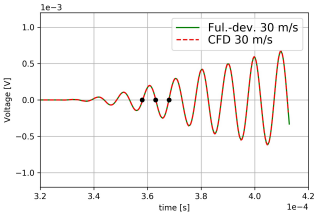

(e) v_{ref} =30 m/s

Figure 6.10: Voltage signal on receiver V_5 against time, solved with SimPAC^2 for downstream flow velocities, with three zero-crossings depicted (a) v_{ref}=5 m/s, (b) v_{ref}=10 m/s, (c) v_{ref}=15 m/s, (d) v_{ref}=20 m/s, and (e) v_{ref}=30 m/s. Flush transducers.

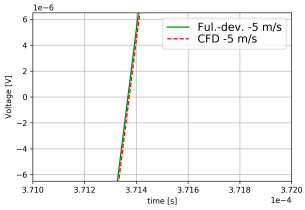

(a) v_{ref} =-5 m/s

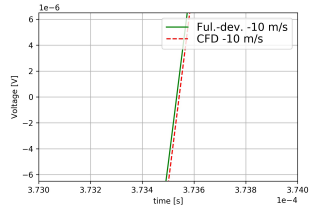

(b) v_{ref} =-10 m/s

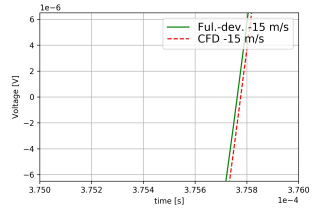

(c) v_{ref} =-15 m/s

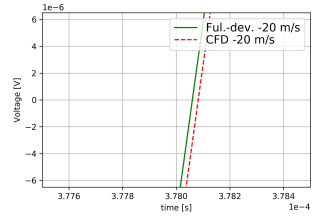

(d) v_{ref} =-20 m/s

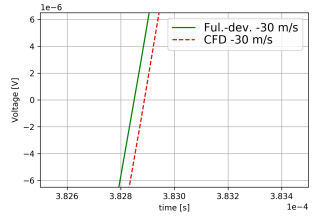

(e) v_{ref} =-30 m/s

Figure 6.11: Voltage signal on receiver V_5 against time, zoomed on the first of the three considered zero-crossings (cf. Fig. 6.9). Upstream flow for fully-developed and CFD flow-field. (a) $v_{ref} = -5$ m/s, (b) $v_{ref} = -10$ m/s, (c) $v_{ref} = -15$ m/s, (d) $v_{ref} = -20$ m/s, and (e) $v_{ref} = -30$ m/s. Flush transducers.

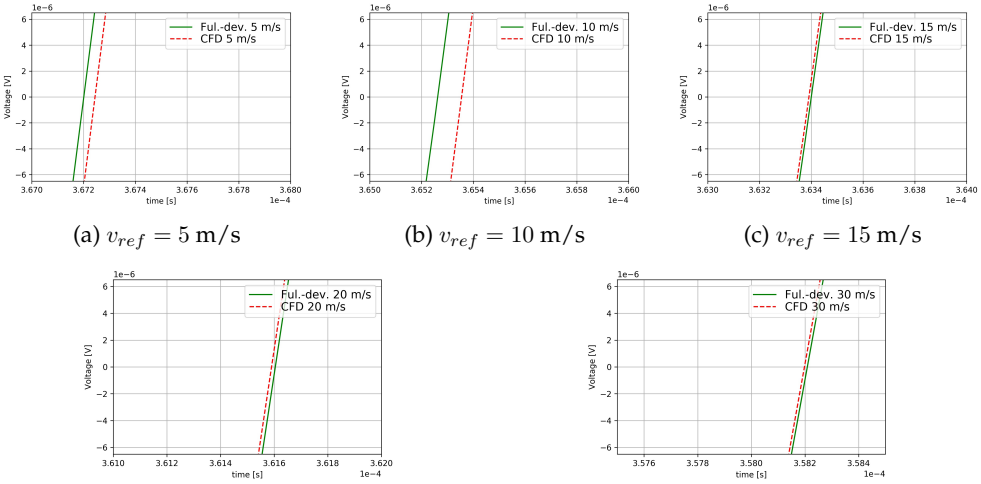

(a) $v_{ref} = 5$ m/s (b) $v_{ref} = 10$ m/s (c) $v_{ref} = 15$ m/s

(d) $v_{ref} = 20$ m/s (e) $v_{ref} = 30$ m/s

Figure 6.12: Voltage signal on receiver V_5 against time, zoomed on the first of the three considered zero-crossings (cf. Fig. 6.10). Downstream flow for fully-developed and CFD flow-field. (a) v_{ref}=5 m/s, (b) v_{ref}=10 m/s, (c) v_{ref}=15 m/s, (d) v_{ref}=20 m/s, and (e) v_{ref}=30 m/s. Flush transducers.

The flow-field near the sending and receiving transducers T1 and T2 is shown in figs. 6.13 and 6.14, where the same information, $Vel_{Norm} = |v_0|/v_{ref}$, is represented with flow vectors and line integral convolution (LIC) [235], respectively. $|v_0| = |v_0|(x, y, z)$ is the magnitude of flow velocity $\boldsymbol{v_0}$ in the fluid. The normalization of $|v_0|$ with v_{ref} helps to directly compare the flow-fields of different flow velocities. It is observed that strong vortices are created in front of the transducers and inside the cavities for the investigated flow velocities.

A close observation of the flow-field in Fig. 6.13 reveals the presence of vortices in both cavities of T1 and T2, as well as the direction of the flow inside them. It is noticed that there is strong secondary flow inside the cavities, while in front of the frontal surfaces of the transducers, vortices are present with positive z-direction (this effect will be further quantified, examined and proven in the present chapter).

In Fig. 6.14 the size of the vortices, as well as the value of Vel_{Norm} are shown in a more intuitive way. From a close observation of the flow-field, one can make several useful remarks:

- the size of the vortices changes with the flow velocity v_{ref}. This is in agreement with the measurements inside the cavity from Kažys et al. [110].
- Vel_{Norm}, inside the cavity and in front of the transducers, changes with the flow velocity v_{ref}, which is in agreement with prior literature from Kažys et al. [110] and Løland [146, 147].
- for a specific flow velocity, the flow-field in front of and inside the cavities of the transducers, varies between T1 and T2 (as expected), as shown before by others [110, 146, 147, 209]

As mentioned, the presence of these vortices in front of the transducers, with flow in the positive direction, indicates a later arrival of the upstream signal for the CFD cases compared

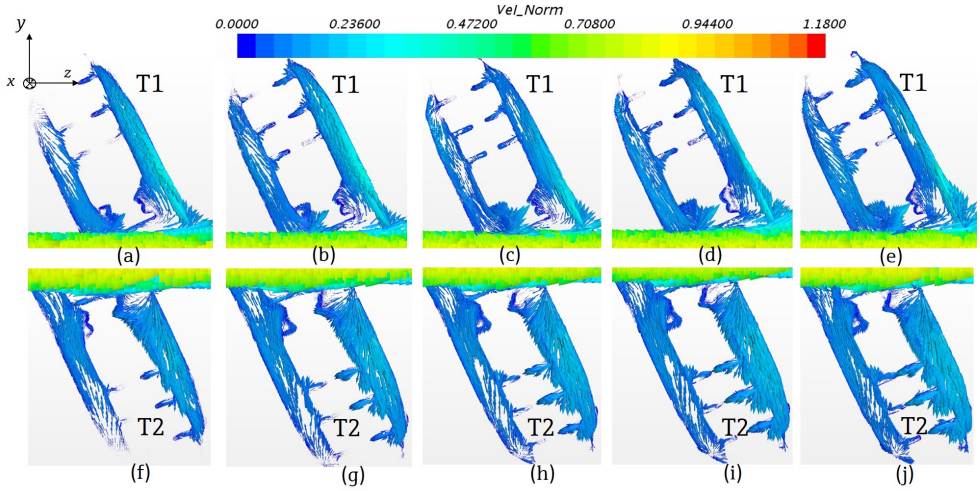

Figure 6.13: Flow-field near the sending and receiving flush transducers T1 and T2, respectively. Normalized velocity $Vel_{Norm} = |v_0|/v_{ref}$ is shown as vector representation for v_{ref}: (a),(f) 5 m/s, (b),(g) 10 m/s, (c),(h)15 m/s, (d),(i) 20 m/s, and (e),(j) 30 m/s.

to the Ful.-dev. ones. A more detailed analysis, with the aid of CFD, regarding the effect of flow on acoustics follows in the present section.

On the other hand, the presence of the described vortices would indicate an earlier arrival of the downstream signal for the CFD cases compared to the Ful.-dev. ones. In this case, this is valid for relatively high flow velocity, $v_{ref} \geq 15$ m/s, where the flow effect is stronger. Especially, for 5 m/s and 10 m/s there is a stronger vortex in front of transducer T1, while especially for $v_{ref} \geq 20$ m/s the vortex is almost disappeared and the flow penetrates inside the cavity in the positive z direction (figs. 6.13, 6.14). Consequently, the flow effect, because of positive flow in front of the transducer T1, is more dominant for higher velocities.

The acoustic waves follow different paths for the upstream and downstream cases [77, 239, 284], and as a result the generated vortices have an apparent different effect in each direction. For the downstream case (from T1 to T2) the main lobe of the acoustic waves fully meets the flow field in front of T1, where the vortex with varying size is located, in contrast with the waves traveling from T2 to T1, which are deflected downstream before meeting T1. Therefore, one can conclude that the downstream waves are more affected by the presence (or no presence) of this vortex.

For a better quantification of the flow effect on the acoustic wave propagation, straight cylindrical sound paths are assumed, in which the volume average velocity is calculated, as described in Sec. 3.1. It should be clarified that this assumption is only made for the CNA and not the SimPAC^2 method. However, it is used as an explanation tool for the flow-field effects. Cylindrical paths do not exactly reproduce reality but they are a good approximation and deliver satisfying results [196] for the quantification of flow effects.

In Fig. 6.15 the cylindrical sound path is depicted in pink color. In Fig. 6.15(a) the complete sound path is shown, named 'All'. It is a cylinder with same radius as the frontal

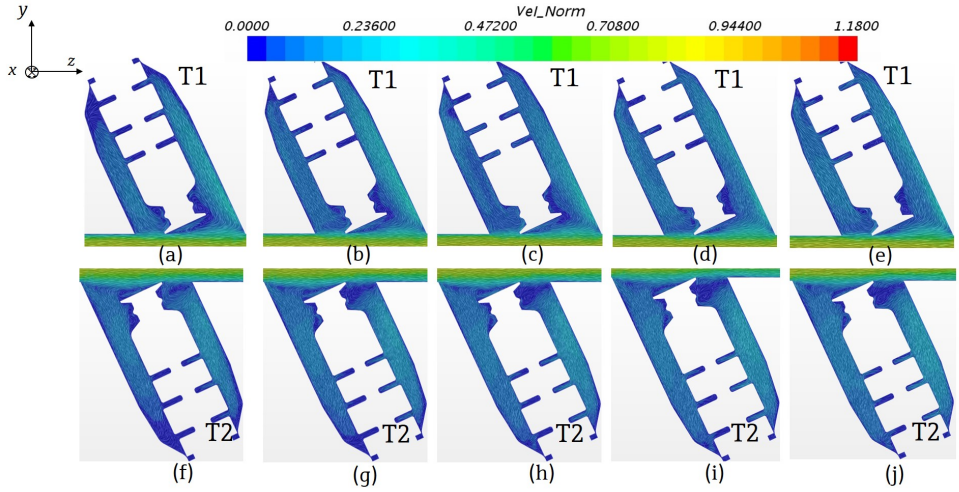

Figure 6.14: Flow-field near the sending and receiving flush transducers T1 and T2, respectively. Normalized velocity $Vel_{Norm} = |v_0|/v_{ref}$ is shown as 'Line Integral Convolution' (LIC) [235] for v_{ref}: (a),(f) 5 m/s, (b),(g) 10 m/s, (c),(h)15 m/s, (d),(i) 20 m/s, and (e),(j) 30 m/s.

surface of the transducer, which extends from transducer T1 to transducer T2. In Fig. 6.15(b) the part of the sound path is depicted, which is inside the pipe ($r \leq$R), and in Fig. 6.15(c)

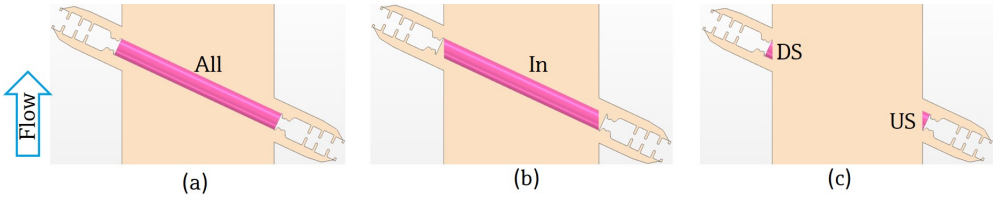

Figure 6.15: Cylindrical sound path geometry. (a) Whole sound path, named 'All', (b) Portion of sound path inside the pipe, named 'In', and (c) Portions of sound path inside the cavities, named 'US' and 'DS' for the upstream and the downstream cavity, respectively. Flush transducers.

the upstream (US) and downstream (DS) parts, which are inside the cavital areas (outside the pipe for $r > R$).

In Fig. 6.16 the normalized axial velocity, $Vel_{Norm}[k] = v_0[k](j)/v_{ref}$ is shown in the 'In' part of the cylindrical sound path for v_{ref} ={5, 10, 20, 30}, for the CFD and Ful.-dev. flow-fields. $v_0[k](j)$ is the axial flow velocity in a cell j of a discretized fluid domain and k indicates the axial, in z direction, component of flow velocity, $\boldsymbol{v_0}$. $Vel_{Norm}[k]$ can be qualitatively inspected in that way and useful remarks can be made, before a further quantitative investigation is made. One can induce that for the CFD flow-field, secondary flow is present i.e. not in the axial direction but towards the cavities, as the contour colors inside the cylindrical paths are shifted from the axial direction in contrast with the Ful.-dev. flow type, where they are directed axially, as expected. Especially for $v_{ref} = \{20, 30\}$ in

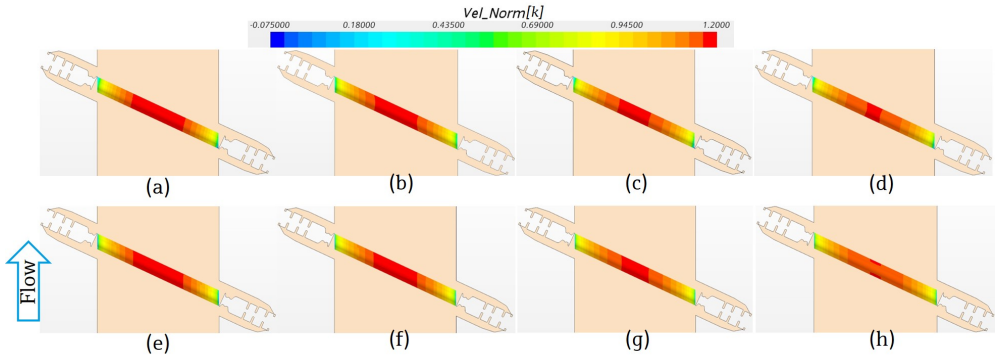

Figure 6.16: Normalized axial flow velocity contours for portion of sound path inside the pipe, 'In' for (a), (b), (c), and (d) 5 m/s, 10 m/s, 20 m/s, and 30 m/s respectively for CFD flow-field and (e), (f), (g), and (h) 5 m/s, 10 m/s, 20 m/s, and 30 m/s respectively for Ful.-dev. flow-field. Flush transducers.

Fig. 6.16(c),(d), one can observe an asymmetry i.e., shift of the red color from the axial direction to the right, towards the US cavity, which makes the flow slightly asymmetric, as it was experimentally observed before by Raišutis [209]. Moreover, for both flow-types the flow profiles depend on the flow velocity i.e., they tend to become flat for increasing Re. This dependency is observed when the Subfigs. of Fig. 6.16 are inspected per row and from left to right i.e., from (a)-(d) for CFD flow profile and from (e)-(f) for Ful.-dev.

In Fig. 6.17 the normalized axial velocity, $Vel_{Norm}[k]$, is shown in the US and DS parts of the cylindrical sound path for v_{ref} ={5, 10, 20, 30}, for the CFD flow-field. The contour for the Ful.-dev. flow-field is not shown separately for the US and DS parts, since it is zero. The flow inside the cavities and in front of the frontal surfaces of the transducers has already been described in detail in the present section in association with Figs. 6.13 and 6.14.

The volume average axial velocity in a discretized part of the fluid domain is given

$$\bar{v}_0[k] = \frac{1}{V}\sum_{j=1}^{n} v_0[k](j)\Delta V(j), \tag{6.6}$$

where n is the number of cells discretizing the part, and $\Delta V(j)$ is the volume of cell j. In order to quantify the qualitative remarks made, $\bar{v}_0[k]$ is calculated in the parts 'All', 'In,' 'US', and 'DS' of the sound paths for both CFD and Ful.-dev. flow-fields for v_{ref} ={5,10,20,30} m/s and is shown in Fig. 6.18. One can make several remarks from this diagram:

- $\bar{v}_0[k]$ is higher in the 'In' part than the 'All' part. This is to be expected, since inside the cavities, which are considered in the 'All' part, the flow velocity is lower.
- $\bar{v}_0[k]$ is almost zero in the 'US' and 'DS' parts for the Ful.-dev. flow-field. The non-zero values are owed to the nearest-neighbor mapping and to the inclusion of cells at the border of R, in which the $v_0 \neq 0$.
- $\bar{v}_0[k]$ is increased with v_{ref} for both 'US' and 'DS' parts in an almost linear way as it was

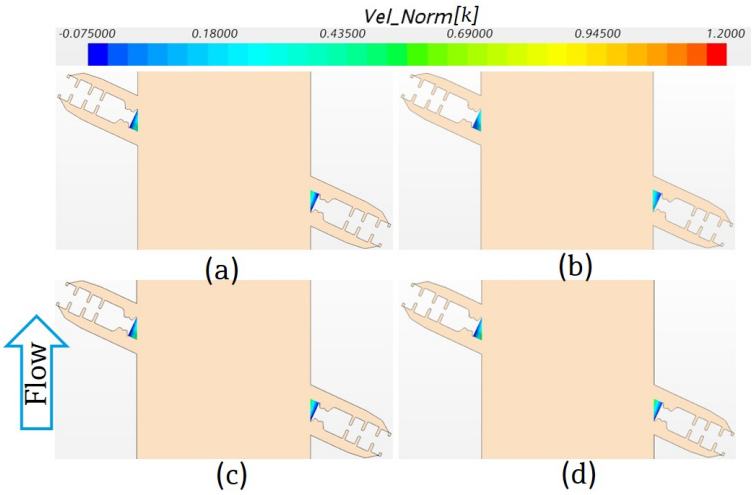

Figure 6.17: Normalized axial velocity contours for portion of sound path inside the pipe, 'In' for (a), (b), (c), and (d) 5 m/s, 10 m/s, 20 m/s, and 30 m/s respectively for CFD flow-field. Flush transducers.

similarly shown by Løland [146].

- $\bar{v}_0[k]$ is consistently higher for the 'DS' part compared to the 'US' one. One can imagine that in the DS part, the flow has the behavior of a nozzle and therefore it is accelerated, while in the US part it has the behavior of an expansion and therefore it is decelerated [14]. Prior literature clearly shows higher velocity in the downstream than in the upstream cavity as well [110, 146, 147, 209].

The above four mentioned remarks are used together with further flow analysis for the explanation of the trend of ToF and Δt in the present section.

$\bar{v}_0[k]$ in the sound paths, may be normalized with v_{ref} for a better depiction of the relative change of flow velocity in parts of the sound paths, as shown in Fig. 6.19. In Fig. 6.19(a) the pure Re dependency [30, 84, 196, 241] of the UTTF is shown. With this depiction, the observation of the differences is facilitated for a specific portion of the sound path and for different flow-fields.

- When the 'In' part is considered, the differences for the two flow-fields are minimum. However, for the CFD flow profile, $\bar{v}_0[k]$ is slightly lower compared to the 'Ful.-dev.' case. This is in agreement with the observation of Raišutis [209], where it was noticed that the flow velocity is reduced in the section of the meter-body due to the cavities.
- For the 'All' part, $\bar{v}_0[k]/v_{ref}$ is higher when the CFD flow-field is considered compared to the Ful.-dev, due to flow inside the cavities.

One can make a step further and evaluate separately the trend of $\bar{v}_{0[k]}/v_{ref}$ for the US and DS parts, as shown in Fig. 6.19(b). An interesting observation is the positive trend of

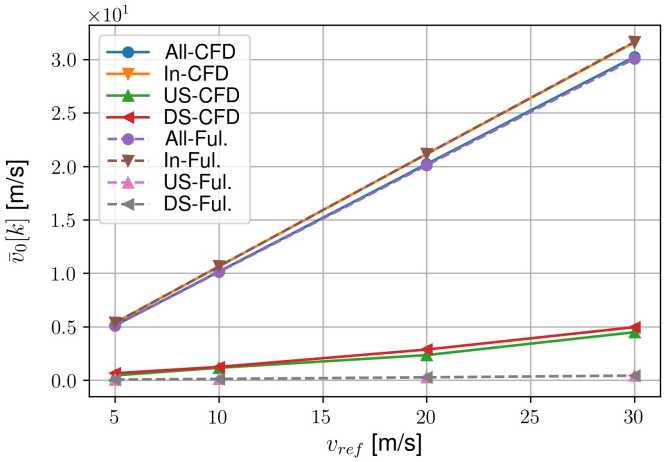

Figure 6.18: Volume average axial velocity $\bar{v}_0[k]$ in the sound paths or portions of them as defined in Fig. 6.15. CFD or Ful.-dev. flow-field considered. Flush transducers.

$\bar{v}_{0[k]}/v_{ref}$ for both US and DS parts, for the CFD flow-field (with the exception of 10 m/s for the DS-CFD), which opposes the typical *Re* effect on an UTTF (see Fig. 6.19).

Consequently, one concludes that the flow inside the cavities is relatively accelerated for increasing flow velocity for this case of flush transducers. This is in agreement with prior literature e.g. [110, 146] and with the qualitative remarks made through the flow-field depiction in figs. 6.13, 6.14 i.e., presence of larger vortices for lower velocities, with the aim of (partially) explaining the later or earlier arrival of the voltage signal because of flow (figs. 6.11, 6.12). Thus, one can say that the axially positive flow inside the cavities, gives an explanation regarding larger t_{21} and lower t_{12} for the CFD flow compared to the 'Ful.-dev.', especially for increasing v_{ref}. The effect of flow on t_{21}, t_{12}, as well as Δt in association with acoustics is further discussed in the present subsection.

In Fig. 6.20 the deviation between the CFD and Ful.-dev. cases is shown for the volume average velocity, $\frac{\bar{v}_{0,CFD}[k]-\bar{v}_{0,Ful}[k]}{\bar{v}_{0,Ful}[k]}100$, in the parts 'All' and 'In'. As already induced from Fig. 6.19 the volume average velocity is higher for the CFD flow field in the 'All' part, while it is slightly lower for the 'In' part. This is because of the flow in the cavities that locally increase the cross-section and therefore, the flow velocity is reduced in the 'In' part, as similarly shown with the aid of measurements by Raišutis [209]. The additional information here, is the relative change of $\bar{v}_0[k]$ when a CFD or Ful.-dev. flow is considered for changing v_{ref}:

- For the 'All' part, $\bar{v}_{0,CFD}[k]$ is relatively increased compared to the $\bar{v}_{0,Ful.}[k]$ for increasing velocities.
- For the 'In' part, the relative differences are lower, however, there is no clear trend.
- Especially for v_{ref}=10 m/s the deviation is the lowest for the 'All' part. For v_{ref}=5 m/s the deviation is similarly low.

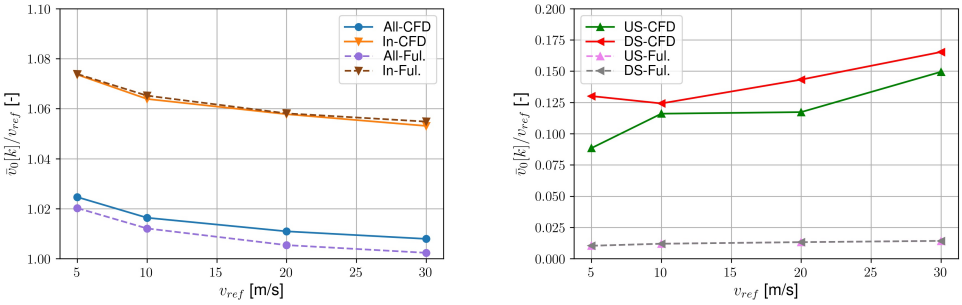

(a) (b)

Figure 6.19: Normalized volume average axial velocity, $\bar{v}_0[k]/v_{ref}$, in (a) 'All' and 'In', (b) 'US' and 'DS' parts. CFD and Ful.-dev. flow-field considered. Flush transducers.

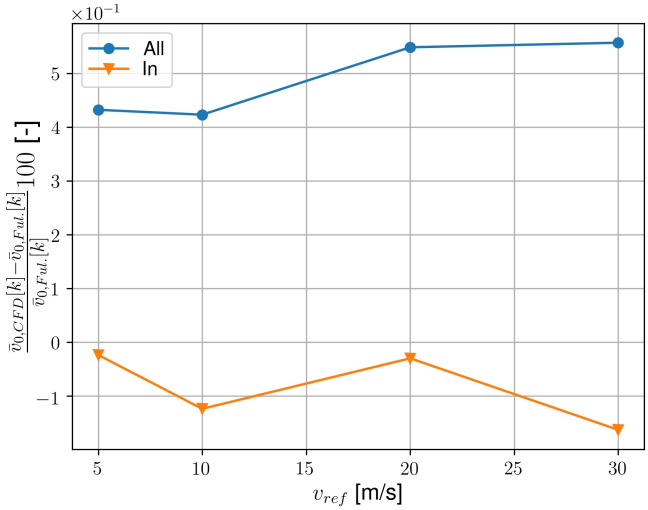

Figure 6.20: deviation in % between the CFD and Ful.-dev. flow-fields for the volume average velocity $\frac{\bar{v}_{0,CFD}[k]-\bar{v}_{0,Ful}[k]}{\bar{v}_{0,Ful}[k]}100$, for the 'All' and 'In' parts. Flush transducers.

- Due to the lower differences in the 'All' part for $v_{ref} = \{5, 10\}$ m/s, combined with the stronger vortex presence, consequences are expected on the ToF and Δt values.

Concluding, one can say that for the studied case of flush transducers the $\bar{v}_0[k]$ is higher along a sound path for the whole range of v_{ref} for the 'real' flow profile represented by the CFD, with an an increasing trend for higher v_{ref}. This means that higher Δt are expected for CFD flow profile especially for high v_{ref}. On the other hand, for lower velocities $v_{ref} = \{5, 10\}$ m/s, this trend of Δt might not be clear, especially due to the presence of stronger vortices in the upstream cavity, as shown in Fig. 6.14. The trends of ToF are already indicated through

Figs. 6.11, 6.12. Further analysis and results on the matter of ToF and Δt follows.

In Fig. 6.21 the acoustic pressure field [Pa] and the magnitude of mechanical displacement [m] are shown in the middle plane section yz in the fluid and in the solid parts of the receiver, respectively, for a number of time-samples, when CFD and Ful.-dev. flow-fields are considered. More specifically, for Fig. 6.21(a)-(f), CFD flow is taken into account, while for Fig. 6.21(g)-(l) Ful.-dev. flow. The reason for the further study of the acoustic field

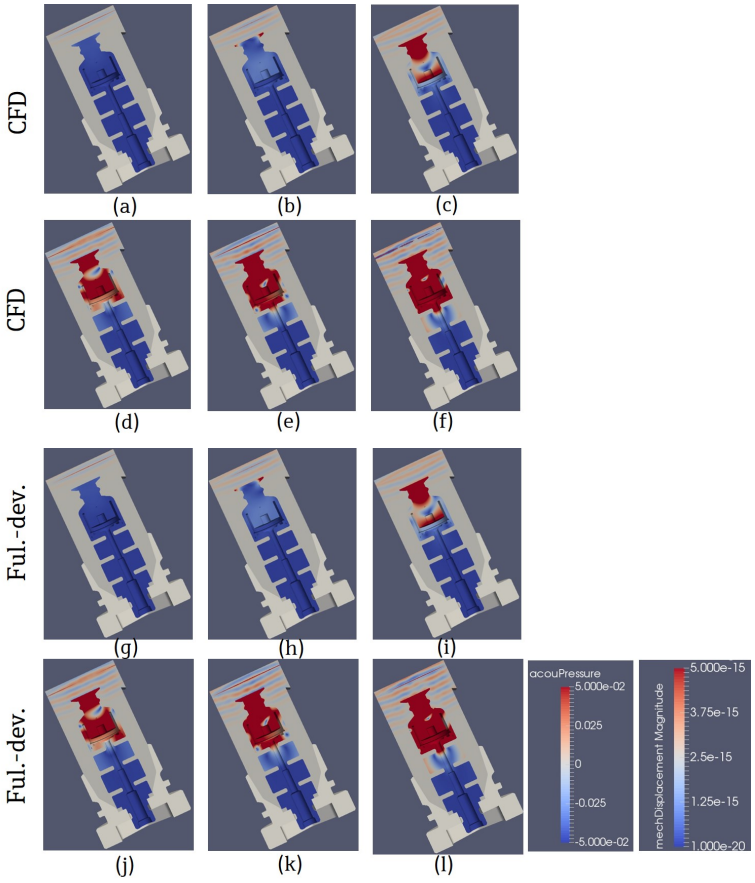

Figure 6.21: Acoustic pressure field and mechanical displacement magnitude in the middle plane section yz in the fluid and in the solid parts of the receiver, respectively, for different time-samples. (a),(g) 333.75 μs (b),(h) 341.25 μs, (c),(i) 348.75 μs, (d),(j) 356.25 μs, (e),(k) 363.75 μs, and (f),(l) 371.25 μs. for CFD, Ful.-dev. flow-fields, respectively. Flush transducers for v_{ref} =10 m/s for all depictions.

for $v_{ref} = 10$ m/s is the unusual observation $t_{12,CFD} > t_{12,Ful.-dev.}$ for that specific case, as seen in Figs. 6.10, 6.12 and will be depicted better in the present subsection. One can make several observations:

- Due to the acoustic pressure BC on Int2 (see Fig. 3.20), sound waves propagate towards

and away from the receiver. However, the absorbing BC (Fig. 3.20) absorbs the artificial acoustic waves traveling away from the receiver so that they are not reflected back to it. A study regarding the effectiveness of the absorbing BC is made in Sec. 5.5.

- Because of the DS propagation, the waves are deflected downstream (to the right).
- Because of the DS deflection of the waves and therefore of the main lobe, the receiver is excited asymmetrically.
- The first mechanical filter of the transducer, where its diameter is reduced, works as an impediment to prevent the waves from freely traveling into the solid parts, and consequently, cross-talk is decreased.
- Waves are reflected from the front surface of the receiver and interference is shown in the acoustic pressure field.

From the representation of the acoustic pressure and mechanical displacement magnitude fields in Fig. 6.21, it is challenging to observe the small differences for the two different flow-fields, since in terms of t_{12}, t_{21}, and Δt they are of the order of ns. However, a close observation may qualitatively reveal small differences as a result of the later or earlier signal arrival. An analysis of the remarks made from Fig. 6.21 follows in the present subsection, while diagrams of ToF and Δt against v_{ref} are shown as well (cf. Fig. 6.23).

In order to enhance the noticeability of the differences due to the flow-field, the same representation as for Fig. 6.21 is shown in Fig. 6.22 but for a later time-sample, t=405 μs, and with a larger range for the contour of the mechanical displacement magnitude. Differences are more easily noticed between the two cases for both the acoustic pressure and

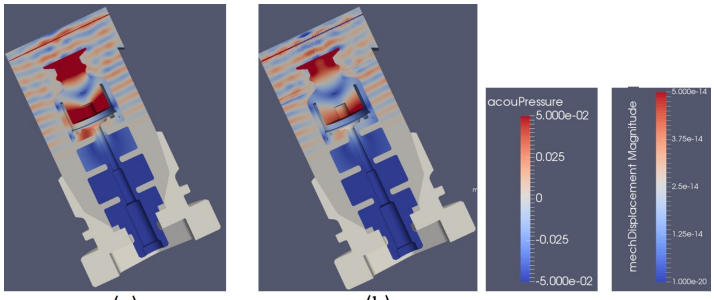

Figure 6.22: Acoustic pressure field and mechanical displacement magnitude in the middle plane section yz in the fluid and in the solid parts of the receiver, respectively, for t= 405 μs. (a) CFD and (b) Ful.-dev. flow-field. Flush transducers for v_{ref} =10 m/s

the mechanical displacement fields, since for a later time-sample the waves have traveled further, especially in the solid domain. The contour-range of the mechanical displacement magnitude is enlarged to [1e-20, 5e-14] m for the same purpose. It should be noted that when the range is too small, the contours do not show the differences well, because the value that exceed the limits become monochromatic i.e., red or blue for the upper or lower limit, respectively. There are apparent differences in the acoustic pressure field in the medium, which seems more distorted with higher interference for the Ful.-dev. flow-field. However,

it is challenging to distinguish the later or earlier arrival of the wavefronts between the two cases. The differences are also obvious for the mechanical displacement magnitude in the solid parts. For the examined time-sample, the displacement is higher for the case with the CFD flow-field, while for both cases it is not symmetric mainly due to the deflection of the sound path in the downstream direction and of the reflections from the walls of the cavity.

In Fig. 6.23 the downstream ToF, t_{12}, upstream ToF, t_{21}, and time difference Δt are shown for a number of flow-velocities, for a CFD and Ful.-dev. flow-field. ToF is defined

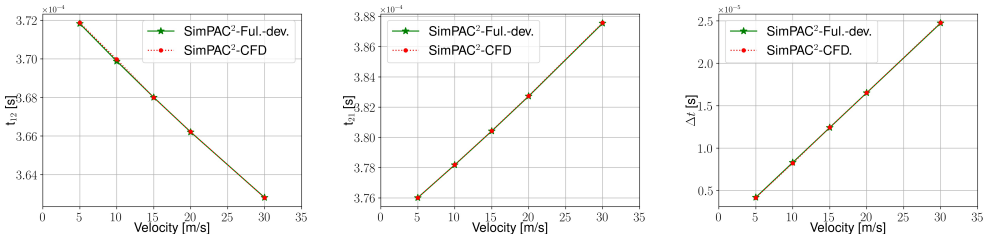

(a) (b) (c)

Figure 6.23: Time-parameters against velocity. (a) t_{12} (downstream wave propagation), (b) t_{21} (upstream wave propagation), and (c) $\Delta t = t_{21} - t_{12}$. Flush transducers.

through the three zero-crossings depicted in figs. 6.9 and 6.10. Differences are difficult to be viewed from this representation, however the linear positive trend is shown for t_{21} and Δt, and negative trend for t_{12}. The ToF differences for the considered flow-fields and flow velocities have already been examined through the velocity contours, the vortex generation near the transducers, the volume average (axial) velocity in the different parts of the sound paths, and the acoustic pressure and mechanical displacement magnitude fields. More specifically, it is reminded that due to higher flow velocities in the cylindrical sound paths for the CFD flow profile compared to the 'Ful.-dev.' (cf. Fig. 6.20), higher Δt values are expected. However, fow lower $v_{ref} = \{5, 10\}$ m/s, due to the presence of strong vortices in front of the transducer T1 for the CFD flow profile (cf. Fig. 6.14) and lower differences in the 'All' part (cf. Fig. 6.20), these Δ values are expected to be relatively reduced for the CFD compared to the 'Ful.-dev.'.

The ToF for US and DS propagation as well as for the two flow-fields, is normalized with the respective v_{ref} as shown in Fig. 6.24. One can clearly notice the flow-effect, i.e. Re effect, [30, 84, 196, 241] on both t_{12} and t_{21}. As expected, $t_{21}/v_{ref} > t_{12}/v_{ref}$ for a specific v_{ref}, with their difference being increased for increasing v_{ref}. The differences between the cases with different flow-fields are still challenging to observe and therefore the ToF for Ful.-dev. and CFD flow-fields are divided with each other for both US and DS propagation as shown in Fig. 6.25. One can make several useful remarks:

- For 2-1 direction (US propagation), t_{21} is consistently higher for the CFD flow, i.e. the voltage signal arrives later, because of higher flow-velocity in the sound path (Fig. 6.18, 6.19, and 6.20) than the Ful.-dev., due to the vortex generation in front of the transducers (Fig. 6.13, 6.14).

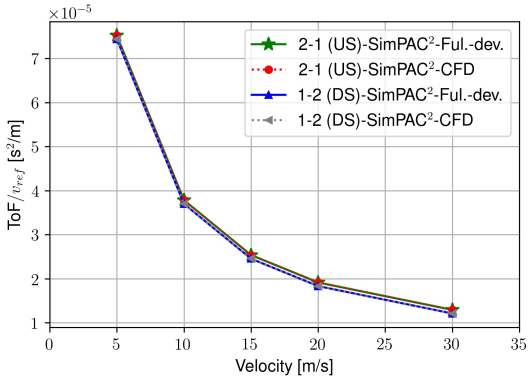

Figure 6.24: ToF/v_{ref} [s^2/m] for 2-1 (US) and 1-2 (DS) propagation, for CFD and Ful.-dev. flow-fields. Flush transducers.

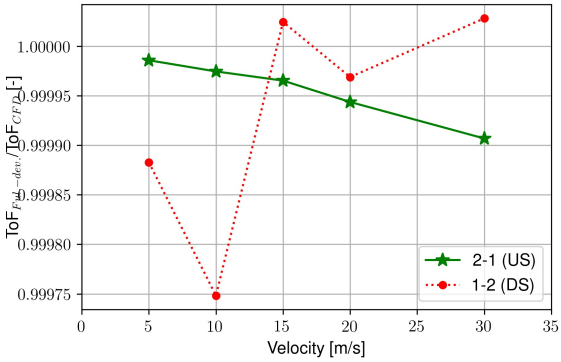

Figure 6.25: $\text{ToF}_{Ful.-dev}/\text{ToF}_{CFD}$ [-] for 2-1 (US) and 1-2 (DS) propagation. Flush transducers.

- $t_{12,CFD}$ and $t_{12,Ful.-dev.}$ are the t_{12} from the SimPAC²-CFD and SimPAC²-Ful.-dev., respectively.
- For 1-2 direction (DS propagation), t_{12} does not present a clear trend unlike the US propagation. For higher flow-velocities ($>$ 15 m/s) $t_{12,CFD}$ tends to be lower or almost equal to $t_{12,Ful.-dev.}$, or in other words the signal arrives earlier. That is because of the higher flow velocities inside the cavities and along the whole sound paths, as explained through the results of figs. 6.13, 6.14, 6.18, 6.19, and 6.20. The increasing of velocity inside the cavity is in agreement with prior literature [110, 146]. For lower flow-velocities (5, 10 m/s), $t_{12,CFD}$ is clearly higher than $t_{12,Ful.-dev.}$, i.e. the signal arrives later, despite the fact that $v_{0,CFD} > v_{0,Ful.-dev.}$ (Fig. 6.20). It is reminded that for downstream propagation the main lobe of the acoustic waves fully propagates through the varying vortex in front of T1, and therefore the downstream propagating waves are affected from the presence of the vortex, especially for low $v_{ref} = \{5, 10\}$ m/s

where the vortex is stronger.

- On the other hand, for US propagation (T2 to T1) the waves are affected less by the vortex in front of T1, since they are deflected downstream before impinging T1 and thus, a consistent behavior of t_{21} is observed.
- One should have in mind that the explanation of the flow-effects through the cylindrical sound path assumption does not tell the whole truth about the sound path, which is otherwise correctly considered and simulated in the case of SimPAC^2. The presence of 3D acoustic-flow interaction effects is also possible, making a definite explanation more challenging.

The Δt for the two flow-fields, is normalized with the respective v_{ref} as shown in Fig. 6.26, with the purpose of directly comparing the two cases. Several useful remarks are made

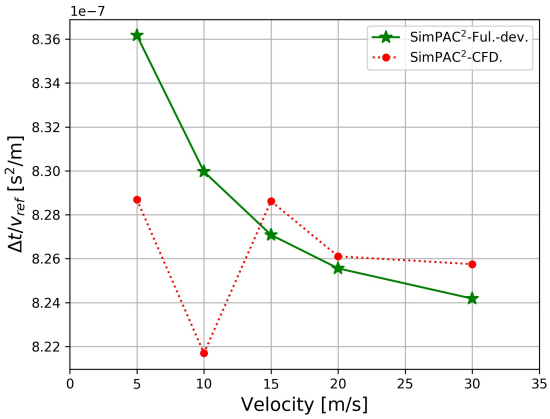

Figure 6.26: $\Delta t/v_{ref}$ [s$^2/m$] for CFD and Ful.-dev. flow-fields. Flush transducers.

regarding the Δt for the two flow-fields considered:

- Δt_{CFD} and $\Delta t_{Ful.-dev.}$ are the Δt from the SimPAC^2-CFD and SimPAC^2-Ful.-dev., respectively.
- The trend of the normalized $\Delta t_{Ful.-dev.}/v_{ref}$ clearly shows the typical flow profile effect, i.e. Re dependency, for a straight pipe [30, 84, 196, 241], since flow is not considered in the cavities. This is not the case for $\Delta t_{CFD}/v_{ref}$, due to the consideration of the vortices in the cavities.
- The trend of the normalized $\Delta t_{CFD}/v_{ref}$ for the CFD flow shows the effect of the CFD flow consideration in the cavities, which consequently affects the acoustic wave propagation and the arrival of the signal on the receiver. For higher flow velocities ($>$ 15 m/s), $\Delta t_{CFD} > \Delta t_{Ful.-dev.}$, since the flow-effect and the higher velocities in the sound path for the CFD flow-field are more dominant i.e., higher velocity inside the cavities for higher v_{ref} as similarly shown in [110, 146]. For low flow-velocities, $\{5, 10\}$ m/s, $\Delta t_{CFD} < \Delta t_{Ful.-dev.}$, due to the larger vortex generation in front of the transducer (as

already explained in the present section regarding the trend of t_{12} (figs. 6.13, 6.14) and the slight reduction of the normalized flow axial velocity (figs. 6.18, 6.19, and 6.20).

- The differences between Δt_{CFD} and $\Delta t_{Ful.-dev.}$ stem mostly from the downstream propagation of the signal, t_{12}, as shown in Fig. 6.25.

In Fig. 6.27 the deviation curves are presented for the 'Only CFD' method when realistic CFD flow-field is considered and for the SimPAC^2 method for CFD and Ful.-dev. flow-fields. A clarification should be made regarding the deviation curve extraction. For the calculation

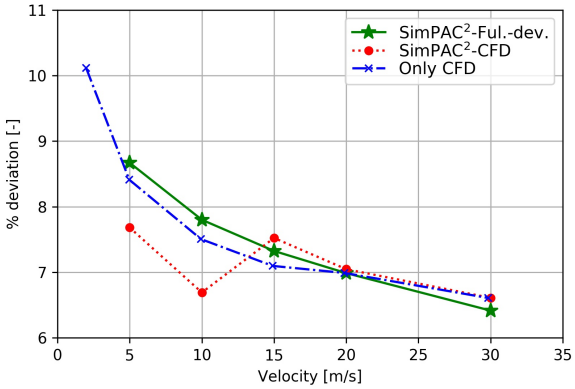

Figure 6.27: Deviation against flow velocity for fully-developed and CFD flow-field. Flush transducers.

of the flow velocity $v_{path,i}$ eq. (2.91) is used for the SimPAC^2 method. However, for the CNA (Only CFD) method eq. (3.13) is used for the direct calculation of the flow velocity inside the cylindrical paths, $v_{0,CFD}$. In the case of SimPAC^2, when eq. (2.91) is used, L_{cav} is deducted, irrespective of the flow-field considered, i.e. for both CFD and 'Ful.-dev.' profiles. Therefore, for comparison reasons, a way should be found in order to perform a similar calculation for the CNA (Only CFD) method. The calculated $v_{0,CFD}$ (eq. (3.10)) should be multiplied with a factor $f_{corr}= L/(L-2L_{cav})$ so that it is directly comparable with the $v_{path,i}$ from eq. (2.91). Therefore, for the direct comparison the corrected flow velocity

$$v_{0,CFD,corr} = v_{0,CFD} \cdot f_{corr} \tag{6.7}$$

is used. While, in order to extract from the CNA (Only CFD) method, a comparable deviation with the one from the SimPAC^2 method, one may use

$$\%\text{deviation}_{corr} = \frac{v_{0,CFD,corr} - v_{ref}}{v_{ref}} \cdot 100. \tag{6.8}$$

Several useful observations are made from the deviation diagram:

- The %deviation is positive for all cases, because of the position of the sound path in the middle of the pipe, where typically higher flow velocity is present (Fig. 3.3) compared to the surface average velocity in a cross-section of the pipe.
- For the 'Only CFD' method, the typical trend, because of the flow profile (Re dependency) is observed, despite the consideration of a CFD flow-field with vortices in the cavities.
- For the SimPAC^2-Ful.-dev. case, the trend of $\Delta t_{Ful.-dev.}$, and consequently %deviation seem to follow the typical trends due to the flow-profile in a straight pipe (Re dependency). The trend is very similar to the %deviation calculated with the 'Only CFD' method, however it is steeper for high flow velocities [20-30] m/s.
- For the SimPAC^2-CFD case, the trends of $t_{12,CFD}, \Delta t_{CFD}$, and consequently %deviation for the lower flow-velocities (5, 10 m/s) is clear that they do not purely originate from flow but from an interaction of acoustic wave propagation and CFD. The reason for this statement is the absence of this 'anomaly' in the deviation curve generated with the 'Only CFD' method. For higher flow velocities ($>$ 15 m/s) the %deviation is very similar to the SimPAC^2-Ful.-dev. case, since the respective t_{12}, t_{21}, and Δt are almost identical. However, for flow-velocities [20-30] m/s the trend of the SimPAC^2-CFD curve is less steep and coincides with the curve from the 'Only CFD' method. This is another hint that the flow effects become more dominant for high flow-velocities and therefore the two cases with the same CFD flow-field coincide.

Concluding, the kink for low velocities in the deviation curve generated with the method SimPAC^2-CFD, is an effect stemming from the downstream propagation, i.e. t_{12}. It is consequently observed in Δt and in turn in the deviation curve of the flowmeter. It is not a pure flow-effect but a 3D flow-acoustics interaction effect in the pipe and the cavities. For high flow-velocities, it seems that the flow effects become more dominant.

Further investigation should be carried out for the complete explanation of the present effect for low flow velocities and the interaction between flow, acoustics and the 3D geometry of the cavity.

6.2.2 Recessed Transducers

The already described one path UTTF geometry (Sec. 6.2.1) is simulated and investigated for transducers recessed inside the cavities, indicated as 'Case 5'.

6.2.2.1 Simulation Setup and Computational Matrix

The sender and the receiver are recessed into the geometrical cavities of the UTTF, as shown in Fig. 6.28. The geometrical parameters D, θ, and D_{cav} are of the same value and b has

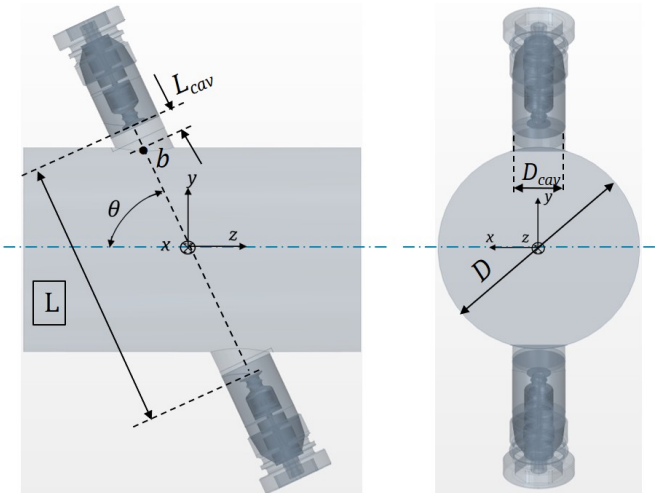

Figure 6.28: 3D geometry of the simulated Case 5 with one diametrical chord sound path and recessed transducers. Left: side view and right: axial view.

the same properties as for the geometry of Sec. 6.2.1, Case 4. The radius of the front face of the transducer is $R_{trans} = 5.75$ mm and the length of simulated device is $L_{dev} = 160$ mm. The distance between the two transducers is changed and therefore L=131.74 mm and $L_{cav} = 12.36$ mm. More details regarding the geometry, the simulated parts, BCs, and general simulation setup are given in Sec. 3.2 and in the beginning of Sec. 6.2. The same piezoelectric elements are used as for the geometry of Sec. 6.2.1, Case 4, shown in Fig. 6.7. The domain is split into parts in the same way as the domain of Case 4, while the parameters L_1, L_2, L_3, L_4, L_5, and L_6 has the same values as for Case 4.

The rest of the setup, i.e. the time and space discretization information, as well as the mesh description, are already given at the end of Sec. 6.2.1.1 and are valid for the case of the present section as well, Case 5.

As for Case 4, the geometry is simulated with both the CNA (Only CFD) and SimPAC^2 methods. For the CNA method a real CFD flow-field is used, while for the SimPAC^2 two different flow-fields are used in couple with acoustics, i.e. a Ful.-dev., and a real CFD flow-field, which is the same as for the CNA. The simulated cases are documented in tab. 6.3.

Velocity [m/s]	CNA (Only CFD)	SimPAC^2-Ful.-dev.	SimPAC^2-CFD
0	✓	✓	✓
2, -2	✓	-	-
5, -5	✓	✓	✓
10, -10	✓	✓	✓
15, -15	✓	-	-
20, -20	✓	✓	✓
30, -30	✓	✓	✓

Table 6.3: Computational matrix of Case 5 with one sound path and recessed transducers.

Compared to Case 4, a simulation is not carried out for 15 m/s with the SimPAC^2-CFD and SimPAC^2-Ful.-dev.. The comments made for Case 4 at the end of Sec. 6.2.1.2 regarding the comparison of different methods and flow-fields are valid for Case 5 as well.

6.2.2.2 Results

For consistency reasons and for the enablement of direct comparisons between the UTTF geometries with different insertion depth of transducers, the results of Case 5 are presented in a similar form as for Case 4. The voltage on the receiver V_5 is calculated with the SimPAC^2 method and presented in figs. 6.29 and 6.30 for upstream and downstream acoustic wave propagation respectively, for the number of cases documented in tab. 6.3. Similarly to Case 4, not the whole received signal is calculated, as it is not necessarily needed for the UTTF evaluation and generation of deviation curves.

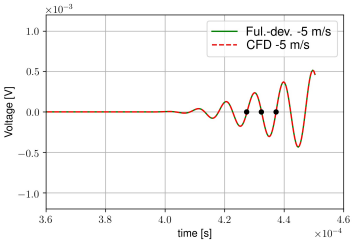

(a) v_{ref} =-5 m/s

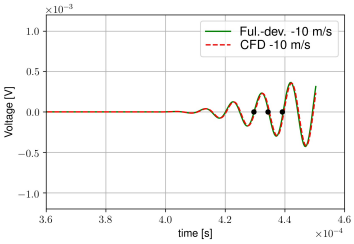

(b) v_{ref} =-10 m/s

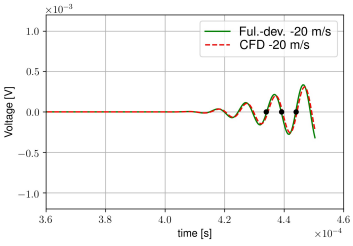

(c) v_{ref} =-20 m/s

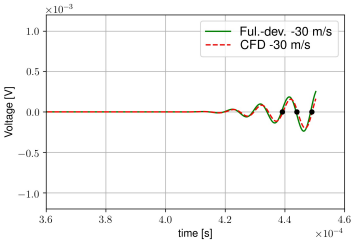

(d) v_{ref} =-30 m/s

Figure 6.29: Voltage signal on receiver V_5 against time, solved with SimPAC^2 for fully-developed and CFD flow-fields, for upstream flow propagation, with three zero-crossings depicted (a) v_{ref}=-5 m/s, (b) v_{ref}=-10 m/s, (c) v_{ref}=-20 m/s, and (d) v_{ref}=-30 m/s. Recessed transducers.

One can already notice that the differences in terms of ToF are larger compared to Case 4 (flush transducers), since they can be noticed without zooming, especially for higher flow velocities.

However, a better depiction of the differences is achieved, when a zoom on the first of the three depicted zero-crossings (with black dots) is made for every flow velocity and for the upstream and downstream propagation, as shown in figs. 6.31 and 6.32, respectively.

- Let us focus first on the upstream wave propagation (Fig. 6.31) and the differences when a CFD or a Ful.-dev. flow-field is considered for recessed transducers. For 5 m/s the ToF difference is very small (<10 ns). However, for increasing flow-velocity, the waves arrive later when a CFD flow is considered, i.e. $t_{21,\text{CFD}} > t_{21,\text{Ful.-dev.}}$, with the difference being larger for increasing flow-velocity. The unambiguous behavior, which correlates with the flow-velocity, gives a hint that it is owed primarily to the flow-differences,

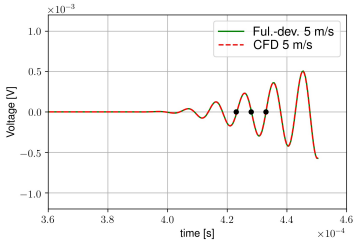

(a) v_{ref} =5 m/s

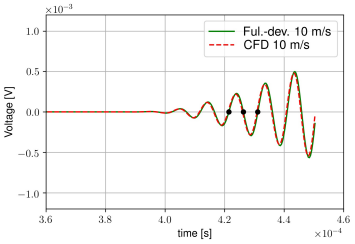

(b) v_{ref} =10 m/s

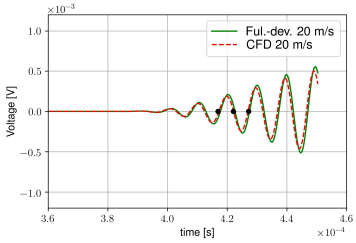

(c) v_{ref} =20 m/s

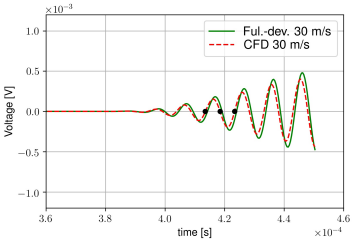

(d) v_{ref} =30 m/s

Figure 6.30: Voltage signal on receiver V_5 against time, solved with SimPAC^2 for fully-developed and CFD flow-fields for downstream flow propagation, with three zero-crossings depicted (a) v_{ref}=5 m/s, (b) v_{ref}=10 m/s, (c) v_{ref}=20 m/s, and (d) v_{ref}=30 m/s. Recessed transducers.

i.e. that the flow-velocity in the sound path is higher for the CFD than the Ful.-dev. flow-field for the same v_{ref}.

- For downstream wave propagation (Fig. 6.32), differences in terms of ToF are already well noticed for v_{ref}=5 m/s, while they are increased for increasing flow-velocity. More specifically, for every v_{ref}, it is valid that $t_{12,\text{CFD}}<t_{12,\text{Ful.-dev.}}$, i.e. the signal arrives earlier when a CFD flow-field is considered. The unambiguous and opposite trend, compared to the respective v_{ref} for upstream wave propagation, gives another hint that the ToF differences are owed to the considered flow-field. In other words, the conclusion is the same as for the upstream wave propagation, i.e. the flow-velocity in the sound path is higher for the CFD than the Ful.-dev. flow-field for the same v_{ref}.

In order to prove these claims, the flow-field is investigated in a similar manner as for the flush transducers (Sec. 6.2.1.3).

In Fig. 6.33 the vortices in front of the upstream and downstream transducers T1 and T2, respectively, are shown, as well as their size and the value of Vel_{Norm} for v_{ref} ={5,10,15,20,30}. One can make several useful observations, many of them similar to Case 4:

- Since the transducers are further recessed in the cavities compared to Case 4, larger vortical structures are generated in front of them.
- the size and location of the vortices, as well as Vel_{Norm} inside the cavities and in front of the transducers change with the flow velocity v_{ref} [110, 146]. For both T1 and T2 the vortices are larger for higher v_{ref}.

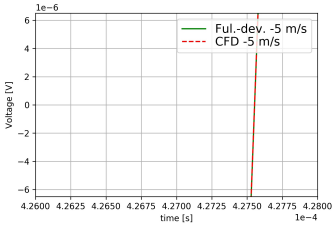

(a) v_{ref} =-5 m/s

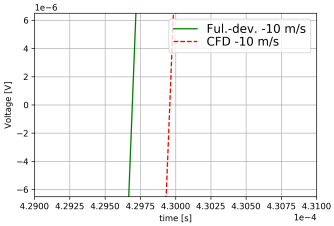

(b) v_{ref} =-10 m/s

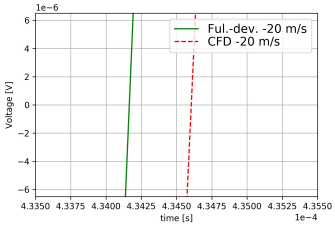

(c) v_{ref} =-20 m/s

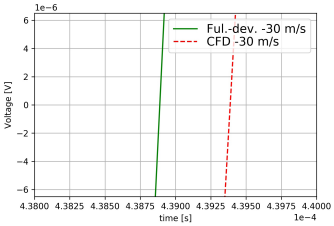

(d) v_{ref} =-30 m/s

Figure 6.31: Voltage signal on receiver V_5 against time, zoomed on the first of the three considered zero-crossings (cf. Fig. 6.29) for different flow types and upstream wave propagation. (a) v_{ref}=-5 m/s, (b) v_{ref}=-10 m/s, (c) v_{ref}=-20 m/s, (d) v_{ref}=-30 m/s. Recessed transducers.

- for a specific flow velocity, the flow-field in front of and inside the cavities of the transducers, is not the same for T1 and T2 (as expected) [110, 146]
- The lowest velocity inside the cavities is observed in different distances in front of the transducers, depending on v_{ref}, as similarly observed by Kažys [110].

The described behavior indicates a consistent later and earlier arrival for US and DS propagation respectively, when a CFD flow-field is considered compared to a Ful.-dev. one. More specifically, the waves propagate through higher flow velocities for CFD, where $\boldsymbol{v_0} \neq 0$ in the cavities compared to the Ful-.dev. flow, where $\boldsymbol{v_0} = 0$ in the cavities. This is confirmed by the results of figs. 6.31 and 6.32.

Due to the different path followed by the US and DS waves [77] the generated vortices have a different effect in each direction, as described already with Case 4 used as an example. There is an abrupt change of Vel_{Norm} inside the cavities for both T1 and T2 and therefore, a full or partial incidence of the major lobe of the waves may have an effect on its propagation. This shall be explained with the example of the highest v_{ref}=30 m/s (Fig. 6.33 (e),(j)).

- A DS wave propagating from T1 to T2 fully meets the vortex in front of transducer T1, while when propagating towards T2 the wave gets deflected and partially meets the vortex in front of T2. A large part of the major lobe of the wave meets the high-velocity area inside the cavity.
- An US wave propagating from T2 to T1 on the other hand, meets larger part of the low velocity vortex in front of the transducer T2 and inside the cavity, while it partially

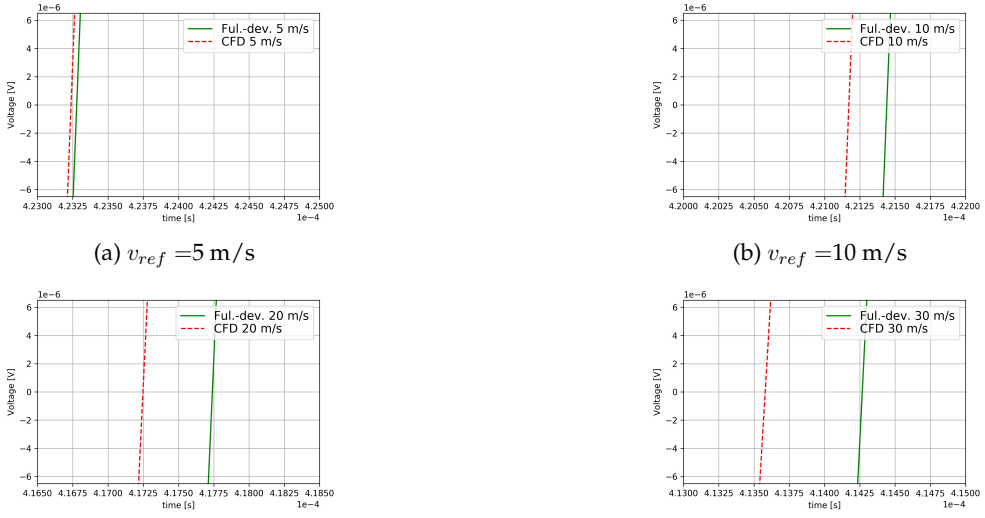

(a) v_{ref} =5 m/s (b) v_{ref} =10 m/s

(c) v_{ref} =20 m/s (d) v_{ref} =30 m/s

Figure 6.32: Voltage signal on receiver V_5 against time, zoomed on the first of the three considered zero-crossings (cf. Fig. 6.30) for different flow types and downstream wave propagation. (a) v_{ref}=5 m/s, (b) v_{ref}=10 m/s, (c) v_{ref}=20 m/s, (d) v_{ref}=30 m/s. Recessed transducers.

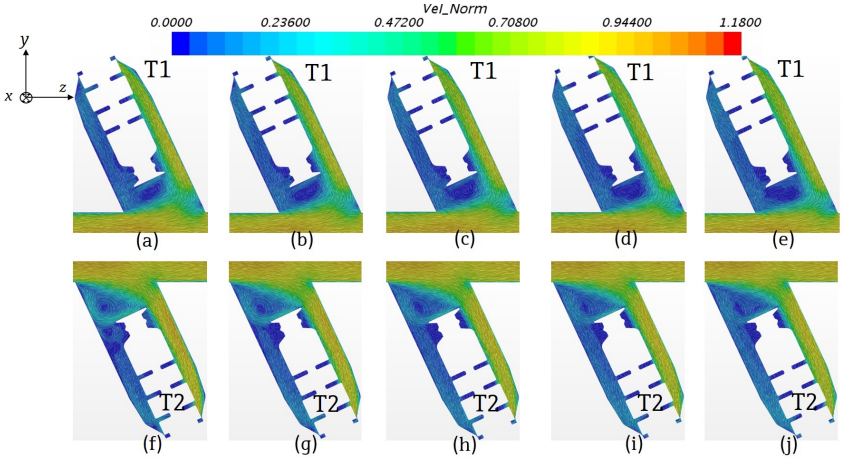

Figure 6.33: Flow-field near the sending and receiving recessed transducers T1 and T2, respectively, for recessed transducers. Flow in the z-direction. Normalized velocity $Vel_{Norm} = |v_0|/v_{ref}$ is shown as 'Line Integral Convolution' (LIC) [235] for positive v_{ref}: (a),(f) 5 m/s, (b),(g) 10 m/s, (c),(h)15 m/s, (d),(i) 20 m/s, and (e),(j) 30 m/s.

meets the big vortex in front of the transducer T1 as it is deflected downstream when propagating towards T1.

The described situation may have consequences on the wave propagation and dissimilar effects of the flow-field on the US and DS propagation.

Similarly to Case 4, cylindrical paths are used for the sake of clarification of flow effects on acoustics. It should be highlighted though that with SimPAC^2 the real path is calculated.

The name convention for the cylindrical sound paths or parts of them is defined as described in Sec. 6.2.1.3 and depicted in Fig. 6.15, with the parts 'US' and 'DS' being larger for the present case, as the transducers are recessed in the cavities.

In Fig. 6.34 the normalized axial velocity, $Vel_{Norm}[k]$, is shown in the 'All' part of the cylindrical sound path for v_{ref} ={5, 10, 20, 30}, for the CFD and Ful.-dev. flow-fields. $Vel_{Norm}[k]$ can be qualitatively inspected in that way and useful remarks can be made.

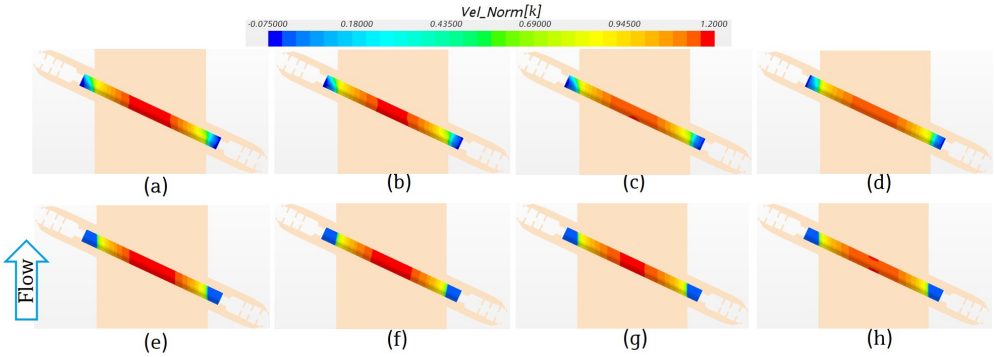

Figure 6.34: Normalized axial flow velocity contours for the whole cylindrical sound path, 'All' for (a), (b), (c), and (d) 5 m/s, 10 m/s, 20 m/s, and 30 m/s respectively for CFD flow-field and (e), (f), (g), and (h) 5 m/s, 10 m/s, 20 m/s, and 30 m/s respectively for Ful.-dev. flow-field. Recessed transducers.

Similarly to Case 4, one can induce that for the CFD flow-field, secondary flow is present, not in the axial direction but towards the cavities. Similarly to the flush transducers, the flow is slightly asymmetric for the CFD case, as it was experimentally observed before by Raišutis [209]. Obviously, flow is present inside the cavities ($r > R$) for the CFD flow-field but not for the Ful.-dev.. Variances are observed also in the flow inside the pipe, as a result of the flow in the cavities [209].

In order to quantify the qualitative remarks made, the volume average axial velocity $\bar{v}_0[k]$ is calculated in the parts 'All', 'In,' 'US', and 'DS' of the sound paths for both CFD and Ful.-dev. flow-fields for v_{ref} ={5,10,20,30} m/s and is shown in Fig. 6.35. One can make several remarks from this diagram:

- All four remarks made for Case 4 (Sec. 6.2.1.3) in connection with Fig. 6.18 are valid for the present case as well.
- However, there is an objection regarding the 3$^{\text{rd}}$ remark, as the curve $\bar{v}_0[k](v_{ref})$ is concave down for Case 5 for the 'US-CFD' and 'DS-CFD' cases in contrast with Case 4, where the curve is concave up. This confirms the qualitative observation in Fig. 6.33 regarding the increasing size of the vortices, and therefore lower $\bar{v}_0[k]/v_{ref}$ in the cavities, for increasing v_{ref}. This phenomenon is further studied in the present section.

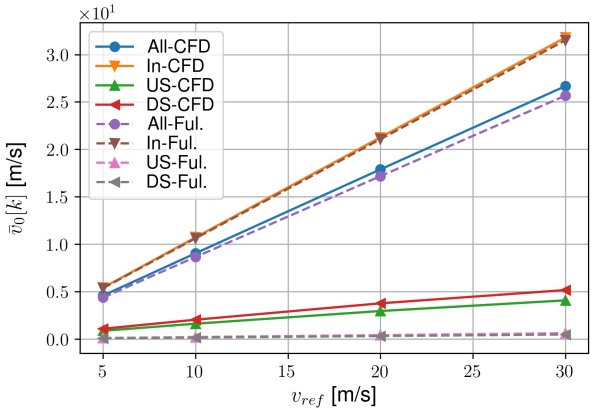

Figure 6.35: Volume average axial velocity $\bar{v}_0[k]$ in the sound paths or portions of them as defined in Fig. 6.15, for the respective recessed transducers. CFD or Ful.-dev. flow-field considered.

The volume average axial velocity in the sound paths, may be normalized with v_{ref} for a better depiction of the relative change of flow velocity in parts of the sound paths, as shown in Fig. 6.36. The pure Re dependency [30, 84, 196, 241] of the UTTF is shown in Fig. 6.36(a)

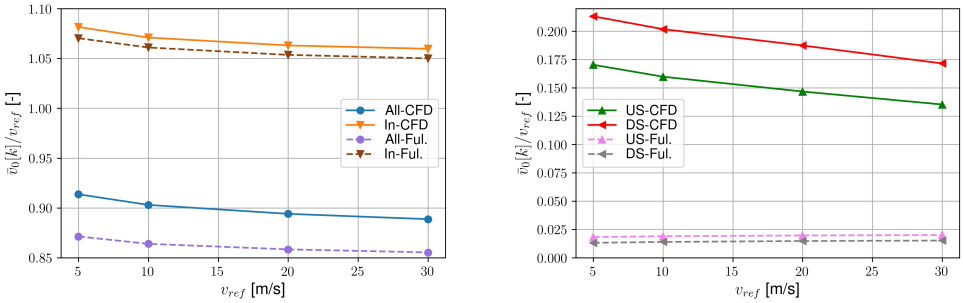

(a) (b)

Figure 6.36: Normalized volume average axial velocity ($\bar{v}_0[k]/v_{ref}$) in (a) 'All' and 'In', (b) 'US' and 'DS' parts. CFD and Ful.-dev. flow-field considered. Recessed transducers.

similarly to Case 4. However, one may observe that the differences of $\bar{v}_0[k]/v_{ref}$ between the 'In' parts for the two flow-fields are larger ($\simeq 1$ %) compared to Case 4, as a result of the larger cavities, which influence more the flow inside the meter body (for $r < R$) [209]. The difference of $\bar{v}_0[k]/v_{ref}$ for the 'All' parts is much larger as well for Case 5 between the CFD and Ful.-dev. ($\simeq 4$ % offset) than for Case 4 (< 1 % offset). This is owed again to the larger cavities, in which v_0=0 for Ful.-dev. flow field. Additionally, for the 'All' parts, $\bar{v}_0[k]/v_{ref}$<1 for Case 5 due to the large cavities as well.

As shown in Fig. 6.36(b), $v_0[k]$ is higher in the downstream cavity compared to the

upstream, which is in agreement with prior literature [110, 146]. An interesting finding is revealed when observing the trend of $\bar{v}_0[k]/v_{ref}$ in Fig. 6.36(b). $\bar{v}_0[k]/v_{ref}$ is reduced for increasing v_{ref} and therefore it follows the trend of the Re dependency, unlike Case 4. This is in agreement with the qualitative observations made regarding the generated vortices in the cavities (Fig. 6.33) as well as with the concave down trend of the 'US-CFD' and 'DS-CFD' cases in Fig. 6.35 (b).

Consequently, one concludes that the flow inside the cavities is relatively lower for increasing flow velocity v_{ref}. for the large recesses of this case. This conclusion is still in agreement with prior literature, where it was shown that $\boldsymbol{v_0}$ is higher, in absolute values, in the cavities for higher v_{ref} [110, 146]. However, the additional finding in the present work, is the relatively lower flow in the cavities for higher v_{ref} due to the trend of $\bar{v}_0[k]/v_{ref}$ with v_{ref} in Fig. 6.36(b). The results regarding the two considered flow-fields and the higher axial volume average velocity in the sound paths for the CFD flow-field explain the later or earlier arrival of the voltage signal because of flow for upstream or downstream wave propagation, respectively (Figs. 6.31, 6.32).

In Fig. 6.37 the deviation between the CFD and Ful.-dev. cases is shown for the volume average axial velocity, $\frac{\bar{v}_{0,CFD}[k]-\bar{v}_{0,Ful}[k]}{\bar{v}_{0,Ful}[k]}100$, in the parts 'All' and 'In'. As already induced

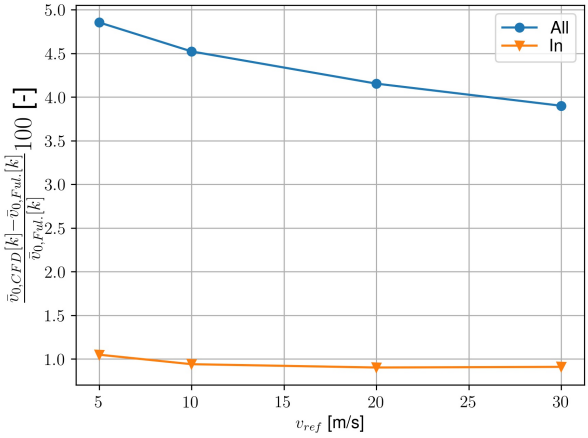

Figure 6.37: deviation in % between the CFD and Ful.-dev. flow-fields for the volume average axial velocity $\frac{\bar{v}_{0,CFD}[k]-\bar{v}_{0,Ful}[k]}{\bar{v}_{0,Ful}[k]}100$, for the 'All' and 'In' parts. Recessed transducers.

from Fig. 6.36 the volume average axial velocity is higher for the CFD flow field in both parts, 'All' and 'In'. One can additionally conclude:

- For the 'All' part, $\bar{v}_{0,CFD}[k]$ is relatively reduced compared to the $\bar{v}_{0,Ful.}[k]$ for increasing velocities.
- For the 'In' part, the relative differences are lower, with slight decreasing trend for increasing v_{ref}.

- The decreasing trend is stronger for the 'All' part compared to the 'In'. This is owed to the flow in cavities included in the 'All' part, where $\bar{v}_0[k]/v_{ref}$ has a clear negative trend for the CFD flow-field inside the cavities, as shown in Fig. 6.36 (b).

In Fig. 6.38 the acoustic pressure field is shown in the middle plane section yz in the fluid near the sending transducer T1 for a number of time-samples, when CFD flow is considered. It is decided to show the acoustic pressure field only for the CFD flow-field, since the differences between the two flow-fields are almost not observable for such an early stage of the propagation. However, one can already notice for an early time-sample (Fig. 6.38

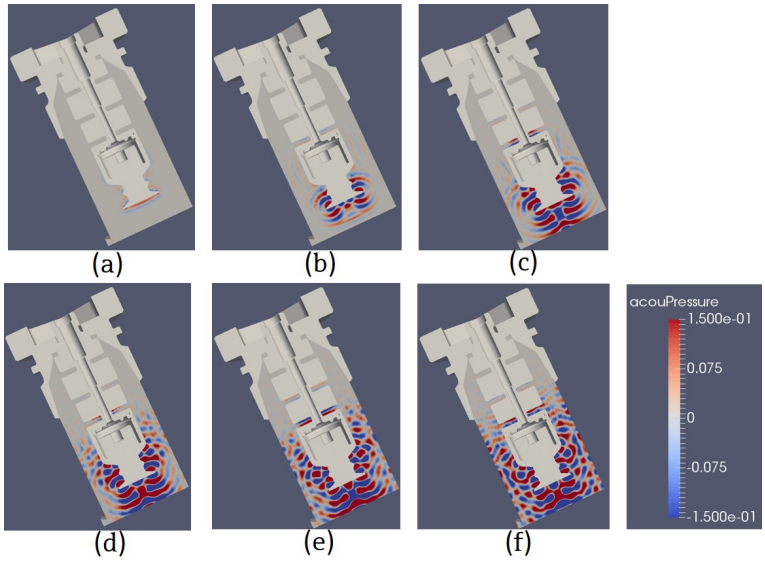

Figure 6.38: Acoustic pressure field [m] in the middle plane section yz in the fluid near the sender, shown for different time samples (a) 7.5 μs (b) 15 μs, (c) 22.5 μs, (d) 30 μs, (e) 37.5 μs, (f) 45 μs. Recessed transducer and CFD flow-field considered for v_{ref} =10 m/s..

(a), 7.5 μs and (b) 15 μs) that the transducer radiates not only on the front towards the receiver but also to the sides and back inside the cavity. This is not an ideal design for a transducer but it is the purpose of this work to capture such effects.

In Fig. 6.39 the acoustic pressure field [Pa] and the magnitude of mechanical displacement [m] are shown in the middle plane section yz in the fluid and in the solid parts of the receiver, respectively, for a number of time-samples, when CFD and Ful.-dev. flow-fields are considered. More specifically, for Fig. 6.39(a)-(f), CFD flow is taken into account and for Fig. 6.39(g)-(l) Ful.-dev. flow-field. The flow velocity v_{ref} = 10 m/s is chosen for further investigation, for comparison reasons with the already investigated respective v_{ref} for Case 4. The observations related to Fig. 6.21 regarding Case 4 (Sec. 6.2.1.3), are valid for the present Case 5 as well.

One may additionally notice that even for earlier stages of the reception, the acoustic pressure signal seems more distorted for Case 5 with recessed transducers, as it is subjected

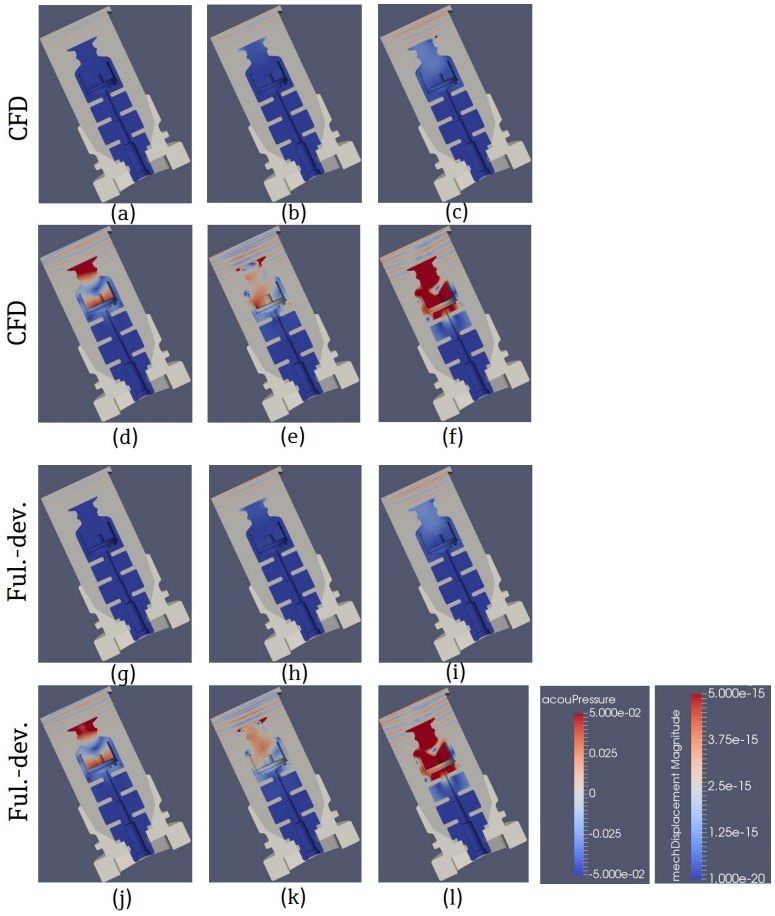

Figure 6.39: Acoustic pressure field and mechanical displacement magnitude in the middle plane section yz in the fluid and in the solid parts of the receiver, respectively, for different time-samples. (a),(g) 386.25 μs (b),(h) 393.75 μs, (c),(i) 401.25 μs, (d),(j) 408.75 μs, (e),(k) 416.25 μs, and (f),(l) 423.75 μs. for CFD, Ful.-dev. flow-fields, respectively. Recessed transducers for v_{ref} =10 m/s for all depictions.

to stronger reflections from the cavities of both T1 and T2, in comparison with the case of flush transducers. For a qualitative proof of the said claim, one may, for example, compare the acoustic pressure field between Case 4 and Case 5 by a direct juxtaposition of figs. 6.21 (c) and 6.39 (d), where the waves have traveled inside the solid domain for a similar amount of time for the two cases, i.e. 21 μs for Case 4 and 23.75 μs for Case 5. From this comparison it can be seen that the reflections are slightly more profound inside the cavity for Case 5 i.e., the wave-fronts are more distorted.

In Fig. 6.40 the downstream ToF, t_{12}, upstream ToF, t_{21}, and time difference Δt are shown for a number of flow-velocities, for a CFD and Ful.-dev. flow-field. Differences due

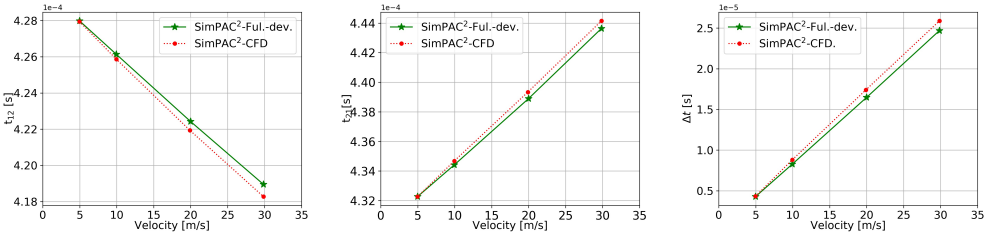

(a) (b) (c)

Figure 6.40: Time-parameters against velocity. (a) t_{12} (downstream wave propagation), (b) t_{21} (upstream wave propagation), and (c) $\Delta t = t_{21} - t_{12}$. Recessed transducers.

to the considered flow-fields can already be viewed from this representation, along with the linear positive trend for t_{21} and Δt, and negative trend for t_{12}. Due to the larger cavities, the differences are more profound compared to Case 4.

The ToF and Δt values are examined further in combination with the already presented and analyzed flow-fields along the sound paths and inside the cavities (cf. Figs. 6.33, 6.34, 6.35, 6.36, and 6.37). The ToF for US and DS propagation, as well as for the two flow-fields, is normalized with the respective v_{ref}, as shown in Fig. 6.41. The flow-effect (Re effect)

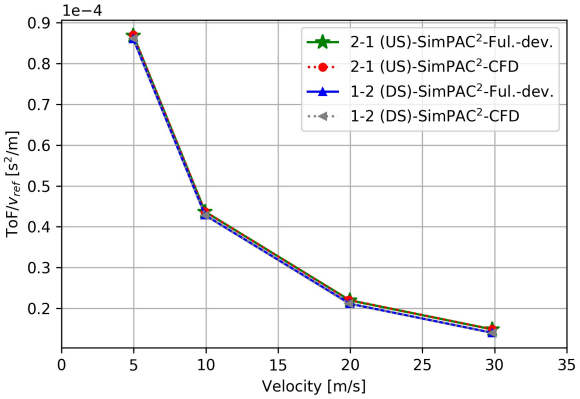

Figure 6.41: ToF/v_{ref} [s$^2/m$] for 2-1 (US) and 1-2 (DS) propagation, for CFD and Ful.-dev. flow-fields. Recessed transducers.

[30, 84, 196, 241] is noticed on both t_{12} and t_{21}. Similarly to Case 4, $t_{21}/v_{ref} > t_{12}/v_{ref}$ for a specific v_{ref}, while their difference is increased for increasing v_{ref}.

The ToF for Ful.-dev. and CFD flow-fields are divided with each other for both US and DS propagation as shown in Fig. 6.42. Unlike Case 4, there is a clear trend of $\text{ToF}_{\text{Ful.-dev}}/\text{ToF}_{\text{CFD}}$ for both US and DS directions. One can make several useful remarks:

- For 2-1 direction (US propagation), t_{21} is consistently longer for the CFD flow i.e., the voltage signal arrives later, because of higher flow-velocity in the sound path (Fig. 6.35,

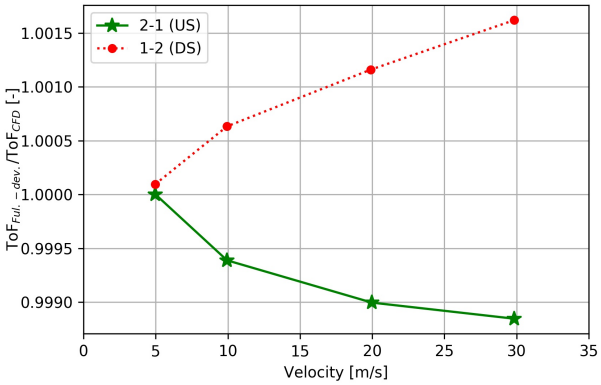

Figure 6.42: $\text{ToF}_{\text{Ful.-dev}}/\text{ToF}_{\text{CFD}}$ [-] for 2-1 (US) and 1-2 (DS) propagation. Recessed transducers.

6.36, and 6.37) than the Ful.-dev. due to, primarily, vortex generation inside the cavities (Fig. 6.33), while for the Ful.-dev. flow-field, $v_0 = 0$ inside the cavities.

- For 1-2 direction (DS propagation), t_{12} is consistently shorter for the CFD flow i.e., the voltage signal arrives earlier for the reasons explained in the previous bullet point.
- The differences between ToF_{CFD} and $\text{ToF}_{\text{Ful.-dev.}}$ are increased for increasing v_{ref}, as the flow inside the cavities becomes stronger, as observed in prior literature [110]. However, the trend of the '2-1 (US)' and '1-2 (DS)' is concave up and down respectively, which is in agreement with the flow-field results (see Fig. 6.37).
- The ToF differences for a specific flow velocity v_{ref} are larger for DS than US propagation i.e. $t_{12,\text{Ful.-dev.}}/t_{12,\text{CFD}} - t_{21,\text{Ful.-dev.}}/t_{21,\text{CFD}} > 0$. This may be explained with the followed sound path for each direction. In front of transducer T2 (Fig. 6.33) there is an abrupt change of $v_0[k]$. This is not the case for the transducer T1, where a vortex covers the whole region in front of T1 and inside the cavity. Therefore, for DS propagation, when the waves are deflected downstream of T2, they pass through high velocity region inside the cavity, and consequently $t_{12\text{CFD}} \gg t_{12\text{Ful.-dev.}}$. However, for US propagation, even when the waves are deflected downstream of T1, the whole area in front of T1 is covered by a low-velocity vortex, and therefore the difference to the respective Ful.-dev. case is not that profound.

The Δt for the two flow-fields, is normalized with the respective v_{ref} as shown in Fig. 6.43, with the purpose of directly comparing the two cases. Several useful remarks are made regarding the Δt for the two flow-fields considered:

- In accordance with Case 4 (cf. Fig. 6.26), the trend of the normalized $\Delta t/v_{ref}$ for the Ful.-dev. flow clearly shows the typical flow profile effect (Re dependency) for a straight pipe [30, 84, 196, 241], since flow is not considered in the cavities. However, for 30 m/s the curve is not monotonic anymore, most likely because of reflections of the strongly deflected waves in the large cavities of the recessed transducers. The latter claim is more of a speculation and it should be further investigated.

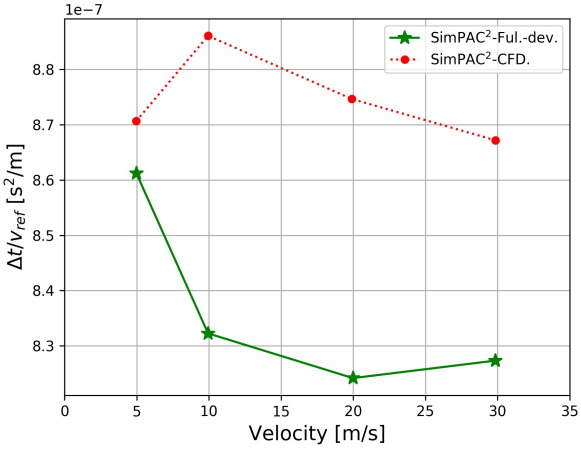

Figure 6.43: $\Delta t/v_{ref}$ [s^2/m] for CFD and Ful.-dev. flow-fields. Recessed transducers.

- For the CFD flow-field, the trend of $\Delta t/v_{ref}$ shows the typical flow-profile effect as well for v_{ref} =[10,30] m/s, however for low flow velocity v_{ref}= 5 m/s, $\Delta t/v_{ref}$ is reduced, despite the monotonic trend of $v_0[k]/v_{ref}$ in every part of the sound path (cf. Fig. 6.36). A conjecture for this behavior is the low $v_0[k]$ inside the cavities, as an absolute value, that resembles the behavior of the Ful.-dev. flow-field. More specifically, it was shown before by Løland [146] that there is an almost linear relation between the flow in the cavity and inside the meter body. In the present case, this relation is almost linear and more specifically, for higher v_{ref}, $v_0[k]$ is increased in absolute values but with a lower gradient $v_0[k]/v_{ref}$, as shown in Fig. 6.36(b). For example, one can say that for 5 m/s the $v_0[k]$ in the cavity is slightly higher than half of the $v_0[k]$ in the cavity for 10 m/s.
- $\Delta t_{\text{CFD}}/v_{ref} > \Delta t_{\text{Ful.-dev.}}/v_{ref}$ for every v_{ref}. This is because of the higher $v_0[k]$ inside the cavities when CFD flow is considered in comparison to the Ful.-dev., for which $v_0[k] \approxeq 0$ (cf. Fig. 6.35). The cavities in Case 5 are larger than in Case 4 and therefore, the effect of considering or not real flow inside them is demonstrated clearer on the values of Δt.
- Similarly to Case 4, the differences between Δt_{CFD} and $\Delta t_{\text{Ful.-dev.}}$ stem to a larger degree from the downstream propagation of the signal (t_{12}), as explained through the last bullet-point in connection with the description of Fig. 6.42.

In Fig. 6.44 the deviation curves are presented for the CNA 'Only CFD' method when realistic CFD flow-field is considered as well as for the SimPAC^2 method for CFD and Ful.-dev. flow-fields.

Similarly to Case 4, eqs. (6.7) and (6.8) are used so that CNA and SimPAC^2 results are directly comparable.

Several useful observations are made from the deviation diagram:

- The first three bullet-points in connection with the explanation of Fig. 6.27, Case 4, flush transducers, are also valid for the present case.

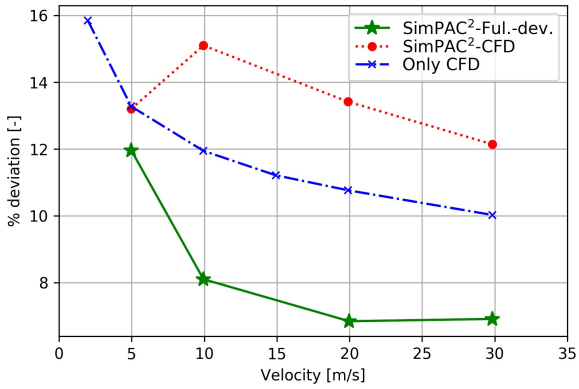

Figure 6.44: Deviation against flow velocity for fully-developed and CFD flow-field. Recessed transducers.

- The %deviation calculated with the SimPAC^2-CFD is higher than the one calculated with the SimPAC^2-Ful.-dev., because of taking into account the flow inside the cavities (figs. 6.33 and 6.37)
- One might suspect that the offset between the deviation curves of SimPAC^2-CFD and Only CFD (CNA) might originate from the fact that only the axial component $v_0[k]$ is considered for the Only CFD method. In tab. 6.4 the values of volume average $\bar{v}_0$ and $\bar{v}_0[k]$ inside the sound path are shown. Due to the small differences ($\simeq 0.01$ %) between

v_{ref} [m/s]	$\bar{v}_0[k]$ [m/s]	$\bar{v}_0$ [m/s]
2	1.8668	1.8670
5	4.5736	4.5739
10	9.0439	9.0440
15	13.4789	13.4791
20	17.9005	17.901
30	26.6691	26.6694

Table 6.4: $\bar{v}_0$ and $\bar{v}_0[k]$ inside the cylindrical sound path calculated with the CNA 'Only CFD' method.

  $\bar{v}_0$ and $\bar{v}_0[k]$, even for this specific case with relatively large cavities that can produce larger vortices, it is concluded that the offset between SimPAC^2-CFD and CNA 'Only CFD' does not originate from the inclusion or not of the secondary flow components.
- One might come to the conclusion that the offset in the deviation curves between CNA 'Only CFD' and SimPAC^2-CFD originates from the difference in the methods themselves i.e., the consideration of a cylindrical sound path, taking into account only flow, for the CNA method and the consideration of the relevant physics and a 'real' sound path for SimPAC^2. As already mentioned in the explanation of the results of Fig. 6.42,

when the sound propagates downstream, the waves are deflected before 'hitting' T2, while they pass through the high-velocity region in front of and slightly downstream of T2 (cf. Fig. 6.33). As a result, $t_{12,\mathrm{CFD}}$ is shorter and $\Delta t_{\mathrm{CFD}}{=}t_{21,\mathrm{CFD}}{-}t_{12,\mathrm{CFD}}$ is longer. Consequently, from eq. (2.91), v_{path} is also increased compared to the CNA 'Only CFD' and SimPAC^2-Ful.-dev. cases.

- The last remark is additionally supported by the fact that for low flow-velocity $v_{ref} = 5$ m/s, $t_{12,\mathrm{CFD}}$ is, relatively to v_{ref}, closer to $t_{12,\text{Ful.-dev.}}$, (Fig. 6.32 (a)) since the waves are not strongly deflected for low flow-velocities and therefore do not pass through the high-velocity region in the cavity (Fig. 6.33 (f)). Consequently, Δt_{CFD} is relatively reduced (Fig. 6.43) and %deviation for SimPAC^2-CFD is respectively reduced for $v_{ref} = 5$ m/s.

Summarizing, one may conclude, that there is a significant offset among the methods CNA 'Only', SimPAC^2-CFD and SimPAC^2-Ful.-dev. for this case, where the transducers are inserted deeper in the pockets of the meter body with larger cavities being formed. The vortices and the spatially and Re highly varying flow-field inside the cavities, especially for DS propagation in front of transducer T2, play a significant role and affect t_{12}, Δt and consequently %deviation. For high-velocities and DS propagation, the sound beam is deflected DS into the high-velocity area in front of T2 (figs. 6.33 and 6.39), and therefore higher v_{path} is calculated with the SimPAC^2-CFD method.

6.2.3 Protruded Transducers

The already described one path UTTF geometry (Sec. 6.2.1) is simulated and investigated for transducers protruded in the meter body of the UTTF.

6.2.3.1 Simulation Setup and Computational Matrix

The sender and the receiver are protruded inside the meter of the UTTF, as shown in Fig. 6.45. This case is denoted from now on as 'Case 6'.

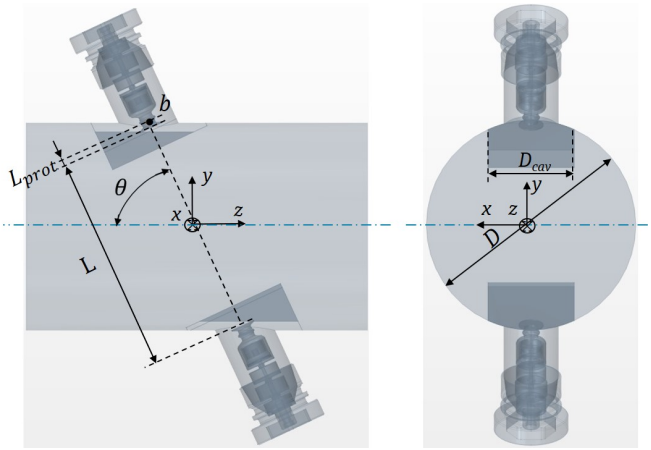

Figure 6.45: 3D geometry of the simulated Case 6 with one diametrical chord sound path and protruded transducers. Left: side view and right: axial view.

The geometrical parameters D, θ, and D_{cav} are of the same value as for Case 4. The radius of the front face of the transducer is $R_{trans} = 5.75$ mm and the length of the simulated device is $L_{dev} = 160$ mm. The distance between the two transducers is changed to L=103 mm and $L_{cav} = 0$ mm, since the transducers are not inside the cavities anymore. On the other hand, each of the transducers is protruded inside the meter body at a distance $L_{prot} = 4.79$ mm. More details regarding the geometry, the simulated parts, BCs, and general simulation setup are given in Sec. 3.2 and in the beginning of Sec. 6.2. The same piezoelectric elements are used as for the geometry of Sec. 6.2.1, Case 4, shown in Fig. 6.7. The domain is split into parts in the same way as the domain of Case 4, while the parameters L_1, L_2, L_3, L_4, L_5, and L_6 has the same values as for Case 4.

The rest of the setup, i.e. the time and space discretization information, as well as the mesh description, are already given at the end of Sec. 6.2.1.1 and are valid for the case of the present section as well, Case 6.

As for Case 4 and Case 5, the geometry is simulated with both the CNA (Only CFD) and SimPAC^2 methods. For the CNA method a real CFD flow-field is used, while for the SimPAC^2 two different flow-fields are used in couple with acoustics, i.e. a Ful.-dev., and a real CFD flow-field, which is the same as for the CNA. More particularly, for the 'Ful.-dev.' flow, the flow profile is fully developed up to $r < R$, as if the transducers did not

exist and therefore, no vortices are generated because of them, while $\boldsymbol{v_0} = 0$ for $r \geq R$. When a real CFD flow-field is considered, vortices are generated because of the protruded transducer, while $\boldsymbol{v_0} \neq 0$ for $r \geq R$ inside the cavities. In Fig. 6.46 the considered flow-fields Ful.-dev. and CFD are shown for indicatively for $v_{ref} = 10$ m/s. When a real CFD flow is considered, vortices and a recirculation zone is observed especially in front of the transducer T1 facing downstream, as already explained in prior literature [239, 259, 286]. The number of simulated cases is the same as for Case 5 (tab. 6.3).

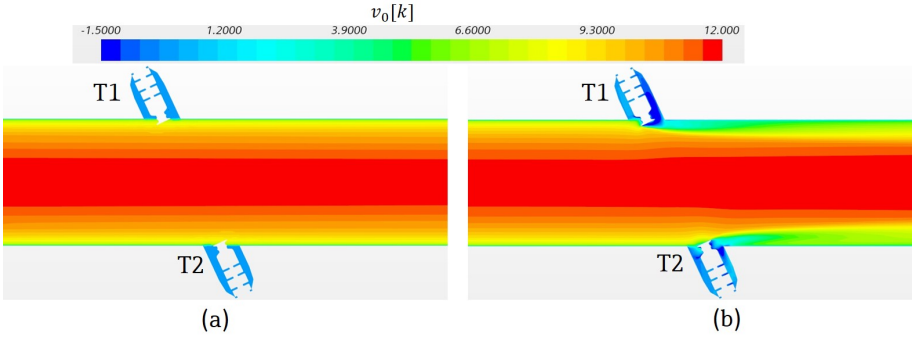

Figure 6.46: Axial flow velocity $v_0[k]$ on middle plane section yz for $v_{ref} = 10$ m/s. a) Ful.-dev. flow and b) CFD flow field.

The comments made for Case 4 at the end of Sec. 6.2.1.2 regarding the comparison of different methods and flow-fields are valid for Case 6 as well.

6.2.3.2 Results

For consistency reasons and for the enablement of direct comparisons between the UTTF geometries with different insertion depth of transducers, the results of Case 6 are presented in a similar form as for Case 4 and Case 5. The voltage on the receiver V_5 is calculated with the SimPAC^2 method and presented in figs. 6.47 and 6.48 for upstream and downstream acoustic wave propagation respectively, for the number of cases documented in tab. 6.3. Similarly to Case 4 and Case 5, not the whole received signal is calculated, as it is not necessarily needed for the UTTF evaluation and generation of deviation curves.

Differences in the voltage signal for a specific flow velocity and different flow-field, are easier to be noticed for higher v_{ref}={-30, -20, 20, 30} m/s, in the diagrams of figs. 6.47 and 6.48.

In the same way as for Case 4 and Case 5, a better depiction of the differences is achieved, when a zoom on the first of the three depicted zero-crossings (black dots) is made for every flow velocity and for the upstream and downstream propagation, as shown in figs. 6.49 and 6.50, respectively.

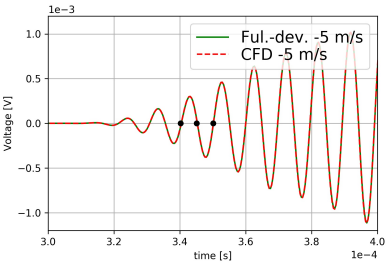

(a) v_{ref} =-5 m/s

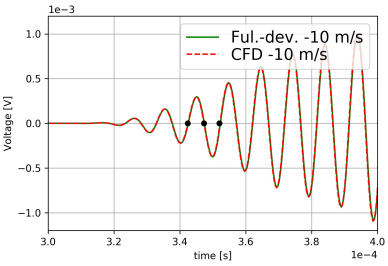

(b) v_{ref} =-10 m/s

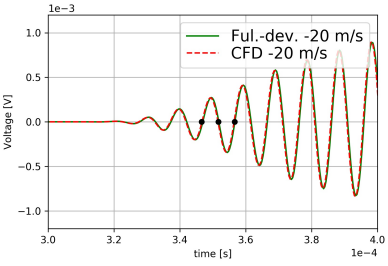

(c) v_{ref} =-20 m/s

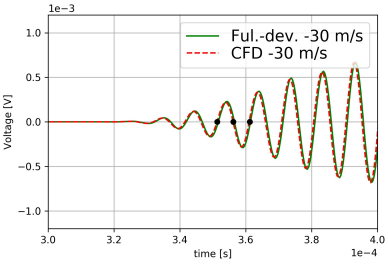

(d) v_{ref} =-30 m/s

Figure 6.47: Voltage signal on receiver V_5 against time, solved with SimPAC^2 for fully-developed and CFD flow-fields and for upstream flow propagation, with three zero-crossings depicted (a) v_{ref}=-5 m/s, (b) v_{ref}=-10 m/s, (c) v_{ref}=-20 m/s, and (d) v_{ref}=-30 m/s. Protruded transducers.

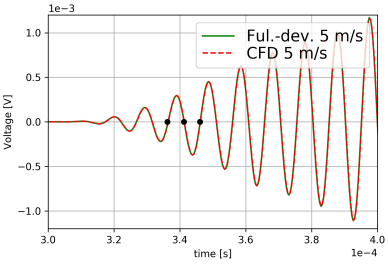

(a) v_{ref} =5 m/s

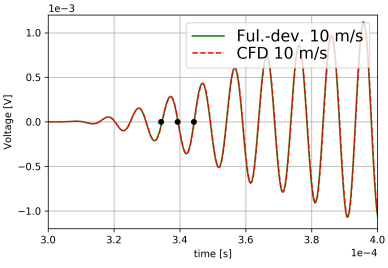

(b) v_{ref} =10 m/s

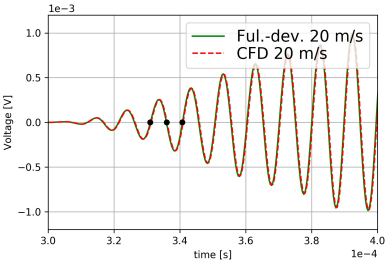

(c) v_{ref} =20 m/s

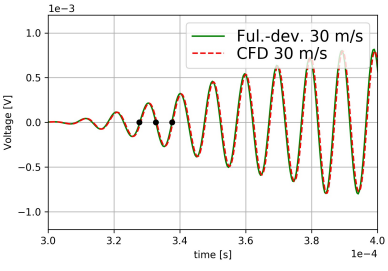

(d) v_{ref} =30 m/s

Figure 6.48: Voltage signal on receiver V_5 against time, solved with SimPAC^2 for fully-developed and CFD flow-fields and for different flow velocities, with three zero-crossings depicted (a) v_{ref}=5 m/s, (b) v_{ref}=10 m/s, (c) v_{ref}=20 m/s, and (d) v_{ref}=30 m/s. Protruded Transducers.

- For upstream wave propagation, (Fig. 6.49) notable differences are observed when a CFD or a Ful.-dev. flow-field is considered for protruded transducers. For all flow-velocities it is valid that $t_{21,\text{CFD}}<t_{21,\text{Ful.-dev.}}$, i.e. the waves arrive earlier when a CFD flow is considered, with the difference being increased for (negatively) increasing v_{ref}, due to the different flow-fields considered. In Fig. 6.46 it is shown that for the CFD case, vortices and low flow-velocity fields are formed in front of the transducers, which are not present for the Ful.-dev. flow field. Therefore, the waves propagate through lower flow-velocity field for the CFD compared to the Ful.-dev. flow. Moreover, the monotonically increasing difference, which correlates with the flow-velocity, is a clue that it is owed, similarly to Case 5, primarily to flow-field differences, i.e. the flow-velocity in the sound path is lower for the CFD than the Ful.-dev. flow-field for the same v_{ref}. An analysis follows based on the flow velocity inside the sound paths, or parts of them, for the two flow-fields considered, as well as the effect of the flow-field on ToF. One should highlight that this time the ToF differences have the opposite sign compared to Case 5. The results of $t_{21,\text{CFD}}<t_{21,\text{Ful.-dev.}}$ is in agreement with the findings of Sun et al. [239] for protruded transducers based on a ray-tracing analysis.
- For downstream wave propagation, (Fig. 6.50) notable differences are observed as well. For all flow-velocities it is valid that $t_{12,\text{CFD}}>t_{12,\text{Ful.-dev.}}$, i.e. the waves arrive later when a CFD flow is considered, with the difference being increased for (positively) increasing v_{ref}. The monotonically increasing difference shows once more that is primarily owed to flow-field effects, for the same reasons explained in the previous bullet point.
- One should highlight that this time, the ToF differences have the opposite sign compared to Case 5 for both US and DS propagation. This means that, in antithesis with the recessed transducers, Case 5, the volume average velocity in the sound path is higher for the Ful.-dev. than for the CFD flow-field. An analysis on that matter follows in the present section. The results of $t_{12,\text{CFD}}>t_{12,\text{Ful.-dev.}}$ is in agreement with the findings of Sun et al. [239] as well.
- It should be noted that the Ful.-dev. flow-field for protruded transducers is an ideal/fictional situation, not possible to be reproduced in reality, as shown in Fig, 6.46. However, the purpose of its investigation is the comparison with a real CFD flow-field and its effect on the flowmeter behavior as well as the comparison with the Case 4 and Case 5 where the transducers' insertion depth is varied.

In order to prove these claims, the flow-field is investigated in a similar manner as for the flush and recessed transducers (Sec. 6.2.1.3 and 6.2.2.2).

In Fig. 6.51 the vortices in front of the upstream and downstream transducers T1 and T2, respectively, are shown, as well as their size and the value of Vel_{Norm} for v_{ref} ={5,10,20,30}. One can make several useful observations:

- Since the transducers are protruded further inside the meter-body of the UTTF compared to Case 4 and Case 5, they significantly disturb the main flow.
- Low and high flow-velocity areas are created in front of T1 and T2 respectively, as similarly observed e.g. in [239, 259].
- A high velocity area is present in front of the protruded transducer T2 in comparison to flush or recessed transducers T2 as in Case 4 and Case 5. A similar observation was made by Kažys et al. [110]

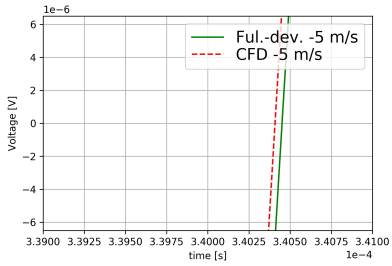

(a) v_{ref} =5 m/s

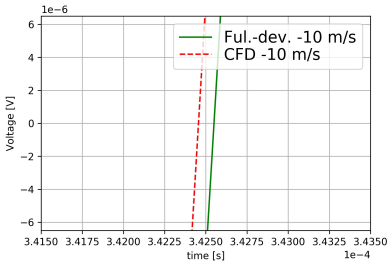

(b) v_{ref} =10 m/s

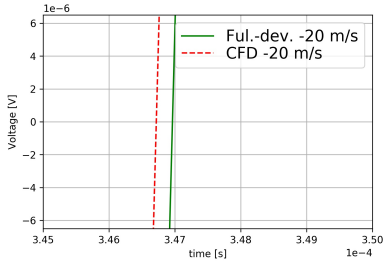

(c) v_{ref} =20 m/s

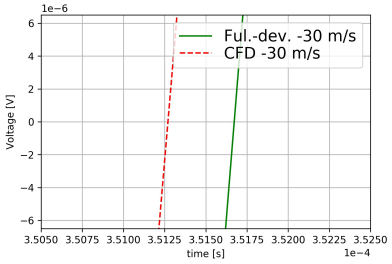

(d) v_{ref} =30 m/s

Figure 6.49: Voltage signal on receiver V_5 against time, zoomed on the first of the three considered zero-crossings (cf. Fig. 6.47). Upstream flow for fully-developed and CFD flow-field. (a) $v_{ref} = -5$ m/s, (b) $v_{ref} = -10$ m/s, (c) $v_{ref} - = 20$ m/s, and (d) $v_{ref} = -30$ m/s. Protruded transducers.

- The size and location of the vortices, as well as Vel_{Norm} in front of the transducers change with the flow velocity v_{ref} but not in the same degree as for the recessed transducers, Case 5. This is further studied in the present section.
- The flow-field in front of and inside the cavities of the transducers T1 and T2, is largely unalike between them, as similarly observed e.g. in [239, 259].
- For a Ful.-dev. profile, such low flow-velocity vortices, as in front of T1, are by definition not generated as shown in Fig. 6.46.

The described behavior indicates a consistent earlier and later arrival for US and DS propagation respectively, when a CFD flow-field is considered compared to a Ful.-dev. one, as seen in Fig. 6.46, where a large vortex is generated in front of the transducer T1 facing downstream. This is confirmed by the results of figs. 6.49 and 6.50 and it is in agreement with the findings regarding ToF from Sun et al. [239].

Due to the different path followed by the US and DS waves [77, 239] the generated vortices have a different effect in each direction, as described already for Case 4 and Case 5. For the present Case 6, there is an abrupt change of flow velocity in front of T1.

- A DS wave propagating from T1 to T2 always passes through the low flow-velocity area in front of T1, as it is not yet deflected in the beginning of its propagation. The vortex in front of T1 decelerates a wave propagating downstream, making it arrive

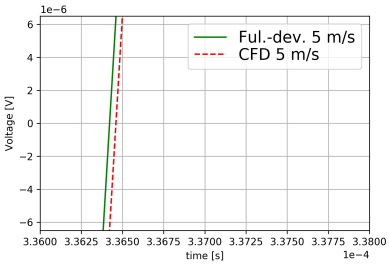

(a) v_{ref} =5 m/s

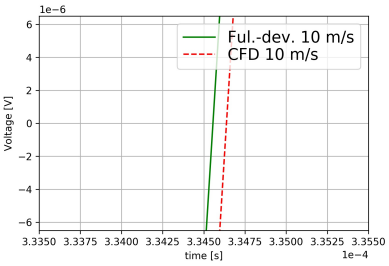

(b) v_{ref} =10 m/s

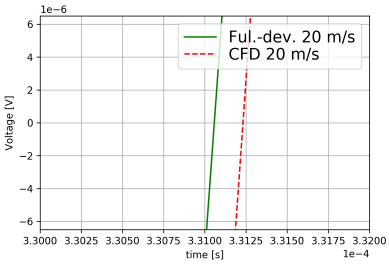

(c) v_{ref} =20 m/s

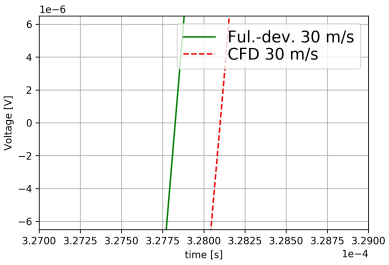

(d) v_{ref} =30 m/s

Figure 6.50: Voltage signal on receiver V_5 against time, zoomed on the first of the three considered zero-crossings (cf. Fig. 6.48). Downstream flow for fully-developed and CFD flow-field. (a) v_{ref}=5 m/s, (b) v_{ref}=10 m/s, (c) v_{ref}=20 m/s, and (d) v_{ref}=30 m/s. Protruded transducers.

later compared to the case of a Ful.-dev. flow field. In the area in front of T2, non-varying higher values of Vel_{Norm} are observed for different v_{ref} and thus, the effect of flow on acoustics for the area in front of T2 is not strongly varying. Voser et al. [259] and Sun et al. [239] similarly noticed the effect of the vortex in front of a protruded transducer facing downstream, such as T1 in the present study.

- An US wave propagating from T2 to T1 always passes through the region in front of T2, where Vel_{Norm} does not vary significantly with v_{ref} or in other words, a constant high-velocity region is present in front of T2 for the whole range of v_{ref}. However, before hitting T1, the wave is deflected weaker or stronger for lower or higher v_{ref} respectively. Consequently, for higher v_{ref} the US wave is expected to arrive increasingly earlier, since it passes through a larger part of the low flow-velocity region in front of and DS of T1. This will be confirmed in the present section.

Similarly to Case 4 and Case 5, cylindrical paths are used for the sake of clarification of flow effects on acoustics. It should be highlighted once more though that with SimPAC^2 the real path is calculated.

The name convention for the cylindrical sound paths is defined as described in Sec. 6.2.1.3 and depicted in Fig. 6.15. In the present case only the 'All' part is defined, since the transducers are protruded and there is no part of the sound path inside the cavities.

In Fig. 6.52 the normalized axial velocity, $Vel_{Norm}[k]$, is shown in the 'All' part of the

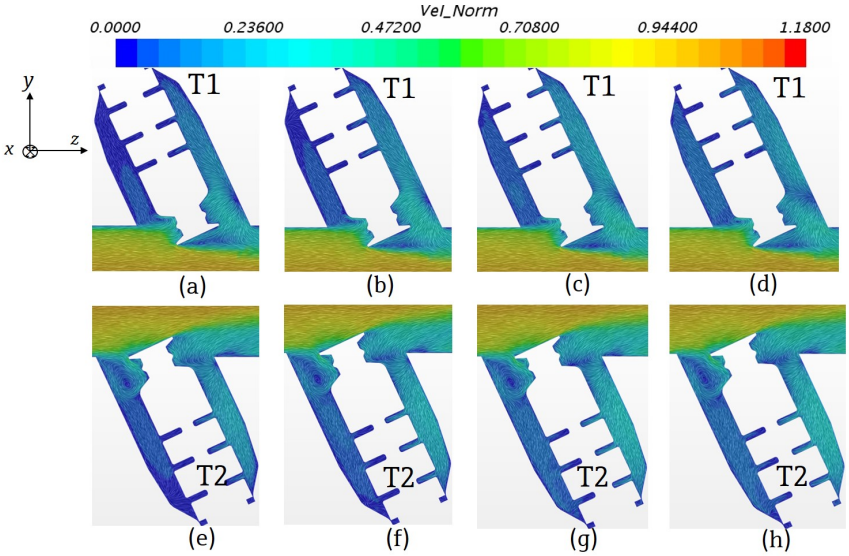

Figure 6.51: Flow-field near the sending and receiving recessed transducers T1 and T2, respectively for protruded transducers. Flow in the z-direction. Normalized velocity $Vel_{Norm} = |v_0|/v_{ref}$ is shown as 'Line Integral Convolution' (LIC) [235] for v_{ref}: (a),(e) 5 m/s, (b),(f) 10 m/s, (c),(g)20 m/s, and (d),(h) 30 m/s.

cylindrical sound path for v_{ref}={5, 10, 20, 30} m/s, for the CFD and Ful.-dev. flow-fields. $Vel_{Norm}[k]$ can be qualitatively inspected in that way and differences between the two flow-

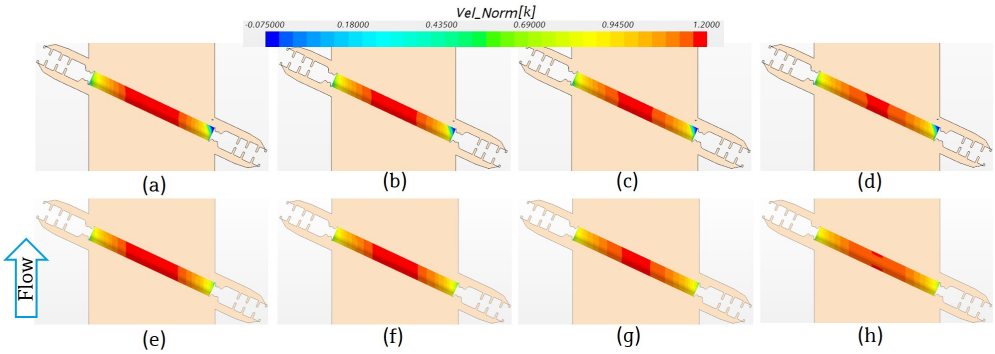

Figure 6.52: Normalized axial flow velocity, $Vel_{Norm}[k]$ contours for the whole cylindrical sound path, 'All' for (a), (b), (c), and (d) 5 m/s, 10 m/s, 20 m/s, and 30 m/s respectively for CFD flow-field and (e), (f), (g), and (h) 5 m/s, 10 m/s, 20 m/s, and 30 m/s respectively for Ful.-dev. flow-field. Protruded transducers.

fields are noticed. The generated vortices in front of the transducers are present for every v_{ref} for the CFD flow-field, as similarly observed in [239, 259]. These vortices are not present

anymore when a Ful.-dev. flow-field is taken into account, where higher velocity areas are present, as shown in Fig. 6.46. Similarly to Case 4 and Case 5, one can induce that for the CFD flow-field, secondary flow is present (not in the axial direction).

In order to quantify the qualitative remarks made, the axial volume average velocity $\bar{v}_0[k]$ is calculated in the parts 'All' for both CFD and Ful.-dev. flow-fields for v_{ref} ={5,10,20,30} m/s and is shown in Fig. 6.53. One can make several remarks from this diagram:

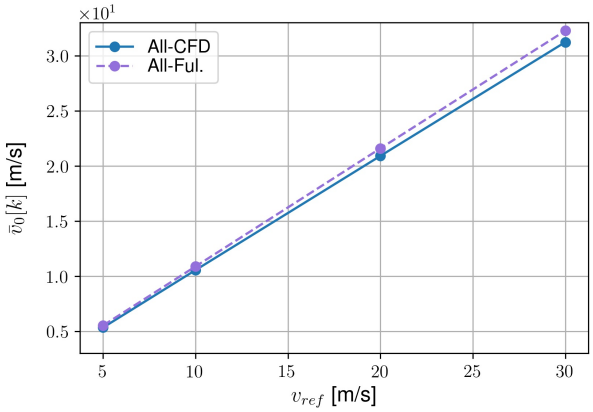

Figure 6.53: Volume average axial velocity $\bar{v}_0[k]$ in the sound paths or portions of them as defined in Fig. 6.15, for the respective protruded transducers. CFD or Ful.-dev. flow-field considered.

- This case is very different from Case 4 and Case 5, as the transducers are protruded inside the meter body and consequently there is only an 'All' part, which would coincide with the 'In' part.
- The qualitative observations made from figs. 6.51, 6.52 regarding the presence of low flow-velocity region in front of T1, are confirmed by the values of $\bar{v}_0[k]$, which are consistently higher for the Ful.-dev. flow-field.

The volume average velocity in the sound paths, is normalized with v_{ref} for a better depiction of the relative change of flow velocity as shown in Fig. 6.54. The pure Re dependency [30, 84, 196, 241] of the UTTF is shown in Fig. 6.54 similarly to Case 4 and Case 5. The offset between $\bar{v}_0[k]$ of the two flow-fields is $\simeq$ 3.04 to 3.38 %, which is closer to the higher values for the recessed transducers. However, this time the values for the Ful.-dev. are higher due to the presence of vortices for the CFD flow-field. Moreover, the weakly varying offset of $\simeq$ 3.04 to 3.38 % between $\bar{v}_0[k]/v_{ref}$ for the respective v_{ref} for CFD and Ful.-dev. flow fields, indicates that the protrusion effect is not constant along the whole range of v_{ref} but it has an effect on %deviation dependent on Re, as indicated by Voser et al. [259]. It is seen as well that $\bar{v}_0[k]/v_{ref}$ is higher for the All-CFD case with protruded transducers than $\bar{v}_0[k]/v_{ref}$ for flush transducers in Fig. 6.19(a), which is in accordance with a similar observation made by Voser et al. [259] i.e., that higher flow velocity values are present in a path for protruded transducers than a path starting and ending at the conduit walls. For recessed transducers, $\bar{v}_0[k]/v_{ref}$ is even lower than for the flush transducers (Fig. 6.36).

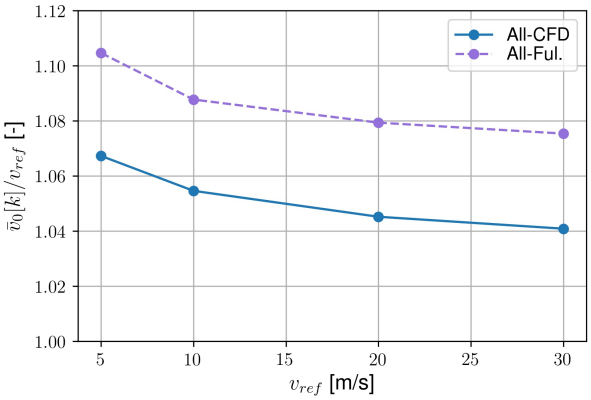

Figure 6.54: Normalized volume average axial velocity ($\bar{v}_0[k]/v_{ref}$) in the 'All' parts. CFD and Ful.-dev. flow-field considered. Protruded transducers.

The results regarding the two considered flow-fields and the higher axial volume average velocity in the sound paths for the Ful.-dev. flow-field explain the later or earlier arrival of the voltage signal because of flow for upstream or downstream wave propagation, respectively (Figs. 6.49, 6.50).

In Fig. 6.55 the deviation between the CFD and Ful.-dev. cases is shown for the volume average axial velocity, $\frac{\bar{v}_{0,CFD}[k]-\bar{v}_{0,Ful}[k]}{\bar{v}_{0,Ful}[k]}100$, in the parts 'All'. As already induced from Fig. 6.54, the volume average axial velocity is higher for the Ful.-dev. flow field in the 'All' parts. One can additionally conclude:

- The flow velocity in the sound paths for the CFD flow-field is lower, as already noticed.
- There is relative change of $\bar{v}_0[k]$ for varying v_{ref} between the two flow-fields, with the lowest value for the CFD flow-field being noticed for $v_{ref} = 5$ m/s. This shows that the effect of protruded transducers is not constant as indicated by Voser et al. [259] but it slightly varies from 3.04% to 3.38% in terms of flow $\frac{\bar{v}_{0,CFD}[k]-\bar{v}_{0,Ful}[k]}{\bar{v}_{0,Ful}[k]}100$.

In Fig. 6.56 the acoustic pressure field [Pa] and the magnitude of mechanical displacement [m] are shown in the middle plane section yz in the fluid and in the solid parts of the receiver, respectively, for a number of time-samples, when CFD flow-field is considered.

The flow velocity $v_{ref} = 10$ m/s is chosen for further investigation, for comparison reasons with the already investigated respective v_{ref} for Case 4 and Case 5. The observations related to Fig. 6.21 regarding Case 4 (Sec. 6.2.1.3), are valid for the present Case 6 as well.

One can notice that weaker reflections are observed, as expected, because the frontal surfaces of both transducers are positioned outside of the cavities and inside the meter body of the UTTF. It is chosen to show a case of wave propagation only for the CFD flow-field, since the qualitative differences of acoustic pressure and magnitude of mechanical displacement are not easy to observe through the contours. Such comparisons have already been made for Case 4 and Case 5.

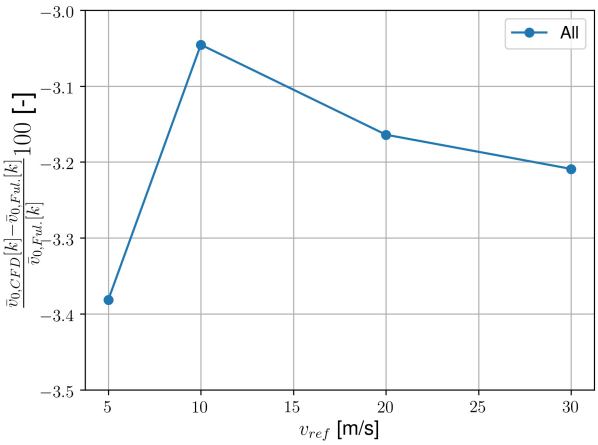

Figure 6.55: deviation in % between the CFD and Ful.-dev. flow-fields for the volume average velocity $\frac{\bar{v}_{0,CFD}[k]-\bar{v}_{0,Ful}[k]}{\bar{v}_{0,Ful}[k]}100$, for the 'All' part. Protruded transducers.

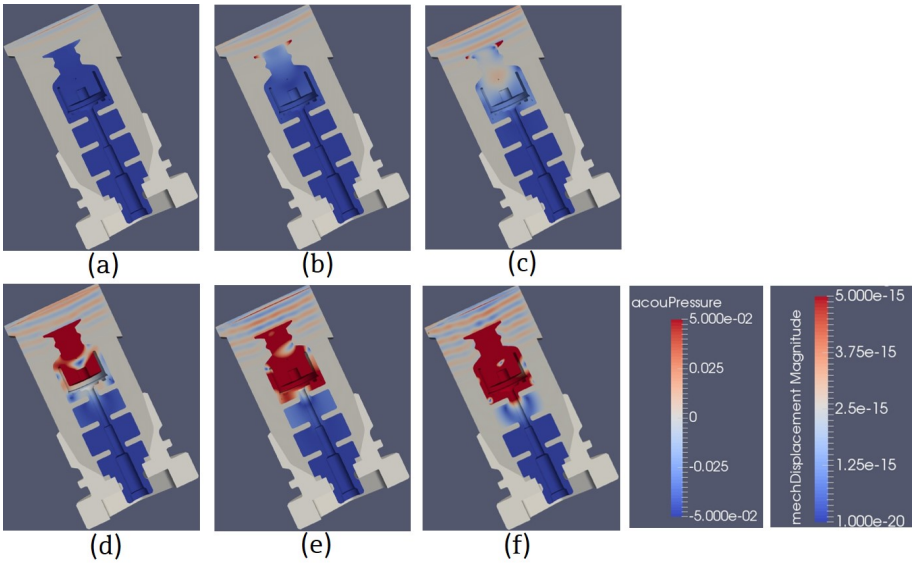

Figure 6.56: Acoustic pressure field [Pa] and mechanical displacement magnitude [m] in the middle plane section yz in the fluid and in the solid parts of the receiver, respectively, for different time samples (a) 296.625 μs (b) 304.125 μs, (c) 311.625 μs, (d) 319.125 μs, (e) 326.625 μs, (f) 334.125 μs. Protruded transducer and CFD flow-field considered for v_{ref} =10 m/s.

In Fig. 6.57 the downstream ToF, t_{12}, upstream ToF, t_{21}, and time difference Δt are

shown for a number of flow-velocities, for a CFD and Ful.-dev. flow-field. Differences due

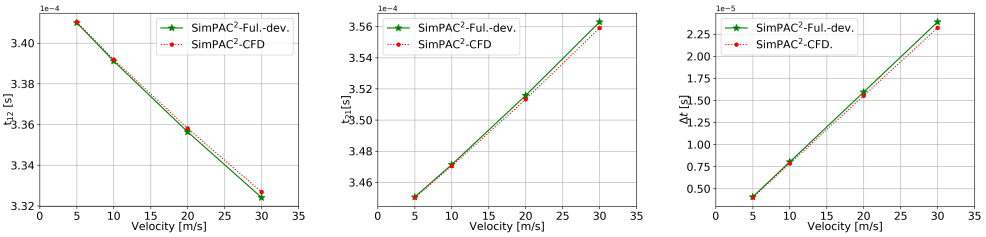

Figure 6.57: Time-parameters against velocity. (a) t_{12} (downstream wave propagation), (b) t_{21} (upstream wave propagation), and (c) $\Delta t = t_{21} - t_{12}$, for protruded transducers.

to the considered flow-fields can already be viewed from this representation, along with the linear positive trend for t_{21} and Δt, and negative trend for t_{12}. For higher v_{ref}, it is easier to notice the differences between SimPAC^2-CFD and SimPAC^2-Ful.-dev. Due to the transducers being protruded in the meter body, the differences are more profound compared to Case 4 (cf. fig. 6.23). The ToF values and their differences for the considered flow-fields and flow velocities have been examined through flow, acoustic and mechanical displacement fields and a further analysis follows.

The ToF for US and DS propagation, as well as for the two flow-fields, is normalized with the respective v_{ref}, as shown in Fig. 6.58. The flow-effect (Re effect) [30, 84, 196, 241] is

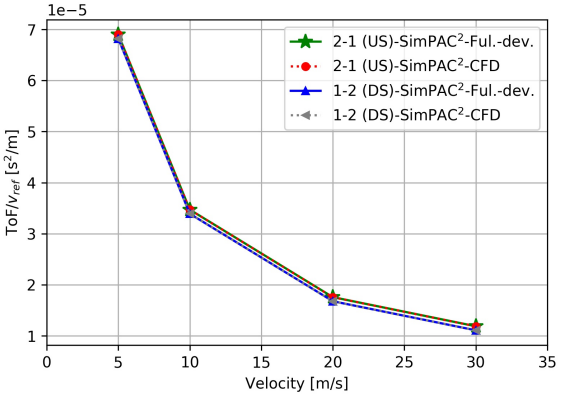

Figure 6.58: ToF/v_{ref} [s$^2/m$] for 2-1 (US) and 1-2 (DS) propagation, for CFD and Ful.-dev. flow-fields. Protruded transducers.

noticed on both t_{12} and t_{21}. Similarly to Case 4 and Case 5, $t_{21}/v_{ref} > t_{12}/v_{ref}$ for a specific v_{ref}, while their difference is increased for increasing v_{ref}.

The ToF for Ful.-dev. and CFD flow-fields are divided with each other for both US and DS propagation as shown in Fig. 6.59. Unlike Case 4, and similar to Case 5, there is a clear

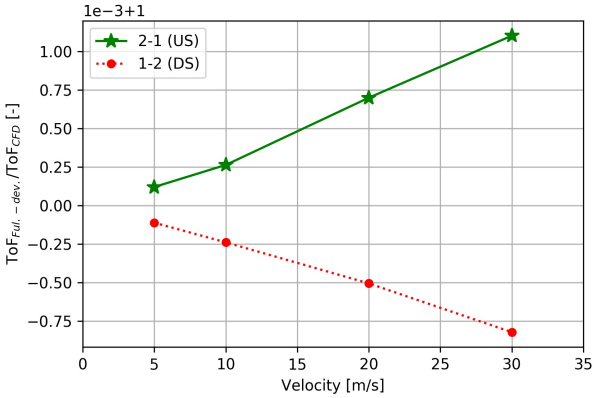

Figure 6.59: ToF$_{Ful.-dev}$/ToF$_{CFD}$ [-] for 2-1 (US) and 1-2 (DS) propagation. Protruded transducers.

trend of ToF$_{\text{Ful.-dev}}$/ToF$_{\text{CFD}}$ for both US and DS directions. One can make several useful remarks:

- The trends of ToF$_{\text{Ful.-dev.}}$/ToF$_{\text{CFD}}$ for US and DS are opposite compared to Case 5, i.e. $t_{12,\text{Ful.-dev.}}/t_{12,\text{CFD}} < 1$ and $t_{21,\text{Ful.-dev.}}/t_{21,\text{CFD}} > 1$.
- For 2-1 direction (US propagation), t_{21} is consistently shorter for the CFD flow, i.e. the voltage signal arrives earlier, because of lower flow-velocity in the sound path (Fig. 6.53, 6.54, and 6.55) than the Ful.-dev. due to vortex generation in front of T1 (Fig. 6.51). This result is in agreement with the findings of Sun et al. [239] i.e., t_{21} is consistently shorter as well for a CFD flow compared to a Ful.-dev. one.
- For 1-2 direction (DS propagation), t_{12} is consistently longer for the CFD flow, i.e. the voltage signal arrives later for the reasons explained in the previous bullet point. This result is in agreement with the findings of Sun et al. [239] as well i.e., t_{12} is consistently longer as well for a CFD flow compared to a Ful.-dev. one.
- The differences between ToF$_{\text{CFD}}$ and ToF$_{\text{Ful.-dev.}}$ are increased for increasing v_{ref}, which shows that this is an effect owed to the flow, as it correlates with the flow-velocity in both US and DS directions. This observation is in agreement with the results of Sun et al. [239] but not in agreement with the observation of Voser et al. [259], where it was described that the protrusion effect is constant for a range of Re.
- The ToF differences for a specific flow velocity v_{ref} are larger for US than DS propagation, unlike Case 5, i.e. $t_{21,\text{Ful.-dev.}}/t_{21,\text{CFD}} - t_{12,\text{Ful.-dev.}}/t_{12,\text{CFD}} > 0$. This may be explained with the followed sound path for each direction. In front of transducer T1 (Fig. 6.51) there is an abrupt change of $v_0[k]$, as a vortex is formed. Depending on v_{ref}, i.e. beam deflection, the waves pass through a larger part of the low flow-velocity region for increasing v_{ref}. Consequently, for US propagation the waves are decelerated less for a CFD flow-field and $t_{21,\text{Ful.-dev.}}/t_{21,\text{CFD}}$ is increased. The observation that the ToF differences between a CFD and a Ful.-dev. flow-field are higher for US than DS propagation are in agreement with the analysis of Sun et al. [239] for protruded

transducers.

The Δt for the two flow-fields, is normalized with the respective v_{ref} as shown in Fig. 6.60, with the purpose of directly comparing the two cases. Several useful remarks are made

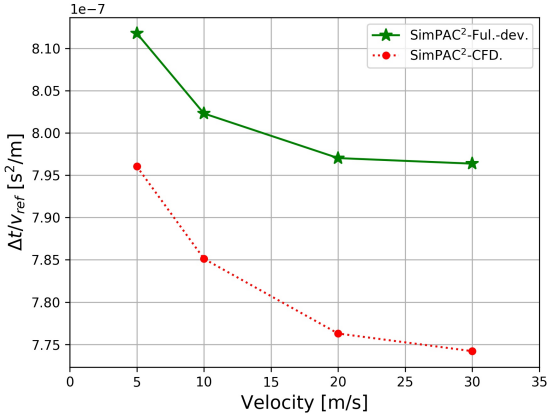

Figure 6.60: $\Delta t/v_{ref}$ [s^2/m] for CFD and Ful.-dev. flow-fields. Protruded transducers.

regarding the Δt for the two flow-fields considered:

- In accordance with Case 4 and Case 5, the trend of the normalized $\Delta t/v_{ref}$ for the Ful.-dev. flow clearly shows the typical flow profile effect (Re dependency) for a straight pipe [30, 84, 196, 241], since flow is not considered in the cavities.
- For the CFD flow-field, the trend of $\Delta t/v_{ref}$ shows the typical flow-profile effect as well, however for increasing v_{ref} the difference between the two cases is increased. As already explained, the main reason is the vortex created in front of T1 combined with the stronger beam deflection for higher v_{ref}, for both US and DS propagation. The effect for US propagation is slightly stronger as described through Figs. 6.51 and 6.59.
- $\Delta t_{\text{CFD}}/v_{ref} < \Delta t_{\text{Ful.-dev.}}/v_{ref}$ for every v_{ref} due to the higher $v_0[k]$ in the sound path for Ful.-dev. flow-field (Fig. 6.53).

In Fig. 6.61 the deviation curves are presented for the CNA 'Only CFD' method when realistic CFD flow-field is considered, as well as for the SimPAC^2 method for CFD and Ful.-dev. flow-fields. Similarly to Case 4, eqs. **(6.7)** and **(6.8)** are used so that CNA and SimPAC^2 results are directly comparable.

Several useful observations are made from the deviation diagram:

- The first two bullet-points in connection with the explanation of Fig. 6.27, Case 4, flush transducers, are also valid for the present case.
- The %deviation calculated for all cases seems to follow the the typical trends due to the flow profile in a straight pipe (Re dependency). The offset among the curves of %deviation varies with v_{ref}, which is a sign that the protrusion effect is Re dependent. This is in agreement with Sun et al. [239] and not in agreement with Voser et al. [259].

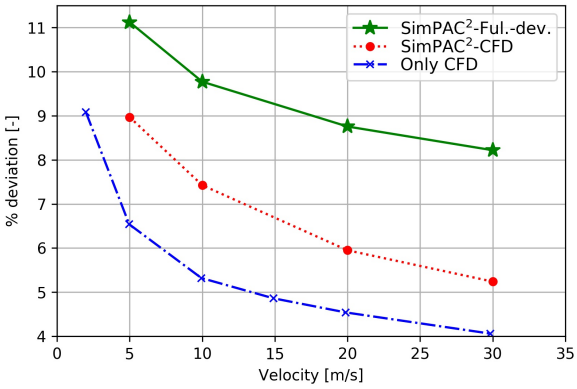

Figure 6.61: Deviation against flow velocity for fully-developed and CFD flow-field, for protruded transducers.

- The %deviation for the Ful.-dev. flow-field is shifted to higher values compared to the CFD, because of higher considered $v_0[k]$ in the sound path.
- The question arises, why is the %deviation of SimPAC²-CFD shifted to higher values compared to the CNA 'Only CFD' method? Similarly to the explanation regarding Case 5, one might come to the conclusion that the differences originate from the methods themselves, i.e. the consideration of a cylindrical sound path, taking into account only flow, for the CNA 'Only CFD' method and the consideration of all the relevant physics and a 'real' sound path for SimPAC².
- The offset between the %deviation of SimPAC²-CFD and SimPAC²-Ful.-dev. is increased for higher velocities, following the trend of Δt (Fig. 6.60), owed to the vortex in front of T1 and beam deflection for both US and DS propagation. However, the effect is stronger for US propagation (cf. Fig. 6.59) as also indicated by Sun et al. [239].

Summarizing, one may conclude, that there is a significant offset among the methods CNA 'Only', SimPAC²-CFD and SimPAC²-Ful.-dev. for this case, where the transducers are protruded in the meter body. The vortices and the spatially highly varying flow-field in front of T1, especially for US propagation, play a significant role and affect t_{21}, Δt and consequently %deviation. For high-velocities and especially for US propagation, the sound beam is deflected downstream into the low-velocity area in front of T1, but not highly varying for different v_{ref} (figs. 6.51 and 6.56), and therefore lower v_0 is calculated with the SimPAC²-CFD method compared to the SimPAC²-Ful.-dev..

6.2.4 Summary of One-Path UTTF and Insertion Depth Variation

Summarizing, and comparing Case 4, flush, Case 5, recessed, and Case 6, protruded, interesting observations are revealed, especially regarding the final result of the deviation curves.

In Fig. 6.62 the already investigated deviation curves are shown from a different perspective. In each Subfig., an insertion depth variation is shown for each method.

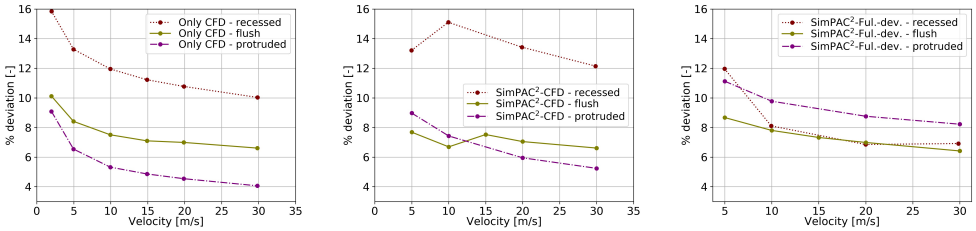

(a) (b) (c)

Figure 6.62: Deviation against flow velocity summarized for recessed, flush, and protruded transducers. (a) CNA 'Only CFD', (b) SimPAC^2-CFD, and (c) SimPAC^2-Ful.-dev..

- The CNA 'Only CFD' method (Fig. 6.62 (a)) quantifies the pure flow-effect, because of the change of the insertion-depth of the transducers. An offset among the deviation curves is observed, which is not proportional to the change of insertion depth, i.e. $L_{cav,\text{recessed}} - L_{cav,\text{flush}} = L_{cav,\text{flush}} - L_{cav,\text{protruded}}$ but $\%\text{deviation}_{\text{recessed}} - \%\text{deviation}_{\text{flush}} \neq \%\text{deviation}_{\text{flush}} - \%\text{deviation}_{\text{protruded}}$ for a specific flow-velocity. In fact, the offset for recessed transducers, with large cavities, is higher, because, despite the flow-field considered in the cavities, a '0' flow-velocity is implied in them due to eqs. (6.7) and (6.8).

  Moreover, the flow-effect is monotonic, while the deviation curve with the lowest values of $|\max(\%\text{deviation}) - \min(\%\text{deviation})|$, i.e. linear, belongs to Case 4 with flush transducers. The main reason of the described effect is the smaller change of the flow-field in regard with flow-velocity compared to Case 5 and Case 6, due to the small cavities and non-protruding transducers, which would function as obstacles in the main flow in the meter body of the UTTF (Fig. 6.51).

  Thus, if one should choose the 'best' i.e. most linear deviation curve based on the 'Only CFD' method, this would be the one for the flush transducers (cf. Fig. 6.62(a)). This statement is not in agreement with a series of prior literature [208, 261, 286], where it was stated that protruded transducers are beneficial. It should be noted though that different geometries were investigated in [208, 261, 286] compared to the present thesis and therefore, a direct comparison should be carried out with caution. It is the author's opinion that a statement regarding a beneficial position should be based on the linearity of the deviation curve e.g.$|\max(\%\text{deviation}) - \min(\%\text{deviation})|$, and not the offset from zero values that can be easily corrected. $|\max(\%\text{deviation}) - \min(\%\text{deviation})|$ was used as criterion in [208] as well, where protruded transducers

were found to present better linearity than half protruded and recessed. In the work of Qin et al. [208] it was found through CFD that the velocity along the sound paths is higher for protruded, lower for half protruded, and the lowest for recessed, which is in agreement with the results of the present work (cf. Figs. 6.19, 6.36 6.54) however, in the course of the analysis of the results the opposite was stated in that same work [208]. The result of higher velocity along a sound path with protruded transducers than with flush ones is in agreement with the findings of Voser et al. [259] as well. Zheng et al. [286] concluded that protruded transducers are beneficial as well, based on the offset of the %deviation from zero values and not on |max(%deviation) − min(%deviation)|. However, if one decides based on |max(%deviation) − min(%deviation)|, then the recessed transducers, or with the respective name convention of the present work the 'flush' transducers, are beneficial in the work of Zheng et al. [286], which agrees with the result of the present thesis. Moreover, it is the author's opinion, that the position of the transducers is only one of the factors affecting the deviation of an UTTF and thus, no general statement can be made regarding the most beneficial position but only a statement for one particular geometry. Other factors, apart from the position of the transducers, affecting the deviation of an UTTF is e.g. the geometry of the transducers, the size of the cavity, the size of the meter body, and the radial position of the transducers. The results of 'Only CFD' method regarding recessed transducers are in agreement with prior literature [110, 146, 208] (cf. Fig. 6.62(a)), where a varying vortex is present in the cavity that at the end affects the %deviation of an UTTF.

- The SimPAC^2-CFD method (Fig. 6.62 (b)) captures the combined acoustic-flow effects for a 'real' CFD flow-field. One can see that for flush and recessed transducers and for flow-velocity $v_{ref} < 10$ m/s, the %deviation does not follow the same monotonic trend as for the 'Only CFD' method, because of combined acoustic-flow effects in the cavities (cf. secs. 6.2.1.3 and 6.2.2.2) and the presence of a vortices with varying size for different v_{ref}, as described by others [110, 146].

  However, for protruded transducers, the %deviation is monotonic, since the vortices generated due to the protruded transducers vary with Re but less significantly than the recessed transducers, as indicated by others as well [208]. The sound waves follow a different path for US and DS propagation [77], while a vortex generated in front of the protruded transducers, especially the T1, affects t_{12} and t_{21} in a different way as described by Sun et al. [239] as well. The most linear deviation curve belongs to the flush transducers for the SimPAC^2-CFD as well, which is in agreement with the work of Zheng et al. [286].

- The SimPAC^2-Ful.-dev. method (Fig. 6.62 (c)) captures flow-acoustic effects, however not for a real but for an ideal Ful.-dev. flow-field. This diagram exposes further the limitations of the consideration of such an ideal flow-field.

  The state-of-the-art Ful.-dev. (or Analytical) flow-field used in many cases [30], flattens out the differences for different insertion-depths of the transducers, i.e. essentially different geometries. Therefore, apart from obviously not considering the correct flow, it is observed that an insertion-depth or other geometrical investigation would lead to incorrect conclusions for the design of an UTTF. This result highlights further the importance of SimPAC^2-CFD.

Moreover, the deviation curve for recessed transducers does not present such a large offset in the positive direction as for the SimPAC^2-CFD, since zero velocity is considered in the cavities, which is in accordance with eqs. (6.7) and (6.8). This highlights further the consistency of the results also for the CNA 'Only CFD' and SimPAC^2-CFD methods.

It is important to note that for protruded transducers, when comparing the two flowfields considered, t_{12} is longer for CFD than for Ful.-dev., while t_{21} is shorter for CFD than for Ful.-dev. for a specific v_{ref} as explained in Sec. 6.2.3, which is in agreement with the work from Sun et al. [239].

6.3 Real Flowmeter with Two Chordal Paths

A real flowmeter with two chordal sound paths, namely 'Case 7', is presented in this chapter. The flowmeter Proline Prosonic Flow G 300 [64] is measured and simulated. Not the final design of the ultrasonic transducers is used but another version, described in chapter 3 that was not included in the end-product [62]. The exact geometry in 3D as well as the simulation files are uploaded in [194]. The measurements took place in a calibration flow rig at Endress+Hauser, while simulations were performed with both the CNA and the SimPAC^2 methods described in chapter 3. The motivation for this comparison between measurements and simulations is the end-verification of the SimPAC^2 method with a real product of complex geometry. The generated measured and simulated results, as well as their agreement help to draw conclusions and identify potential limitations of the method.

6.3.1 Geometry and Simulation Setup

The full geometry of the meter body of the investigated flowmeter Proline Prosonic Flow G 300 [64], as well as the simulation setup are already shown and described in secs. 3.1 and 3.2. For more information on the investigated flowmeter, the interested reader may refer to [64], while the transducers' and cavities' dimensions are given in [62].

In connection with the SimPAC^2 method, as already described in chapter 3, a CFD simulation is performed separately (cf. Subsec. 3.2.5) and the flow-field data, $\boldsymbol{v_0}$, are given to the the fluid in parts (I), (II), and (III) (cf. Subsecs. 3.2.2, 3.2.3, 3.2.4). However, an analytical expression of the flow-field is also possible to be given (cf. Subsec. 3.2.5).

The exact dimensions of the fluid domain and the mesh used for the CFD simulation of the present geometry are given in Subsec. 3.1. This CFD simulation is used either for the CNA method when further post-processing is made in the way described in Sec. 3.1, or as an input to the SimPAC^2 (cf. Sec. 3.2.1).

The dimensions of the solid parts considered and the fluid domain simulated with the SimPAC^2 method are given in Sec. 3.2. A full description and documentation of the dimensions is given in [62]. The material properties of the solid parts are given in tab. 3.1 and the cell-size of the cells comprising the mesh are given in tab. 3.2 and in Sec. 3.2. It is reminded that half of the UTTF is simulated and therefore, a symmetry plane is applied on the $yz-$plane, as shown in Fig. 3.14. For the selected radial position of the two sound-paths at $R_{dp} = 0.5 \cdot R$, the weight factor $w_i = 1$ [176]. Consequently, according to eq. (1.8), $v_{path,i} = v_{path,1} = v_{path,2} = v_{calc}$ for the investigated case.

The fluid medium considered in the simulations is air, at temperature $T_0 = 19.4^o$C, pressure, p_0=1 bar, and speed of sound, $c = 342.8$ m/s. The carrier frequency used is $f_c = 100$ kHz for a sinusoidal input voltage signal V_1 of length $4T_c$, where $T_c = 1/f_c$. More specifically the input voltage signal V_1 for the simulation, is given as

$$V_1 = 5\sin(2\pi f_c t), \qquad t \leq 4T_c, \tag{6.9}$$

meaning that an amplitude of 5 V is considered in contrast with Case 4, Case 5, and Case 6, where an amplitude of 1 V was considered. However, the equations are linear (cf. ch. 2)

and linear scaling of the results is possible for a direct comparison of the cases. It should be noted that non-linearities have been identified before when the amplitude is increased to 10 V for a different case investigated in [277] however, internal verifications do not show signs of non-linearities in the case studied in the present subsection for an amplitude of 5 V.

The measurement equipment of the signal generator, the oscilloscope and the cables connecting them to the transmitter and the receiver are not included in the simulation. The implications of this matter are discussed further in the present chapter.

6.3.2 Experimental Setup

Measurements are conducted in an air calibration rig at Endress+Hauser designed with the help of CFD simulations in order to achieve a fully-developed flow profile [58] upstream of the flowmeter [193].

The minimum flow of the rig is 0.555 liters/sec and the maximum flow is 2416.667 liters/Sec. Rotary piston flowmeters are used as master meters. The total measurement uncertainty of the rig is ± 0.25 % m/s, and the temperature stability is $\pm 0.5\ ^oC$.

The measured device Proline Prosonic Flow G 300 [64], as well as a detail of the experimental transducer used are shown in Fig. 6.63. The dimensions of the measured device are

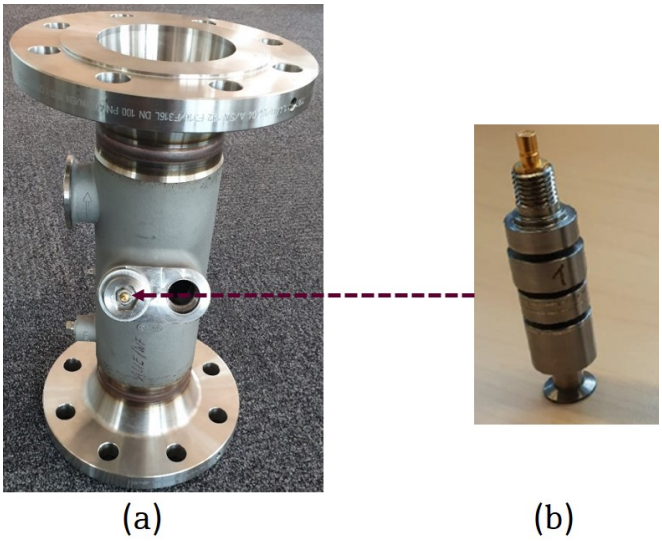

Figure 6.63: Measured geometry of (a) flowmeter Proline Prosonic Flow G 300 with internal diameter $D = 97$ mm, and (b) detail of the experimental transducer.

given in Sec. 3.2, as they are the same as the dimensions of the simulated device. It should be highlighted that the transducer shown in Fig. 6.63 is not the final design of the transducer used in the product but one of the experimental designs [62]. More information regarding the geometry and the materials of the flowmeter and the transducer is given in Sec. 3.2 and Subsec. 6.3.1. It is reminded that the transducers are slightly recessed with $L_{cav} = 5.8$ mm and $\theta = 65^o$.

A schematic representation of the experimental setup is shown in Fig. 6.64. The inline flowmeter Proline Prosonic Flow G 300 is mounted in the calibration rig with enough inlet run of 72 D for the flow profile to develop. The straight pipe of 72 D is located after a package of flow conditioners that help the flow development and achieve a fully-developed profile upstream of the UTTF. The UTTF is schematically shown as the domain in the dashed lines in Fig. 6.64. A signal generator Agilent 33250A [7] is used for the signal generation on either of the transducers T1 and T2, while an oscilloscope Agilent MSO6014A [8] is used

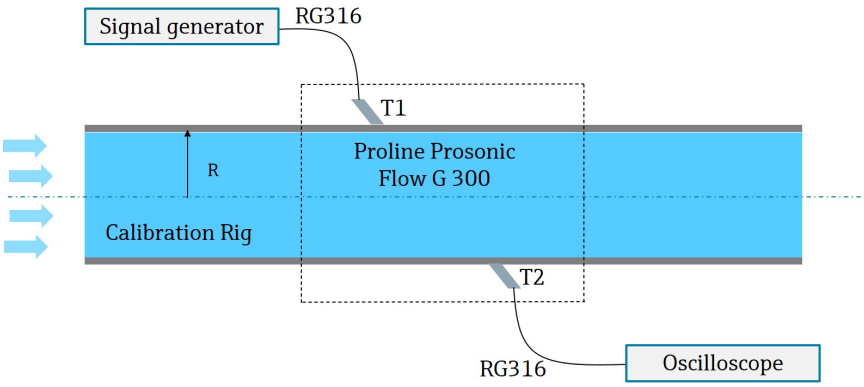

Figure 6.64: Schematic representation of experimental setup for Case 7.

for the signal recording on either of the transducers T1 and T2. In Fig. 6.64, the state is shown, where the signal generator is connected to T1 and the oscilloscope to T2. The signal generator and the oscilloscope are directly connected to the transducers with flexible coaxial cables RG316, 1 meter long. The reason for not using the flowmeter electronics, is the approximation of a voltage driven source for the transmitter and an open circuit for the receiver, in order to minimize the influence of the electronics' impedance on the transmitted and received signals (cf. Sec. 1.5).

One path of the device is measured, because of symmetry, while the ports of the transducers for the second path are sealed. When stability is achieved in the calibration rig, according to the above mentioned criteria, a measurement takes place, i.e. voltage is generated by the signal generator on the transmitter side. A sinusoidal burst is generated with amplitude of 5 V and a time-length of 4 periods, as given in eq. (6.9) where $f_c = 100$ kHz and $T_c = 1/f_c$. The sampling frequency of V_5 is $f_s = 50$ MHz. The input voltage signal V_1 for the measurements is the same as for the simulations.

The waves travel from T1 into the medium and then into T2, which is connected with the oscilloscope that measures the received voltage signal V_5. In that way, a measurement for a downstream wave propagation is performed. Under the same flow conditions, the cables connecting T1 with the signal generator and T2 with the oscilloscope are interchanged immediately on-site in order to perform a measurement for an upstream wave propagation. After the flow is measured in both directions, the reference flow velocity, v_{ref}, is adjusted to a different value. When stability in the rig is newly achieved, the next set of downstream and upstream flow measurement takes place. The received signal V_5 is averaged over 64·4=256 periods T_c in order to increase the signal strength compared to the random noise [164].

Measurements in zero flow are performed as well with T1 used as a transmitter, T2 as a receiver and vice-versa. For the zero flow to be guaranteed, the device is placed in a room with constant temperature and both ends of the meter-body are sealed. The purpose of such a measurement is the identification of $\Delta t_{i,0} = \Delta t_0$ [155], as described in Sec. 2.5. The results of the simulations and the measurement follow in the next subsection.

6.3.3 Analysis and Results

Simulations and measurements are performed for a number of reference flow velocities v_{ref}, as shown in tab. 6.5. A larger number of measurements than simulations was made, due to the ease and short time needed for the measurement execution and setting of v_{ref}. Obviously, the initial time and effort needed for setting up the experiment (cf. 6.3.2) remains constant, irrespectively of the number of measurements made.

Velocity v_{ref} [m/s]	Only CFD (CNA)	SimPAC^2-Ful.-dev.	SimPAC^2-CFD.	Measurements
0	✓	✓	✓	✓
2, -2	✓	-	-	✓
5, -5	✓	✓	✓	✓
10, -10	✓	✓	✓	✓
15, -15	✓	-	✓	✓
20, -20	✓	✓	✓	✓
25, -25	-	-	-	✓
30, -30	✓	✓	✓	✓

Table 6.5: Computational and measurement matrix of Case 7, Proline Prosonic Flow G 300 [64] with two sound paths.

For consistency reasons and for the enablement of direct comparisons with Case 4, Case 5, and Case 6, the results of Case 7 are presented in a similar form as for Case 4, Case 5, and Case 6. The received voltage signals V_5 are measured and calculated with the SimPAC^2 method. Afterwards, an analysis of the flow-field in the cavities and near the transducers takes place that gives insight on the impact of the flow on acoustics. The volume average velocity in an assumed cylindrical sound path, or parts of it, is calculated for a number of v_{ref} in order to assess the flow-field effect on acoustics, in the space between the transducers. The acoustic pressure field in the fluid in front of the receiver, as well as the mechanical displacement magnitude in the solid parts of the receiver, are shown for a number of time samples. The ToF, Δt, as well as the normalized parameters ToF/v_{ref} and $\Delta t/v_{ref}$ reveal interesting findings regarding the flowmeter operation and its comparison with the one-path flowmeters of Case 4, Case 5, and Case 6. Finally, the deviation curve is presented and conclusions are drawn from the results obtained with the different simulation methods and the measurements. The limitations of the SimPAC^2 method and the parts that are not considered are mentioned. Results that were not able to be fully clarified either from the measurements or from the simulations are discussed as well.

The voltage on the receiver V_5 is calculated with the SimPAC^2 method and presented in figs. 6.65 and 6.66 for upstream and downstream acoustic wave propagation respectively, for some of the cases documented in tab. 6.5. The measured received voltage V_5 is also presented in figs. 6.65, 6.66. Similarly to Case 4, Case 5, and Case 6, not the whole received signal is calculated with the SimPAC^2 method, as it is not necessarily needed for the UTTF evaluation and generation of deviation curves.

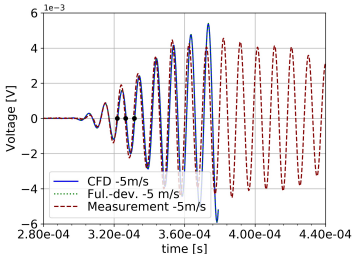

(a) v_{ref} =-5 m/s

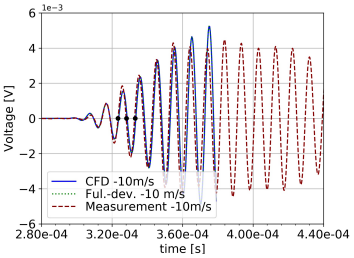

(b) v_{ref} =-10 m/s

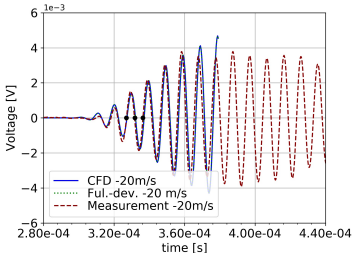

(c) v_{ref} =-20 m/s

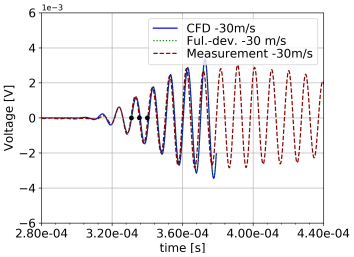

(d) v_{ref} =-30 m/s

Figure 6.65: Voltage signal on receiver V_5 against time, measured and solved with SimPAC^2 for fully-developed and CFD flow-fields and for upstream propagation, with three zero-crossings depicted (a) v_{ref}=-5 m/s, (b) v_{ref}=-10 m/s, (c) v_{ref}=-20 m/s, and (d) v_{ref}=-30 m/s. Real two-path ultrasonic flowmeter, Case 7.

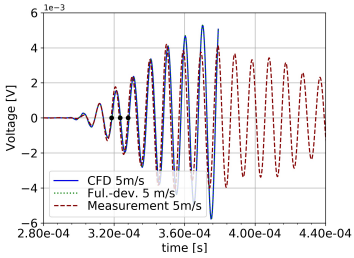

(a) v_{ref} =5 m/s

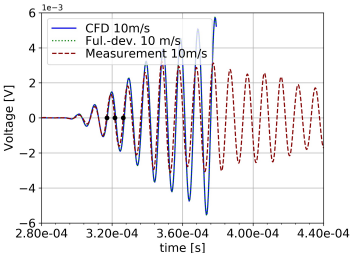

(b) v_{ref} =10 m/s

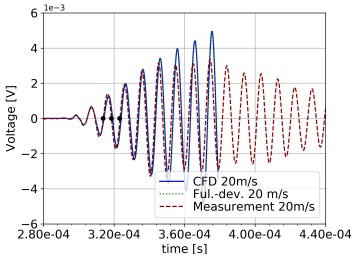

(c) v_{ref} =20 m/s

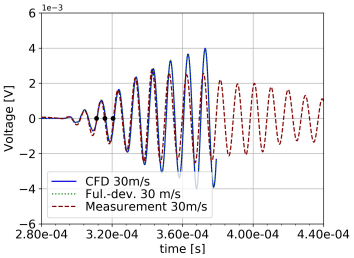

(d) v_{ref} =30 m/s

Figure 6.66: Voltage signal on receiver V_5 against time, measured and solved with SimPAC^2 for fully-developed and CFD flow-fields and for downstream propagation, with three zero-crossings depicted (a) v_{ref}=5 m/s, (b) v_{ref}=10 m/s, (c) v_{ref}=20 m/s, and (d) v_{ref}=30 m/s. Real two-path ultrasonic flowmeter, Case 7.

The differences between the voltage signals for a specific v_{ref} cannot be easily noticed due to the scale of the axes in figs. 6.65 and 6.66. In the same way as for Case 4, 5, and 6 a better depiction of the differences is achieved, when a zoom on the first of the three depicted zero-crossings (black dots) is made for every flow velocity and for the upstream and downstream propagation, as shown in figs. 6.67 and 6.68, respectively.

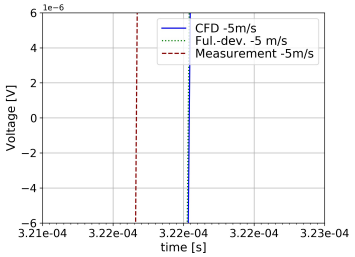

(a) $v_{ref} = -5$ m/s

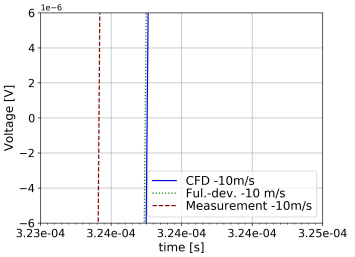

(b) $v_{ref} = -10$ m/s

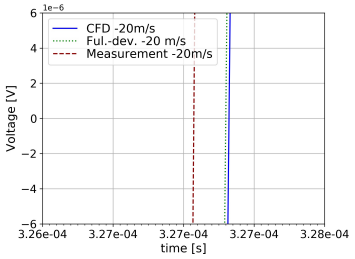

(c) $v_{ref} = -20$ m/s

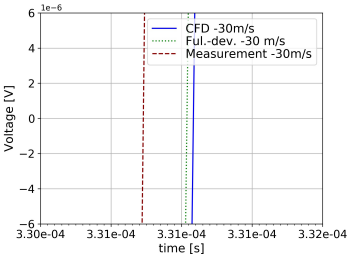

(d) $v_{ref} = -30$ m/s

Figure 6.67: Voltage signal on receiver V_5 against time, zoomed on the first of the three considered zero-crossings (cf. Fig. 6.65). Upstream flow for fully-developed and CFD flow-field. (a) $v_{ref} = -5$ m/s, (b) $v_{ref} = -10$ m/s, (c) $v_{ref} = -20$ m/s, and (d) $v_{ref} = -30$ m/s. Real two-path ultrasonic flowmeter, Case 7.

- In figs. 6.67, 6.68, it is noticed that the measured voltage signal V_5 arrives earlier compared to the simulated one for all cases, according to the first of the three depicted zero-crossings. The same applies for the 2$^{\text{nd}}$ and 3$^{\text{rd}}$ of the 3 depicted zero-crossings, which are used for the calculation of ToF, as described in Sec. 2.5.1. This behavior and possible explanations are investigated further in the present section.
- In figs. 6.65, 6.66, 6.67, and 6.68, a deviation between the measured and simulated amplitudes of V_5 is observed. This inconsistency may be attributed to numerical dispersion [223], as well as to potential measurement uncertainty, due to the experimental setup (cf. Subsec. 6.3.2), because of factors such as external electromagnetic interference. Precise quantification of these potential attributes of uncertainty is not provided.
- For increasing positive or negative v_{ref}, the amplitude of the voltage signal V_5 is reduced, due to beam deflection [197], which is in agreement with Sun et al. [239].

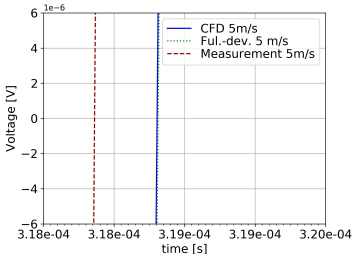

(a) v_{ref} =5 m/s

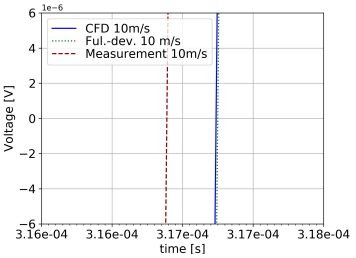

(b) v_{ref} =10 m/s

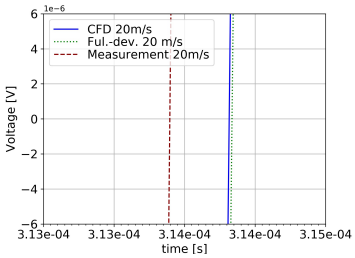

(c) v_{ref} =20 m/s

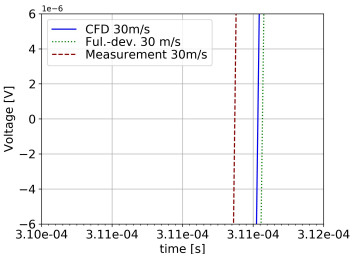

(d) v_{ref} =30 m/s

Figure 6.68: Voltage signal on receiver V_5 against time, zoomed on the first of the three considered zero-crossings (cf. Fig. 6.66). Downstream flow for fully-developed and CFD flow-field. (a) v_{ref}=5 m/s, (b) v_{ref}=10 m/s, (c) v_{ref}=20 m/s, and (d) v_{ref}=30 m/s. Real two-path ultrasonic flowmeter, Case 7.

- For upstream wave propagation, (Fig. 6.67) differences are observed when a CFD or a Ful.-dev. flow-field is considered, for Case 7. For all flow-velocities it is valid that $t_{21,\text{CFD}} > t_{21,\text{Ful.-dev.}}$, i.e. the waves arrive later when a CFD flow is considered, with the difference being increased for (negatively) increasing v_{ref}. The monotonically increasing difference, which correlates with the flow-velocity, is a clue that it is owed, similarly to Case 5 and Case 6 primarily to flow-field differences, i.e. the flow-velocity in the sound path is higher for the CFD than the Ful.-dev. flow-field for the same v_{ref}, as it is investigated further in the present section. One should highlight that the ToF differences have the same sign as Case 5, i.e. one path device with recessed transducers. The transducers are also recessed for the present investigated Case 7.
- For downstream wave propagation, (Fig. 6.68) differences are observed as well in terms of ToF between the two SimPAC^2 cases. For all flow-velocities it is valid that $t_{12,\text{CFD}} < t_{12,\text{Ful.-dev.}}$, i.e. the waves arrive earlier when a CFD flow is considered, with the difference being increased for (positively) increasing v_{ref}. The monotonically increasing difference shows once more that the earlier arrival of the voltage signal for CFD compared to Ful.-dev. flow is primarily owed to flow-field effects.
- The monotonic increase of ToF difference for increasing positive or negative v_{ref} between SimPAC^2-CFD and SimPAC^2-Ful.-dev. shows that the flow velocity is higher in the sound path when a CFD flow field is considered, as it is investigated further in the

present section.

- The ToF maintains the same behavior, in contrast to the comparison with the measurements, for all three considered zero-crossings between the SimPAC^2-CFD and SimPAC^2-Ful.-dev, since the numerical setup for the two cases is otherwise the same. More specifically, $t_{21,\text{CFD}}>t_{21,\text{Ful.-dev.}}$ and $t_{12,\text{CFD}}<t_{12,\text{Ful.-dev.}}$ for all v_{ref}, which can be attributed to a flow-effect (cf. Sec. 5.4) but the ToF of measurements is always shorter compared to the simulations irrespective of the direction of propagation. This behavior is investigated further in the present subsection.

In order to shed light to these claims, the flow-field is investigated in a similar manner as for Case 4, Case 5, and Case 6 (Sec. 6.2.1.3, 6.2.2.2, and 6.2.3.2). The CFD flow-field is investigated through contours, since for the 'Ful.-dev.' it is clear that the flow inside the cavities is zero. Of course, in the measurements the flow-field resembles the CFD with vortices in the cavities.

In Fig. 6.69 the vortices in front of and inside the cavities of the upstream T1 and downstream T2 transducers are shown, as well as their size and the value of Vel_{Norm} for v_{ref} ={5,10,15,20,30} m/s for the CFD flow-field. The coordinate system is only indicative of the directions, while the correct coordinate system is shown in Fig. 3.4. The medium flows in the z-direction. One can make several useful observations:

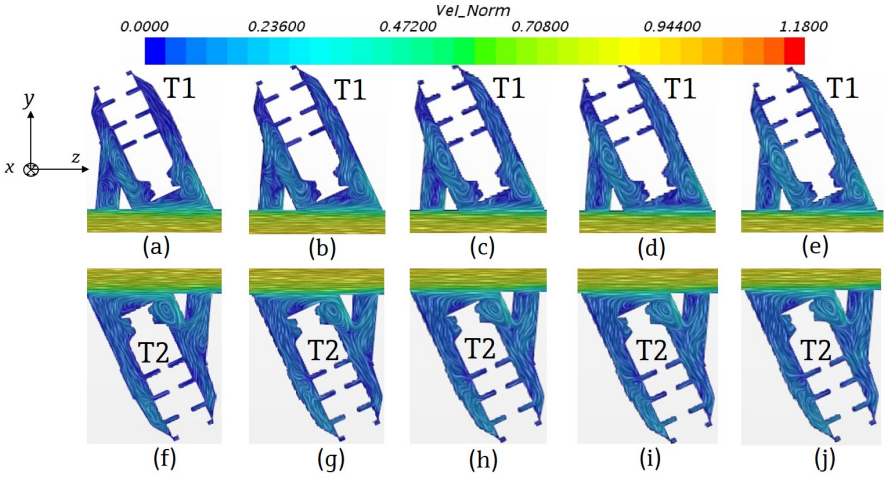

Figure 6.69: CFD flow-field near the sending and receiving recessed transducers T1 and T2, respectively for real two-path ultrasonic flowmeter, Case 7. Flow in the z-direction. Normalized velocity $Vel_{Norm} = |v_0|/v_{ref}$ is shown as 'Line Integral Convolution' (LIC) [235] for v_{ref}: (a) 5 m/s, (b) 10 m/s, (c) 15 m/s, and (d) 20 m/s, (e) 30 m/s, (f) 5 m/s, (g) 10 m/s, (h) 15 m/s, (i) 20 m/s, and (j) 30 m/s.

- the size of the vortex qualitatively changes with v_{ref}.
- Vel_{Norm}, inside the cavity and in front of the transducers, changes with the flow velocity v_{ref}, as already observed e.g. by [110] and Løland [146, 147] as well.

- for a specific flow velocity, the flow-field in front of and inside the cavities of the transducers, varies between T1 and T2, as expected, as similarly observed by others [110, 146, 147, 209].
- The lowest velocity inside the cavities is observed in different distances in front of the transducers, depending on v_{ref}, as similarly observed by Kažys [110].

As mentioned, the presence of these vortices in front of the transducers, with flow in the positive direction, indicates a later arrival of the upstream signal for the CFD cases compared to the Ful.-dev. ones. On the other hand, the presence of the described vortices would indicate an earlier arrival of the downstream signal for the CFD cases compared to the Ful.-dev. ones.

- Since the transducers are recessed in cavities, they do not significantly disturb the main flow however, slight asymmetries in the main flow inside the meter body are expected, as experimentally observed by Raišutis [209].
- Low flow velocity areas are created in front of T1 and T2, as similarly observed e.g. by Kažys et al. [110] and Løland [146]. The exact value of the flow velocity in front of the transducers will be calculated in the present section.
- For a Ful.-dev. profile, the flow-velocity inside the cavities is 'zero', i.e. lower than the CFD case. This is expected to increase t_{12} and reduce t_{21} for the 'Ful.-dev.' compared to the CFD flow-field, as similarly shown in Subsec. 6.2.2.

The described behavior indicates a consistent later and earlier arrival for US and DS propagation respectively, when a CFD flow-field is considered compared to a Ful.-dev. one. This is confirmed by the results of figs. 6.65, 6.66, 6.67, and 6.68. However, the differences between the ToF for Ful.-dev. and CFD for a specific v_{ref} are smaller compared to the respective differences for a recessed diametrical path (cf. figs. 6.31, 6.31). This is in agreement with prior literature [176, 208], where it was indicated that a diametrical path is more sensitive to flow changes compared to side chordal paths.

Due to the different path followed by the US and DS waves [77] the generated vortices have a different effect in each direction, as described already for Case 4, Case 5, and Case 6. There is an abrupt change of Vel_{Norm} inside the cavities for both T1 and T2 and therefore, a full or partial incidence of the major lobe of the waves may have an effect on its propagation. A similar explanation regarding the path followed may be given as for Case 5 with recessed transducers, through Fig. 6.33(e),(j) and the respective Fig. 6.69 for Case 7. However, the transducers are less recessed inside the cavities compared to Case 5, while the path is located at $R_{rp} = 0.5 \cdot R$ making it less sensitive to flow changes compared to a diametrical path [176, 208]. Therefore, the vortices in front of T1 and T2 (cf. Fig. 6.69 (e),(j)) are not as dissimilar as for Case 5. The described situation may have consequences on the wave propagation and differing effects of the flow-field on the US and DS propagation, as it is further explained.

Similarly to Case 4, Case 5, and Case 6, cylindrical paths are used for the sake of clarification of flow effects on acoustics. It should be highlighted though that with SimPAC^2 the real paths are calculated.

The name convention for the cylindrical sound paths is defined as described in Sec. 6.2.1.3 and depicted in Fig. 6.15. In the present case, two sound paths are taken into account. However, due to symmetry on plane yz only one of them is enough to be investigated.

In Fig. 6.70 the normalized axial velocity, Vel_{Norm}[k], is shown in the 'All' part of the cylindrical sound path for v_{ref}={5, 10, 20, 30}, for the CFD and Ful.-dev. flow-fields.

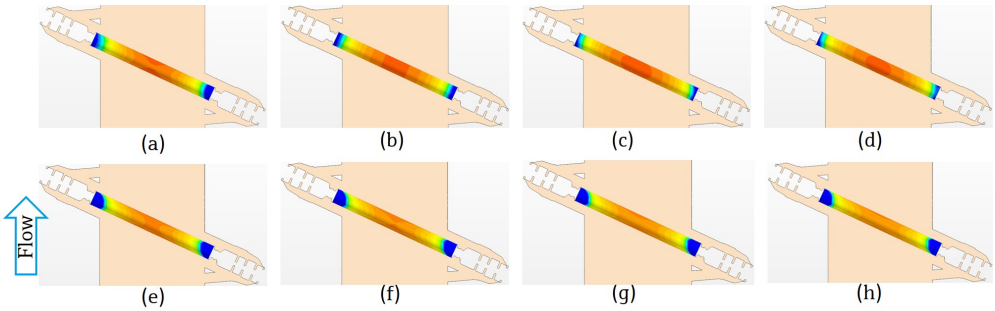

Figure 6.70: Normalized axial flow velocity contours for the whole cylindrical sound path 'All'. For CFD flow-field at v_{ref}: (a) 5 m/s (b), 10 m/s, (c) 20 m/s, and (d) 30 m/s. For 'Ful.-dev.' flow-field at v_{ref}: (e) 5 m/s (f), 10 m/s, (g) 20 m/s, and (h) 30 m/s. Real two-path ultrasonic flowmeter, Case 7.

In order to quantify the qualitative remarks made, the volume average axial velocity $\bar{v}_0[k]$ is calculated in the parts 'All', 'In,' 'US', and 'DS' of the sound paths for both CFD and Ful.-dev. flow-fields for v_{ref} ={5,10,20,30} m/s, as shown in Fig. 6.71. One can make several

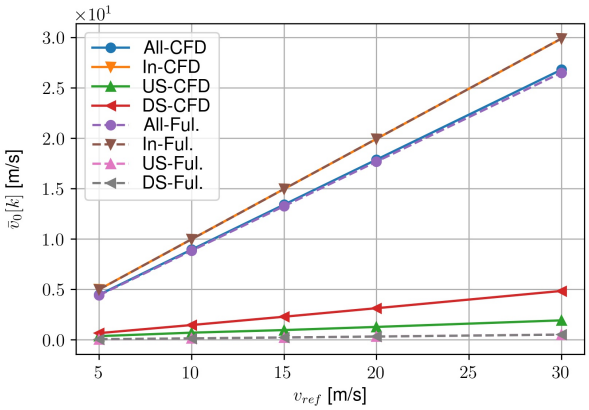

Figure 6.71: Volume average axial velocity $\bar{v}_0[k]$ in the sound paths or portions of them as defined in Fig. 6.15, for the respective recessed transducers. CFD or Ful.-dev. flow-field considered.

remarks from this diagram:

- The curves present several differences in terms of flow in the depicted cylindrical sound

paths compared to the previously investigated cases due to the two-path configuration and the paths' radial position.

- All four remarks made for Case 4 (Sec. 6.2.1.3) in connection with Fig. 6.18 are valid for the present case as well.
- The difference of the volume average axial velocity $\bar{v}_0[k]$ in the 'All' part for a CFD and a Ful.-dev. flow field is smaller compared to Case 4, Case 5, and Case 6. The exact differences may be deduced from the diagrams. Similarly, the difference of the volume average axial velocity $\bar{v}_0[k]$ in the 'In' part for a CFD and a Ful.-dev. flow field is smaller compared to Case 4 and Case 5. This is owed to the radial position of the path at $R_{dp} = 0.5 \cdot R$ compared to Case 4 and Case 5, where $R_{dp} = 0$. As already noted, this is in agreement with prior literature [176, 208], where it was noted that diametrical paths are more sensitive to flow changes compared to side paths. Case 6 is irrelevant in this instance, due to the absence of cavities, i.e. protruded transducers, which leads to a coincidence of the 'All' and 'In' part.
- It is observed that the values of $\bar{v}_0[k]$ are lower in the upstream cavity, 'US-CFD' for Case 7 compared to Case 4 and Case 5. This is also owed to the radial position of the path for Case 7. Similarly, Case 6 is irrelevant in this instance, due to the absence of cavities, i.e. protruded transducers. The lower values of $\bar{v}_0[k]$ in 'US-CFD' compared to Case 4 and Case 5 lead to the smaller differences of $\bar{v}_0[k]$ in the 'All' part between a CFD and a Ful.-dev. flow field.
- The described observations indicate that a sound path placed at $R_{dp} = 0.5 \cdot R$ is more robust to flow variations compared to a sound path placed at $R_{dp} = 0$ [163, 176].

The volume average axial velocity, $\bar{v}_0[k]$, in the sound paths, is normalized with v_{ref} for a better depiction of the relative change of flow velocity in parts of the sound paths, as shown in Fig. 6.72.

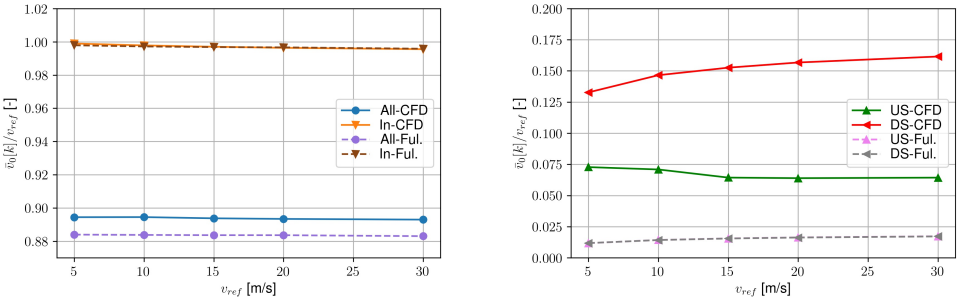

(a) (b)

Figure 6.72: Normalized volume average axial velocity ($\bar{v}_0[k]/v_{ref}$) in (a) 'All' and 'In', (b) 'US' and 'DS' parts. CFD and Ful.-dev. flow-field considered. Real two-path ultrasonic flowmeter, Case 7.

The Re dependency of the UTTF, previously shown in figs. 6.19(a), 6.36(a), and 6.54 is not as profound for Case 7. As shown in Fig. 6.72, the curves are rather flat compared to Case 4, Case 5, and Case 6. The differences of $\bar{v}_0[k]/v_{ref}$ between the 'In' parts for the

two flow-fields are lower (< 0.12 % for $v_{ref} = 5$ m/s) compared to Case 4 and Case 5, as a result of the radial position [176] and the slightly recessed transducers, which minimally influence the flow inside the meter body (for $r < R$). The difference of $\bar{v}_0[k]/v_{ref}$ between the 'All' parts presents a fairly constant offset of $\simeq 1.2$ %, which is lower than for Case 5 ($\simeq 4$ %) and higher than for Case 4 (< 1 %). This is owed again to the radial position of the sound paths and the size of the cavities, which correlates with the above observation, i.e. the cavity is larger than for Case 4 with the flush transducers and smaller than for Case 5 with the recessed transducers.

An interesting finding is revealed when observing the trend of $\bar{v}_0[k]/v_{ref}$ in Fig. 6.72(b). $\bar{v}_0[k]/v_{ref}$ is reduced for increasing v_{ref} in 'US-CFD', while it is increased for 'DS-CFD'. This is in agreement with Kažys et al. [110] and Løland [146], where it was observed that the flow inside the cavity changes faster with v_{ref} for a DS than a US cavity. The opposite trend of $\bar{v}_0[k]/v_{ref}$ inside the cavities additionally compensates for the Re dependency effect in the whole sound path 'All'. However, the main contribution for the constant behavior of $\bar{v}_0[k]/v_{ref}$ is owed to the radial position of the sound paths [176], since a similar behavior is observed when a 'Ful.-dev.' flow field is considered.

Consequently, one concludes that the flow inside the DS cavities is relatively accelerated and inside the US cavities it is relatively, decelerated for increasing flow velocity v_{ref}. It should be noted that in absolute numbers, $\bar{v}_0[k]$ is always accelerated with v_{ref} but more profoundly for DS compared to US cavities [110, 146]. The results regarding the two considered flow-fields and the higher axial volume average velocity in the sound paths for the CFD flow-field explain the later or earlier arrival of the voltage signal because of flow for upstream or downstream wave propagation, respectively (Figs. 6.67, 6.68).

In Fig. 6.73 the deviation between the CFD and Ful.-dev. cases is shown for the volume average axial velocity, $\frac{\bar{v}_{0,CFD}[k]-\bar{v}_{0,Ful}[k]}{\bar{v}_{0,Ful}[k]}100$, in the parts 'All' and 'In'. As already induced from Fig. 6.36 the volume average axial velocity is higher for the CFD flow field in both parts, 'All' and 'In'. One can additionally conclude:

- For the 'All' part, $\bar{v}_{0,CFD}[k]$ is fairly constant with a slight relative reduction compared to the $\bar{v}_{0,Ful.}[k]$ for increasing velocities. An offset of $\simeq 1.2$ % is present. The offset is higher compared to Case 4 (Fig. 6.20) because of the larger cavities of Case 7. On the other hand, the offset is lower compared to Case 5 (Fig. 6.37) because of the smaller cavities of Case 7 compared to Case 5.
- For the 'In' part, the relative differences are lower than for 'All' part, since the differences are owed mainly in the flow inside the cavities. A slight decreasing trend for increasing v_{ref} is observed. This shows that there is an effect of the cavities on the flow inside the meter body [209] however, it is of less significance.
- The trend for the 'All' part is not exactly the same as for the 'In' part, due to the reduction and increase of $\bar{v}_0[k]/v_{ref}$ in US-CFD and DS-CFD, respectively, for increasing v_{ref}.

In Fig. 6.74 the acoustic pressure field and the magnitude of mechanical displacement are shown in the middle plane section yz in the fluid and in the solid parts of the receiver, respectively, for a number of time-samples, when CFD flow-field is considered. As already shown in figs. 6.67, 6.68, the difference between the received voltage signal for a CFD or Ful.-dev. flow-field is low and therefore, contours of acoustic pressure and mechanical displacement only for the CFD flow-field are shown in Fig. 6.74.

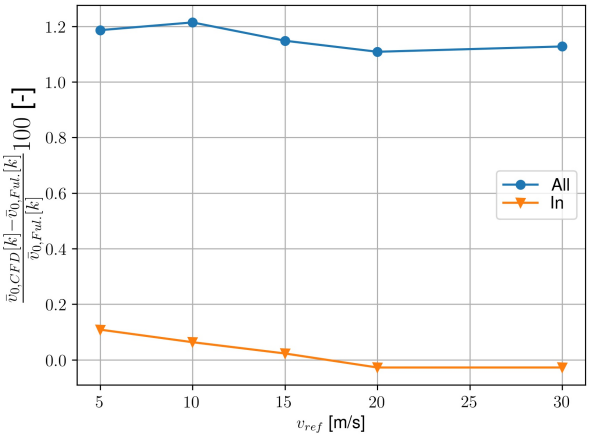

Figure 6.73: deviation in % between the CFD and Ful.-dev. flow-fields for the volume average axial velocity $\frac{\bar{v}_{0,CFD}[k]-\bar{v}_{0,Ful}[k]}{\bar{v}_{0,Ful}[k]}100$, for the 'All' and 'In' parts. Real two-path ultrasonic flowmeter, Case 7.

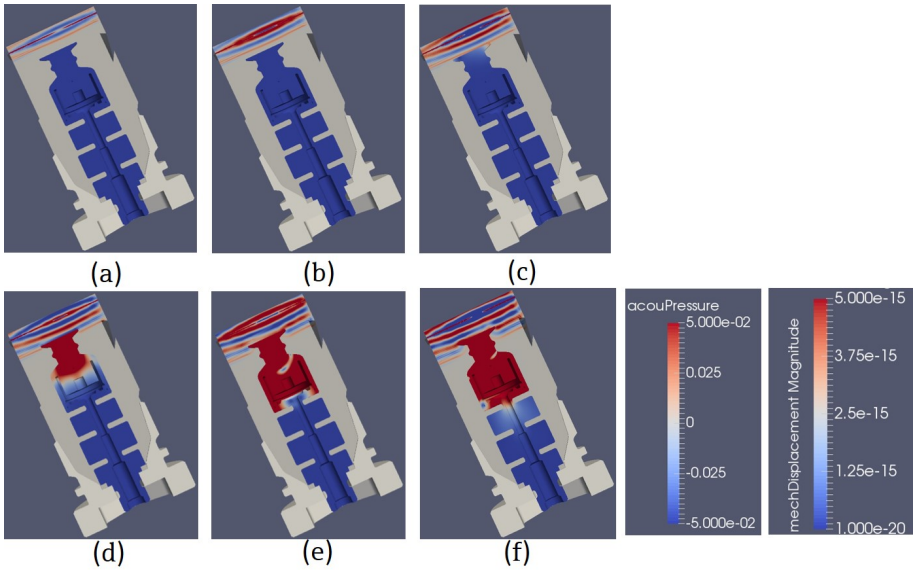

Figure 6.74: Acoustic pressure field [Pa] and mechanical displacement magnitude [m] in the middle plane section yz in the fluid and in the solid parts of the receiver, respectively, for different time samples (a) 292.875 μs (b) 300.375 μs, (c) 307.875 μs, (d) 315.375 μs, (e) 322.875 μs, (f) 330.375 μs. CFD flow-field considered for real two-path flowmeter, v_{ref} =10 m/s.

The flow velocity $v_{ref} = 10$ m/s is chosen for further investigation, for comparison reasons with the already investigated respective v_{ref} for Case 4, Case 5, and Case 6. The observations related to Fig. 6.21 regarding Case 4 (Sec. 6.2.1.3), are valid for the present Case 7 as well.

One may additionally notice the distorted acoustic pressure field due to reflections in the cavities. For a reminder of the description of the operation of Int2, the reader is referred to Subsec. 3.2.4.

In Fig. 6.75 the downstream ToF, t_{12}, upstream ToF, t_{21}, and time difference Δt are shown for a number of flow-velocities, for SimPAC^2 with CFD and Ful.-dev. flow-fields considered, as well as for measurements. Differences due to the considered flow-fields cannot

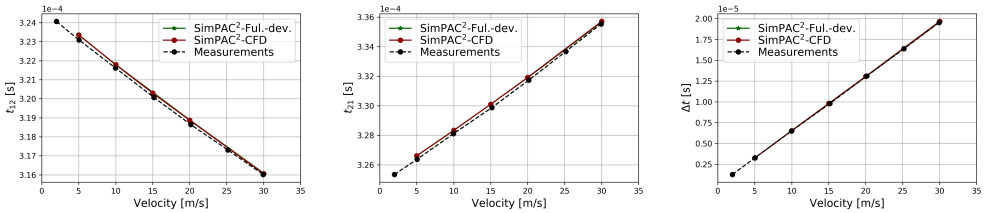

(a) (b) (c)

Figure 6.75: Time-parameters against velocity. (a) t_{12} (downstream wave propagation), (b) t_{21} (upstream wave propagation), and (c) $\Delta t = t_{21} - t_{12}$, for real two-path flowmeter.

easily be viewed from this representation, as expected from the results in figs. 6.65, 6.66. Typically, there is a linear positive and negative trend for t_{12} and Δt, t_{21}, respectively. From the flow investigation made in the present subsection, and due to the vortices inside the cavities for the CFD flow field, which are not present present for the 'Ful.-dev.', it is expected $t_{12,CFD} < t_{12,Ful.-dev.}$ and $t_{21,CFD} > t_{21,Ful.-dev.}$, as it is better shown in the further analysis in the present subsection. However, there is a clear offset between the measurements and the simulations for t_{12} and t_{21}. This offset is similar for both the downstream and the upstream propagation and therefore, it gets canceled to some extent for Δt. In order to clarify this claim, the differences of t_{12}, t_{21}, and Δt between the SimPAC^2-CFD and the measurements are shown in Fig. 6.76. t_{12,SimPAC^2}, t_{21,SimPAC^2}, and $\Delta t_{\text{SimPAC}^2}$ are the downstream, upstream ToF and Δt obtained from the SimPAC^2-CFD case, while $t_{12,\text{Meas}}$, $t_{21,\text{Meas}}$, and Δt_{Meas} are the measured ones. The offset between the measured and simulated values of ToF is fairly constant apart from the downstream propagation 1-2 for $v_{ref} = 30$ m/s. One can speculate that part of the fairly constant offset, or in other words delay, of t_{12} and t_{21} between the measurements and the simulations is owed to the measurement equipment, which is not taken into account in the simulations, i.e. signal generator, oscilloscope, cables connecting the signal generator with the transmitter, and the oscilloscope with the receiver. This is not proved or separately measured and therefore, it is highlighted that it is only a hypothesis. Moreover, it should be noted that a larger difference of Δt for higher v_{ref} has a smaller effect on the calculated v_{path}, because of the linear relation between v_{path} and Δt (eq. (2.91)).

It is important to control if the difference between the measured and simulated ToF is inside the set criterion $ToF_{crit,m}$ (eq. (4.8)), i.e. the percentage difference of ToF should between measurements and simulations should be < 0.2 %. The difference of ToF between SimPAC^2-CFD and measurements is presented in Fig. 6.77. As it is observed, the criterion

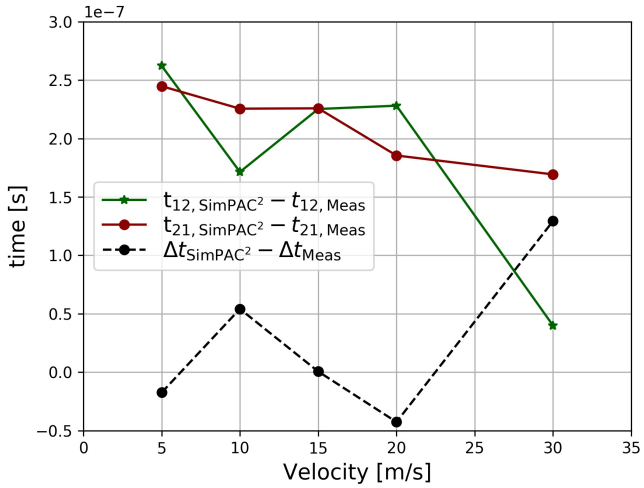

Figure 6.76: Offset of ToF and Δt between simulated case SimPAC^2-CFD and measurements. Real two-path flowmeter.

$ToF_{crit,m} \in [-0.2, 0.2]$ % is satisfied for all the calculated and measured flow velocities.

The ToF for US and DS propagation, as well as for the two flow-fields, and the measurements is normalized with the respective v_{ref}, as shown in Fig. 6.78. The flow-effect, i.e. Re effect [30, 84, 196, 241] is noticed on both t_{12} and t_{21}. However, a comparison with the respective results of Case 4, Case 5, and Case 6 in figs. 6.24, 6.41, and 6.58, shows that the Re effect for Case 7 is lower, i.e. there is lower difference between the values in the y-axis for the range between 5-30 m/s. This is in accordance with the low Re effect observed in Fig. 6.72. The lower effect of flow on the deviation of UTTF for side paths compared to a diametrical path is well known in prior literature as well [176, 208].

The Δt for the two flow-fields, is normalized with the respective v_{ref} as shown in Fig. 6.79, with the purpose of directly comparing the simulation results of SimPAC^2-CFD, SimPAC^2-Ful.-dev., and the measurements.

Several useful remarks are made regarding the Δt for the two flow-fields considered and the measurements:

- A typical Re effect [30, 84, 196, 241] is not observed in the curves of the diagram neither for the simulations nor for the measurements. As already explained in the present chapter, the avoidance of the effect is mainly associated with the radial position of the paths $R_{dp} = 0.5 \cdot R$ instead of the $R_{dp} = 0$ of Case 4, Case 5, and Case 6, which is in agreement with prior literature observations [176, 208]. Moreover, the increase and reduction of $\bar{v}_0[k]/v_{ref}$ in DS-CFD and US-CFD, respectively, as shown in Fig. 6.72 weakens the Re effect. The higher velocity in a DS compared to a US cavity is in agreement with prior literature as well [110, 146].
- A fairly constant offset is observed between the $\Delta t/v_{ref}$ of the two simulated cases SimPAC^2-CFD and SimPAC^2-Ful.-dev..

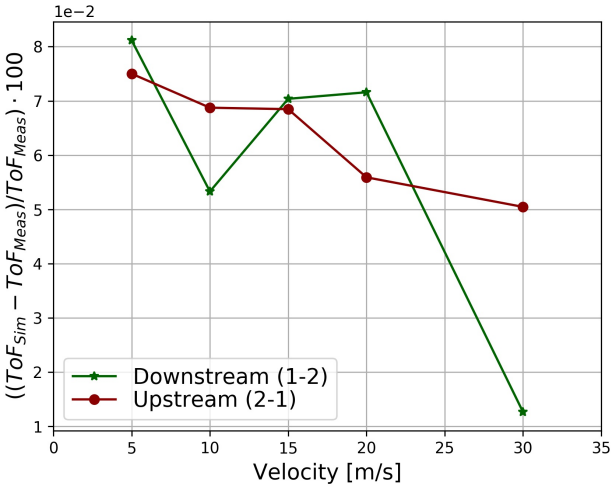

Figure 6.77: Percentage difference of ToF between SimPAC^2-CFD and measurements. Real two-path flowmeter.

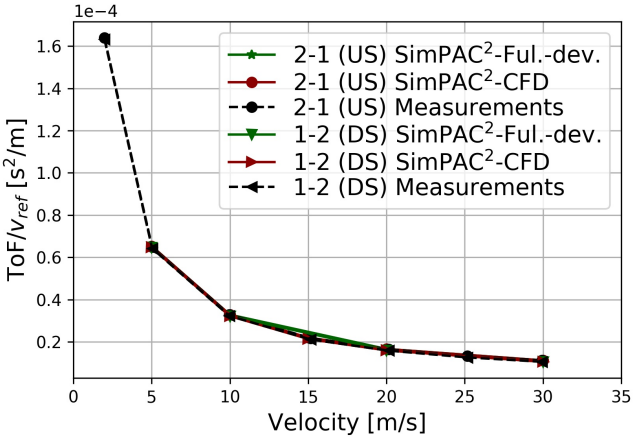

Figure 6.78: ToF/v_{ref} [s$^2/m$] for 2-1 (US) and 1-2 (DS) propagation, for CFD and Ful.-dev. flow-fields. Real two-path flowmeter.

- $\Delta t/v_{ref}$ follows the same trend among the simulations and the measurements for $v_{ref} \geq$ 20 m/s.
- A kink is observed at $v_{ref} = 15$ m/s for the measurements, which is not captured by neither of the simulated cases. The reason for the kink is not clarified and therefore, it is speculated that is owed to a measurement effect, which is not reproduced by the simulations.

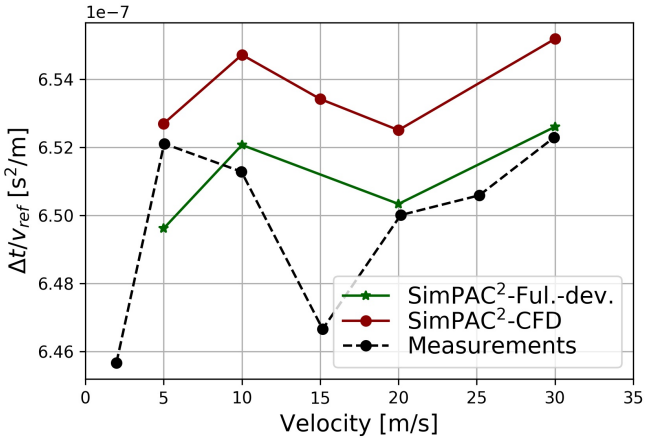

Figure 6.79: $\Delta t/v_{ref}$ [s$^2/m$] for SimPAC^2-CFD, SimPAC^2-Ful.-dev., and measurements. Real two-path flowmeter.

- $\Delta t_{\text{CFD}}/v_{ref} > \Delta t_{\text{Ful.-dev.}}/v_{ref}$ for every v_{ref} due to the higher $\bar{v}_0[k]/v_{ref}$ inside the cavities, as shown in Fig. 6.72. This is in agreement with Sun et al. [239], where $\Delta t_{\text{CFD}} > \Delta t_{\text{Ful.-dev.}}$ although the this observation was made for protruded transducers in [239].
- The differences between Δt_{CFD} and $\Delta t_{\text{Ful.-dev.}}$ stem from both the upstream and downstream propagation of the signal as shown in Figs. 6.67 and 6.68.

In Fig. 6.80 the deviation curves are presented for the CNA 'Only CFD' method when realistic CFD flow-field is considered, for the SimPAC^2 method with CFD and Ful.-dev. flow-fields, as well as for measurements.

Several useful observations are made from the deviation diagram:

- Due to the ± 0.25 % total uncertainty of the calibration rig itself in terms of %deviation (cf. Sec. 6.3.2) the experimental results should be treated with care. The simulations' uncertainty regarding ToF, as well as %deviation is investigated through the convergence studies made in secs. 4.2, 4.3.
- Due to the same parameters set for SimPAC^2-CFD and SimPAC^2-Ful.-dev., a potential uncertainty would be of the same value for them and therefore, their relative difference is valid.
- The %deviation is positive for the Only CFD (CNA) case but negative for the SimPAC^2 simulations and the measurements. This observation shows the limitations of the Only CFD (CNA) method in terms of offset of %deviation.
- The trend of the %deviation is very similar with the trend of the $\Delta t/v_{ref}$ for the SimPAC^2 cases and the measurements, confirming that Δt is the most important parameter for the deviation curves of the flowmeter.
- The uncertainty of the flowmeter Proline Prosonic Flow G 300 [64] is ± 1 %. The offset between the SimPAC^2 cases varies from 0.32 % to 0.47 %, which is comparable with

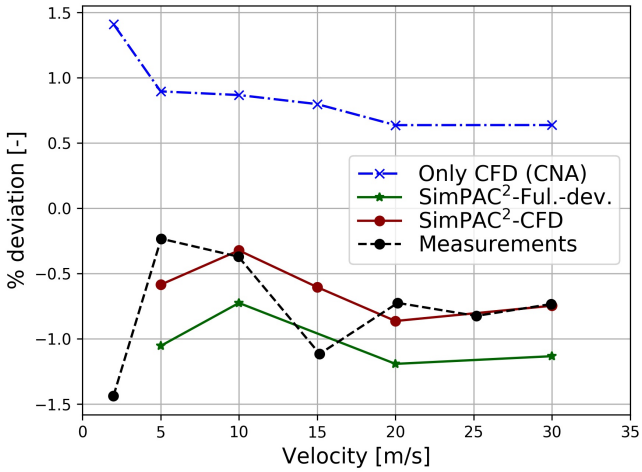

Figure 6.80: Deviation against flow velocity obtained with Only CFD (CNA) method, SimPAC^2-Ful.-dev., SimPAC^2-CFD, and measurements. Real two-path flowmeter.

the uncertainty. Therefore, it is concluded that also for this industrial two sound-path device [64], it is important to consider a real CFD profile and not a Ful.-dev. or an analytical one. However, the offset between SimPAC^2-CFD and SimPAC^2-Ful.-dev. is lower compared to the offset between the respective SimPAC^2-CFD and SimPAC^2-Ful.-dev. of Case 4, Case 5, and Case 6 due to the radial position of the sound paths $R_{dp} = 0.5 \cdot R$ [159, 176].

- The Only CFD (CNA) method presents a trend of Re dependency, which is though much weaker compared to Case 4, Case 5, and Case 6 due to the $R_{dp} = 0.5 \cdot R$ [159, 176].
- One might wonder why the %deviation is higher for the Only CFD (CNA) compared to the SimPAC^2 cases and the measurements. The specific reason is not fully identified. One must bear in mind the simplicity of the Only CFD (CNA) method and the lack of simulation of acoustic sound path propagating in fluid flow and of transducer in antithesis to the SimPAC^2 method.
- The %deviation is closer to '0' for all cases, because of the position of the sound paths at $R_{dp} = 0.5 \cdot R$, where, typically, a similar flow velocity to v_{ref} is measured [176] (Fig. 3.3).
- As for the $\Delta t/v_{ref}$, a kink is observed at $v_{ref} = 15$ m/s for the measurements, which is not captured by neither of the simulated cases. The difference between the %deviation of the measurements and the SimPAC^2-CFD for $v_{ref} = 15$ m/s is 0.51 %. Similarly to the $\Delta t/v_{ref}$, the reason for the kink is not clarified and therefore, it is speculated that is owed to a measurement effect, which is not reproduced by the simulations.
- The opposite trend of $\bar{v}_{0,CFD}/v_{ref}$ in US-CFD and DS-CFD, as shown in Fig. 6.72 and similarly observed before by others [110, 146], as well as the radial position of the

paths, $R_{dp} = 0.5 \cdot R$ [176], helps in the better linearity of the flowmeter.

- %deviation for the SimPAC^2-CFD is higher than for the SimPAC^2-Ful.-dev. due to $\Delta t_{\text{CFD}}/v_{ref} > \Delta t_{\text{Ful.-dev.}}/v_{ref}$ for every v_{ref} (cf. Fig. 6.79), which is subsequently higher because of the higher velocity along the sound path for the SimPAC^2-CFD compared to the SimPAC^2-Ful.-dev. (cf. Fig. 6.73).
- For the velocities $v_{ref} = \{10, 20, 30\}$ m/s the difference between the %deviation of the measurements and the SimPAC^2-CFD is <0.15 %, while for $v_{ref} = 5$ m/s the respective difference is 0.35 %.

Moreover, there are still open points for discussion, where further understanding or analysis is necessary:

- The kinks in the measurements and not present in the simulations, as shown in Fig. 6.80 is an open topic of discussion, which needs to be further clarified.
- The offset in the same direction in terms of ToF between measurements and simulations, as shown in Fig. 6.76 is an open topic for further discussion. It is speculated that part of the offset is owed to the delay inside the measurement equipment, which is not taken into account in the simulations. Moreover, the two transducers are identical in the simulations but not in the measurements, which can arise differences in terms of ToF, Δt, and subsequently %deviation [157].
- The measurement equipment can be simulated in the future for a more complete simulation, i.e. signal generator, oscilloscope, cables connecting the signal generator with the transmitter, and the oscilloscope with the receiver. Another way would be to calculate the exact voltage signal applied on the transmitter in reality and give it as an input to the simulated transducer, as well as calculate the exact measured voltage signal on the electrodes of the receiver, and not of the oscilloscope, and compare it with the simulated one. A similar process, as the described one in order to compare measurements with simulation one to one, is followed by Øyerhamn et al. [277].
- Further investigation may be carried out for the flow-velocities that presented higher differences in terms of %deviation such as $v_{ref} = \{2, 15\}$ m/s.
- The difference between the Only CFD (CNA) method, in terms of %deviation, and the rest of the simulations, as well as the measurements should be clarified.
- Further visual inspection of the 3D acoustic pressure field would be beneficial in the future.

6.3.4 Conclusion and Summary of Results

Measurements and simulations of the flowmeter Proline Prosonic Flow G 300 [64] were performed to assess the performance of the Only CFD (CNA) and especially the SimPAC^2 method for a real flowmeter case. The investigation of a two-path device showcases the different behavior compared to a one-path device considered in case 4, case 5, and case 6.

The deviation for a one-path device is shifted to positive values, as shown in Fig. 6.62, while the values of deviation for a two-path device is closer to '0', as shown in Fig. 6.80, due to the radial position of the paths at $R_{dp} = 0.5 \cdot R$ [176]. Moreover, the real two-path device does not present such a strong Re effect in its deviation curve as the one-path device [159, 176, 190].

The comparison of ToF between SimPAC^2-CFD and SimPAC^2-Ful.-dev., as shown in Figs. 6.67, 6.68 indicates that higher velocities are present in the sound paths when CFD flow is considered, mainly due to the flow inside the cavities. This is confirmed from the flow field findings shown in Figs. 6.72, 6.73. The presence of flow inside the cavities with $v_0[k]>0$ has been studied before by others as well [110, 146].

The received voltage V_5 arrives earlier for measurements compared to the simulations for both upstream and downstream propagation. The reliability of the simulations was controlled with the set criterion $ToF_{crit,m}$ (eq. (4.8)), which was satisfied.

In terms of %deviation, the importance of multiphysics simulations with the consideration of CFD generated flow-fields is highlighted through the deviation curves shown in Fig. 6.80. The accuracy demands of the investigated flowmeter [64] is $\pm 1\%$ and therefore, the %deviation calculated with the Only CFD (CNA) method presents a large difference compared to the measured as well as the calculated %deviation with the SimPAC^2 method. On the other hand, there is a satisfying agreement of %deviation between the measurements and the SimPAC^2-CFD, which is the most accurate method proposed in the thesis, with the intention to be used for design of UTTF and understanding of the underlying phenomena. The simulation of acoustic sound paths, transducers, and CFD is important for the comprehension of the flowmeter operation and for achievement of accurate results. An analysis of both flow and acoustics in 3D domain, as well as their interaction is important for the description of the behavior of an UTTF.

Chapter 7

Summary, Conclusions, and Outlook

7.1 Summary and conclusions

The **objective** of this research work has been the development of a hybrid FEM-FVM numerical method, which couples piezoelectricity, wave propagation in solid structures, acoustic wave propagation in moving fluid media, and CFD for the purpose of 3D simulations of UTTF and study of physical phenomena that influence the behavior of the flowmeters.

Accurate flow measurement with the aid of UTTF is crucial, as even small errors of < 1 % give rise to large inaccuracies, deviations in terms of total volume flow and consequently, additional profit or loss between parties due to the large amounts of fluid media measured. Innovation, continuous measurement accuracy and technology improvement can be achieved with the use of simulations for the fast growing market of UTTF [163]. The present thesis used simulations for that scope.

The main **achievement** and highlight of the present thesis is that it is the first work, to the author's knowledge, which combines FEM, CFD, and 3D wave-acoustics with the aid of FVM for the simulation of a full 3D geometry of an UTTF from input voltage on the transmitter to output voltage on the receiver. The method gives the possibility to systematically investigate effects of 3D wave propagation in moving fluid media and 3D flow, as well as their interconnection, on the flowmeter behavior. It can be used for the comprehension and assessment of physical effects that are not easily quantified through measurements, such as cavity, flow, material, geometrical, coupling of acoustics and flow effects, and therefore new optimized designs of UTTF can be proposed.

7.1.1 The Hybrid FEM-FVM Simulation Method: SimPAC^2

The proposed method for 3D simulation of UTTF, namely the SimPAC^2 method [197], is of hybrid nature, i.e. FEM and FVM were combined. FEM is long established in piezoelectricity and wave propagation in solid media [107, 135, 136] and therefore, it was used for that part of the flowmeter simulation. FVM, on the other hand, was used for the CFD simulations, as it is long established in the field of flow simulations [72]. For the wave propagation

in quiescent or moving fluid media both FEM and FVM were employed. FEM was used for the part of fluid near the transducers, while FVM was used for the larger part of fluid in the meter body of the flowmeter (cf. Sec. 3.2).

The use of FVM [235] for the simulation of acoustics in moving fluid media was decisive for the success of the method. Large meshes of up to 317 millions of cells were used for the simulation of acoustics in a moving fluid for ultrasonic flowmeters with a diameter of $D = 97$ mm. An HPC cluster was employed, where up to 320 cores were used in order to resolve acoustics in a moving fluid for voltage input signals of $f_c = 112$ kHz. Such an efficient parallelization is not possible for the available FEM programs, such as NACS [183] or other commercial FEM software, to the author's knowledge. High-end CFD simulations with the aid of FVM, in particular Star-CCM+®, are important as well in order to capture the flow-field in the cavities around the transducers of an inline UTTF.

The development of the connection between the FEM software, NACS [183], and the FVM software, Star-CCM+® [235], was part of the present thesis. Interfaces were created in the fluid domain, where the information was transferred from NACS to Star-CCM+® via the interface Int1 in the fluid near the transmitter and from Star-CCM+® to NACS via the interface Int2 in the fluid near the receiver. Python [206] was used for the data conversion in a suitable form for the interfaces. Moreover, an internal meshing conversion tool was used [250] in order to convert the generated meshes into a suitable format for NACS.

A number of different equations were used for the simulations of acoustics in moving fluid media. For the simulation with NACS, the PE equation was used [183, 203], while for the simulation with Star-CCM+® the CAWE equation was used [116, 235]. The considered equations are derived with the approximation of slow variation of ambient properties in relation to the acoustic properties, which is a good approximation for the application of UTTF [31, 203].

State-of-the-art CFD simulations were utilized for the calculation of the flow-field in the simulated devices with the aid of Star-CCM+®. In connection with the SimPAC^2 method, static CFD simulations were performed with the RANS model RKEPS [227, 229], which has been thoroughly tested for such cases [192, 193, 196, 197].

Important aspects of the SimPAC^2 method, i.e. advantages and disadvantages, may be summarized:

- 3D acoustic simulations enables the investigation of effects that were not possible to be fully investigated before with either 2D simulations of acoustics [151, 152, 153, 231, 232, 239] or ray-tracing methods [30]. Such an effect that was quantified for a number of geometries was the effect of the cavity on the UTTF behavior and the interaction of 3D acoustics with 3D flow.
- The simulation of piezoelectric transducers, wave propagation in solids and moving fluid media, as well as flow permits the full 3D simulation of an UTTF from input voltage signal on the transmitter to output voltage signal on the receiver.
- The inclusion of state-of-the-art 3D CFD simulations and their connection with 3D simulations of acoustics makes possible the quantification of flow effects on acoustics.
- Systematic studies are performed with the help of SimPAC^2 regarding flow, material, or geometry changes.

- The geometry of the meter body was not simulated in the cases studied here, however its consideration in the simulation is straightforward without any further altering of the method. Due to the lack of the meter body geometry, no crosstalk effects were studied.
- Due to the large 3D models, a long computational time is needed for the voltage-to-voltage simulation, For the largest case simulated i.e., case 3, a voltage-to-voltage simulation is accomplished in ≃80 hours. This time can be significantly lowered if further mesh optimization is made. E.g. case 3 may also be simulated as half, since it is symmetrical on plane yz. Moreover, the convergence studies are challenging when carried out for a UTTF, because of the long time needed when fine temporal and spatial discretizations are chosen e.g. $n_t > 25$ and $n_x > 20$ for UTTF with $D \geq 80$ mm.
- The hybrid nature of the method possesses the advantage of using FEM or FVM methods is judged to be more suitable for each part of the UTTF to be modeled. However, the connection of the methods is not effortless; it has to be made cautiously in order to avoid potential sources of errors, related to the mesh, the connecting interfaces and the user.

7.1.2 The 'CFD-Non-acoustic' or 'Only CFD-CNA' method

A simpler method was utilized as well that includes only CFD, called the CNA, i.e., 'CFD-Non-acoustic' or 'Only CFD-CNA' method [195, 196]. Due to the consideration of flow only, the method does not capture the real acoustic effects in the solid or fluid media, while modeling of piezoelectric transducers is not included either. Thus, the method presents known limitations and must be carefully used as described in ch. 3.1. On the other hand, due to the simplicity of the method, a relatively short time is needed for the generation of a complete deviation curve, i.e., typically 1-2 hours depending on the mesh and the number of calculated flow velocities. On the other hand, the consideration of flow solely enables pure quantification of flow effects exclusively. Thereby, it can be used for the optimization of the flow related part of the UTTF, as well as for the comparison to the SimPAC^2 method or to measurements, in order to assess the flow and multiphysics related effects, as well as their difference.

7.1.3 Overview of Cases, Conclusions and Results

The studies in this work included a large number of cases, simulated with NACS, StarCCM+®, i.e. 'Only CFD-CNA', and the SimPAC^2 method. It was decided to start with simple geometries and flow conditions and lead into more complex ones. The reasoning for that trail was a chain comparison or verification.

The studied cases are listed briefly for a better overview.

- An UTTF for water measurements was simulated with the 'Only CFD-CNA' method and measured.
- Piezoelectric elements in zero flow were simulated and compared with prior measurements [277].

- Piezoelectric elements in uniform flow were simulated with NACS and SimPAC^2.
- Simulations of a single-path flowmeter with piezoelectric elements as transducers were performed with SimPAC^2.
- The material parameters of the piezoelectric elements were determined and optimized with simulations.
- A single-path UTTF with industrial transducers was simulated with SimPAC^2.
- A real flowmeter with two chordal paths was simulated with SimPAC^2 and measured in a flow rig.

In the next paragraphs of the present subsection, the results and conclusions for each case are summarized.

Regarding the 'Only CFD-CNA' method, a comparison took place between measurements [196] and simulation results in order to find the optimum parameters of CFD simulations of a water UTTF [66]. As described in Sec. 4.1, the case of a water UTTF was used as a comparison case, despite the fact that the thesis is focused on gas UTTF. Several turbulence models were considered, such as the EBRSM [18, 33, 166], the RKEPS [227] and IDDES simulations [228]. According to the findings in Sec. 4.1, the models delivered reliable results for the UTTF applications [196], however the heavily tested RKEPS model [11, 227, 229] was chosen for further use in combination with the SimPAC^2 method.

Further on regarding the quantified reliability of the 'Only CFD-CNA' method, for the water UTTF studied in ch. 4, a difference of %deviation<0.4% was observed between the measurements and simulations when the UTTF is mounted downstream of a straight pipe for $Re > 3000$. The respective difference for an installation $8D$ downstream of an asymmetric flow disturber is <0.8% and for $12D$ it is <1.2%. These numbers gave a quantification of the reliability of the 'Only CFD-CNA' method, especially for the installation downstream of a straight pipe, which is the setup for Case 4, Case 5, and Case 6. Moreover, due to beam deflection for high flow velocities for gas UTTF, less reliable results are expected. The exact 'reliability' of the 'Only CFD-CNA' method was not tested in ch. 4 however, a quantification was given in Sec. 6.3, where offsets of %deviation >1.5% were observed between measurements and the 'Only CFD-CNA' method.

Similar studies have been performed before with the inclusion of CFD only in order to analyze the behavior of UTTF or extract %deviation e.g. in [84, 92, 94, 168, 286]. More particularly, Holm et al. found, for a different flowmeter from the one calculated here, that a good agreement of %deviation between simulations and measurements is achieved for high Re for undisturbed flow of the order of <0.25% which is close to the <0.4% calculated in the present thesis. Moreover, it was challenging to calculate the transition from laminar to turbulent for undisturbed flow, where estimated differences of ≈15% occurred between measurements and simulations as extracted from their diagrams [94]. In the present work, similar difficulties occurred for low Re, with the differences between measurements and simulations in terms of %deviation being ≈3.5-4.0%. When swirl was introduced, Holm et al. [94] experienced difficulties as well in the prediction of swirl due to the use of k-ε

model, with the differences reaching ≈3.0% for the turbulent region. With the 'Only CFD-CNA' method and the RKEPS [227] used in the present work, an agreement of <1.2% was achieved even for $12D$ downstream of an asymmetric swirl generator. Hallanger et al. [84] faced similar difficulties in modeling the flow in UTTF for low Re or downstream of bends especially, for swirling flow. Thus, one can say that with the 'Only CFD-CNA' method an improvement was achieved in terms of prediction of the flow in an UTTF particularly for low Re and installation downstream of swirling flow [196].

Regarding the chain verification of the SimPAC^2 method, initially, the FEM program NACS was compared with well verified, published measurements [277] for a simple axisymmetric geometry of two piezoelectric elements in zero flow, with the aim to finding the optimum parameters for NACS. Convergence studies were carried out in order to choose the optimum temporal and spatial discretization until the set convergence criteria were satisfied. As a convergence criterion, it was set $ToF_{crit} \in [-0.02, 0.02]$ in agreement with the requirements of a typical two sound path gas UTTF [64]. After the convergence studies, it was found that the values of n_t>25 and n_x>20 should be used with an optimum ratio $n_t/n_x \approx [1.36, 1.38]$. The mentioned values are similar to the ones used by Beždek [30] with the FEM program CAPA [137], which is the predecessor of NACS [183]. Moreover, comparisons of NACS with measurements [277] were performed that showed an agreement in terms of ToF in the set criteria $ToF_{crit,m} \in [-0.2, 0.2]$, as documented in ch. 4.

Afterwards, SimPAC^2 for a 3D simulation was mobilized. Complexity was added by considering uniform flow for two piezoelectric elements opposite to each other. The SimPAC^2 method was mobilized for the 3D simulation and was compared with the NACS simulation with the respective n_t and n_x set according to the convergence studies. Numerical comparisons were carried out, such as the comparison of the acoustic pressure on the interface, Int1, connecting NACS and Star-CCM+®, in order to assess the validity of SimPAC^2. Moreover, ToF was compared between NACS and SimPAC^2 in order to choose the suitable temporal and spatial resolution for all parts considered in SimPAC^2. A criterion $ToF_{crit,sim} \in [-0.2, 0.2]$ was set for the comparison between NACS and SimPAC^2 that was satisfied, as documented in ch. 4. The maximum difference of %deviation between NACS and SimPAC^2 is ≈ 0.22%, which is absolutely acceptable for a device such as the Proline Prosonic Flow G 300 [64] with accuracy specification of ±1% in terms of volume flow. Therefore, with this chain verification and convergence studies, the accuracy requirements were set and achieved in order to be used further in more complex cases.

Subsequently, simulations of a one-path flowmeter took place, with two piezoelectric elements in oblique angle relative to the flow. Several effects were studied, such as the cavity effect, with the consideration of two different geometries, one 'with cavity' and one 'without cavity'. The cavity effect was quantified in terms of ToF, dt and %deviation, for a number of flow velocities and it was found to be of significance, since for $v_{ref} = 30$ m/s uniform flow, the difference between the deviations of the two cases, 'with cavity' and 'without cavity', reaches 0.7% (cf. Sec. 5.3). As mentioned in Sec. 5.6, the novelty of such a study, which has not been performed before to the author's knowledge, is the quantification of the 'cavity-effect' due to the geometrical difference of the cavity, but exactly the same flow-field.

For the case 'with cavity' a number of different flow profiles were studied, such as uniform, fully developed and CFD generated in order to estimate the flow effect on the flowmeter with the use of both the 'Only CFD-CNA' and the SimPAC^2 methods. It was observed that the 'flow effect' can affect the acoustic propagation and consequently important parameters of the flowmeter, i.e. ToF, Δt and %deviation. It was concluded that the non-linearities in terms of %deviation were caused mainly by the flow-field, as shown before in [197]. A significant difference of up to 0.505% was observed in deviation between the case of a fully developed flow ('SimPAC^2-Ful.-dev.'), and the 'SimPAC^2-CFD' case. The non-linearities were present also in the 'Only CFD' (CNA) case, which is in agreement with the respective SimPAC^2 cases. Similarly to the present study, Løland showed before [146] that the flow inside the cavities should not be neglected, while he suggested a correction due to the flow in cavities. The different effect of the upstream and downstream cavity described in Sec. 5.4 were in agreement with previous studies e.g. [110, 146, 284]. Moreover, it was shown that t_{21} increases more than t_{12} decreases for the same v_{ref}, which is in agreement with the study of Zheng et al. [284], where it was described that the downstream propagating waves are shifted more compared to the upstream ones. The consideration of a fully-developed flow profile has been so far the state-of-the-art when combined with acoustics and piezoelectricity for the simulation of a 3D UTTF [30, 31, 32]. A CFD profile in combination with acoustics has been simulated previously [239] but for a 2D geometry without the consideration of piezoelectric transducers. Recently, Mousavi et al. [179] presented a semi-3D simulation of an UTTF with CFD and piezoelectric transducers included. The effect of inlet flow conditions or position of the transducers on UTTF has been systematically studied before with simulations, e.g. in [84, 264, 286] but only with the help of CFD. However, there is no such systematic study of flow-effects for 3D UTTF geometry, with the use and combination of piezoelectric transducers, acoustic wave propagation, and CFD simulations in 3D, to the author's knowledge.

Thereafter, a single-path UTTF with real transducers, in order to obtain real industrial flowmeter geometries. A method was presented for the determination of the piezoelectric material parameters. Measurements of impedance were performed and an optimization took place with the help of python™ [206], optiSLang® [16], and NACS [183] in order to assure that the simulated piezoelectric elements represented the measured ones. One diametrical sound path UTTF were simulated with a varying insertion depth of the transducers, i.e. recessed, protruded, and flush transducers, in order to estimate the cavity and flow effects on acoustic propagation, ToF, Δt and $\%deviation$ of the UTTF.

With the use of the 'Only CFD-CNA' method it was possible to quantify the pure flow effect on %deviation for the three studied insertion depths of the transducers, which was manifested with a typical monotonic Re effect seen also by others [30, 84, 196, 241]. Based on the 'Only CFD-CNA' method the 'best' i.e. most linear deviation curve was the one for flush transducers (cf. Fig. 6.62(a)). This statement is not in agreement with a series of prior literature [208, 261, 286], where it was stated that protruded transducers are beneficial. It should be noted though that different geometries were investigated in [208, 261, 286] compared to the present thesis and therefore, a direct comparison should be carried out with caution. In the work of Qin et al. [208] it was found through CFD that the velocity along the sound paths is higher for protruded, lower for half protruded, and the lowest for recessed,

which is in agreement with the results of the present work (cf. Figs. 6.19, 6.36 6.54). The result of higher velocity along a sound path with protruded transducers than with flush ones is in agreement with the findings of Voser et al. [259] as well. Zheng et al. [286] concluded that protruded transducers are beneficial as well, based on the offset of the %deviation from zero values and not on |max(%deviation) − min(%deviation)|. However, if one decides based on |max(%deviation) − min(%deviation)|, then the recessed transducers, or with the respective name convention of the present work the 'flush' transducers, are beneficial in the work of Zheng et al. [286], which agrees with the result of the present thesis. Moreover, it is the author's opinion, that the position of the transducers is only one of the factors affecting the deviation of an UTTF and thus, no general statement can be made regarding the most beneficial position but only a statement for one particular geometry. Other factors, apart from the position of the transducers, affecting the deviation of an UTTF is e.g. the geometry of the transducers, the size of the cavity, the size of the meter body, and the radial position of the transducers. The results of 'Only CFD' method regarding recessed transducers are in agreement with prior literature [110, 146, 208] (cf. Fig. 6.62(a)), where a varying vortex is present in the cavity that at the end affects the %deviation of an UTTF.

With the utilization of the Only CFD-CNA method it was possible to assess the pure flow effect on %deviation, while with the SimPAC^2-CFD the combined flow-acoustic effect on %deviation, as well as their difference. Summarizing, for flush transducers and high velocities, the %deviation for SimPAC^2-CFD almost coincides with the 'Only CFD-CNA', while the difference is <0.25% as well with the SimPAC^2-Ful.-dev., which shows the small effect of the cavities for this configuration. For recessed transducers and high velocities, the %deviation for SimPAC^2-CFD is ≈2% higher than for the 'Only CFD-CNA' method, which is ≈3% higher than for the SimPAC^2-Ful.-dev.. For protruded transducers and high velocities, the %deviation for SimPAC^2-Ful.-dev. is ≈3% higher than for the SimPAC^2-CFD, which is ≈1% higher than for the 'Only CFD-CNA'. It is important to note that for protruded transducers, when comparing the two flow-fields considered, t_{12} is longer for CFD than for Ful.-dev., while t_{21} is shorter for CFD than for Ful.-dev. for a specific v_{ref} as explained in Sec. 6.2.3, which is in agreement with the work from Sun et al. [239]. The above differences show the effect of cavities and different flow-fields on the %deviation for an UTTF. The different vortices present in front of each of the US and DS transducers [110, 146, 147, 208, 239, 259], as well as the different sound paths for US and DS propagation [208, 239, 284], affect the ToF differently depending on the propagation direction, which affect the Δt, and finally has consequences on the %deviation. For more detailed results and explanations cf. Subsecs. 6.2.1.3, 6.2.2.2, 6.2.3.2, and 6.2.4.

The SimPAC^2-CFD method (Fig. 6.62 (b)) captures the combined acoustic-flow effects for a 'real' CFD flow-field. For flush and recessed transducers and for flow-velocity $v_{ref} <$ 10 m/s, the %deviation does not follow the same monotonic trend as for the 'Only CFD' method, because of combined acoustic-flow effects in the cavities (cf. secs. 6.2.1.3 and 6.2.2.2) and the presence of a vortices with varying size for different v_{ref}, as described by others [110, 146]. However, for protruded transducers, the %deviation is monotonic, since the vortices generated due to the protruded transducers vary with Re but less significantly than the recessed transducers, as indicated by others as well [208]. The sound waves follow a different path for US and DS propagation [77], while a vortex generated in front of the protruded transducers, especially the T1, affects t_{12} and t_{21} in a different way as described by Sun et

al. [239] as well. The most linear deviation curve belongs to the flush transducers for the SimPAC^2-CFD as well, which is in agreement with the work of Zheng et al. [286].

The SimPAC^2-Ful.-dev. method (Fig. 6.62 (c)) captures flow-acoustic effects, however not for a real but for an ideal Ful.-dev. flow-field. This diagram exposes further the limitations of the consideration of such an ideal flow-field. The state-of-the-art Ful.-dev. (or Analytical) flow-field used in many cases [30], flattens out the differences for different insertion-depths of the transducers, i.e. essentially different geometries. Therefore, apart from obviously not considering the correct flow, it is observed that an insertion-depth or other geometrical investigation would lead to incorrect conclusions for the design of an UTTF. This result highlights further the importance of SimPAC^2-CFD.

A real two-path UTTF [64] was finally measured and simulated with the 'Only CFD-CNA' and the SimPAC^2 methods. In terms of %deviation, it is reminded the 'Only CFD-CNA' method presented a high offset $> 1.5\%$ compared to the SimPAC^2 method and the measurements, which shows the limitations of the 'Only CFD-CNA'. An offset was observed as well when different flow fields were considered, while the best agreement in terms of *%deviation* between simulations and measurements was achieved with the SimPAC^2 method combined with a real CFD flow field.

The investigation of a two-path device demonstrated the different behavior compared to a one-path device considered in case 4, case 5, and case 6.

The deviation for a one-path device is shifted to positive values, as shown in Fig. 6.62, while the values of deviation for a two-path device is closer to '0', as shown in Fig. 6.80, due to the radial position of the paths at $R_{dp} = 0.5 \cdot R$ [176]. Moreover, the real two-path device does not present such a strong Re effect in its deviation curve as the one-path device [159, 176, 190].

The comparison of ToF between SimPAC^2-CFD and SimPAC^2-Ful.-dev., as shown in Figs. 6.67, 6.68 indicates that higher velocities are present in the sound paths when CFD flow is considered, mainly due to the flow inside the cavities. This is confirmed from the flow field findings shown in Figs. 6.72, 6.73. The presence of flow inside the cavities with $v_0[k]>0$ has been studied before by others as well [110, 146].

The received voltage V_5 arrives earlier for measurements compared to the simulations for both upstream and downstream propagation. The reliability of the simulations was controlled with the set criterion $ToF_{crit,m}$ (eq. (4.8)), which was satisfied.

In terms of %deviation, the importance of multiphysics simulations with the consideration of CFD generated flow-fields is highlighted through the deviation curves shown in Fig. 6.80. The accuracy demands of the investigated flowmeter [64] is $\pm 1\%$ and therefore, the %deviation calculated with the Only CFD (CNA) method presents a large difference compared to the measured as well as the calculated %deviation with the SimPAC^2 method. On the other hand, there is a satisfying agreement of %deviation between the measurements and the SimPAC^2-CFD, which is the most accurate method proposed in the thesis, with the intention to be used for design of UTTF and understanding of the underlying phenomena. The simulation of acoustic sound paths, transducers, and CFD is important for the comprehension of the flowmeter operation and for achievement of accurate results. An analysis of both flow and acoustics in 3D domain, as well as their interaction is important for the description of the behavior of an UTTF.

7.1.4 Conclusion - Summary of results and achievements

Concluding, the development of the SimPAC^2 method, its comparison with pure CFD, i.e. 'Only CFD - CNA' method and with measurements, as well as the systematic cavity, flow, insertion depth studies, and the gradual addition of complexity gave insight regarding the 3D flow-field, the presence of vortices in front of the transducers and their effect on acoustics as well as on the %deviation of UTTF.

The pure cavity effect (cf. Sec. 5.3) i.e., the effect of the geometry of the cavity with the same uniform flow-field, was investigated in 3D and with the combination of piezoelectric elements, acoustic wave propagation and flow for the first time.

It was made possible to systematically study and quantify in 3D the flow effects on %deviation with the 'Only CFD-CNA' method and the combined acoustic-flow effects with the SimPAC^2 method, as well as their difference for a single-path UTTF and for recessed, flush, and protruded real transducers (cf. Sec. 6.2).

The SimPAC^2 method gives the advantage of computing the mentioned cavity and flow effects with 3D simulations of piezoelectric transducers, wave acoustics and CFD in contrast to previous studies where only CFD was included [286] or multiphysics simulations but only in 2D and without the inclusion of piezoelectric transducers [239].

For a real two-path UTTF (cf. Sec. 6.3) a difference of %deviation $<0.15\%$ was achieved between the measurements and the SimPAC^2-CFD for $v_{ref} = \{10, 20, 30\}$ m/s. The agreement achieved between measurements and simulations in terms of %deviation, in Sec. 6.3, for a real two-path UTTF [64] gives confidence for further usage of SimPAC^2, with the scope of evaluation of the above mentioned effects related to the UTTF and suggestion of new UTTF designs through the obtained results.

7.2 Outlook and Method Application

7.2.1 UTTF Size Considerations

In the present thesis, the SimPAC^2 method was used for a typical inline gas UTTF [64] with diameter $D = 97$ mm. A typical range of diameters for such a flowmeter is between 25 mm and 300 mm [64]. The method was not tested for smaller diameters, e.g. 25 mm and 50 mm, however its nature of FEM and FVM does not prevent it from being utilized for small diameters, in contrast to the FEM-HIRM method [30] for example, which faces difficulties for UTTF with diameter $\lesssim 50$ mm. The key factor for the successful simulations of flowmeters with small diameters $\lesssim 50$ mm would be the correct setting of the respective absorbing BCs and interfaces connecting the different parts of the divided simulation in distances according to the guidelines given in ch. 4 and 5. However, the FEM-HIRM method is suitable for the range of very large geometries, even > 1000 mm, for which it would be challenging to obtain results of acceptable accuracy according to the set ToF criteria, with the demanded n_t, and n_x discretization described in ch. 4, 5, and 6, due to the high demands of computational power.

A question also arises regarding the possibility to simulate with the SimPAC^2 method an inline gas flowmeter of larger geometry, such as the largest variant of Proline Prosonic Flow G 300, with a diameter $D = 300$ mm. The hindering factor in that case, is the computational power needed. Part (**I**) and part (**III**) need about the same number of finite elements as for Case 7 if the same transducers are used. Part (**II**) however, would need approximately $(300 \text{ mm } / 97 \text{ mm})^3 \simeq 29.58$ times more computational cells if the same meshing strategy is followed. For Case 7, 151 million cells were needed, therefore for a device with $D = 300$ mm, $\simeq$4.4 billion cells would be needed. The mesh though is not scalable one to one and therefore a different meshing strategy would be followed, for which the computational cells for Part (**II**) can easily be reduced to 1 billion. This number of cells is certainly manageable to be solved with the help of Star-CCM+® and an HPC cluster.

7.2.2 Expansion and Potential of the SimPAC^2 Method

The proposed SimPAC^2 method is tailored for inline gas UTTF applications with wetted transducers and their cavities included. However, there is no factor preventing the method from being used for inline UTTF with wetted transducers for liquids or clamp-on UTTF for gas or liquid flows as well.

The expansion of the method to other applications of coupling acoustics with flow is plausible. It has not been tested for other applications, however possible candidates would be atmospheric or underwater acoustics, external flows and internal pipe flows with general complex domains.

A semi-automation of the method has taken place in the operating system Linux [144] with python™ [206]. A further, complete automation and connection of Parts (**I**), (**II**), (**III**), and (**IV**) will help tremendously in its easier and friendlier utilization. Systematic studies of either 2D or 3D geometries will be simplified and consequently, material or ge-

ometrical studies will be easier to perform. If this automation is combined with reduction of computational time, then design optimizations of 3D geometries of UTTF can be carried out.

With the use of the SimPAC^2 method, it is possible to gain deeper insight of the behavior of the flowmeter, not only through the calculation of measurable parameters, such as ToF, Δt, and $\%deviation$ but also of parameters or fields that are difficult to measure. For example, a complete depiction of the acoustic pressure, flow velocity, or mechanical displacement in the solid parts can be obtained, which helps in the design of new generation flowmeters and further understanding of underlying phenomena in UTTF measurement.

Further plans regarding the SimPAC^2 method encompass the inclusion of the meter electronics with simple $1D$ models and the relevant BCs, for the simulation of the whole system.

A suggestion for future work is the extension of piezoelectricity in FVM, as it would greatly facilitate the connection between parts **(I)-(IV)** in the SimPAC^2 method. Furthermore, the optimization of material parameters for piezoelectric elements has always been a challenging topic, as the properties given from manufacturing companies are usually indicative, e.g. [244], and further optimization must be conducted [30], as in Sec. 6.1.

7.2.3 Future Studies in UTTF with the Use of SimPAC^2

The method SimPAC^2 itself or even the 'Only CFD-CNA' can be used in the future for the extraction of optimum sound path position and calculation of the respective weight factors [155, 176]. It is possible to apply either of the methods on multipath inline or clamp-on UTTF for that purpose.

Further studies to be performed with the SimPAC^2 method involve the effect of a number of different flows due to upstream inlet disturbances. This topic is of high interest in the industry and in combination with the 'Only CFD-CNA' method [196], useful results can be delivered.

The simulation of the solid part of the meter body is planned as well, which can, in effect, already be simulated. However, it was omitted in order to save computational time and power. Due to omitting the meter body, no crosstalk effects were investigated and therefore, such a study may be performed in the future.

Another topic that has not been studied in depth yet is the potential effect of turbulence on acoustics. It seems that the frequency of turbulence [58] is much lower than a typical frequency in UTTF [163] and therefore, it might be speculated that the effect is minimum. A systematic study with the assistance of the SimPAC^2 method would shed light into this matter.

The main product of this work, the SimPAC^2 method, allows for systematic studies, 3D simulations and optimization of USM designs. The method is intended to be used as an integral part of the R&D process and as a design-tool of USM in industry with the aim of accelerating the development, gaining understanding, and improving the performance of USM.

Bibliography

[1] M. Aanes, R. A. Kippersund, K. D. Lohne, K.-E. Frøysa, and P. Lunde. Time-of-flight dependency on transducer separation distance in a reflective-path guided-wave ultrasonic flow meter at zero flow conditions. *The Journal of the Acoustical Society of America*, 142(2), 2017.

[2] M. Aanes, K. Lohne, P. Lunde, and M. Vestrheim. Normal incidence ultrasonic beam transmission through a water-immersed plate using a piezoelectric transducer. finite element modeling, angular spectrum method and measurements. In *Proc. of the 19th International Congress on Sound and Vibration (ICSV19)*, page 8 p., Vilnius, Lithuania.

[3] N. Abboud, G. Wojcik, D. Vaughan, J. Mould, D. Powell, and L. Nikodym. Finite element modeling for ultrasonic transducers. In *Proc. SPIE 3341, Medical Imaging 1998: Ultrasonic Transducer Engineering*, San Diego, CA, USA.

[4] A. Abdullah, M. Shahini, and A. Pak. An approach to design high power piezoelectric ultrasonic transducer. *Journal of Electroceramics*, 22:369–382, January 2008.

[5] J. D. Achenbach. *Wave Propagation in Elastic Solids*, volume 16. NORTH-HOLLAND PUBLISHING COMPANY, Amsterdam, London, 1973.

[6] M. J. Aftomsis, M. J. Berger, and M. J. E. Adaptive cartesian mesh generation, 1998.

[7] Agilent Technologies Inc. Agilent 33250A 80 MHz Function/Arbitrary Waveform Generator User's Guide. http://www.ece.mtu.edu/labs/EElabs/EE3306/Revisions_2008/agt33250aman.pdf. Accessed: 2021-04-14.

[8] Agilent Technologies Inc. InfiniiVision 5000/60007000A Series Oscilloscopes User's Guide. https://www.keysight.com/ch/de/assets/9018-01896/user-manuals/9018-01896.pdf. Accessed: 2021-04-14.

[9] F. Akasheh, T. Myers, J. Fraser, S. Bose, and A. Bandyopadhyay. Development of piezoelectric micromachined ultrasonic transducers. *Sensors and Actuators A:Physical*, 111(2-3):275–287, 2004.

[10] K. Aki and P. G. Richards. *Quantitative Seismology*. University Science Books, 2 edition, 2009.

[11] G. Alfonsi. Reynolds-Averaged Navier-Stokes Equations for Turbulence Modeling. *Applied Mechanics Reviews*, 62(4):040802–1 –040802–20, 2009.

[12] H. Allik and T. J. R. Hughes. Finite element method for piezoelectric vibration. *Int. J. Numerical Methods in Engineering*, 2:151–157, 1970.

[13] J. J. D. Anderson. *Computational Fluid Dynamics - The Basics With Applications*. McGraw-Hill, Singapore, 1995.

[14] J. J. D. Anderson. *Fundamentals of Aerodynamics*. McGraw-Hill, New York, USA, 5th edition, 2010.

[15] ANSI/IEEE. IEEE Standard on Piezoelectricity. Technical Report Std 176-1987, The Institute of Electrical and Electronics Engineers, Inc, 1987.

[16] Ansys/DYNARDO. optiSLang®. https://www.dynardo.de/en/software/optislang.html. © Copyright Dynardo - dynamic software & engineering, Accessed: 2020-07-07.

[17] Information on the simulation program Ansys®
https://www.ansys.com/ (Last viewed October 26, 2020).

[18] N. Ashton and M. Stoellinger. Computation of turbulent flow in a rotating pipe using the wlliptic blending reynolds stress model. In *46th AIAA Fluid Dynamics Conference*, Washington DC. the American Institute of Aeronautics and Astronautics.

[19] B. A. Auld. *Acoustic fields and waves in solids*, volume 1. Krieger Publishing Company, Malabar, Florida, 1990.

[20] S. Avdiaj, J. Setina, and N. Syla. Modeling of piezoelectric effect using the finite-element method (FEM). *Materials and Technologies*, 49(4):283, 2009.

[21] AZO MATERIALS. Stainless Steel - Grade 431 (UNS S43100). https://www.azom.com/properties.aspx?ArticleID=1023. Accessed: 2020-11-30.

[22] A. Baker. *Finite element computational fluid mechanics*. McGraw-Hill, New York, 1983.

[23] X. Bao, Q. Xu, and D. Wang. Vibration and acoustic radiation of piezoelectric transducers - fem-equivalent circuit. *Science in China Series A-Mathematics, Physics, Astronomy & Technological Science*, 26(12):1285–1294, 1983.

[24] Z. Belligoli, R. P. Dwight, G. Kok, and P. Lucas. A bayesian study of uncertainty in ultrasonic flow meters under non-ideal flow conditions. *Metrologia*, 54(4), June 2017.

[25] A. Benjeddou. Advances in piezoelectric finite element modeling of adaptive structural elements: a survey. *Computers & Structures*, 76(1-3):347–363, June 2000.

[26] P. G. Bergmann. The wave equation in a medium with a variable index of refraction. *J. Acoust. Soc. Am.*, 17:329 –333, 1946.

[27] A. Bermudez, P. Gamallo, L. Hervella-Nieto, and D. Santamarina. *Fluid-Structure Acoustic Interaction*, chapter 9. Springer-Verlag, 2008.

[28] A. Bermúdez, L. Hervella-Nietto, and R. Rodríguez. Finite element computation of three-dimensional elastroacoustic vibrations. *J. Sound Vibr.*, 219(2):276–306, 1999.

[29] K. Beyer, J. Goldstein, R. Ramakrishnan, and U. Shaft. When is nearest neighbor meaningful? In *Database Theory-ICDT'99*, Israel. Springer.

[30] M. Bezděk. *A Boundary Integral Method for Modeling Sound Waves in Moving Media and its Application to Ultrasonic Flowmeters*. PhD thesis, Universität Erlangen-Nürnberg, Erlangen, 2006.

[31] M. Bezděk, H. Landes, A. Rieder, and R. Lerch. A coupled finite-element, boundary-integral method for simulating ultrasonic flowmeters. *IEEE Trans. Ultrason., Ferroelect., Freq. Contr.*, 54(3):636–646, 2007.

[32] M. Bezděk, A. Rieder, T. Landes, H. Struntz, and R. Lerch. Numerical analysis of wave propagation in an ultrasonic flowmeter. In *Proc. First Congress of Alps Adria Acoustics Association*, pages 573–580, Portoroz, Slovenia, 1-2 Sept. 2003.

[33] F. Billard and D. Laurence. A robust k-ε-v2-k elliptic blending turbulence model applied to near-wall, separated buoyant flows. *International Journal of Heat and Fluid Flow*, 33(1):45–58, 2012.

[34] U. Bülent. *Time-Dependent Laminar, Transitional and Turbulent Pipe Flows*. PhD thesis, Universität Erlangen-Nürnberg, Erlangen, 2008.

[35] D. I. Blokhintzev. The propagation of sound in an inhomogeneous and moving medium. I. *J. Acoust. Soc. Am.*, 18:322 – 328, 1946.

[36] R. Boyer, G. Welsch, and E. W. Collings, editors. *Materials Properties Handbook: Titanium Alloys*. ASM International, Materials Park, OH, 1994.

[37] S. Cen, C.-F. Li, S. Rajendran, and Z. Hu. Advances in finite element method. *Mathematical Problems in Engineering*, 2014:2, March 2014.

[38] Y. A. Cengel and J. M. Cimbala. *Fluid Mechanics - Fundamentals and Applications*. McGraw-Hill Series in Mechanical Engineering, New York, 2006.

[39] CGNS cfd data standard. CFD General Notation System an AIAA Recommended Practice. https://cgns.github.io/index.html. Accessed: 2021-04-20.

[40] P. Challande. Optimizing ultrasonic transducers based on piezoelectric composites using a finite-element method. *IEEE Transactions on Ultrasonics, Ferroelectrics, and Frequency Control*, 37(3):135–140, 1990.

[41] Q. Chen, W. Li, and J. Wu. Realization of a multipath ultrasonic gas flowmeter based on transit-time technique. *Ultrasonics*, 54(1):285–290, January 2014.

[42] I. Chowdhury and S. Dasgupta. Computation of rayleigh damping coefficients for large systems. *Int. J. Space Struct.*, 43(1):6855–6868, 2003.

[43] T. Chung. *Finite element analysis in fluid dynamics*. McGraw-Hill, New York, 1978.

[44] R. Clayton and B. Engquist. Absorbing boundary conditions for acoustic and elastic wave equations. *Bulletin of the Seismological Society of America*, 67(6):1529–1540, 1977.

[45] B. Cockburn, G. E. G. E. Karniadakis, and C. Shu. *Discontinuous Galerkin Methods*, volume 11, chapter 1. Springer-Verlag, Berlin Heidelberg, 2000, 2000.

[46] Comite Europeen de Normalisation. SAI Global Store. https://infostore.saiglobal.com/en-gb/Standards/EN-1434-4-2015-330798_SAIG_CEN_CEN_760908/. Accessed: 2020-06-14.

[47] Information on the simulation program COMSOL Multiphysics® https://www.comsol.com/ (Last viewed October 26, 2020).

[48] COMSOL Multiphysics®, Acoustics module, User's Guide. p. 491, p. 504, (Last viewed on September 13 2018).

[49] K. Conrad and L. Lynnworth. Fundamentals of ultrasonic flowmeters. In *American School of Gas Measurement Technology, 2002 Proceedings*, pages 52–61. Panametrics, 2002.

[50] R. Courant. Variational methods for the solution of problems of equilibrium and vibrations. *Bull. Amer. Math. Soc.*, 69:1–23, 1943.

[51] R. Courant, K. Friedrichs, and H. Lewy. On the partial difference equations of mathematical physics. *IBM Journal of Research and Development*, 11(2):215–234, 1967.

[52] J. L. Davis. *Wave Propagation in Solids and Fluids*. Springer-Verlag, 175 Fifth Avenue, New York, NY 10010, 1988.

[53] F. Delfino and M. Rossi. Finite element techniques for acoustics. In C. Leondes, editor, *MEMS/NEMS*. Springer, Boston, 2006.

[54] J. Delsing. The zero-flow performance of a sing-around ultrasonic flowmeter. *Flow Measurement and Instrumentation*, 2(4):205–208, 1991.

[55] W. Desmet and D. Vandepitte. Finite element modeling for acoustics. In *Numerical Acoustics*. LMS International, 2005.

[56] J. Drenthen. Method and device for determining characteristics of the flow of a medium, 1996.

[57] J. G. Drenthen, M. Kurth, J. van Klooster, and M. Vermeulen. The manufacturing of ultrasonic gas flowmeters. In *27th North Sea Flow Measurement Conference*, Tonsberg, 2009.

[58] F. Durst. *Fluid Mechanics, An Introduction to the Theory of Fluid Flows*. Springer-Verlag, Berlin Heidelberg, 2008.

[59] P.-C. Eccardt, H. Landes, and R. Lerch. Finite element simulation of acoustic wave propagation within flowing media. In *1996 IEEE Ultrasonics Symposium. Proceedings*, San Antonio, TX, USA, USA. IEEE.

[60] P.-C. Eccardt, H. Landes, and R. Lerch. Applications of finite element simulations to acoustic wave propagation within flowing media. *Int. J. of Computer Applications in Technology*, 11(3/4/5):163–169, 1998.

[61] Endress+Hauser. *Flow Handbook, A practical guide: Measurement Technologies - Applications - Solutions*. Endress+Hauser, Reinach, Switzerland, 2004.

[62] Endress+Hauser Flow. Design and sketch of developed unused ultrasonic transducers for Proline Prosonic Flow G 300. Internal report, 2019.

[63] Endress+Hauser Flow. Internal report of Proline Prosonic Flow G 300. Internal report, 2019.

[64] Endress+Hauser Group Services AG. Proline Prosonic Flow G 300 ultrasonic flowmeter. https://www.ch.endress.com/en/field-instruments-overview/flow-measurement-product-overview/Ultrasonic-Flow-Meter-Prosonic-Flow-G300-9G3B. Accessed: 2023-01-24.

[65] Endress+Hauser Group Services AG. Proline Prosonic Flow P 500 ultrasonic flowmeter. https://www.ch.endress.com/en/field-instruments-overview/flow-measurement-product-overview/ultrasonic-flow-meter-prosonic-flow-p500-9p5b?t.tabId=product-overview. Accessed: 2023-01-24.

[66] Endress+Hauser Group Services AG. Prosonic Flow E Heat ultrasonic flowmeter. https://www.ch.endress.com/en/field-instruments-overview/flow-measurement-product-overview/Product-Ultrasonic-flowmeter-Prosonic-Flow-E-Heat. Accessed: 2020-06-14.

[67] B. Engquist and A. Majda. Absorbing boundary conditions for the numerical simulation of waves. *Mathematics of Computation*, 31:629–651, 1977.

[68] R. Ewert and W. Schröder. Acoustic perturbation equations based on flow decomposition via source filtering. *Journal of Computational Physics*, 188(2):365–398, 2003.

[69] F. Fahy. *Foundations of Engineering Acoustics*. Elsevier Academic Press, London, 2001.

[70] H. F. Fasel and S. W.S., editors. *Laminar-Turbulent Transition*, September 13 -17 1999.

[71] J. Ferziger. *Numerical methods for engineering application*. Wiley, New York, 1998.

[72] J. H. Ferziger and M. Peric. *Computational Methods for Fluid Dynamics*. Springer-Verlag, Berlin Heidelberg New York, 2002.

[73] S. Fisher and P. Spink. Ultrasonics as a standard for volumetric flow measurement. In *C.G. Clayton (Ed.), Modern Developments in Flow Measurement*, pages 139–159. Peregrinus, 1972.

[74] S. Franchini, C. Sanz-Andres A., and A. Cuerva. Measurement of velocity in rotational flows using ultrasonic anemometry: The flowmeter. *Experiments in Fluids*, 42(6).

[75] T. Fröhlich, O. Berberig, B. Kissling, Q. Müller, and K. Bussinger. Method for ascertaining a compensated flow and/or a compensated flow speed and ultrasonic flow measuring device, 11 2019.

[76] W. Friedrich, R. Lerch, K. Prestelle, and R. Soldner. Simulations of piezoelectric lamb wave delay lines using a finite element method. *IEEE Transactions on Ultrasonics, Ferroelectrics, and Frequency Control*, 37(3):248–254, May 1990.

[77] K.-E. Frøysa, P. Lunde, and M. Vestrheim. A ray theory approach to investigate the influence of flow velocity profiles on transit times in ultrasonic flow meters for gas and liquid. In *19th International North Sea Flow Measurement Workshop*, Kristiansand, Norway, 22-25 October 2001.

[78] J. A. GallegoJuarez. Piezoelectric ceramics and ultrasonic transducers. *Journal of Physics E: Scientific Intstruments*, 22(10):804–816, 1989.

[79] W. K. Genthe and M. Yamamoto. A new ultrasonic flowmeter for flows in large conduits and open channels. In *R.B. Dowell (Ed.) Flow- Its Measurement and Control in Science and Industry, 1, ISA*, pages 947–955. 1974.

[80] V. Girault and P.-A. Raviart. *Finite element methods for Navier-Stokes equations*. Springer, Berlin, 1986.

[81] O. A. Godin. An exact wave equation for sound in inhomogeneous, moving, and non-stationary fluids. In *Proc. Oceans 2011*, pages 1–5, Waikoloa, HI, USA, 19-22 Sept. 2011. Institute of Electrical and Electronics Engineers.

[82] M. N. Guddati and J. L. Tassoulas. Continued-fraction absorbing boundary conditions for the wave equation. *J. Comp. Acoustics*, 8(1):139–156, 2000.

[83] J. Gwinner and E. Stephan. FEM-BEM coupling. In *Advanced Boundary Element Methods*, volume 52 of *Springer Series in Computational Mathematics*. Springer, Cham, 2018.

[84] A. Hallanger, K.-E. Frøysa, and P. Lunde. Cfd-simulation and installation effects for ultrasonic flowmters in pipes with bends. *Int. J. of Applied Mechanics and Engineering*, 7(1):33–64, 2002.

[85] R. W. Hamming. *Numerical Methods for Scientists and Engineers*. Mc-Graw-Hill, New Jersey, USA, 2 edition, 1973.

[86] A. Hamouda, O. Manck, M. L. Hafiane, and N.-E. Bouguechal. An enhanced technique for ultrasonic flow metering featuring very low jitter and offset. *sensors*, 16:1–12, 2016.

[87] F. Hartmann and C. Katz. *Structural Analysis with Finite Elements*. Springer, Berlin Heidelberg, 2 edition, 2007.

[88] G. Hayward and M. N. Jackson. Discrete-time modeling of the thickness mode piezoelectric transducer. *IEEE Trans. Son. Ultras.*, 31(3):137–150, 1984.

[89] J. Hemp. Theory of transit time ultrasonic flowmeters. *Journal of Sound and Vibration*, 84(1):133–147, 1982.

[90] J. S. Hesthaven and T. Warburton. *Nodal Discontinuous Galerkin Methods: Algorithms, Analysis, and Applications*. Springer-Verlag, New York, USA, 2008.

[91] W. Heywang, K. Lubitz, and W. Wersing, editors. *Piezoelectricity, Evolution and Future of a Technology*, volume 114. Springer-Verlag, Berlin Heidelberg, 2008.

[92] A. Hilgenstock and R. Ernst. Analysis of installation effects by means of computational fluid dynamics—cfd vs experiments? *Flow Measurement and Instrumentation*, 7(3):161–171, September 1996.

[93] R. Holland and E. P. EerNisse. *Design and analysis of piezoelectric resonant devices*. The M.I.T. press, Cambridge, Massachussets and London, England, 1969.

[94] M. Holm, J. Stang, and J. Delsing. Simulation of flowmeter calibration factors for various installation effects. *Measurement*, 15(4):235–244, 1995.

[95] M. W. Hooker. Properties of pzt-based piezoelectric ceramics between -150 and 250^{o}c. Technical Report CR-1009-208708, NASA, 1998.

[96] L. Hu, N. Zhao, Z. Gao, K. Mao, W. Chen, and X. Fu. Calculation of acoustic field based on laser-measured vibration velocities on ultrasonic transducer surface. *Meas. Sci. Technol.*, 29:133–147, 2018.

[97] K. Huebner, E. Thornton, and T. Byrom. *The finite element method for engineers*. John Wiley and Sons, Inc., New York, 1995.

[98] W.-S. Hwang and H. Park. Finite element modeling of piezoelectric sensors and actuators.

[99] B. Iooss, C. Lhuillier, and H. Jeanneau. Numerical simulation of transit-time ultrasonic flowmeters: uncertainties due to flow profile and fluid turbulence. *Ultrasonics*, 40:1009–1015, 2002.

[100] S. A. Jacobson, P. N. Denbigh, and D. E. H. Naude. A new method for the demodulation of ultrasonic signals. *Ultrasonics*, 23(3):128–132, 1985.

[101] N. Jarrin, S. Benamadouche, D. Laurence, and R. Prosser. A synthetic-eddy-method for generating inflow conditions for large eddy simulations. *International Journal of Heat and Fluid Flow*, 27:585–593, 2006.

[102] J. H. Jeng, X. Bao, V. Varadan, and V. Varadan. A complete finite element-eigenmode analysis for a 1-3 type of piezoelectric composite transducer including the effect of fluid loading and internal losses. In *IEEE 1988 Ultrasonics Symposium Proceedings*, Chicago, IL, USA.

[103] J.-M. Jin. *The Finite Element Method in Electromagnetics*. Wiley-IEEE Press, New York, 2014.

[104] Y. Kagawa, T. Tsuchiya, T. Yamabuchi, and T. Furukawa. Finite element simulation of dynamic responses of piezoelectric actuators. *Journal of Sound and Vibration*, 191(4):519–538, 1996.

[105] Y. Kagawa and T. Yamabuchi. Finite element simulation of a composite piezoelectric ultrasonic transducer. *IEEE Transactions on Sonics and Ultrasonics*, 26(2):81–87, 1979.

[106] A. Kalpakli. *Experimental study of turbulent flows through pipe bends*. PhD thesis, Royal Institute of Technology, KTH Mechanics, SE-100 44 Stockholm, Sweden, 2012.

[107] M. Kaltenbacher. *Numerical Simulations of Mechatronics Sensors and Actuators*. Springer-Verlag, Berlin Heidelberg, 2nd edition, 2007.

[108] M. Kaltenbacher. Fundamental equations of acoustics. In M. Kaltenbacher, editor, *Computational Acoustics*. Springer International Publishing, 2018.

[109] M. Kaltenbacher. Non-conforming finite elements for flexible discretization with applications to aeroacoustics. In M. Kaltenbacher, editor, *Computational Acoustics*. Springer International Publishing, 2018.

[110] R. Kažys, A. Vladišauskas, and R. Raišutis. Experimental investigation of gas flow in pipes with recesses for ultrasonic transducers. *Ultragarsas*, 43(2):13–16, 2002.

[111] H. Köchner and A. Melling. Numerical simulation of ultrasonic flowmeters. *Acta Acustica united with Acustica*, 86(1):39–48, 2000.

[112] Keysight Technologies. Keysight | E5100A Network Analyzer - Data Sheet. https://www.keysight.com/ch/de/assets/7018-06686/data-sheets/5966-2888.pdf. Accessed: 2022-01-31.

[113] D. A. Kiefer. *Elastodynamic quasi-guided waves for transit-time ultrasonic flow metering*. PhD thesis, Friedrich-Alexander-Universität Erlangen-Nürnberg, July 2022.

[114] D. A. Kiefer, A. Benkert, and S. J. Rupitsch. Transit time of lamb wave-based ultrasonic flow meters and the effect of temperature. *IEEE transactions on ultrasonics, ferroelectrics, and frequency control*, 69(10):2975–2983, September 2022.

[115] D. A. Kiefer, M. Ponschab, S. J. Rupitsch, and M. Mayle. Calculating the full leaky lamb wave spectrum with exact fluid interaction. *The Journal of the Acoustical Society of America*, 145(6):3341–3350, June 2019.

[116] A. Kierkegaard, A. West, and S. Caro. HVAC noise simulations using direct and hybrid methods. In *Proc. 22nd AIAA/CEAS Aeroacoustics Conference*, Lyon, France, 30 May - 1 June 2016. American Institute of Aeronautics and Astronautics.

[117] L. E. Kinsler, A. R. Frey, A. B. Coppens, and J. V. Sanders. *Fundamentals of Acoustics*. Wiley, New Jersey, USA, 4th edition, 2000.

[118] L. E. Kinsler, A. R. Frey, A. B. Coppens, and J. V. Sanders. *Fundamentals of Acoustics*, pages pp. 120–121, 179–184. Wiley, New Jersey, USA, 4th edition, 2000.

[119] Kitware. ParaView. https://www.paraview.org/. Accessed: 2021-01-25.

[120] Kitware. Paraview. https://www.paraview.org/documentation. Accessed: 2021-01-25.

[121] V. Knappskog. Radiellmode svingninger i piezoelektriske ultralydstransdusere for luft. målinger og endelig-element analyser [radial mode vibrations in piezoe-lectric ultrasound transducers for air. measurements and finite element analyses]. Master's thesis, Dept. of Physics and Techn., Univ. of Bergen, Ber-gen, Norway, 2007.

[122] J. Kocbach. *Finite Element Modeling of Ultrasonic Piezoelectric Transducers, Influence of geometry and material parameters on vibration, response functions and radiated field*. PhD thesis, University of Bergen, Department of Physics, September 2000.

[123] J. Kocbach, P. Lunde, and M. Vestrheim. Fe simulations of piezoceramic disks with a front layer of varying thickness. pages 1113–1117, 1999.

[124] J. Kocbach, P. Lunde, and M. Vestrheim. Resonance frequency spectra with convergence tests of piezoceramic disks using the finite element method. *Acta Acustica united with Acustica*, pages 271–285, 2001.

[125] J. Kocbach, P. Lunde, and M. Vestrheim. Finite element modeling of piezoelectric disks including the radiation into a fluid medium. In *Proc. of 23rd Scandinavian Symposium of on Physical Acoustics*, pages 43–46, Ustaoset, Norway, February 2000.

[126] O. Kolditz. *Computational Methods in Environmental Fluid Mechanics*, chapter Finite Volume Method, pages 173–190. Springer, Berlin Heidelberg, 2002.

[127] J. Kritz. Ultrasonic flowmeter. *Instr. and Automation*, 28(11):1912–1913, November 1955.

[128] H. Kunkel, S. Locke, and B. Pikeoren. Finite-element analysis of vibrational modes in piezoelectric ceramic disks. *IEEE Transactions on Ultrasonics, Ferroelectrics, and Frequency Control*, 37(4):316–328, 1990.

[129] M. Kupnik, P. O'Leary, A. Schroder, and I. Rungger. Numerical simulation of ultrasonic transit-time flowmeter performance in high temperature gas flows. In *IEEE Symposium on Ultrasonics*, Honolulu, HI, USA, 5-8 October 2003.

[130] D. Kurniadi and A. Trisnobudi. A multi-path ultrasonic transit time flow meter using a tomography method for gas flow velocity profile measurement. *Particle and Particle Systems Characterization*, 23(3-4):330–338, October 2006.

[131] T. Lahmer, M. Kaltenbacher, B. Kaltenbacher, R. Lerch, and E. Leder. Fem-based determination of real and complex elastic, dielectric, and piezoelectric moduli in piezoceramic materials. *IEEE Transactions on Ultrasonics, Ferroelectrics, and Frequency Control*, 55(2):465–475, March 2008.

[132] L. D. Landau and E. M. Lifshitz. *Fluid Mechanics*, volume 6. Pergamon Press, Oxford, New York, Beijing, Frankfurt, Sao Paulo, Sydney, Tokyo, Toronto, 2 edition, 1987.

[133] J. Langguth and X. Cai. Heterogeneous cpu-gpu computing for the finite volume method on 3d unstructured meshes. In *2014 20th IEEE International Conference on Parallel and Distributed Systems*, 2014.

[134] V. Leontidis, C. Cuvier, G. Caignaert, P. Dupont, O. Roussette, S. Fammery, P. Nivet, and A. Dazin. Experimental validation of an ultrasonic flowmeter for unsteady flows. *Measurement Science and Technology*, 29(4):330–338, March 2018.

[135] R. Lerch. Finite element analysis of piezoelectric transducers. In *Proc. IEEE Ultrasonics Symposium*, pages 643–654, 1988.

[136] R. Lerch. Simulation of piezoelectric devices by two- and three-dimensional finite elements. *IEEE Transactions on Ultrasonics, Ferroelectrics, and Frequency Control*, 37(3):233–247, 1990.

[137] R. Lerch and H. Landes. CAPA user's manual. Technical report, Institute of Measurement Technology, University of Linz, Austria, 1995.

[138] M. Lesieur, O. Métais, and P. Comte. *Large-Eddy Simulations and Turbulence*. Cambridge University Press, Cambridge, 2005.

[139] R. J. LeVeque. *Finite Difference Methods for Ordinary and Partial Differential Equations: Steady-State and Time-Dependent Problems*. SIAM, Seattle, Washington, 2007.

[140] R. W. Lewis, K. Morgan, H. Thomas, and K. Seetharamu. *The Finite Element Method in Heat Transfer Analysis*. Wiley, New York, 1996.

[141] C. Lhuillier, D. Fiorina, and D. Juvé. Simulation of ultrasound propagation in a thermally turbulent fluid using gaussian beam summation and fourier modes superposition techniques. In *Proceedings of 135th Meeting of the Acoustical Society of America*, pages 1963–1964, 1998.

[142] Y.-z. Li and K.-M. Wu, J.-t. Hu. Numerical simulating nonlinear effects of ultrasonic propagation on high-speed ultrasonic gas flow measurement. *Applied Mathematics & Information Sciences*, 7(5):1963–1967, September 2013.

[143] I. Lie and M. E. Tanase. A sing-around ultrasonic low power flowmeter. In *Int. Conf. on Dynamical Systems and Control*, pages 174–176, Venice, Italy.

[144] LINUX.ORG. Linux operating system. https://www.linux.org/. Accessed: 2021-04-23.

[145] B. Liptak. *Flow Measurement*. Taylor & Francis, Radnor, Pennsylvania 19089, 1993.

[146] T. Løland. *Experimental Investigation of Cavity Flows*. PhD thesis, Norwegian University of Science and Technology, Trondheim, 1998.

[147] T. Løland, L. R. Sætran, R. Olsen, I. R. Gran, and R. Sakariassen. Fluid motion in ultrasonic flowmeter cavities. *J. Fluids Eng.*, 121(2):422–426, Jun 1999.

[148] S. H. Lo. *Finite Element Mesh Generation*. CRC Press, 2015.

[149] P. Loveday. Analysis of piezoelectric ultrasonic transducers attached to waveguides using waveguide finite elements. *IEEE Transactions on Ultrasonics, Ferroelectrics, and Frequency Control*, 54(10):2045–2051, October 2007.

[150] P. Lowe, S. Fateri, R. Sanderson, and N. boulgouris. Finite element modelling of the interaction of ultrasonic guided waves with coupled piezoelectric transducers. *Insight - Non-Destructive Testing and Condition Monitoring*, 56(9):505–509, September 2014.

[151] A. Luca, K. Fodil, and A. Zerarka. Full-wave numerical simulation of ultrasonic transit-time gas flowmeters. In *2016 IEEE International Ultrasonics Symposium (IUS)*, Tours, France, Sept. 2016.

[152] A. Luca, R. Marchiano, and J.-C. Chassaing. Numerical simulation of transit-time ultrasonic flowmeters by a direct approach. *IEEE Transactions on Ultrasonics, Ferroelectrics, and Frequency Control*, 63(6):886–897, 2016.

[153] A. Luca, R. Marchiano, and J.-C. Chassaing. A discontinuous galerkin approach for the numerical simulation of transit-time ultrasonic flowmeters. In *2014 IEEE International Ultrasonics Symposium*, Chicago, IL, USA, 3-6 Sept. 2014.

[154] P. Lunde, K.-E. Frøysa, R. A. Kippersund, and M. Vestrheim. Transient diffraction effects in ultrasonic meters for volumetric, mass and energy flow measurement of natural gas. In *21st International North Sea Flow Measurement Workshop*, Tønsberg, Norway, 28-31 October 2003.

[155] P. Lunde, K. E. Frøysa, and M. Vestrheim, editors. *GERG Project on Ultrasonic Gas Flow Meters, Phase II*. VDI Verlag, Düsseldorf, 2000.

[156] P. Lunde, R. A. Kippersund, and M. Vestrheim. Signal modelling using the *FLOSIM* system model in ultrasonic instrumentation for industrial applications. In *Proc. of NORSIG 2003, Norwegian Symposium on Signal Processing*, Bergen, Norway.

[157] P. Lunde and M. Vestrheim. Reciprocity and its utilization in ultrasonic flow meters. In *23rd International North Sea Flow Measurement Workshop*, pages 85–112, Tønsberg, Norway.

[158] A. Lygre, M. Vestrheim, P. Lunde, and V. Berge. Numerical simulation of ultrasonic flowmeters. In *Ultrasonics International 87 Conf. Proc.*, pages 196–201, 1987.

[159] A. M. Lynnworth and L. C. Lynnworth. Calculated turbulent flowmeter factors for nondiametrical paths used in ultrasonic flow meters. *Trans. ASME*, 107:44–48, 1985.

[160] L. C. Lynnworth. *Ultrasonic Flowmeters*, chapter 5, pages 407–525. Academic Press, INC, 1979.

[161] L. C. Lynnworth. Ultrasonic flowmeters. *Transactions of the Institute of Measurement and Control*, 3(4):217–223, October 1981.

[162] L. C. Lynnworth. Ultrasonic transducer system with crosstalk isolation. *The Journal of the Acoustical Society of America*, November 1995.

[163] L. C. Lynnworth and Y. Liu. Ultrasonic flowmeters: Half-century progress report, 1955-2005. *Ultrasonics*, 44:e1371–e1378, June 2006.

[164] R.-G. Lyons. *Understanding Digital Signal Processing*. Pearson Academic, 3 edition, 2010.

[165] B. Mahbaz, C. G., and M. Dusseault. Calibration of a piezoelectric transducer through laser measurements and numerical simulation. *Journal of Environmental & Engineering Geophysics*, 24(1):39–48, April 2019.

[166] R. Manceau and K. Hanjalic. Elliptic blending model: A new near-wall reynolds-stress turbulence closure. *Physics of Fluids*, 14(2):744–754, 2002.

[167] R. S. Martins, G. S. de Aquino, M. F. Martins, and R. Ramos. Sensitivity analysis for numerical simulations of disturbed flows aiming ultrasonic flow measurement. *Measurement*, 185:110015, Nov. 2021.

[168] R. S. Martins and R. Ramos. Bend installation effects on the correction factor of single-path ultrasonic flow meters. In *XXXII Iberian Latin American Congress on Computational Methods in Engineering*, Outo Preto, Brazil, November 2011.

[169] W. P. Mason. *Electro-Mechanical Transducers and Wave Filters*. D. Van Nostrand Co., 1948.

[170] C. Mattiussi. An analysis of finite volume, finite element, and finite difference methods using some concepts from algebraic topology. *Journal of Computational Physics*, 133:289–309, 1997.

[171] M. McCartney, C. Mudd, and R. Livengood. A corrected ray theory for acoustic velocimetry. *J. Acoust. Soc. Am.*, 65:50–55, 1979.

[172] P. W. McDonald. The computation of transonic flow through two-dimensional gas turbine cascades. In *Turbo Expo: Power for Land, Sea, and Air*, number 71-GT-89, Houston, Texas, USA, 1971.

[173] F. R. Menter, J. Schütze, K. A. Kurbatskii, M. Gritskevich, and A. Garbaruk. Scale-resolving simulation techniques in industrial cfd. In *6th AIAA Theoretical Fluid Mechanics Conference*, 06 2011.

[174] W. L. Meyer, W. A. Bell, and B. T. Zinn. Boundary integral solutions of three dimensional acoustic radiation problems. *J. Sound and Vibr.*, 59(2):245–262, 1978.

[175] E. Mitsoulis and J. Vlachopoulos. The finite element method for flow and heat transfer. *Advances in Polymer Technology*, 4(2):107–121, June 1984.

[176] P. I. Moore, G. J. Brown, and B. P. Stimpson. Ultrasonic transit-time flowmeters modelled with theoretical velocity profiles: methodology. *Meas. Sci. Technol.*, 11:1802–1811, 2000.

[177] F. Moukalled, L. Mangani, and M. Darwish. *The Finite Volume Method in Computational Fluid Dynamics*, volume 113. Springer International Publishing, Switzerland, 2016.

[178] S. Mousavi, S. Hashemabadi, and J. Jamali. New semi three-dimensional approach for simulation of lamb wave clamp-on ultrasonic gas flowmeter. *Sensor Review*, 40(4):465–476, June 2020.

[179] S. Mousavi, S. Hashemabadi, and J. Jamali. Calculation of geometric flow profile correction factor for ultrasonic flow meter using semi-3d simulation technique. *Ultrasonics*, 106:106165, April 2020.

[180] S. Mousavi, S. Hashemabadi, and H. A. Moghaddam. Design, simulation, fabrication and testing of ultrasonic gas flowmeter transducer (sensor). *Sensor Review*, 39(2):277–287, March 2019.

[181] M. K. Myers. On the acoustic boundary condition in the presence of flow. *J. Sound and Vibration*, 71(3):429–434, 1980.

[182] K. S. Mylvaganam. High-rangeability ultrasonic gas flowmeter for monitoring flare gas. *IEEE Trans. Ultrason. Ferroelectr. Freq. Control*, 26(2):144–149, 1989.

[183] Information on the simulation program NACS https://www.simetris.de/en/Table/Products/NACS-Finite-Element-Simulation/ (Last viewed April 1, 2020).

[184] Z. Nazarchuk, V. Skalskyi, and O. Serhiyenko. *Acoustic Emission, Methodology and Application*, chapter 2. Springer International Publishing AG, 2017.

[185] N. M. Newmark. A method of computation for structural dynamics. *Journal of Engineering Mechanics*, 85(EM3):67–94, 1959.

[186] M. Nishi. *Laminar to turbulent transition in pipe flow through puffs and slugs*. PhD thesis, Erlangen: Technische Fakultät der Friedrich-Alexander-Universität Erlangen-Nürnberg, 2009.

[187] V. E. Ostashev and D. K. Wilson. *Acoustics in Moving Inhomogeneous Media, Second Edition*. CRC Press, Boca Raton, FL, USA, 2015.

[188] V. E. Ostashev, D. K. Wilson, L. Liu, D. F. Aldridge, N. P. Symons, and D. Marlin. Equations for finite-difference, time-domain simulation of sound propagation in moving inhomogeneous media and numerical implementaion. *J. Acoust. Soc. Am.*, 117:503–517, 2005.

[189] I. J. O'Sullivan and W. M. D. Wright. Ultrasonic measurement of gas flow using electrostatic transducers. *Ultrasonics*, 40(1-8):407–411, June 2002.

[190] C.-N. Pannell, W. A. B. Evans, and D. A. Jackson. A new integration technique for flowmeters with chordal paths. *Flow Measurement and Instrumentation*, 1(4):216–224, 1990.

[191] E. Papadakis. Ultrasonic transducer evaluation in five "domains": time, space, frequency, surface motion, and theory. In *IEEE Ultrason. Symp.*, pages 104–112, Phoenix, Arizone, USA.

[192] P. Papathanasiou. CFD simulations of ultrasonic flowmeters: The effect of line, volume, and Gauss-weighted integration of sound paths on the flowmeter's linearity. Internal presentation, 2015.

[193] P. Papathanasiou. CFD simulations for the optimization of the flow-field of a gas calibration rig. Internal presentation, 2016.

[194] P. Papathanasiou. ResearchGate, 2023. https://www.researchgate.net/profile/Panagiotis-Papathanasiou, (Last viewed January, 2023).

[195] P. Papathanasiou, B. Kissling, O. Berberig, V. Kumar, A. Rohner, and M. Bezděk. Flow disturbance compensation calculated with flow simulations for ultrasonic clamp-on flowmeters with optimized path arrangement. *Flow Measurement and Instrumentation*, 85(4):102–167, March 2022.

[196] P. Papathanasiou, B. Kissling, V. Kumar, A. Rohner, O. Berberig, and M. Bezděk. Effect of an asymmetric flow disturber on an ultrasonic flowmeter. *Technisches Messen*, 87:3–17, 2019.

[197] P. Papathanasiou, P. Lunde, M. Bezděk, and V. Kumar. 3D simulation of ultrasonic flowmeters using a hybrid FEM-FVM method. In *ULTRASONICS 2020, Proceedings Book*, Caparica, Lisbon, Portugal, 20th - 23rd July 2020.

[198] A. Pascau, C. Pérez, and F. J. Serón. A comparison of segregated and coupled methods for the solution of the incompressible navier-stokes equations. *Numerical Methods in Biomedical Engineering*, 12(10):617–630, 1996.

[199] S. V. Patankar and D. B. Spalding. A calculation procedure for heat, mass and momentum transfer in three-dimensional parabolic flows. *International Journal of Heat and Mass Transfer*, 15:1787–1806, 1972.

[200] M. Petyt. Finite element techniques for acoustics. In P. Filippi, editor, *Theoretical Acoustics and Numerical Techniques*, volume 217. Springer, Vienna, 1983.

[201] C. Peyret and G. Élias. Finite-element method to study harmonic aeroacoustics problems. *Journal of the Acoustical Society of America*, 110(2):661, August 2001.

[202] C. Piao and J. Kim. Vibration characteristics of an ultrasonic transducer of two piezoelectric discs. *Ultrasonics*, 74:72–80, February 2017.

[203] A. D. Pierce. Wave equation for sound in fluids with unsteady inhomogeneous flow. *J. Acoust. Soc. Am.*, 87(6):2292–2299, 1990.

[204] A. D. Pierce. *Acoustics: An Introduction to Its Physical Principles and Applications*. Acoustical Society of America, New York, USA, 1991.

[205] S. B. Pope. *Turbulent Flows*. Cambridge University Press, 2000.

[206] Python Software Foundation. python™. https://www.python.org/. Accessed: 2020-10-19.

[207] L. Qin, L. Hu, K. Mao, W. Chen, and X. Fu. Flow profile identification with multipath transducers. *Flow Measurement and Instrumentation*, 52:148–156, 2016.

[208] L. H. Qin, Z.-Y. Tang, L. Hu, X. Fu, and P. Ye. Numerical analysis of transducer installation effect on ultrasonic gas flow meter. *Applied Mechanics and Materials*, 687-691:1019–1025, 2014.

[209] R. Raišutis. Investigation of the flow velocity profile in a metering section of an invasive ultrasonic flowmeter. *Flow Measurement and Instrumentation*, 17(4):201–206, 2006.

[210] V. T. Rathod. A review of electric impedance matching techniques for piezoelectric sensors, actuators and transducers. *Electronics*, 169(8), 2019.

[211] J. W. S. Rayleigh. *The theory of sound*, volume I. Macmillan and Co., London, 1877.

[212] J. W. S. Rayleigh. *The theory of sound*, volume II. Macmillan and Co., London, 1878.

[213] P. D. rer. nat. Heinz Antes. A short course on boundary element methods, November 2010.

[214] J. J. Reyes and A. Acevedo. Modeling and simulation of ultrasonic flow meters: State of art. *IEEE ANDESCON*, page 7, September 2010.

[215] J. J. Reyes and A. Acevedo. Simulation and experimental validation of a transit time in an ultrasonic gas flow meter using air. *2010 IEEE ANDESCON Conference Proceedings, ANDESCON 2010*, September 2010.

[216] J. Ruge and K. Stüben. Algebraic multigrid (amg), multigrid methods. In *Frontiers in Applied Mathematics*, volume 5, pages 73–130. SIAM, 1986.

[217] S. J. Rupitsch, F. Wolf, A. Sutor, and R. Lerch. Estimation of material parameters for piezoelectric actuators using electrical and mechanical quantities. In *Ultrasonics Symposium (IUS), 2009 IEEE International*, pages 1–4, 2009.

[218] M. N. Rychagov and S. Tereshchenko. Multi-path flow rate measurements of symmetric and asymmetric flows. *Inverse Problems*, 16(2):495, April 2000.

[219] D. Saravanos, P. Heyliger, and D. Hopkins. Layerwise mechanics and finite element for the dynamic analysis of piezoelectric composite plates. *International Journal of Solids and Structures*, 34(3):359–378, 1997.

[220] H. Schlichting and K. Gersten. *Boundary-Layer Theory*. Springer-Verlag Berlin Heidelberg, Berlin, Heidelberg, 9 edition, 2017.

[221] Schweizerische Eidgenossenschaft. Swiss Accreditation Service SAS. https://www.sas.admin.ch/sas/en/home.html, 2019. Accessed: 2020-06-14.

[222] T. Sengupta and B. Swagata. *DNS of Wall-Bounded Turbulent Flows*. Springer Singapore, Singapore, 2019.

[223] T. K. Sengupta. *High Accuracy Computing Methods*. Cambridge University Press, Delhi, India, 1 edition, May 2013.

[224] R. Shakar. *Fundamentals of Physics*, volume II. Yale University Press, New Haven and London, 2016.

[225] H. Sheng, P. Lihui, and H. Nakazato. Computational fluid dynamics based sound path optimization for ultrasonic flow meter. *Chinese Journal of Scientific Instrument*, 4, 2009.

[226] A. V. Shenoy. Power-law fluid velocity profiles in turbulent pipe flow. In *Flow Dynamics and Frictional Behavior*, chapter 31, pages 1034–1059. 1986.

[227] T.-H. Shih, W. W. Liou, A. Shabbir, Z. Yang, and J. Zhu. A new k-ε eddy viscosity model for high reynolds number turbulent flows. *Computers & Fluids*, 24(3):227–238, 1995.

[228] M. Shur, P. R. Spalart, M. K. Strelets, and A. K. Travin. A hybrid rans-les approach with delay-des and wall-modelled les capabilities. *International J. Heat and Fluid Flow*, 29(6):1638–1649, 2008.

[229] Siemens. STAR-CCM+® Documentation, 2022. (Last viewed December 14, 2022).

[230] R. Simkovics, H. Landes, M. Kaltenbacher, and R. Lerch. Nonlinear finite element analysis of piezoelectric transducers. *Proceedings of the IEEE Ultrasonics Symposium 2*, 2:1057–1060, 1999.

[231] M. Simurda, L. Duggen, N. T. Basse, and B. Lassen. Fourier collocation approach with mesh refinement method for simulating transit-time ultrasonic flowmeters under multiphase flow conditions. *IEEE Transactions on Ultrasonics, Ferroelectrics, and Frequency Control*, 65(2):244–257, 2018.

[232] M. Simurda, B. Lassen, L. Duggen, and N. T. Basse. A fourier collocation approach for transit-time ultrasonic flowmeter under multiphase flow conditions. *Journal of Computational Acoustics*, 25(4), 2017.

[233] K. Smyth and S.-G. Kim. Experiment and simulation validated analytical equivalent circuit model for piezoelectric micromachined ultrasonic transducers. *IEEE Transactions on Ultrasonics, Ferroelectrics, and Frequency Control*, 62(4):744–765, 14 April 2015.

[234] C. Song and J. Wolf. The scaled boundary finite-element method: analytical solution in frequency domain. *Computer Methods in Applied Mechanics and Engineering*, 164(1-2):249–264, 2 October 1998.

[235] Information on the simulation program STAR-CCM+® https://mdx.plm.automation.siemens.com/star-ccm-plus (Last viewed August, 2020).

[236] W. Steenbergen. *Turbulent Pipe Flow with Swirl*. PhD thesis, Eindhoven University of Technology, 1996.

[237] P. R. Stepanishen. Pulsed transmit/receive response of ultrasonic piezoelectric transducers. *J. Acoust. Soc. Amer.*, 69(6):1815–1827, 1981.

[238] E. Storheim, P. Lunde, and M. Vestrheim. Diffraction correction in ultrasonic fields for measurements of sound velocity in gas. conventional and alternative methods. In *34th Scandinavian Symposium on Physical Acoustics*, Geilo, Norway.

[239] Y. Sun, T. Zhang, and D. Zheng. New analysis scheme of flow-acoustics coupling for gas ultrasonic flowmeter with vortex near transducer. *Sensors*, 18:1–22, 2018.

[240] H. Suzuki, H. Nakabori, and M. Yamamoto. In *C.G. Clayton (Ed.), Modern Developments in Flow Measurement*, pages 115–138. Peregrinus, London, 1972.

[241] K. Tawackolian. *Fluiddynamische Aswirkungen auf die Messabweichung von Ultraschall-Durchflussmessgeräten*. PhD thesis, Technische Universität Berlin, 2013.

[242] N. C. Temperley, M. Behnia, and A. F. Collings. Application of computational fluid dynamics and laser doppler velocimetry to liquid ultrasonic flow meter design. *Flow Measurement and Instrumentation*, 15(3):155–165, 2004.

[243] ©2020 ZWorkstations.com, All Rights Reserved. Z WORKSTATIONS. https://zworkstations.com/products/z840/. Accessed: 2020-10-20.

[244] ©Meggit A/S. MEGGIT Ferroperm$_{TM}$ piezoceramics. https://www.meggittferroperm.com/materials/. Accessed: 2020-07-07.

[245] ©Meggit A/S. MEGGIT Ferroperm$_{TM}$ piezoceramics. https://www.meggittferroperm.com/. Accessed: 2022-01-31.

[246] THE EUROPEAN PARLIAMENT. EUR-Lex. https://eur-lex.europa.eu/legal-content/EN/TXT/?uri=CELEX%3A32014L0032. Accessed: 2020-06-14.

[247] The SciPy community. SciPy.org. https://docs.scipy.org/doc/scipy/reference/generated/scipy.signal.welch.html. © Copyright 2008-2020, Accessed: 2021-01-13.

[248] L. Thompson. A review of finite-element methods for time-harmonic acoustics. *Journal of the Acoustical Society of America*, 20(3):1315–1330, March 2006.

[249] TOP500.org (c). TOP500 Supercomputer Sites. https://www.top500.org/. Accessed: 2020-03-30.

[250] S. Triebenbacher. mesh2mesh: Mesh conversion tool for fem solvers at e+h. Internal presentation, 2018.

[251] M. Turiso, M. Straka, J. Rose, C. Bombis, and D. F. Hinz. The asymmetric swirl disturbance generator: Towards a realistic and reproducible standard. *Flow Measurement and Instrumentation*, 60:144–154, April 2018.

[252] H. Tzou. Development of a light-weight robot end-effector using polymeric piezoelectric bimorph. In *1989 IEEE International Conference on Robotics and Automation*, Los Angeles, CA, USA.

[253] J. Štigler. Introduction of the analytical turbulent velocity profile between two parallel plates. pages 1343–1352, Svratka, Czech Rebublic, May 14-17, 2012.

[254] H. Versteeg and W. Malalasekera. *An Introduction to Computational Fluid Dynamics: The Finite Volume Method*. Pearson, Edinburgh Gate, Harlow, 2 edition, 2007.

[255] S. Vervik. *Methods for characterization of gas-coupled ultrasonic sender-receiver measurement systems*. PhD thesis, Dept. of Physics, Univ. of Bergen, Bergen, Norway, 2000.

[256] I. A. Viktorov. *Rayleigh and Lamb Waves, Physical Theory and Applications*. Springer Science+Business Media, New York, 1967.

[257] H. von Garßen and V. Mágori. *Modelling of Ultrasonic Flow Meters by Acoustical Raytracing*, volume 22, pages 507–512. Springer, Boston, MA, 1996.

[258] A. von Jena and V. Mágori. Ultrasound gas-flow meter for household application. *Sensor and Actuators A: Physical*, 37-38:135–140, June-August 1993.

[259] A. Voser and T. Staubli. CFD calculations of the protrusion effect and impact on the acoustic discharge measurement accuracy. In *IGHEM*, Montreal, Canada, 1996.

[260] B. Wang, Y. Cui, W. Liu, and X. Luo. Study of transducer installation effects on ultrasonic flow metering using computational fluid dynamics. *Advanced Materials Research*, 629:676–681, December 2012.

[261] B. Wang, Y. Cui, and X. Luo. Study of transducer installation effects on ultrasonic flow metering using computational fluid dynamics. *Advanced Materials Research*, 629:676–681, 2012.

[262] G. G. Wang, Z. Dong, and P. Aitchison. Adaptive response surface method - a global optimization scheme for approximation-based design problems. *Engineering Optimization*, 33(6):707–733, 2001.

[263] F. J. J. Weber. *Ultrasonic Beam Propagation in Turbulent Flow.* PhD thesis, Worchester Polytechnic Institute, 2003.

[264] A. Weissenbrunner, A. Fiebach, S. Schmelter, M. Bär, P. Thamsen, and T. Lederer. Simulation-based determination of systematic errors of flow meters due to uncertain flow conditions. *Flow Meas. Instrum.*, 14:25–39, 2016.

[265] P. D. Welch. The use of fast fourier transform for the estimation of power spectra: A method based on time averaging over short, modified periodograms. *IEEE Transactions on Audio and Electroacoustics*, AU-15(2):70–73, 1967.

[266] P. Wesseling. Multigrid methods in computational fluid dynamics. *ZAMM - Z. Angew. Math. Mech.*, 70:T337–T347, 1990.

[267] B. A. Wilcox. *Turbulence Modeling for CFD.* D C W Industries, 3 edition, 2006.

[268] L. C. Wilcox, G. Stadler, C. Burstedde, and O. Ghattas. A high-order discontinuous galerkin method for wave propagation through coupled elastic-acoustic media. *J. Comput. Phys.*, 229(24):9373–9396, 2010.

[269] P. Wilcox, R. Monkhouse, P. Cawley, M. Lowe, and B. Auld. Development of a computer model for an ultrasonic polymer film transducer system. *NDT & E International*, 31(1):51–64, 1998.

[270] M. Willatzen. Ultrasound transducer modeling - general theory and applications to ultrasound reciprocal systems. *IEEE Trans. Ultrason., Ferroelect., Freq. Contr.*, 48:100–112, 2001.

[271] M. Willatzen. Flow acoustics modelling and implications for ultrasonic flow measurement based on the transit-time method. *Ultrasonics*, 41:805–810, 2003.

[272] A. O. Williams. The piston source at high frequencies. *J. Acoust. Soc. Am.*, 23:1–6, 1951.

[273] M. Wolfstein. The velocity and temperature distribution of one-dimensional flow with turbulence augentation and pressure gradient. *Int. J. of Heat and Mass Transfer*, 12:301–318, 1969.

[274] W. L. Wood, M. Bossak, and O. C. Zienkiewicz. An alpha modification of Newmark's method. *International Journal for Numerical Methods in Engineering*, 15:1562–1566, 1980.

[275] I. J. Wygmanski and F. H. Champagne. On transition in a pipe. part 1. the origin of puffs and slugs and the flow in a turbulent slug. *J. Fluid Mech.*, 59:281–351, 1973.

[276] K. Yamaguchi, H. Yagami, and T. Fuji. New method of time domain analysis of the performance of multilayered ultrasonic transducers. *IEEE Trans. Ultras., Ferroelect., Freq., Contr.*, 33(6):669–678, 1986.

[277] R. Øyerhamn, E. N. Mosland, E. Storheim, P. Lunde, and M. Vestrheim. Finite element modeling of ultrasound measurement systems for gas. comparison with experiments in air. *J. Acoust. Soc. Am.*, 144(4):2613–2625, 2018.

[278] Y. Yu and G. Zong. Note: Ultrasonic liquid flow meter for small pipes. *Rev Sci Instrum.*, 83(2), 2012.

[279] W. Zeng and G. Liu. Smoothed finite element methods (s-fem): An overview and recent developments. *Archives of Computational Methods in Engineering*, 25:397–435, 2018.

[280] J. Zhang. Wave propagation accross fluid-solid interfaces: A grid method approach. *Geophys. J. Int.*, 159(1):240–252, 2004.

[281] H. Zhao, L. Peng, S. Stephane, H. Ishikawa, K. Shimizu, and M. Takamoto. CFD aided investigation of multipath ultrasonic gas flow meter performance under complex flow profile. *IEEE Sens. J.*, 14:897–907, 2014.

[282] N. Zhao, L. Hu, X. Peng, Z. Fang, W. Chen, and X. Fu. A method combining measurement tool and numerical simulation for calculating acoustic signals of ultrasonic flowmeters. *IEEE Sensors Journal*, 19(24):11805–11813, 2019.

[283] D. Zheng, S.-H. Lv, and Y. Mao. Effect mechanism of non-ideal flow field on acoustic field in gas ultrasonic flowmeter. *IET Science, Measurement & Technology*, 13(4):469–477, 2019.

[284] D. Zheng, J. Mei, and M. Wang. Improvement of gas ultrasonic flowmeter measurement non-linearity based on ray tracing method. *IET Science, Measurement & Technology*, 10(6):602–606, 2016.

[285] D. Zheng, L. S.-H., and Y. Mao. A new method for researching the acoustic field of gas ultrasonic flowmeter based on a Gaussian beam. *Meas. Sci. Technol.*, 30, 2019.

[286] D. Zheng, P. Zhang, and T. Xu. Study of acoustic transducer protrusion and recess effects on ultrasonic flowmeter measurement by numerical simulation. *Flow Measurement and Instrumentation*, 22:488–493, 2011.

[287] H. Zhou, T. Ji, R. Wang, X. Ge, X. Tang, and S. Tang. Multipath ultrasonic gas flow-meter based on multiple reference waves. *Ultrasonics*, 82:145–152, January 2018.

[288] F. Ziegler. *Mechanics of Solids and Fluids*. Springer, New York, USA, 1995.

[289] O. C. Zienkiewicz, R. L. Taylor, and J. Z. Zhu. *The Finite Element Method: Its Basis and Fundamentals*. Elsevier Butterworth-Heinemann, Oxford, UK, 7 edition, 2013.

Graphic design: Communication Division, UiB / Print: Skipnes Kommunikasjon AS

uib.no

ISBN: 9788230859841 (print)
9788230852910 (PDF)